G9a and EZH2 histone methyltransferase inhibition modulates the immune microenvironment of ovarian cancer

Pavlina Spiliopoulou

MRCP(UK), MSc

A thesis submitted in fulfilment of the requirements for the degree of

Doctor of Philosophy

College of Medical, Veterinary and Life Sciences

University of Glasgow

November 2020

Abstract

Despite ample clinical evidence that prognosis of patients with advanced ovarian cancer is critically dependent on the anti-tumour immune response, cancer immunotherapy treatments have failed to achieve a meaningful survival benefit for many patients. A need to potentiate the host's immune response against ovarian cancer cells is therefore imperative. Ovarian cancer cells manage to evade immune responses by altering the epigenome in a way that it can modulate all steps of the immune cycle. This includes antigen presentation, lymphocyte priming, activation and trafficking, as well as cytotoxic lymphocyte effector functions. DNA methylation and histone deacetylation were the two mechanisms initially identified to play a crucial role in immune evasion, with histone methylation being an important emerging pathway too.

In this PhD project, I initially sought to discover novel epigenetic mechanisms involved in the immune process in a *Trp53*$^{-/-}$ murine model of ovarian cancer by undertaking a medium-throughput screening with a library of novel epigenetic probes. G9a and EZH2 histone lysine methyltransferases emerged as mechanisms implicated in the release of lymphocyte chemotactic chemokines, such as CXCL9, CXCL10 and CXCL11. By using a novel dual inhibitor and with a combination of cellular, transcriptional and chromatin accessibility assays, I observed that simultaneous inhibition of G9a and EZH2 modulated the tumour immune microenvironment. I observed a transcriptional upregulation of immune pathways, coupled with cellular changes that represented a favourable immune profile intratumorally. The cellular changes included modulation of CD8^{+} lymphocyte phenotype, an increase in the presence of Natural Killer cells and an increase in expression of CXCR3, the receptor for CXCL9-11 chemokines. Moreover, these alterations in the immune microenvironment were accompanied by a modest therapeutic effect.

The results of this thesis highlight the importance of inhibiting G9a/EZH2 in *Trp53*$^{-/-}$ ovarian cancer.

Contents

List of figures

List of tables

List of Appendices

Acknowledgement

I had the luck (and challenge) to carry out my PhD in two different laboratories, at the Wolfson Wohl Cancer Research Centre in the University of Glasgow (UoG) and at the Institute of Reproductive and Developmental Biology, at Imperial College in London. There is, therefore, a long list of people whose help I owe to acknowledge here.

First and foremost, I would like to wholeheartedly thank my primary supervisor, Iain, for being a great supervisor and mentor throughout an adventurous PhD. Iain was pivotal in my decision to pursue a lab-based PhD in the first place, by being the most inspirational example of a clinician scientist. Iain has the great quality to encourage people to strive for improvement, in the most supporting and nurturing way. I will always be grateful to him for the opportunity to experience - what now seems - a short journey in cancer science.

I am also extremely thankful to Tricia Roxburgh for participating in my supervision at the crucial last few months of my PhD and allowing some of my experiments to take place in her lab in Glasgow. Seth Coffelt provided his expertise in immunology, as well as crucial mentorship when I needed it the most, and Bob Brown provided his expertise in epigenetics and a warm welcome at Imperial. A big thank you to Peter Adams who instilled the first ideas about epigenetics and immune response in cancer, to Matt Fuchter for allowing me to work with the HKMTI-1-005 compound and Anthony Chalmers for reviewing my progress.

From my time in the “Glasgow lab”, I owe a massive thank you to: Josephine for generating the cell lines that I have worked with throughout my project; Suzanne for teaching me basic lab techniques when I could not tell the difference between a pipette and a stripette (as well as endless conversations on music, politics and the intersection of both); Alex for sharing a desk, a mini-pharmacy and his crucial lab recipes with me; Malcolm and Elaine for the clinician-in-the-lab camaraderie; Darren for always giving me sensible life-

advice; Aula for her inspirational life stories and of course the numerous lab allies, Eirini Lampraki, Lynn McGarry, Susan Mason, Karen Blyth and Colin Dixon.

From the “London lab”, I will be eternally grateful to Sarah Spear for helping me settle in a new lab, for teaching me flow cytometry (or at least trying her very hardest to teach me) and infecting me with some of her endless passion for cancer immunology. I am also thankful to her for some quite enjoyable bouldering sessions. Many thanks to Sophie for the slightly morbid lunch discussions that nobody else enjoyed apart from us; to Jaya for the philosophical evening discussions that nobody else heard apart from us; Ian G for showing me a glimpse of hands-on epigenetics; Hasan for his expertise in bioinformatics and Marina Natoli for helping me with “ERV-ology”. I am also grateful to Paula and Natasha for being my 4th floor buddies and also, Zhao, Carmen and Keira for all their help.

From the “real life lab”, I should thank my family and my close friends for supporting me in so many different ways through the years and particularly my sisters, Alexandra and Anna, who were always available to lend an ear and graciously pretend they sympathised with my sense of disappointment following failed experiments. And last, but certainly not least, a warm thank you to my partner, Victoria, for all the obvious reasons; these are perhaps too many for an 80,000-word limited thesis to encompass.

Author's declaration

The work presented in this thesis was performed entirely by the author, except as acknowledged at the Wolfson Wohl Cancer Research Centre, Institute of Cancer Sciences, University of Glasgow and at the Institute of Reproductive and Developmental Biology, Imperial College in London. This thesis has not been previously submitted for a degree or diploma at this or any other institution.

Pavlina Spiliopoulou

November 2020

Abbreviations

AF	autologous fluid
ANOVA	analysis of variance
APS	ammonium persulphate
ATAC	assay for Transposase-Accessible chromatin
ATACseq	ATAC sequencing
BD	twice daily
BSA	bovine serum albumin
BRCA1	breast cancer 1 susceptibility protein
BRCA2	breast cancer 2 susceptibility protein
CA125	cancer antigen 125
CCL5	C-C motif chemokine ligand 5
CCL20	C-C motif chemokine ligand 20
CD	cluster of differentiation
cDNA	complementary deoxyribonucleic acid
C_T	cycle threshold
CTLA4	Cytotoxic T-lymphocyte-associated protein 4
CXCL9	C-X-C motif chemokine ligand 9
CXCL10	C-X-C motif chemokine ligand 10
CXCL11	C-X-C motif chemokine ligand 11
CXCR3	C-X-C motif chemokine receptor 3
DAMPs	danger-associated molecular patterns
DAPI	4′,6-diamidino-2-phenylindole

DAVID	Database for Annotation, Visualization and Integrated Discovery
DEG	differentially expressed gene
dH_2O	distilled H_2O
DMEM	Dulbecco's Modified Eagle Medium
DMSO	dimethyl sulfoxide
DNMT	DNA methyltransferase
DNA	deoxyribonucleic acid
dNTPs	deoxynucleoside triphosphate
DPBS	Dulbecco’s phosphate-buffered saline
DTT	dithiothreitol
ELISA	enzyme-linked immunosorbent assay
ERV	endogenous retrovirus
FACS	fluorescence-activated cell sorting
FBS	foetal bovine serum
FFPE	formalin-fixed paraffin-embedded
FSC-A	forward scatter area
FSC-H	forward scatter height
GZMB	granzyme B
GSEA	gene set enrichment analysis
H3K9me1/2/3	Mono-, di-, trimethylation of lysine 9 on histone 3
H3K27me3	trimethylation of lysine 27 on histone 3
HDAC	histone deacetylase
HGSC	high grade serous carcinoma

HCC	hepatocellular carcinoma
HIER	heat-induced epitope retrieval
H-score	histoscore
IFNγ	Interferon gamma
IHC	immunohistochemistry
IP	intraperitoneal
IV	intravenous
LCMS	liquid chromatography–mass spectrometry
mAb	monoclonal antibody
MDSC	myeloid-derived suppressor cell
MEK	Mitogen-activated protein kinase kinase
MICA	MHC class I polypeptide-related sequence A
MICB	MHC class I polypeptide-related sequence B
mg	milligram
ml	millilitre
mM	millimolar
MW	molecular weight
NACT	neo-adjuvant chemotherapy
NBF	neutral buffered formalin
NF-H_2O	nuclease-free H_2O
ng	nanogram
NK1.1 (or KLRB1 or CD161)	killer cell lectin-like receptor subfamily B, member 1
nM	nanomolar
nm	nanometre

NK cells	natural killer cells
NGS	next-generation sequencing
OD	optical density
OD	once daily
PARP	poly (ADP-ribose) polymerase
PBMC	peripheral blood mononuclear cell
PBS	phosphate buffered saline
PD1 (or CD279)	programmed cell death protein 1
PD-L1 (or CD274)	programmed cell death-ligand 1
PMA	phorbol 12-myristate 13-acetate
PRC2	Polycomb Repressive Complex 2
Repbase	Database of repetitive DNA elements
RIN	RNA Integrity number
RNA	ribonucleic acid
RNAseq	RNA sequencing
Rpm	rotations per minute
rRNA	ribosomal RNA
RPMI	Roswell Park Memorial Institute medium
RT-qPCR	quantitative reverse-transcription polymerase chain reaction
SAM	S-adenosyl methionine
SD	standard deviation of the mean
SDS	sodium dodecyl sulphate
SGC	Structural Genomics Consortium
SSC-A	side scatter area

SSC-W	side scatter width
STR	short-tandem repeat
TAM	tumour-associated macrophage
TAm-seq	tagged-amplicon sequencing
TEMED	tetramethylethylenediamine
TGF-ß1	transforming growth factor-ß1
TNFα	tumour-necrosis factor alpha
VEGF-A	vascular endothelial growth factor-A
mg	milligram
ml	millilitre
µM	micromolar
µm	micrometer

Chapter 1. Introduction

Chapter 1 Introduction

1.1. Epithelial ovarian cancer

1.1.1 General

Globally, 295,500 new cases of ovarian cancer (OC) were diagnosed in 2018 with almost 185,000 deaths recorded in the same year (1). Even though OC is not among the most common cancers worldwide, it is the second most deadly gynaecological malignancy after cervical cancer, and, without an established screening strategy as yet, the death rate will certainly remain high (1-3).

Thought to be a single entity until recently, epithelial OC is now subdivided into different histological subtypes that have individual molecular characteristics, risk factors and different response to treatments. Epithelial OC accounts for ~90% of OCs and includes high-grade and low grade serous, high-grade and low-grade endometrioid, clear-cell, ovarian carcinosarcoma and mucinous carcinomas. Of these types, high-grade serous carcinoma (HGSC) is the most commonly diagnosed. Low-grade endometrioid and low-grade serous carcinoma (LGSC) are different to their high-grade counterparts from a clinical and histopathological point of view, whereas high-grade endometrioid carcinoma behaves similarly to HGSC (4, 5). The sub-characterisation of epithelial OC has been a step of paramount significance for OC research as we can now design clinical trials specifically for each sub-type, with an aim to answer questions more precisely (figure 1.1). Small-cell ovarian carcinoma is an extremely rare and separate histology that affects young women, has a particularly poor prognosis and is associated with *SMARCA4* mutations (6, 7). Non-epithelial ovarian cancers include tumours arising from ovarian germ-cells and the sex cord stroma and account for the remaining 10% of OC. They affect patients of a younger age than epithelial OC and the oncological management is totally different (8).

The site of OC origin has also been a topic of on-going research and speculation. Tumours that have until now been described clinically and histopathologically as HGSC probably originate in the fallopian tube (9) and although the term ovarian cancer is still widely used, it is acceptable within the scientific and clinical community that only a subset of them actually originate from the ovarian

epithelium. Endometrioid and clear-cell carcinomas can originate from endometrial tissue migrating outside the uterine endometrium, through the process of endometriosis; still, uncertainty still exists over the exact cell of origin.

Effective screening strategies for the early detection of ovarian cancer are not established yet. Screening modalities such as the use of CA125 biomarker and transvaginal ultrasonography may have utility in detecting early-stage cancer (10). In UKCTOCS study, 202,638 women were allocated to either annual multimodal screening (MMS), annual transvaginal ultrasound (USS) or no screening at all. In the MMS group, serum CA125 concentration was used, with its trend over time interpreted with an algorithm of OC risk calculation, which identifies significant rises in CA125 concentration above baseline. Following this, women with suspicious rises in CA125 would undergo transvaginal USS. In the USS group, primary test was annual transvaginal USS. Within a year of screening, overall sensitivity for detection of OC was 84% (95% CI 79–88) in the MMS group and 73% (66–79) in the USS group (3). Mature results from large screening trials on the overall mortality benefit of these modalities are still awaited (3). Nevertheless, individuals at high risk of developing ovarian cancer, such as those with germline mutations in *BRCA1*, *BRCA2* or other high-risk genes, can access risk-reducing surgery, such as bilateral salpingo-oophorectomy.

First-line management of newly diagnosed OC includes a combination of surgery and cytotoxic treatment. This is either primary surgical cytoreduction followed by combination platinum-based chemotherapy or neoadjuvant chemotherapy (NACT), followed by interval surgical cytoreduction and further additional chemotherapy after surgery. The platinum analogues cisplatin and carboplatin are the most active therapeutic agents against newly diagnosed OC and are usually administered with the addition of a taxane (11-16). Recurrence of cancer and platinum treatment resistance are very common and still pose a great challenge as therapeutic options at this point are limited (17). New therapeutic advances for recurrent OC include angiogenesis inhibitors and poly (ADP-ribose) polymerase (PARP) inhibitors (18-21) whilst immunotherapy agents are still under testing for a definitive benefit in prolonging patient survival (22, 23). OC

biology and clinical management are exciting and ever-evolving fields; in this introduction, I will summarise the main molecular and immunological characteristics of OC and how these intersect with recent discoveries in the field of cancer epigenetics.

1.1.2 Risk factors

Genetics

Genetic predisposition -with or without known family history of breast and/or ovarian cancer- is the most important OC risk factor. Germline *BRCA1* or *BRCA2 (gBRCA1/gBRCA2)* mutations account for approximately 15% of cases (24-26) and although they are mainly associated with high-grade serous subtype of OC (26), they are occasionally observed in other types too (27, 28). Women with OC carrying germline mutations in *BRCA1* or *BRCA2* have better overall survival compared to women with wild-type genes (29) and *BRCA2* mutations confer a survival advantage compared to *BRCA1* mutations, possibly secondary to enhanced platinum response (29, 30). In patients with germline *BRCA1* or *BRCA2* mutations, the risk of developing OC and average age of peak risk can be affected, amongst other reasons, by the location of the mutation within the genes and the functional deficit of the protein products (31). Other genes that are critical in increasing the risk of developing ovarian cancer are *PALB2, RAD51C, RAD51D, BRIP1* and *BARD1*, some of which belong to the Fanconi anaemia–BRCA pathway (32). Inherited mutations in genes such as *CHEK2*, *MRE11A*, *RAD50*, *ATM* and of course *TP53*, might also increase the risk of developing OC.(28, 33-35). Lynch syndrome is a well-recognised familial syndrome associated with endometrial, colorectal and ovarian cancers and is characterized by germline mutations resulting in deficient mismatch repair system. It most frequently results in mal-functioning MLH1, PMS2, MSH2 or MSH6 proteins (36-38).

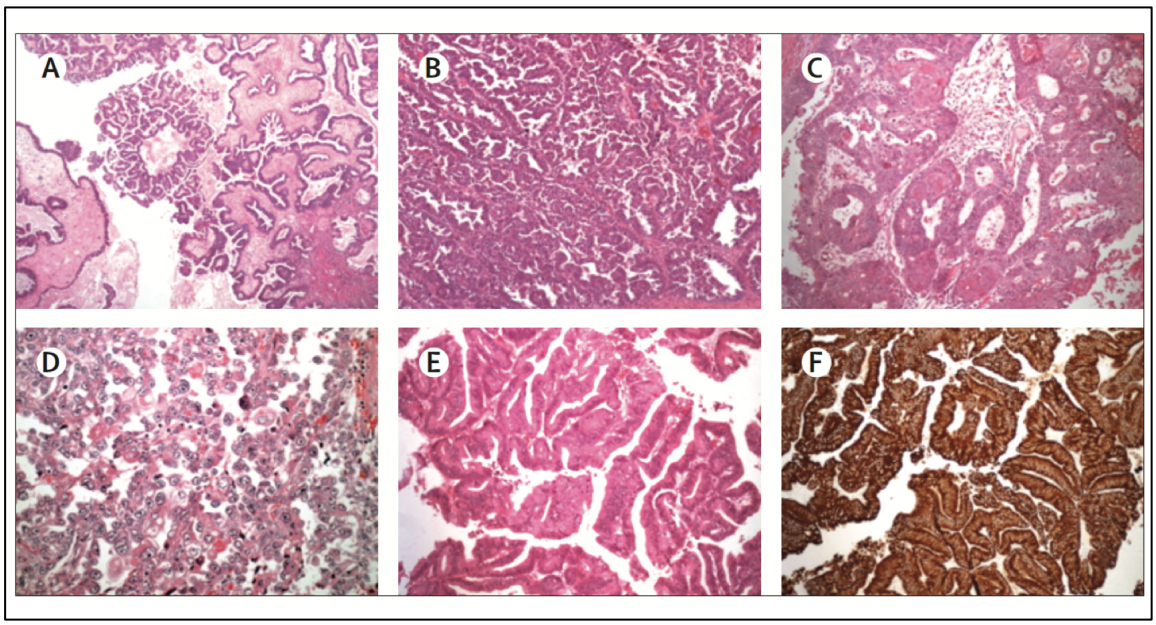

Figure 1.1: Histological subtypes of epithelial ovarian cancer
(a) Borderline tumour: serous epithelium with progressive branching architectural complexity. Some epithelial cells have detached (b) High-grade serous tumour: serous epithelium with increased architectural complexity. Glands are elongated with narrow cleft-like spaces showing foci of necrosis and exfoliation. (c) High-grade endometrioid carcinoma: foci of squamous metaplasia, not seen in (pure) variants of other ovarian carcinomas, are evident. The glands are crowded and fused the epithelium is generally non-exfoliative. (d) Clear cell carcinoma: uniform high-grade nuclear features with clear cytoplasm; solid and papillary areas are visible with some hob nailing and tufting. The carcinoma is invasive. (E) Mucinous carcinoma (haematoxylin and eosin) showing progressive architectural complexity and nuclear atypia. The epithelium towards the benign end of the spectrum shows tall columnar cells with basal nuclei. (F) Mucinous carcinoma: cytokeratin 7 (CK7)—diffuse staining of tumour cells. CK7 staining in conjunction with patchy CK20 and CDX-2 (CK20 and CDX-2 not shown) are consistent with a primary tumour of ovarian origin. (Adapted from Jayson et al, Lancet 2014, with permission from Elsevier, under license number 4947611089815).

Patients with Lynch syndrome-associated ovarian cancer present with a higher prevalence of endometrioid and clear-cell carcinomas, than would be predicted for sporadic OC (37) (table 1.1).

Reproductive system

In addition to genetic factors, the risk of ovarian cancer can be affected by reproductive system factors such as salpingectomy and unilateral/bilateral oophorectomy, tubal ligation and parity (39, 40).

Gene	Protein	Protein function
BRCA1	Breast cancer type 1 susceptibility protein	Repair of double-strand breaks by homologous recombination
BRCA2	Breast cancer type 2 susceptibility protein	Serves as a scaffold for other proteins involved in double-strand DNA repair, mostly through defective homologous recombination Stabilizes RAD51–ssDNA complexes
BARD1	BRCA1-associated RING domain protein 1	Forms a heterodimer with BRCA1 - essential for mutual stability
BRIP1	BRCA1-interacting protein 1 (also known as Fanconi anaemia group J protein)	The BRCA1–BRIP1 complex is required for S phase checkpoint activation
PALB2	Partner and localizer of BRCA2	A bridging protein that connects BRCA1 and BRCA2 at sites of DNA damage Helps load RAD51 onto ssDNA
RAD51C	DNA repair protein RAD51 homologue 3	Strand exchange proteins that bind to ssDNA breaks to form nucleoprotein filaments and initiate DNA repair
RAD51D	DNA repair protein RAD51 homologue 4	
MSH2	MutS protein homologue 2	Mismatch repair proteins that recognize and repair base-pairing errors occurring during DNA replication Mutations in mismatch repair genes are associated with Lynch syndrome
MLH1	MutL protein homologue 1	
MSH6	MutS protein homologue 6	
PMS2	Mismatch repair endonuclease PMS2	

Table 1.1: Common germline gene mutations associated with hereditary ovarian cancer. (Adapted from Matulonis et al, Nat Rev 2016, with permission from Springer Nature, under license number 4947611489069).

Parity has a reduced risk of all subtypes of OC compared to nulliparity, with the strongest risk reduction noted for clear-cell carcinomas. Irrespective of histological subtype, unilateral oophorectomy is associated with a 30% reduction in the risk of OC. Bilateral oophorectomy also reduces the risk of OC in women with a genetic predisposition (41, 42).

Only 1.1% of women with *gBRCA1* mutation and no women with *gBRCA2* mutations developed a tubo-ovarian carcinoma following bilateral salpingo-oophorectomy. This rate is even lower, i.e. 0% for both genotypes, when surgery takes place at the younger age of 35 years. In addition to oophorectomy, tubal ligation and breastfeeding have similarly been associated with a decreased risk of OC in women with *gBRCA* mutations (39). Hysterectomy is linked to the reduction in the risk of clear-cell carcinoma, whereas tubal ligation is associated with reduction in the

risk of both clear-cell and endometrioid carcinomas (39-41, 43). Lastly, endometriosis has been associated with endometrioid and clear-cell ovarian cancer, as well as low-grade cancers (43).

Sex hormones

Both in individuals with a *gBRCA1* mutation as well as in those without a genetic predisposition, the oral contraceptive pill reduces the risk of OC (44, 45). It has been shown that the use of oral contraceptives for an average of 5 years leads to a lifetime reduction of 0.54% for OC (45, 46). Interestingly, an analysis from the Ovarian Cancer Cohort Consortium (including data on 1.3 million women and 5,584 ovarian cancers) showed that oral contraceptive use was associated with reduction in serous, endometrioid and clear-cell carcinomas, but not mucinous carcinomas (43). The risk reduction of OC incidence is associated with the duration of oral contraceptive use but not the relative oestrogen and progestin doses contained in the oral contraceptives (46). Nevertheless, this reduction risk needs to be weighed against potential harmful effects of the oral contraceptive pill, such as minimal increase of breast cancer risk and adverse vascular events. More evidence will be required in order for the contraceptive pill to be recommended as a safe prevention strategy against OC (46).

On the contrary, hormone replacement therapy has been shown to increase the risk of developing OC in post-menopausal women. Some studies showed that combined oestrogen/progesterone therapy and oestrogen-only therapy increase the risk by 10% and 22%, respectively (47-49). Nonetheless, a meta-analysis showed that hormone replacement therapy has a similar increase in the risk of OC development in post-menopausal women, regardless of the hormonal content of the therapy; this risk was specifically associated with the development of serous and endometrioid carcinomas (50). This finding has been confirmed by others but in addition, a reduced risk of clear-cell cancer in women using hormone replacement therapy has been observed (43). Intriguingly, the use of hormone replacement therapy seems to be safe and to have no adverse effect on overall survival of women already diagnosed with OC, suffering from menopausal

symptoms. A study showed that women who took hormone replacement therapy after diagnosis of stage I-IV OC had better survival than the ones who did not; however, it is not clear if oestrogen-receptor positive low-grade serous cancer patients were included in this analysis (51).

Other factors

Both weight and height have been linked to the risk of developing OC. A meta-analysis showed an ~13% increase in the risk of OC in post-menopausal women for every 5kg gain in weight (52). This risk is more tightly related to mucinous and endometrioid carcinomas, but not HGSC (53). Meta-analyses have also suggested that regular physical activity has a beneficial effect on the risk of OC, with a 30–60% reduction in the most active women (54). After the diagnosis of OC, overweight women with either LGSC, HGSC or endometrioid carcinoma have worse outcomes than non-overweight women (55). In addition to weight, a recent study in almost 16,400 patients and 23,000 matched controls showed that taller height is linked to higher risk of OC too (56).

Dietary factors and the risk of developing OC has also been studied. The intake of vitamin A, C or E and folate or the intake of a specific diet (as defined by the study's diet scores) during adulthood, does not alter the risk of OC (57, 58). Interestingly, the consumption of flavonoids and black tea show a trend to decrease the risk of OC, but results need to be validated further (59). An inverse association between the intake of skimmed milk and lactose and the risk of developing OC was observed in one study (60).
Daily, low-dose aspirin use by women of all ages was associated with reduced risk of endometrioid and mucinous carcinomas and a significant reduction in the risk of serous carcinomas; however, the same associations were not drawn for paracetamol (61). Nonetheless, these are results from retrospective studies and prospective trials testing aspirin for OC risk reduction would need to be conducted. NSAID use only showed a trend towards a lower risk of OC, specifically, of serous carcinomas (61).

Lastly, the use of talc powder in the genital area had triggered a lot of discussion and media attention in the past, with variable study results being clearly as possible that talc use is not associated with increased risk (62) reported (63-65). However, a recent study on 252,745 women demonstrated as

1.1.3 Pathophysiology and molecular alterations

Figure 1.1 shows the major histological sub-classifications of epithelial ovarian cancer with their associated molecular perturbations depicted in figure 1.2.

High-grade serous and endometrioid ovarian cancers

Most patients with epithelial OC present with high grade serous carcinoma and associated *TP53* abnormalities, which are also seen in endometrioid and other high-grade undifferentiated histologies. Ovarian HGSC was found to harbour *TP53* mutations in 97% of cases, as described by Ahmed et al (66) and confirmed by others subsequently (67). Approximately 20% of these tumours also carry a *BRCA1/2* mutation due to either germline or somatic mutations (68).
In recent years, accumulating evidence has shown that the majority of high-grade serous OC (and what was previously described as peritoneal tumours), originate in the fimbria of the fallopian tube from the precursor, serous tubal intraepithelial carcinoma (69, 70).
Prophylactic salpingo-oophorectomies for familial risk showed a high prevalence of tubal carcinoma or serous tubal intraepithelial carcinoma in resected tissue, supporting the hypothesis that HGSC starts in the tubal fimbriae (9, 71). HGSC is characterised by extreme genomic instability, DNA copy number abnormalities (72), and only few distinct and recurrent mutations (68). Further subdivision of high-grade tumours into four subgroups termed proliferative, immunologic, mesenchymal, and differentiated (68, 73) based upon gene expression analyses has been suggested;

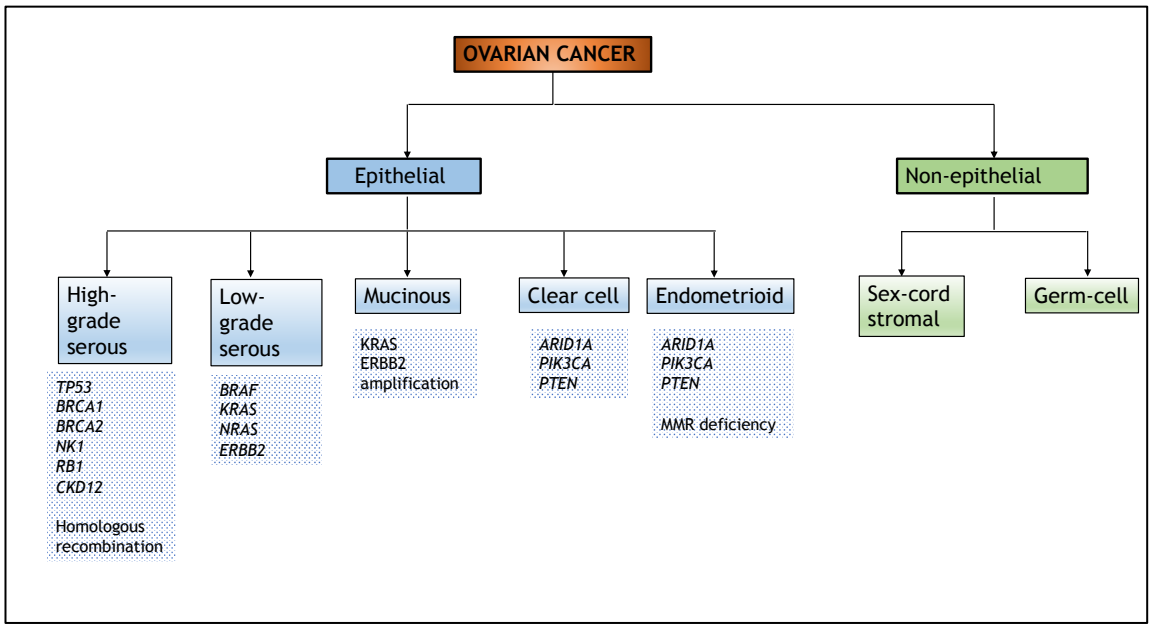

Figure 1.2: Molecular aberrations of epithelial OC, classified by histological type.

However, this classification has not yet been applied to clinical care. High-grade cancers are initially sensitive to platinum-based chemotherapy; however eventually, resistance emerges.

Low-grade serous and endometrioid ovarian cancer

Low-grade serous ovarian cancer (LGSC) shows an indolent behaviour and response rates to cytotoxic or hormonal agents are low (4). Mutations in *PI3KCA*, *BRAF*, and *KRAS* are frequent and, although MEK inhibitors can result in a 15% response rate and improved progression-free survival compared to standard-of-care chemotherapy and hormone therapy, these mutations are often not associated with increased response rates (74, 75). More research is required in LGSC, in order to identify novel treatments and discover predictive biomarkers for these patients who do respond to MEK inhibition.

Clear-cell ovarian cancer

Clear cell carcinomas of the ovary are rare tumours and are associated with endometriosis. They respond poorly to conventional platinum-based chemotherapy and have an invariably poor prognosis when diagnosed in an advanced stage (76, 77). Molecular biology is distinct from that of HGSC with clear cell carcinomas exhibiting chromosomal stability and being typically *TP53* wild type. Recently, a high frequency of mutations of the chromatin remodeller *ARID1A* (46 %) (78, 79) was found, as well as mutations in *PIK3CA* gene (33 %) (80). Their co-dependency in promoting tumorigenesis in this OC subtype was highlighted by Chandler et al (81). In a preclinical study, it was observed that EZH2 inhibition causes tumour regression in *ARID1A* mutated tumours(82). Moreover, the IL-6/STAT and VEGF pathways show hyperactivation in clear cell carcinoma (83-85). Thus, the PI3K/AKT/mTOR, VEGF and IL-6/STAT3 pathways are promising therapeutic targets in ovarian clear cell cancer.

Mucinous ovarian cancers

Mucinous OC only occurs in 3% of women presenting with epithelial OC and shares many molecular characteristics with the mucinous cancers arising in the gastrointestinal tract (86, 87). In contrast to HGSC, mucinous OC typically demonstrates mutations of the KRAS oncogene. Recent genomic interrogation of 134 mucinous OC human samples showed that the most frequent genetic event was copy number loss or mutation in CDKN2A (76% of cases). This was followed by mutations in *KRAS* and *TP53* (both 64%) with amplification of ERBB2 (26% of cases) and mutations in BRAF, PIK3CA, RNF43 and ARID1A (8–12% of cases) being the next most frequent (88). ERBB2 overexpression has been observed by other studies in up to 35% of mucinous OC cases (89-93). The suggested stepwise model of tumorigenesis is therefore that benign mucinous tumours initiate with either a *KRAS* or *CDKN2A* aberration. Borderline mucinous tumours thereafter develop additional copy number alterations and true mucinous cancers are more likely to additionally have a *TP53* mutation. Increasing grade and metastatic

potential depend on the frequency of copy number alterations which are potential prognostic markers (88). Despite our comprehensive knowledge of these genetic aberrations, targeted treatment has not showed promising results to date. Sadly, this disease is underrepresented in clinical trials and its rarity makes basic and clinical research quite challenging. For mucinous OC, platinum-based chemotherapy remains the standard-of-care oncological treatment.

1.1.4 Management of ovarian cancer

Newly diagnosed ovarian cancer

Surgical cytoreduction is the primary aim for all patients with newly diagnosed OC. Surgery aims to achieve macroscopic disease clearance with hysterectomy, salpingo-oophorectomy and omentectomy, as well as intestinal resection, peritoneal stripping, diaphragmatic resection, removal of bulky para-aortic lymph nodes and splenectomy when necessary. The removal of bulky lymph nodes takes place routinely in order to achieve maximum cytoreduction, however, there is a lack of unifying guidelines on the appropriate approach to systemic lymphadenectomy. In a retrospective analysis of 1,900 patients with no gross residual disease, lymphadenectomy was associated with a prolonged survival in a patient population, the 25% of whom had histologically involved lymph nodes post-surgery (94); however, in a randomised study that was conducted recently, systemic pelvic and abdominal lymphadenectomy added no additional benefit in PFS and OS and it was, in fact, associated with more post-operative complications. Given the strong association between optimal cytoreduction of macroscopic disease and prognosis, efforts should be focused on primary surgery (95, 96). This should be followed up by adjuvant chemotherapy. Patients with low-grade, stage 1 cancer are not treated with chemotherapy post-surgery, but those with higher stages and/or specific histologies (such as HGSC and clear-cell carcinoma) undergo adjuvant systemic platinum-based chemotherapy (97). In advanced stages, several adjuvant chemotherapy strategies have led to an improvement in overall survival for

patients with newly diagnosed, advanced-stage ovarian cancer. The addition of a taxane to platinum chemotherapy, as well as the substitution of cisplatin compound with the less toxic carboplatin, are some of the most pivotal recent changes in the systemic cytotoxic treatment prescribed in OC (14, 98, 99).

Neo-adjuvant chemotherapy (NACT) consists of 3 cycles of carboplatin/paclitaxel, followed by interval surgical cytoreduction and further chemotherapy post-surgery for a total of six cycles of chemotherapy. NACT replaces upfront surgery for patients who are not fit for initial surgery or when uncertainty about achieving macroscopic complete resection exists. NACT followed by surgery and postoperative chemotherapy confers comparable PFS and overall survival to primary surgery followed by adjuvant chemotherapy (100, 101).

Maintenance therapy after completion of adjuvant systemic treatment aims to prolong progression free (and overall) survival whilst also preserving the quality of life of the patient. The use of maintenance bevacizumab, a monoclonal antibody against VEGF-A, for a maximum of 15 months, is now routinely considered for patients with high-risk disease (defined as those patients with stage III–IV) (102-104).

In some centres, mainly in the US, intraperitoneal chemotherapy is a therapeutic option for patient who have optimal cytoreduction at surgery and for whom, bevacizumab treatment is not considered. Based on results from studies GOG 172 and GOG 252, delivering the platinum compound intraperitoneally and the taxane compound both intravenously and interperitoneally, results in better PFS and OS; however, quality of life during or soon after the end of treatment seems to be adversely affected (105, 106).

More recently, the SOLO1 trial showed that treatment with PARP inhibition (PARPi) after first-line chemotherapy in patients with BRCA mutations (germline but also somatic), without bevacizumab, confers a 70% risk reduction of disease progression or death (107). These patients had complete or partial response to first-line standard, platinum-based chemotherapy. This significant risk reduction

for patients with mutated BRCA genes has been confirmed in the VELIA study with the PARPi veliparib. In this study, PARPi reduced the risk of disease progression not only in patients with mutated BRCA genes but also in patients with wild-type BRCA genes, both those with some other form of homologous recombination deficiency (HRD), and those with no detectable HRD (108). This was further supported with an alternative PARPi, niraparib, in the PRIMA study (109). In this study, PARP inhibition doubled PFS for patients with HRD (21.9 months *vs.* 10.4 months; hazard ratio for disease progression or death, 0.43; 95% confidence interval [CI], 0.31 to 0.59; P<0.001) but also improved PFS for the sub-group of patients with HR proficiency [8.1 months in the niraparib group and 5.4 months in the placebo group (hazard ratio, 0.68; 95% CI, 0.49 to 0.94)].

Given the benefit observed both with angiogenesis and PARP inhibition, respectively, the PAOLA study was designed and aim at examining whether the combination VEGF/PARP inhibition would benefit patients, after completion of adjuvant chemotherapy (110). In this study, women with who had experienced a response to platinum-based chemotherapy plus bevacizumab were randomly assigned to the PARPi, olaparib, and bevacizumab maintenance versus placebo and bevacizumab maintenance. The combined inhibition was associated with an improved median PFS (22.1 versus 16.6 months; HR 0.59, 95% CI 0.49-0.72). Even among patient with tumours lacking *BRCA* mutations, PFS was 18.9 months with olaparib versus 16 months with placebo (HR 0.71, 95% CI 0.58-0.88). The addition of olaparib to bevacizumab however did not add any PFS improvement for patients without (or unknown) HRD status (110).

Recurrent disease

Most patients with advanced-stage ovarian cancer will experience disease recurrence. Recurrent ovarian cancer is generally incurable, although in rare cases, patients with isolated or oligometastatic recurrent disease that can be fully resected can experience long survival. In a retrospective analysis, surgery at disease relapse was associated with longer survival when achieved complete resection, as opposed to resection with residual disease left behind [median 45.2

vs. 19.7 months; hazard ratio (HR) 3.71; 95% confidence interval (CI) 2.27–6.05; P<0.0001] (111). On the grounds of this retrospective study, the prospective surgical study DESKTOP III was conducted. Interim results confirmed that combination surgery and chemotherapy at disease relapse, confers an OS advantage when compared to chemotherapy alone (53.7 *vs.* 46.2, HR 0.76, 95%CI 0.59-0.97, p=0.03) (112).

Relapse is almost always accompanied by symptoms, and an increase in cancer antigen 25 (CA125) serum levels. CA125 test has a sensitivity and specificity for recurrence detection ranging from ~60% to 94% and ~91% to 100%, respectively (113, 114). An increase in CA125, in the absence of clinical symptoms, is generally not an indication to initiate treatment, unless otherwise specified by a trial protocol (115).

Treatment options

Recurrent ovarian cancer is still classified as platinum-sensitive or platinum-resistant based on the time since last platinum chemotherapy, despite the widespread notion that this stratification is arbitrary. It has been suggested that other key factors such as molecular aberrations, *BRCA* status, histology and immunological parameters are more accurate in defining this disease. However, platinum sensitivity is still the language used amongst oncologists (116).

More recently, the treatment of recurrent OC has become more complex with the addition of tumour histology, underlying *BRCA* status and potential of secondary cytoreduction, being major factors in deciding the appropriate next step. Secondary surgical cytoreduction should be considered and discussed with patients who have a long progression free interval, especially if the site of recurrence is limited and isolated, as there is evidence of progression-free survival benefit in patients with no post-operative residual disease (111); that being said, concrete results on survival benefit are still missing (117, 118).

For patients with platinum-sensitive recurrent OC, the standard of care globally is re-challenging with a platinum-based regimen (119). In this setting, response rates can be approximately 50% and certainly the use of combination platinum regimens improves outcomes compared with the use of single-agent platinum (119-122). Nonetheless, the length of the progression free interval tends to decrease with every platinum use. Moreover, caution needs to be exercised with platinum re-challenging as the emergence of potentially life-threatening drug allergy can occur (123).

Moreover, bevacizumab can be added to carboplatin/gemcitabine for the treatment of platinum-sensitive recurrent OC, in patients who have not received it before. The addition of bevacizumab to chemotherapy increases significantly PFS (HR 0.48, 95% CI 0.38–0.60) and improves response rate by 21% (ORR 78.5% versus 57.4%, P < 0.0001) (124). Trabectedin, a tetrahydro-isoquinoline alkaloid that binds to DNA in its minor groove and results in cycle arrest, is also active in combination with pegylated liposomal doxorubicin (PLD); although not widely licensed for use, it prolongs median survival by approximately 6 months, when compared to PLD alone (125-128).

PARP inhibition has also been approved for recurrent platinum-sensitive OC, after response and completion of platinum-based chemotherapy in patients with germline BRCA mutations as it is associated with a PFS of 19.1 months [95% CI 16.3–25.7]) compared with placebo [5·5 months (95% CI 5.2–5.8)] with a hazard ratio of 0.30 (95% CI 0.22–0.41, p<0.0001 (129). Similarly to the first line setting, maintenance treatment with PARP inhibition is not only effective in patients with confirmed deleterious germline or somatic *BRCA* mutations whose OC recurs after one (or more) platinum-based treatments [PFS of 16.6 months with the PARP inhibitor rucaparib versus 5.4 months with placebo (p<0.0001)] but also patients with deficient homologous recombination through *BRCA* loss of heterozygosity [PFS of 13.6 months versus 5.4 months (p<0.0001)] (130). More recently, PARPi was examined in combination with the programmed cell death ligand-1 (PD-L1), durvalumab, in the platinum-sensitive setting, specifically in patients with germline *BRCA* mutations (131). Olaparib administration started 4 weeks before durvalumab and the response rate observed was as high as almost

72%. The combination treatment is currently being explored in an attempt to find novel treatment that will spare patients of repeated lines of chemotherapy.

For patients with platinum-resistant OC, bevacizumab in combination with paclitaxel, topotecan or PLD can be used in the first platinum-resistant setting, following the results of the AURELIA trial (132, 133). Gemcitabine, etoposide, vinorelbine or cyclophosphamide are alternative single agents that could be offered but have response rates not higher than 10–15% (16, 134-136) and can sometimes be challenging to deliver to heavily pre-treated patients. Apart from bevacizumab, oral anti-angiogenic therapies that have been studied in recurrent OC include cabozantinib, nintedanib, sunitinib and cediranib (137, 138) with the latter showing activity in both platinum-resistant and platinum- sensitive recurrent OC (139).

1.1.5 Immune microenvironment in ovarian cancer

Tumour microenvironment (TME) and more specifically the immune cell subsets within ovarian cancer deposits play a critical role in OC tumorigenesis and progression (140, 141). When OC cells spread within the peritoneal cavity, they most frequently infiltrate the omentum. Omentum is the adipose tissue occupying large part of the peritoneal cavity. It is also an area wherein a great deal of immune cells reside or migrate and therefore, a great deal of immune interactions take place in the omentum (142). The immune interaction has various steps (figure 1.3) that separately contribute to the efficacy of the immune response and subsequent tumour cell killing. Ample clinical evidence has repeatedly shown that the immune microenvironment composition is correlated strongly with OC prognosis.

The presence of tumour-infiltrating T lymphocytes (TILs), such as $CD3^+$, $CD8^+$ and $CD4^+$ have generally been associated with better prognosis (143-148). Notably, in a pivotal study, patients with pre-existing $CD3^+$ TILs in their ovarian cancers had a complete response rate of 73.9% following surgical debulking and platinum-based chemotherapy, whereas patients without TILs had an 11.9% complete

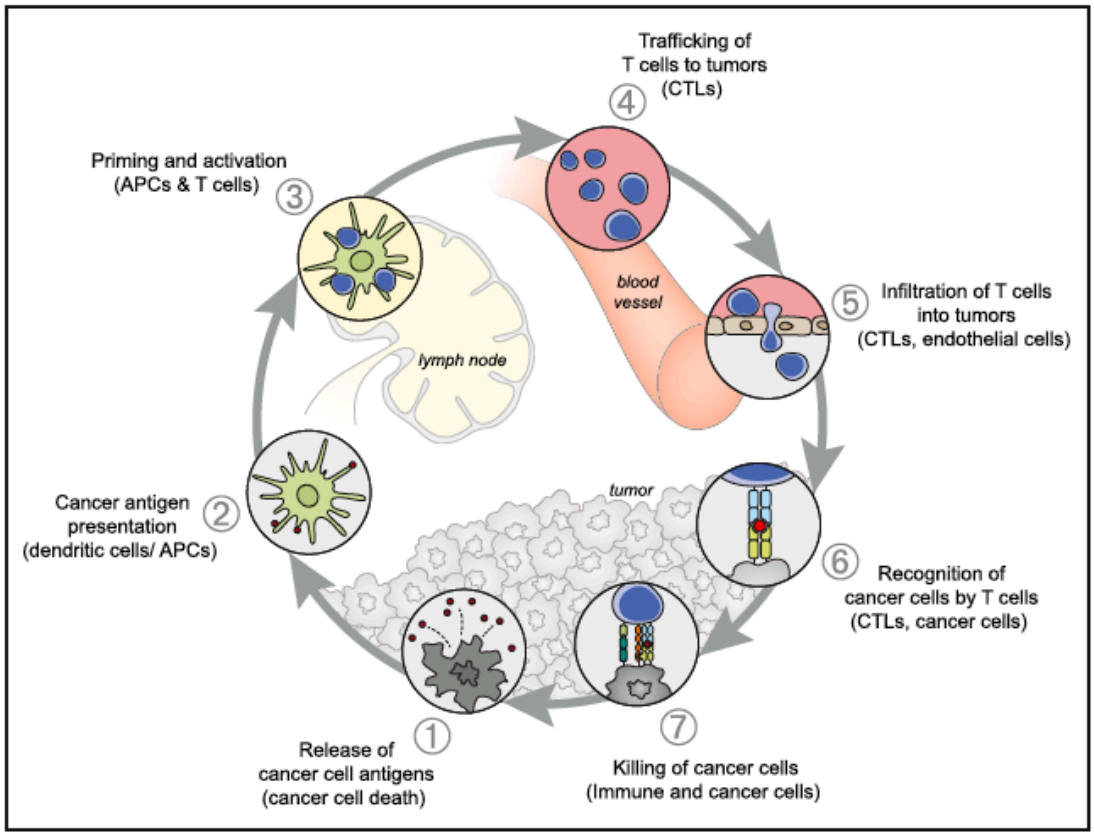

Figure 1.3: Steps of anti-cancer immunity cycle. APC: antigen-presenting cell, CTL: cytotoxic T lymphocyte. (Figure taken from Chen DS et al, Immunity 2013, with permission from Elsevier, under license number 4947620286912).

response rate. Moreover, the presence of $CD3^+$ TILs was associated with a 55% five-year survival, versus 4.5% in patients without CD3+ TILs (149). A meta-analysis of 1,815 patients showed that the subset of $CD8^+$ TILs is, unsurprisingly, more significant than the overall $CD3^+$ population (150). More specifically, $CD8^+$ T cells expressing the αE integrin subunit CD103 can directly mediate anticancer immune killing (151-153).

More recently, in a study of 5,500 women with OC, of whom 3,196 had HGSC histology, tumour infiltration by $CD8^+$ cells were graded by IHC into negative, low, moderate and high levels. Median survival was 2.8 years for patients with no $CD8^+$ TILs and 3.0 years, 3.8 years, and 5.1 years for patients with low, moderate, or high levels of $CD8^+$ cells, respectively ($p= 4.2 \times 10^{-16}$) (154). This study underpins the critical role of $CD8^+$ cytotoxic cells in OC prognosis and

contains the largest patient dataset published to date in relation to $CD8^+$ T cells in the OC TME and survival outcomes.

HGSC TME can also contain $FoxP3^+$ $CD4^+$ T cells, otherwise known as T regulatory cells (Tregs). This population normally elicits potent immunosuppressive mechanisms in order to achieve immunosurveillance and control auto-immunity but it can also limit the potency of anti-tumour immune responses (155). Tregs employ protumour cytokines, such as IL-10 or TGF-ß, to exert their immunosuppressive functions on effector or antigen-presenting cells and they can also directly kill effector T cells (156). In OC, migration of Tregs in the TME is primarily mediated by CCL22, which binds to the receptor CCR4 present on the Treg surface (157). Several reports associate Tregs cells with a poor outcome in OC (158, 159). And although a meta-analysis of 869 patients concluded that Tregs in OC tumours are not a significant prognostic indicator of survival, perhaps their role should be considered in conjunction with the other lymphoid sub-populations present in the TME (151, 160, 161).

Natural killer (NK) cells are part of the innate immune system and have an integral role in the anti-tumour response. NK cells do not require HLA-mediated recognition of target cancer cells, but rather rely on activating and inhibitor receptors in order to execute their cytotoxicity. In OC, possible mechanisms of immune escape can result from defective NK cell function (aberrant ligand/receptor expression), lower NK cell frequency intra-tumorally or reduced NK cell ability to achieve their cytotoxicity (162). NK cells are able to recruit immature dendritic cells (iDCs) with the release of CCL3 and CCL4 and to encourage their maturation via CCR5 receptor, which in turn leads to upregulation of CCL5, CXCL10 and CXCL9 on the surface of DCs (163). Following this, DCs are able to attract and activate $CD8^+$ T cells in the OC TME, where they can achieve immune clearance. Conversely, OC cells can transcriptionally downregulate the activating receptor NKG2D on the NK cell surface by releasing macrophage migration inhibitory factor (MIF); this subsequently leads to reduced NK cell cytotoxicity (164). OC cells also have the ability to adversely affect NK cell response to IL-2 in ascites and thereby, contribute to immune suppression (165). Interestingly, in preclinical models of renal cancer and melanoma, NK

cells exhibit a stronger migration potential towards CXCL10-transfected cancer cells and result in significant tumour regression and improved survival, via immune cell killing (166). This highlights their role in anti-tumour immune response and their dependency on CXCL10.

In contrast to the lymphocyte populations, the role of myeloid lineage cells is less well defined and thought to be mainly pro-tumorigenic (167). Tumour-associated macrophages are the most abundant myeloid subpopulation in the OC TME, and they are characterised by great plasticity. Various soluble ligands can alter the phenotype of TAMs, which are recruited either from circulating blood monocytes or arise from resident tissue macrophages (162, 168-170). In the TME, they can mediate angiogenesis via the release of growth factors. OC cells mediate the upregulation of mannose receptor (CD206) on the surface of TAMS. In turn, CD206 binds cellular mucins and this interaction promotes an immune-suppressive phenotype, via the release of IL-10 and IL-12 (171). TAMS can orchestrate extracellular matrix remodelling in OC TME and promote metastasis, angiogenesis, and early relapse (172-174). In multiple tumour types, but also specifically in OC, prognosis of patients is worsened when their tumours are infiltrated by TAMs (175).

Dendritic cells (DCs) capture, process and present antigenic peptides to other immune system cells. They present either endogenous or exogenous captured peptides to $CD4^+$ and $CD8^+$ T cells via MHC class II and class I, respectively. For the lymphocytes to be adequately activated by DCs, costimulatory molecules such as CD40, CD80 and CD86 are also essential on DCs (or other antigen-presenting cells), as well as the abundance of immune-stimulatory chemokines (176-179). Any of these signals (figure 1.4) can be disrupted by cancer cells with strategies such as loss of tumour antigens and/or by the secretion of immunosuppressive factors in the TME that can result in DC dysfunction (180, 181). Immature myeloid DCs reside in lymph nodes or other tissues in a relatively deactivated state with low levels of costimulatory molecules and low levels of cytokine release. The most abundant chemokine receptors on their surface are CXCR3, CXCR4, CCR1, 2, 5, and 6. Upon stimulation by antigen, immature DC

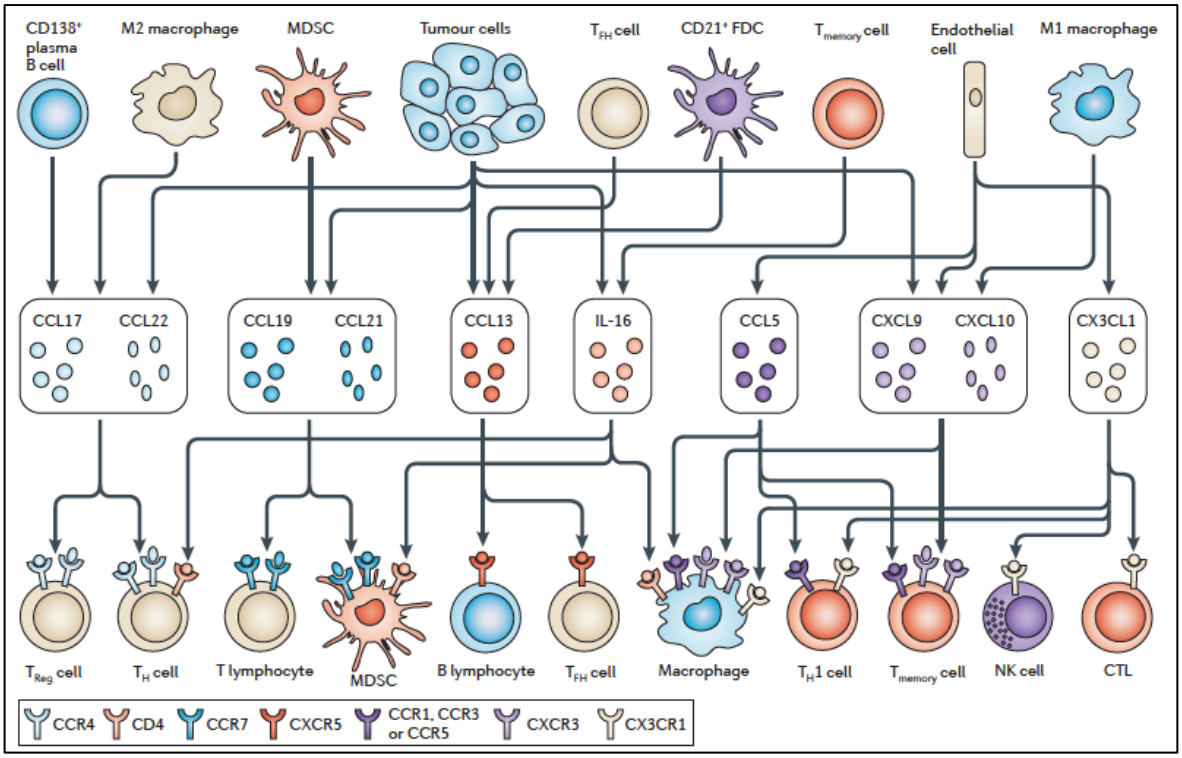

Figure 1.4: Cells and chemokines orchestrating the tumour immune microenvironment. (Figure taken from Fridman et al, Nat Rev Cancer 2012, with permission from Springer Nature, under license number 4947620520749).

migrate to lymph nodes from tissues and begin the antigen presentation process in order to activate other immune cells (182, 183). The DCs that are found in tumours are low in number and they mostly exhibit features of immature DCs. In OC, the immunosuppressive environment created by cancer cells secreting TGF-β, VEGF, IL-10 and the PD1/PD-L1 axis drives deactivation of DCs, followed by establishment of T cell anergy and immune tolerance (184, 185). In melanoma, DCs with high expression of CXCR3 and the transcription molecule Batf3 were essential to the recruitment of effector $CD8^+$ cells in the TME (186, 187). DCs that stem from a Batf3-lineage correlate with the presence of CXCR3-binding chemokines CXCL9/CXCL10/CXCL11, which mediate effector T cell trafficking in cancers such as OC (188, 189). Maintaining mature DCs activation is therefore paramount in providing continuous T cell priming and consequently in generating a successful anti-tumour response (143, 190, 191).

There is ample evidence in the literature on the importance of immune cell composition of ovarian cancer TME. Delineating the molecular signatures that are associated with the presence of certain immune cellular phenotype is of paramount significance and to this end, mechanisms related to chemokine biology are unsurprisingly being investigated extensively (figure 1.4).

Specifically, two chemokine pathways, the CXCR3/CXCL9-11 axis and the CCR5/CCL3 axis were found to be associated with an immune-reactive OC microenvironment and improved patient prognosis (149, 192, 193). Genomic analysis of 489 patient samples by the Cancer Genomic Atlas Research Network confirmed the presence of a defined subgroup of OC patients with an activated CXCR3/CXCL9-11 pathway (68). The primary role of the IFN-γ-inducible chemokines CXCL9-11 is trafficking of activated $CD8^+$, $CD4^+$ T cells and NK cells (194) and when these chemokines are present at high concentrations in tumours, patients with OC achieve longer disease-free interval and overall survival (148, 195).

Recently, Dangaj et al showed that a chemokine hierarchy determines the immune microenvironment of ovarian and other tumours, such as breast, kidney and lung cancer (196). Specifically, tumour derived CCL5 chemokine drives $CD8^+$ T cell engraftment in the TME and this CCL5 expression can be epigenetically silenced in tumours by DNA methylation. When present intratumorally, TILs become activated by tumour cognate antigen and secrete IFNγ, which in turn activates TAMs and DCs to secrete CXCL9 chemokine. CCL5, antigen presence and CXCL9 are all essential in amplifying T cell recruitment through the positive feedback loop described above. Patients whose tumours have a $CCL5^{hi}CXCL9^{hi}$ signature, exhibited strong T cell intratumoral infiltration and longer survival (196).

Asides from their role in lymphocyte migration, CXCL9-11 can mediate tumour regression through their angiostatic effects (197). In the ID8 syngeneic preclinical ovarian cancer model, overexpression of CXCL10 reduced tumour burden and ascites accumulation in mice. This was accompanied by a decrease in IL-6 and VEGF levels and transcriptional upregulation of genes associated with

antigen presentation and T cell effector function (198). Unsurprisingly, strategies to induce expression of CXCL9-11 chemokines via activation of IFN-γ and IL-17 pathways have been designed; however, clinical results are not reported as yet (199-202).

1.2. Epigenetics

1.2.1 Biology and background

Our understanding of epigenetic regulation in both normal and cancer cells has rapidly increased over the last couple of decades. Improvements in genome-wide DNA sequencing and recently developed assays on DNA methylation and chromatin, coupled with advancements in bioinformatics, are providing a better insight in the epigenome biology and enable us to develop novel epigenetic therapies (203-205).

DNA methylation and chromatin, the latter consisting of DNA plus interacting proteins, create the epigenetic landscape (206, 207). The nucleosome, a core of histone proteins around which approximately 146 base pairs of DNA are wrapped, is the main structure determining DNA conformation, which in turn is regulated by histone modification (figure 1.5a). When in a compacted nucleosome occupancy, gene expression is repressed, whereas when transcription start sites (TSS) are in a nucleosome-free state, gene transcription is facilitated (206).

Epigenetic control by DNA methylation and histone modification is accomplished by the "four Rs" of epigenetics (Figure 1.5b): the writer, eraser, reader, and remodeller proteins. These function in a harmonious collaboration to achieve tight regulation of gene expression (204, 206, 208-210). Histones are subject to modification by multiple chemical groups, including acetyl, methyl, phosphoryl and ubiquityl groups. These alterations lead to opening or closing the chromatin structure and support or impede other proteins from binding to chromatin. The writers deposit histone modifications, which can subsequently be removed by erasers. Readers bind to chromatin through specific domains that read the histone modifications and can facilitate the function of nucleosome, histone or DNA-modifying enzymes. Lastly, the remodelers mobilise and exchange histones.

In almost all tumour types a high frequency of mutations in the genes encoding proteins of the epigenome, has been observed (203, 209, 211-213). Mutations in

DNA (cytosine-5)-methyltransferase 3A (DNMT3A) for example is found in up to 25% of patients with acute myeloid leukaemia (AML).

In OC, aberrant DNA methylation is observed early in carcinogenesis and could be mechanistically involved in tumorigenesis. DNA methylation is the process by which methyl group is added to cytosine nucleotides in DNA, typically in the C5 position (5mC) in the context of CpG islands. Normally, 60%-90% of all CpG loci are methylated in human DNA (214), and this widespread methylation plays an important role in maintaining stable tissue-specific gene expression, inactivation of one X-chromosome in women, transcriptional repression of repetitive elements in the genome, and allele-specific expression. In all OC sub-histologies, hypomethylation of repeat elements (such as LINE1 or Alu) is increased in tumours when compared to their non-neoplastic precursors (215-218). Moreover, increasing hypomethylation is associated with advanced grade, advanced stage and poor prognosis. DNA methylation in OC has also been investigated as a mechanism of acquired resistance to treatment. Methylation of *MLH1* which is involved in the DNA mismatch repair (MMR) pathway has been associated with resistance to platinum-based chemotherapy in epithelial OC cell lines (219, 220). This was also observed in samples derived from patients who have had platinum-based chemotherapy and when MLH1 methylation is detected in patients' plasma at relapse, it is associated with poorer overall survival outcome (221, 222).

In contrast, methylation of *BRCA1* is documented in 9-20% of epithelial OCs and is associated with an improved response to treatment (223-227). Patients with hypermethylated *BRCA1* may have an augmented response to DNA damaging chemotherapy (25, 228) and PARP inhibitors (229, 230).

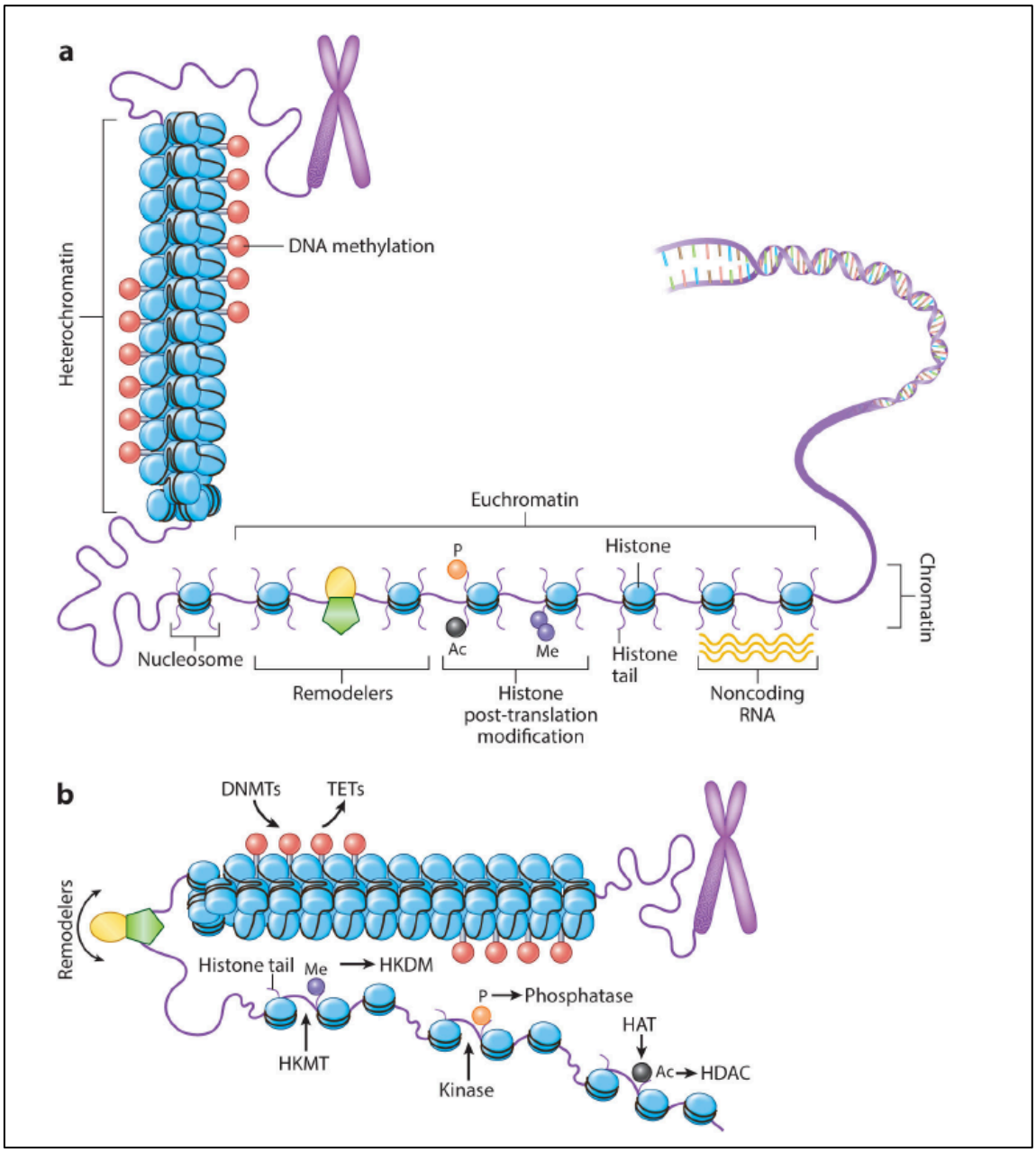

Figure 1.5: The epigenome landscape. (a) Heterochromatin state supports transcriptional silencing of genes through DNA methylation (red lollipops). Open chromatin conformations (euchromatin) leave the transcription start site nucleosome (blue ovals) free. Modifications of nucleosome histone tails (purple lines extending from ovals) regulate the process, including lysine methylation (purple circle), serine phosphorylation (orange circle), lysine acetylation (black circle) and nucleosome remodeller complexes (green pentagon with yellow oval). Noncoding RNAs (yellow waves) can participate in these regulatory steps (b) Control of histone modifications and of DNA methylation by proteins: writers (DNMTs, HKMTs, HATs), readers, erasers (TETs for DNA methylation, HKDMs for lysine methylation, HDACs, phosphatases for removing phosphorylation) and nucleosome remodeller. DNMT, DNA methyltransferase; HAT, histone acetylases; HDAC, histone deacetylases; HKDM, histone lysine demethylase; HKMT, histone lysine methyltransferase; TET, ten-eleven translocation protein. (Figure taken from Ahuja et al, Annu Rev Med 2016, with permission from Annual Reviews, under the license number 1077379-1).

Mutations in chromatin remodelling proteins occur in a multitude of solid cancers including OC (79, 206, 231). Lysine residue acetylation and methylation are critical histone modifications that facilitate active versus repressed states of gene expression (206-208). Histone acetylases (HATs) are the writers of acetylation; whereas the removal of the acetyl group is catalysed by histone deacetylases (HDACs) (figure 1.5b). Usually, lysine acetylation at gene start sites is associated with gene transcription and deacetylation with gene repression (232). Lysine methylation is mediated by histone methyltransferases (HTMs) and removed by histone demethylases (HDMs) (233). Such modifications can induce either gene expression or repression. For example, methylation of lysine 4 on histone 3 (H3K4) marks gene activation (207). In contrast, methylation of lysine 9 or lysine 27 (H3K9me3, H3K27me3) marks repressed gene promoters (233-236). This repressive mark is deposited by the Polycomb complex of proteins (PcG), which consists of Polycomb-repressive complexes, PRC1 and PRC2, and which are not only crucial for development but are also critical to carcinogenesis. The PcG enzyme Enhancer of Zeste homolog 2 (EZH2) is the main writer for the H3K27me3 mark and its levels are elevated in numerous cancers (236-239). EZH2 is often over-expressed in epithelial OC cells and promotes cell proliferation, inhibits apoptosis and enhances angiogenesis in epithelial OC (240).

1.3 Epigenetics and immune response

1.3.1 Background

Immuno-oncology (IO), in the form of immune checkpoint inhibitors, has revolutionised anti-cancer treatment over the last decade by improving patient survival for various different tumour types. We have recently seen practice-changing drug approvals in malignancies including melanoma, thoracic and urothelial cancers, Hodgkin lymphoma as well as mismatch repair deficient tumours of any origin (241-245). Despite the significant advances however, perhaps with the exception of melanoma, only a minority of patients respond to IO, highlighting the need for developing rational approaches to augment IO efficacy. The likelihood of response to IO can be influenced by factors including neoantigen load and mutational burden (246), quality and clonality of these neoantigens (247, 248), expression of antigen presenting molecules and immune checkpoints (249), responsiveness to interferon-gamma (IFNγ) (250), and of course, the immune cell composition of the tumour microenvironment ('hot' versus 'cold' tumours) (251-254). Combination treatment with different immune checkpoint inhibitors are certainly producing better efficacy, although this comes at the cost of a significant increase in severe immune-related toxicities (255). The potential of utilising non-immune therapies to augment the immunomodulatory effect of existing treatments appears therefore as an interesting alternative option to convert immune-resistant tumours to immune sensitive ones.

1.3.2 Epigenetic regulation of immunity – cell types

Tumour cells

The ability to upregulate expression of immune signalling components in cancer cells via blocking DNA methylation and histone deacetylation is now well established (256-258). Drugs blocking these epigenetic mechanisms upregulate the expression of components of the antigen-presenting machinery (APM), tumour associated antigens (TAAs), co-stimulatory molecules, checkpoint

ligands, stress-induced ligands and death-inducing receptors on tumour cells. Cancer-testis antigens (CTAs) are expressed in embryonic and germ cells but silenced in mature somatic cells by DNA methylation (259); treatment with epigenetic drugs can increase their expression (260). DNMT inhibitors result in de-repression of CTAs in many different solid tumours (261-264). CTA induction is also observed with HDAC inhibitors, albeit at a lower level than DNMT inhibitors (265). In OC, treatment of cell lines and patients with the DNMT1 inhibitor decitabine resulted in the increase of OC specific antigen NY-ESO-1 which led to augmented T cell responses (266). Asides from NY-ESO-1, the gene promoter of the high molecular weight melanoma-associated antigen (HMW-MAAs) was also found to undergo demethylation following treatment with decitabine in melanoma cells. This was associated with re-expression of HMW-MAA at both the mRNA and protein levels (267). APM components can be epigenetically deregulated in cancer cell. Both HDAC and DNMT inhibitors can induce or enhance the expression of parts of the APM pathway including MHC molecules, LMP2, LMP7, TAP-1 and TAP-2 in a wide range of cancers (268-270). Moreover, exposure to epigenetic inhibitors can also enhance expression of death receptors and stress-induced ligands as well as upregulate surface expression of several co-stimulatory molecules (e.g., CD40, CD80, CD86, and ICAM-1) on cancer cells. (270-274).

Lymphocytes – innate and adaptive immunity

Whilst effector $CD8^+$ T cells are dependent on antigen presence, have a limited survival and become easily exhausted upon chronic antigen exposure, memory $CD8^+$ cells can typically maintain long-term plasticity and survival. The generation and maintenance of memory $CD8^+$ T cells is paramount in achieving long-lasting responses on immune therapy. Lineage differentiation and establishment of effector or memory T cell phenotype are tightly regulated by histone modifications and DNA methylation. EZH2 and Suv391 deposit H3K27me3 or H3K9me3, respectively, in order to silence pro-memory genes (275-277).

Similarly, gene specific demethylation has been found to mediate T cell differentiation fate and engagement into a more long-lived memory cell phenotype in $CD8^+$ cells derived from humans to (278). Moreover, DNA methylation programmes are also found to be activated in exhausted $CD8^+$ cells following chronic antigen exposure. Gene specific methylation could be a mechanism of developing resistance to the re-invigoration that immune checkpoints inhibitors can achieve and in fact, treatment with DNA methyltransferase inhibitors can reverse immune checkpoint resistance (279, 280). Robust evidence showing an association between chromatin accessibility around key immune related genes involved in JAK/STAT signalling, and the ageing process proves that the epigenome is regulating T cell responses very tightly (281).

It has been shown that epigenetic modulators can also increase T cell infiltration into the TME and augment responses to immune checkpoint blockade via removal of the repressive histone or DNA marks that suppress chemokine expression in ovarian and lung cancer (282-284). Peng et al. showed that treatment of OC murine cells with decitabine upregulates tumour release of Th1 chemokines CXCL9 and CXCL10. This results in increased tumour T cell infiltration and an improved response to PD-L1 checkpoint blockade. In a similar fashion, HDAC inhibitors transcriptionally activate T cell chemokine expression and enhance responses to PD-1 therapy in lung cancer (283) and DNA methyltransferase inhibitors enhance responses in an ovarian cancer model (284).

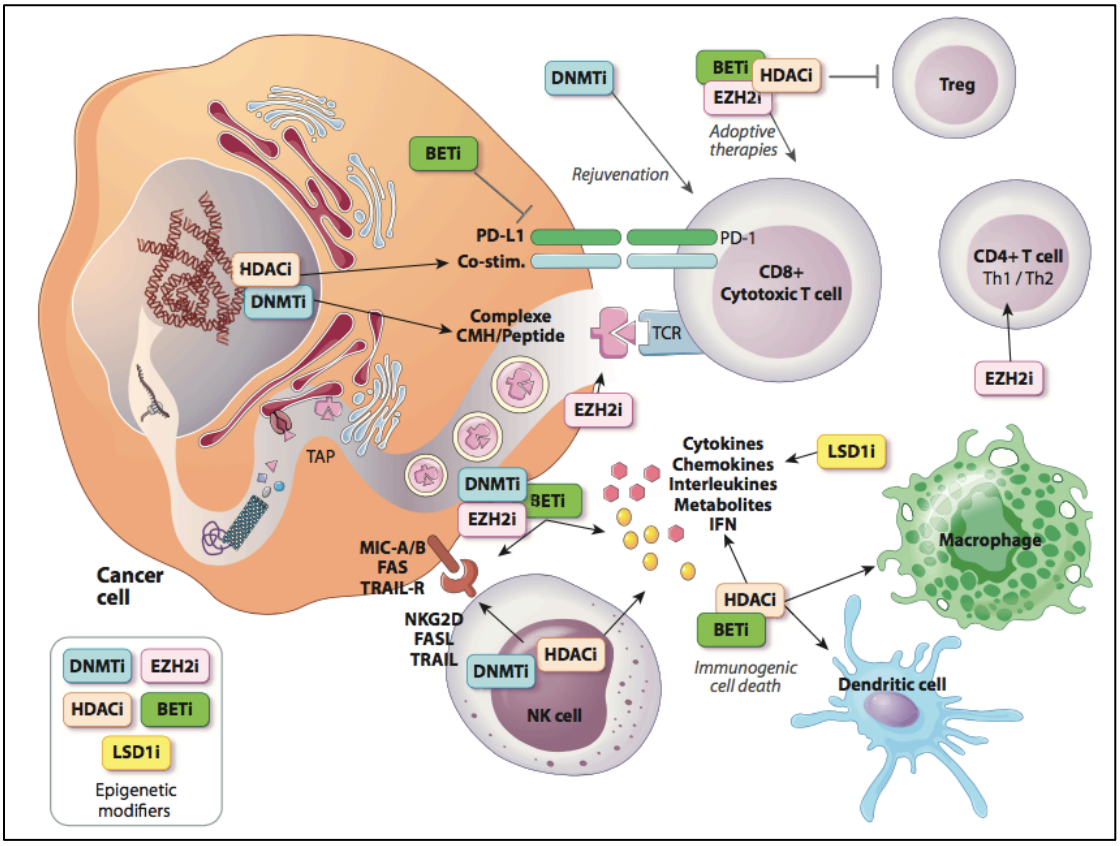

Figure 1.6: Immunomodulatory effects of epigenetic target inhibition. TCR=T-cell receptor; DNMTi=DNA methyltransferase inhibitor; EZH2i=enhancer of zeste homolog 2 inhibitor; HDACi=histone deacetylase inhibitor; BETi=bromodomain and extra-terminal inhibitor; LSD1i=lysine-specific demethylase 1 inhibitor. (Figure taken from Aspeslagh et al, Annals of Oncology 2018, with permission from Elsevier, under license number 4951201076433).

Epigenetic pathways can also modulate $CD4^+$ T cell plasticity via specific PRC2-regulated transcription factors. Methylation of H3K9 and acetylation of H3K9 can direct their phenotype to either Th1 $CD4^+$ T cells that have antitumor properties, or Th2 $CD4^+$ T cells that are thought to be pro-tumorigenic (285, 286). Once again, in the preclinical setting, deficiencies in EZH2 have been found to favour Th1 orientation (285).

Regulatory $CD4^+$ T cells (Treg) are characterized by the expression of the transcription factor FOXP3, which is critical in suppressing the perpetuation of immune response under normal conditions (287, 288). FOXP3 expression is subject to regulation by DNA methylation and EZH2-dependent chromatin

modification and is pivotal in directing $CD4^+$ cells towards an immunosuppressive phenotype (289, 290). Abrogation of histone deacetylation (HDAC6) in combination with inhibiting the BET family of bromodomain proteins (who are readers of acetylated lysine), decrease Treg mediated immune suppression in lung cancer (231). Moreover, in OC cell lines, BET inhibition with the compound JQ1 suppressed the expression of PD-L1 on tumour cells, DCs and macrophages and correlated with an increase in cytotoxic activity of effector cells (291)

Natural killer cells have tumour cell-killing properties that are regulated by various stimulatory and inhibitory receptors such as NKG2D or KIR and NKG2A, respectively (292). Once again, EZH2 is crucial here. EZH2 depletion or pharmacological inhibition increases generation of IL-15 receptor (IL-15R) positive $CD122^+$ NK precursors in both mouse and human hematopoietic progenitors. Upregulation of CD122 is associated with enhanced NK cell expansion and tumour cell immune killing and is accompanied with an increase of the stimulatory receptor NKG2D (293). This EZH2-dependent NKG2D activity has also been demonstrated in preclinical experiment in hepatocellular carcinoma (294).

Macrophages and dendritic cells

Tumour associated macrophages (TAMs) are a major component of the leucocyte composition of tumours and have previously been characterised as M1-like - macrophages displaying anti-tumour properties- and M2-like, which are macrophages that are pro-tumorigenic (167, 169, 295). These roles have been defined as such in tumours (296, 297); however, there is still a lot to understand on macrophage plasticity and on how to better delineate these two roles. By depositing H3K27me marks, EZH2 has been found to control gene networks that drive monocyte-to-phagocyte differentiation and, moreover, to regulate macrophage activation (298-300). The intertumoral metabolic conditions, as well as the cytokine milieu present can both be influenced by the epigenetic status of TAM and this in turn affects activation status (301-303). The histone

demethylase Jumonji domain-containing protein 3 modulates glutamine metabolism pathways and thereby directs TAM polarisation towards a M2 phenotype (304). Hypoxia is an element that favours M2 polarisation in TAMs; it was recently shown that inhibition of HDAC6 can mediate intratumoral vasculature normalization in a murine breast cancer model, with subsequent TAM infiltration and tumour regression (305).

TAMs of patients with malignant melanoma overexpress the DNA methylcytosine dioxygenase TET2; when TET2 is depleted in melanoma mouse models, the transcriptional program of intratumoral myeloid cells changes to a less immunosuppressive one and this change abolished tumour growth (306).

With regards to DC, Tesone et al showed that their maturation can be directed by chromatin regulators, such as the special AT-rich sequence-binding protein 1, SATB1, via regulation of MHC-II expression (307). DNA methylation, histone deacetylation and methylation, as well as the function of bromodomain proteins have all been found to be implicated in antigen presentation and consequently, in the activation of dendritic cells (231, 308).

Viral mimicry

Human endogenous retroviruses (ERVs) started integrating into the germ line million years ago and currently make up approximately 8.5% of our DNA (309). ERV silencing is essential to ensure their transcriptional quiescence, and cytosine methylation is the predominant mechanism for silencing expression of newly transposed ERVs, particularly within their long-terminal repeats (LTR) regions (310, 311). Nevertheless, some ERVs become activated during specific phases of development. Reactivation by DNMT inhibitors is rapid, effective and can generate an innate immune response akin to the one following infection by a retrovirus; this can lead to type I and type III interferon response (312, 313). Nonetheless, 5-methylcytosine has a propensity to deaminate to thymine and this can lead to gradual loss of CpG sites in ERVs (314). If LTRs are not amenable to effective silencing by DNA methylation, then histone modifications become

more important in their repression (315). In addition, a degree of cooperation between DNA methylation and histone marks exists, as evidenced by the observation that DNA methylation blockade works more effectively after histone-modifying genes have been knocked down (315).

Ishak et al demonstrated that the RB tumour suppressor recruits EZH2 to ERV regions in order to silence their expression (316). Moreover, inhibition of the histone demethylase LSD1 augments anti-tumour immune responses and potentially increase sensitivity to immune checkpoints inhibitors, via induction of ERV-associated viral mimicry response (317). Lastly, combination of HDAC and DNA methylation inhibition mediates de novo transcription of TLR belonging to LTR12 family of ERVs (318).

All the examples above highlight that cancer cells employ epigenetic mechanisms to achieve regulation of immune gene networks, in order to evade immune response. Discovering novel treatments to target epigenetic pathways could augment the immune responses engendered by the existing anti-cancer immunotherapies.

1.4 Aims

Based on the existing evidence on how the epigenome regulates almost every step of the cancer-immunity cycle, I sought to discover novel epigenetic mechanisms that could potentially be involved in the anti-tumour immune response. My project aims were as follows:

1.4.1 To perform a medium-scale drug screening of novel epigenetic compounds on a *Trp53*$^{-/-}$ murine ovarian cancer cell line that is representative of HGSC.

- Use CXCL10 chemokine production by ELISA as the starting output of this screening.
- Validate any potential hits that emerge from the screening above on ascites-derived human ovarian HGSC samples.

1.4.2 Investigate the hit(s) in an *in vivo* setting using a syngeneic murine ovarian cancer model, focusing on potential changes of the immune cell composition in the TME, by flow cytometry.

- Combine epigenetic target inhibition with standard therapies, such as chemotherapy and/or immunotherapy, that are also known to alter the immune TME.

1.4.3 Confirm that treatment with the hit(s) results in transcriptional reprogramming that would support the potential changes seen in the immune cellular level.

Chapter 2. Materials and Methods

2.1 Cell Culture

2.1.1 Immortalised human and murine cell lines

Human ovarian cancer cell lines (table 2.1) were cultured in T75 or T150 Corning® flasks in RPMI 1640 medium with 25 mM HEPES (Roswell Park Memorial Institute medium, Sigma-Aldrich, R5886) at 95% humidity, 5% CO_2 and 37°C. Medium was supplemented with 10% heat-inactivated foetal bovine serum (FBS) (Thermofisher, 16140071), 100 U/ml penicillin plus 100 µg/ml streptomycin (penicillin/streptomycin Thermofisher, 15140-122), and 2 mM L-glutamine (Thermofisher, 25030-081). The medium for the human cell line OVCAR-3 was also supplemented with 10 µg/ml bovine insulin (Sigma-Aldrich, I6634). All human cell lines were subjected to short-tandem repeat (STR) profiling validation by Eurofins Genomics cell line authentication service.

The ID8 murine cell line (319) was cultured in T75 or T150 flasks in Dulbecco's Modified Eagle Medium (DMEM, Thermofisher, 21969035), supplemented with 4% FBS, 100 U/ml penicillin, 100 µg/ml streptomycin, 10 µg/ml insulin- 5.5 µg/ml transferrin- 6.7 ng/ml sodium selenite (ITS-G, Thermofisher, 41400-045) and 2 mM L-glutamine at the same incubating conditions as above. The ID8 cell line used for both *in vitro* and *in vivo* experiments had been previously genetically modified by Dr Josephine Walton (PhD student in the McNeish lab), using CRISPRR/Cas9 technique as described here (320). More specifically, the F3 subclone used in my experiments contained bi-allelic deletions in *Trp53* exon 5, which led to significant reduction in *Trp53* transcription and absent production of p53 protein (320).

Adherent cultured cells were passaged when they reached 80-90% confluency. Cells were washed once with phosphate buffered saline (PBS, one tablet of 0.01 M phosphate buffer, 0.0027 M potassium chloride and 0.137 M sodium chloride, pH 7.4, dissolved per 200 ml deionized water) and detached using 1.5-2.0 ml 2 x 0.5% trypsin-EDTA (Thermofisher, 15400-054) in PBS, depending on the flask size. Cells were cryopreserved for long-term storage; cells were centrifuged at 260 x *g* for 5 minutes and the cell pellet resuspended in freezing medium [FBS

containing 10% dimethyl sulfoxide (DMSO, Sigma, D2650)]. Cells were then stored overnight in a Thermofisher™ Mr Frosty™ box containing isopropanol at -80°C prior to transfer to liquid nitrogen after 24-48 hours.

Non-adherent cells, such as murine splenocytes, were seeded at a density of $8x10^5$ cells per well, in Corning® 96-well Clear Round Bottom Polystyrene Microplates (Corning, 3788), in RPMI 1640 medium with 25 mM HEPES. Medium was also supplemented with 10% heat-inactivated FBS, 100 U/ml penicillin plus 100 µg/ml streptomycin, 2 mM L-glutamine, 1x MEM non-essential amino acids solution (Gibco, 11140035), 1 mM sodium pyruvate (Gibco, 11360070) and 10 µM ß-mercaptoethanol (Sigma-Aldrich, M6250). For the selective growth of T lymphocytes, recombinant mouse interleukin-2 (IL-2, Biolegend, 575402) was added to the medium with every medium change at a concentration of 30 U/ml. For the selective growth of natural killer cells, the concentration of IL-2 was increased to 1000 U/ml.

Cell lines were routinely tested for mycoplasma at the Wolfson Wohl Cancer Research Centre (WWCRC), University of Glasgow and subsequently at the Institute of Reproductive and Developmental Biology (IRDB), Imperial College London, using MycoAlert™, Mycoplasma Detection Kit (Lonza, LT01-318).

Cell line	Origin	Morphology	Background genetic events	Citation
Kuramochi	Malignant ascites	Epithelial	*TP53* and *BRCA2* mutation, *MYC* and *KRAS* amplification	Kuramochi (RRID: CVCL_1345)
OVCAR-3	Malignant ascites	Epithelial	*TP53* mutation, *C11orf30* and *CCNE1* amplification	NIH: OVCAR-3 [OVCAR3] (ATCC® HTB-161™)
OVCAR-4	Malignant ascites	Epithelial	*TP53* mutation	OVCAR-4 (RRID: CVCL_1627)

Table 2.1: Immortalised human cell lines used throughout this thesis.

2.1.2 Primary human samples

Primary human epithelial ovarian cancer cells from patients' ascites were collected under the approval of Imperial College Healthcare NHS Trust Tissue Bank (ICHTB HTA license: 12275, project title: Analysis of ascites from women with ovarian cancer) with the help of Dr Darren Ennis (translational research scientist, McNeish lab). The protocol described below was developed and optimised by Dr Darren Ennis.

After sterile collection from patients, ascites was poured into a 1000 ml sterile beaker, through an embroidery hoop covered with sterile gauze. This captured any large pieces of tissue that may have been collected in the sample, whereas it allows all cell types to pass freely through. The sterile gauze was removed from the embroidery wheel and replaced with autoclaved 40 µm membrane filter. Ascites was slowly poured through the 40 µm membrane into a separate 1000 ml sterile beaker. During this step, malignant spheroids were captured on the membrane, whereas other non-epithelial cell types passed through. The membrane was then removed, inverted and placed over a sterile 10 cm petri-dish and then washed with 25 ml sterile PBS twice. The 50 ml PBS (containing spheroids) were then pipetted from the petri-dish into a 50 ml falcon tube and centrifuged at 260 x *g* for 5 mins. The ascitic fluid that went through the 40 µm membrane was centrifuged at 260 x *g* for 5 mins in a 50 ml falcon tube. The supernatant was henceforth named Autologous fluid (AF) and it was decanted into a new falcon tube. The AF could be stored for up to 4 weeks at 4^{o}C or for long-term storage at -80^{o}C.

Following this, supernatant was aspirated from the falcon containing the spheroids, and the spheroids were resuspended in 5 ml autologous fluid (AF). The resuspended spheroids were placed into a T75 ultra-low attachment tissue culture flask (ULA, Corning 3814) in 20 ml advanced DMEM/F12 medium (Life Technologies, 12634010), supplemented with 10 mM HEPES, 1x N-2 supplement (ThermoFischer, 17502048), 1x serum-free B-27 supplement (ThermoFischer, 17504044), L-glutamine and penicillin/streptomycin at the concentrations described in 2.1.1. Spheroids were allowed to grow in the above conditions for a

few days and provided they showed adequate growth, they were dissociated and treated as a monolayer with the indicated drug for the desired number of days. Before growing them as monolayer, spheroids were collected, centrifuged at 260 x *g* for 5 mins and dissociated by adding 5 ml 1% Trypsin/EDTA. The single cell suspension was then transferred into conventional T75 flasks and cultured in the aforementioned medium, always supplemented with 20% AF.

In work previously done in the McNeish lab (unpublished data by Dr Elaine Leung and Dr Darren Ennis), these spheroids were subjected to tagged-amplicon sequencing (TAm-seq), looking specifically into the coding regions of *TP53* gene, using a method developed by Forshew et al (321). Results showed that cells derived from these organoids harbour *TP53* mutations with a high mutant allele fraction (unpublished data). The aforementioned protocol of organoid extraction from human ascites, followed by TAm-seq for *TP53* targeted sequencing has therefore become the method of validating HGSC cells from patients with histopathological diagnosis of ovarian HGSC, in the McNeish lab.

2.2 Survival and cell cycle assays

2.2.1 MTT cell viability assay

MTT assay was performed on cells seeded at a density of $3x10^3$ cells (for the ID8 cell line) per well in 24-well Corning plates in 700 µl medium. This protocol had previously been optimised by the McNeish lab. Cells were treated with the indicated drug and for the desired duration (usually 48-72 hours). Thiazolyl blue tetrazolium bromide powder (Sigma Aldrich, M2128) was dissolved in PBS to a 5 mg/ml concentration (MTT reagent). At the desired endpoint, medium was aspirated and replaced with 700 µl MTT reagent diluted 1 in 10 with culture medium. Cells were then incubated for 4 hours at 37°C. During this 4-hour period, viable cells with active metabolism are expected to convert MTT reagent into formazan crystals. Crystals were then dissolved in 500 µl DMSO. Plates were gently mixed for 5 minutes, then immediately transferred to an Infinite® 200

Tecan plate reader for analysis of absorbance (as a marker of cell viability) at 560 nm wavelength. Neat DMSO absorbance was measured in DMSO-only dedicated wells and subtracted from all other detected absorbances.

2.2.2 Cell cycle assay – bromodeoxyuridine (BrdU) assay

In order to assess cell cycle phase in cultured cells, the BrdU flow cytometry assay was used (BD Pharmingen, 559619). This assay was optimised by me. Cells were cultured in 6-well Corning plates in 2 ml medium for the indicated time. At the desired endpoint, 10 μM of BrdU solution [BrdU 10 mg/ml stock diluted with appropriate volume of 1 x Dulbecco's PBS (DPBS)] was added per well and plates were incubated for a further 30 minutes. Following incubation, cells were washed with PBS and trypsinised with 500 μl trypsin. Trypsin was de-activated with 1 ml medium, cells were transferred to 1.5 ml Eppendorf tubes and centrifuged at 200 x *g*. Supernatant was discarded and cell pellets were resuspended in 100 μl BD Cytofix/Cytoperm™ Fixation/Permeabilisation buffer, in which they were incubated for 15 minutes at 20° C. Cells were washed with 1 ml 1 x BD Perm/Wash™ Buffer [(10 x stock diluted to 1 x with deionized H_2O (dH_2O)] and centrifuged at 200 x *g* for 5 minutes. All the following wash steps were performed with 1 ml 1 x BD Perm/Wash™ Buffer. Supernatant was discarded and cells were resuspended in 100 μl BD Cytoperm™ Plus Permeabilization Buffer for 10 minutes on ice in order to enhance staining and permeabilisation. Cells were further washed and re-fixed in 100 μl BD Cytofix/Cytoperm™ for 5 minutes. Following a further wash, cells were resuspended in 100 μl DNase 300 μg/ml and incubated at 37° C for 60 minutes. Cells were then washed and stained with 50 μl fluorescent anti-BrdU antibody (diluted 1 in 50 in 1 x BD Perm/Wash™ Buffer). After a 20-minute incubation at 20° C, cells were washed and resuspended in 10 μl fluorescent 7-amino-actinomycin D (7-AAD). Following staining with 7-AAD, cells were resuspended in 500 μl staining buffer (1 x DPBS plus 3% heat-inactivated FBS plus 0.09% sodium azide) and samples were analysed on a BD Fortessa (BD Biosciences) flow cytometer.

2.3 Protein assays

2.3.1 Enzyme-linked immunosorbent assay (ELISA)

This ELISA assay was optimised by me. Mouse and human CXCL10 chemokines were detected in cell culture supernatant using the sandwich ELISA R&D Systems kits DY466 and DY266, respectively. Mouse CCL20 chemokine was detected using the sandwich ELISA R&D Systems kit DY760. Cells were seeded in 6-well plates and neat supernatant was harvested after indicated period of incubation with indicated treatment. The supernatant was aliquoted and stored at -80^{o} C.

96-well microplates (R&D, DY990) were coated with 100 µl coating antibodies (see table 2.1) diluted in coating buffer (PBS without carrier protein R&D part 896036). They were sealed with plate sealers (R&D, DY992) and left to incubate overnight at 20^{o} C. The following day, wells were aspirated and washed three times with 1 x Wash Buffer [0.05% Tween 20 (Sigma-Aldrich P9416) in PBS, pH 7.2-7.4)]. Wells were then blocked with 300 µl 1 x Reagent Diluent [10% BSA in PBS (pH 7.2-7.4, 0.2 µm filtered, R&D DY995), diluted to 1 x with dH_2O] for 90 minutes at 20^{o} C. Following blocking, wells were aspirated and washed with 1 x wash buffer as before.

At this point, the samples for the standard curve were prepared, whilst the supernatant samples of interest were thawing on ice. Standard curve samples were prepared using 2 x dilutions of the respective recombinant chemokine protein into Reagent Diluent, to produce a concentration gradient between 0 pg/ml - 4000 pg/ml. For the concentration of 0 pg/ml, neat Reagent Diluent was added into wells. Per well, 100 µl the standard curve samples were added in duplicate and 100 µl the supernatant samples of interest in triplicates. Plates were incubated at 20^{o} C for 2 hours. Then, wells were aspirated and washed three times with Washing Buffer as per the washing step above. Per well, 100 µl detection antibodies (table 2.1) were added and wells were incubated for 2 hours at 20^{o} C. They were then aspirated and washed as before. Per well, 100 µl

streptavidin conjugated to horseradish-peroxidase (streptavidin-HRP) were added and allowed to incubate for 30 minutes. Streptavidin-HRP was diluted in Reagent Diluent with a dilution factor varying dependent on the chemokine of interest (table 2.2). After another washing step, 100 µl 1:1 mixture of Colour Reagent A (H_2O_2) and Colour Reagent B (tetramethylbenzidine, R&D DY999) was added and again allowed to incubate in the dark. After 30 minutes, 50 µl Stop solution 2 N H_2SO_4 (R&D DY994) were added to the wells and then the plate was transferred to an Infinite® 200 Tecan reader to analyse optical density (OD) at 450 nm. OD at 570 nm was also read and subtracted from the 450 nm reading.

2.3.2 Protein/histone extraction from cultured cells

Protein extraction, quantification and Western Blot analysis was previously developed by the McNeish lab. The protocol was modified and optimised for histone extraction/analysis by me. Cells cultured in 6-well plates were treated with indicated treatment for the desired duration. At endpoint, plates were placed on ice, medium aspirated and cells were washed with ice-cold PBS twice. To extract the whole protein fraction at endpoint, cells were lysed with RIPA buffer (150 mM NaCl, 10 mM Tris - HCl pH 7.5, 1 mM EDTA, 1% Triton X-100 and 0.1% SDS) containing 1x protease inhibitor (cOmplete™, EDTA-free protease inhibitor Cocktail tablets, Roche, 05056489001) and 1x phosphatase inhibitor (PhosSTOP, Phosphatase inhibitor cocktail tablets, EASYpack, Roche, 04906837001). After washing the wells with PBS, 80 µl RIPA buffer were added per well and allowed to rest for 30 minutes on ice. Cell lysates were then scraped, transferred to chilled Eppendorf tubes and centrifuged at 14,000 x g in for 30 minutes at 4oC. The supernatant containing the protein fraction was then aspirated, aliquoted and stored at -20^{o}C.To preserve and study histone post-translational modifications, histones were extracted using acid precipitation with a histone extraction kit (Active Motif, 40028). Cells were cultured and treated in T75 flasks, in order to achieve higher histone concentrations required

for immuno-blotting analysis. At endpoint, cells were washed twice with PBS and lysed with 2 ml 2 x Trypsin-EDTA. Cells were transferred to 15 ml Falcon tubes and counted. Cells were pelleted by centrifugation at 200 x *g* for 5 minutes at 4ºC. After centrifugation, 250 µl ice-cold Complete Lysis Buffer AM8 (Active Motif, 40028) were added per cell pellet and allowed to incubate on ice for 30 minutes. The lysis buffer was supplemented with 100 x deacetylase/phosphatase and protease inhibitors (all included in the Active Motif kit, 40028). The samples were then centrifuged at 2,600 x *g* for 2 minutes at 4ºC to isolate the nuclei. After removing the supernatant, 100 µl extraction buffer were added per million cells on each nuclear pellet and the solution was mixed by pipetting up and down. Samples were incubated on an end-to-end rotator for 2 hours at 4º C and vortexed periodically.

Following incubation, the tubes were centrifuged at 20,800 x *g* for 10 minutes at 4ºC to pellet the acid-insoluble material. The histone-containing supernatant was collected and aliquoted in pre-chilled tubes for storage at -20ºC, whilst a small aliquot was used for immediate Bradford quantification. Prior to Bradford quantification or downstream Western blot analysis, the histones were neutralised with Complete Neutralisation Buffer (Active Motif, 40028) supplemented with 1.1 M dithiothreitol (DTT) and deacetylase/phosphatase and protease inhibitors.

2.3.3 Protein quantification by Bradford assay

To quantify the whole protein fraction or the histone fraction extracted, the Bradford assay was used. A standard curve of known protein concentration was created with a concentration gradient of bovine serum albumin (BSA, Life Technologies, 10500064), ranging from 0-2.5 mg/ml by diluting BSA in PBS. Per well, 10 µl standards (in triplicates) and samples of unknown protein concentration were added in a 96-well Corning© plate. Following this, 200 µl Bradford Assay Reagent (diluted 1:5 in dH_2O, Bio-Rad, 5000001) were added to the wells and left to rest for 5-10 minutes at 20^{o} C. After this, the plate was

Description	Working concentration	Catalogue number
Capture Antibody; rat anti-mouse CXCL10	2 µg/ml	840734
Detection Antibody: goat biotinylated anti-mouse CXCL10	0.1 µg/ml	840735
Recombinant mouse CXCL10	0-4000 pg/ml	840736
Capture Antibody; mouse anti-human CXCL10	2 µg/ml	840420
Detection Antibody: goat biotinylated anti-human CXCL10	12.5 ng/ml	840421
Recombinant human CXCL10	31.2-2000 pg/ml	893975
Anti-human/mouse CXCL10 Streptavidin-HRP	40-fold dilution	840422
Capture Antibody; rat anti-mouse CCL20	2 µg/ml	841034
Detection antibody: goat biotinylated anti-mouse CCL20	0.02 µg/ml	841035
Recombinant mouse CCL20	31.2-2000 pg/ml	841036
Anti-mouse CCL20 Streptavidin-HRP	200-fold dilution	890803

Table 2.2: Antibodies and recombinant proteins for ELISA

transferred to a TECAN reader and OD of the wells was read at 595 nm. The protein concentration of samples of interest was then extrapolated from the standard curve and expressed as µg/µl.

2.3.4 Protein sample preparation

Total protein or histone fraction samples were made up to a maximum of 20 µl/sample using a 5 x Laemmli buffer (0.01% bromophenol blue, 2% SDS, 10% glycerol, 60 mM Tris-HCl pH 6.8 and 5% ß-mercaptoethanol in dH_2O) and dH_2O on ice. Western blot lanes were loaded with equal amounts of protein (20-25 µg) for each experiment. The quantity varied between experiments, dependent on the protein concentrations achieved during extraction.

Samples were then vortexed, centrifuged briefly at 4°C and denatured at 98°C for 10 minutes in a heat block. Samples were then loaded into polyacrylamide gels that were made prior to sample preparation as described in section 2.3.5 below.

2.3.5 Preparation of polyacrylamide gels.

Polyacrylamide gels were prepared using the Bio-rad Mini-Protean Tetra Handcast System. Typically, 8% resolving gels were used for analysis of proteins of 50-200 kDa size, whereas 15% gels were used for smaller proteins between approximately 12-45 kDa size, including histones. Recipes for resolving and stacking gels are described in table 2.2. When making the gels, the crosslinking reagents ammonium persulphate (AMPS) and tetramethylethylenediamine (TEMED), were added last, before gentle mixing.

Approximately 5 ml resolving gel mix was pipetted between the two glass plates of the Bio-rad Mini-Protean Tetra Handcast System and a layer of dH_2O carefully pipetted on top. While waiting for it to set, the stacking gel was prepared as per table 2.3. Once set, the dH_2O on the resolving gel was discarded and the crosslinking agents were added to the stacking gel. The stacking gel was then carefully added on top of the resolving gel, until overflowing to avoid bubbles, and a comb was immediately inserted into the stacking gel. Once set, gels were either used immediately or stored at 4°C in 1x running buffer (see 2.3.6) for short-term storage.

	8% Resolving gel		15% Resolving gel	
	Resolving gel	Stacking gel	Resolving gel	Stacking gel
dH_2O	10.5 ml	3.7 ml	5.5 ml	3.3 ml
30% Acrylamide	5.35 ml	0.85 ml	12 ml	0.92 ml
2 M Tris-HCl pH 8.8	3.75 ml		6 ml	
1 M Tris-HCl pH 6.8		0.3125 ml		0.63 ml
10% SDS	0.2 ml	0.05 ml	0.240 ml	0.1 ml
10% AMPS	0.2 ml	0.05 ml	0.240 ml	0.050 ml
TEMED	0.012 ml	0.005 ml	0.024 ml	0.010 ml

Table 2.3: Recipes for acrylamide gels (volumes for 3 gels shown)

2.3.6 Western blot running and transfer

A 10 x Transfer Buffer stock was prepared in advance with 288 gr of glycine and 60.6 g Tris base made up in 2 L of dH_2O). Running the acrylamide gel and transfer onto a nitrocellulose membrane was performed using the Bio-rad Mini-Protean Tetra Vertical Electrophoresis Cell. A 1 x running buffer [100 ml 10 x Transfer Buffer with 10 ml 10% sodium dodecyl sulphate (SDS), up to 1 L in dH_2O] was made and poured between two gels in the tank and into the space either side of the gels and the tank. Samples were then added into the gel lanes and run at a maximum of 150V, until the bromophenol blue dye had visibly reached the bottom of the gel. Running was then terminated, and proteins were transferred onto a nitrocellulose membrane.

A 1 x Transfer Buffer solution was made in advance (100 ml 10 x Transfer Buffer stock and 100 ml methanol, made up to 1 L in dH_2O). Sponges, filter papers and nitrocellulose membranes were soaked in 1 x Transfer Buffer, before assembly of a sandwich, consisting of the acrylamide gel, the nitrocellulose membrane, two filter papers and two sponges on either side. The sandwich was fitted into the Bio-rad tank with an ice pack, and transfer of proteins from gel to membrane

took place at 150 mA for 80 minutes. The transfer of protein was confirmed by immersing the membrane into Ponceau Red solution (Sigma-Aldrich, P7170) to observe lanes of transferred protein bands. After successful transfer, blocking and staining of the membrane followed.

2.3.7 Antibody staining

A 10 x TBS stock was made up in advance with 175 g NaCl and 48 g Tris base. From this stock, a 1x TBST solution was made using 100 ml 10x TBS and 1 ml Tween20 in 1 L dH_2O. Ponceau Red staining was removed from the membrane with 3 washes in TBST (volume approximately enough to cover the membrane in a washing dish). Following this, membranes were blocked in 5% (w/v) BSA in TBST (blocking buffer) for 60 minutes at 20° C and incubated with primary antibodies (table 2.3) overnight at 4°C in blocking buffer. Membranes were then washed 3 times for 5 minutes in TBST before incubating with secondary antibody in blocking buffer for one hour at 20° C. Membranes were washed a further 3 times for 5 minutes in TBST and developed using enhanced chemiluminescence (ECL, GE Healthcare, RPN2106) or ECL prime (GE Healthcare, RPN2232), if the signal was expected to be weak.

Images were visualised using the ChemiDoc imaging system. Loading was assessed using antibodies against ß-actin or histone H3. Antibody suppliers, catalogue numbers and dilutions are listed in table 2.4.

Antibody	Supplier	Cat number	Dilution
Primaries			
Anti-DNMT1 (rabbit)	Abcam	ab 188453	1:1000
Anti-H3K27me3 (mouse)	Abcam	ab 6001	1:1000
Anti-H3K9me (rabbit)	Abcam	ab 9045	1:1000
Anti-H3K9me2 (mouse)	Abcam	ab 1220	1:1000
Anti-H3K9me3 (rabbit)	Abcam	ab 176916	1:1000
Anti-ß-actin (mouse)	Sigma-Aldrich	A1978	1:5000
Anti-H3 (mouse)	Abcam	ab 24834	1:2000
Secondaries			
Anti-mouse	DAKO	P0448	1:5000
Anti-rabbit	DAKO	P0447	1:2000

Table 2.4: Antibodies for Western Blot

2.3.8 Liquid chromatography-mass spectrometry

This protocol was kindly shared by Dr Oliver Maddocks, who developed and optimised it. To quantify the ratio of methylcytosine:cytosine via liquid chromatography-mass spectrometry (LCMS), 1 µg of DNA was extracted and subjected to acid hydrolysis. At endpoint, cells were trypsinised and harvested as cell pellets. DNA was extracted from cell pellets using the Qiagen QIAamp DNA mini kit (Qiagen 51304). Cell pellets were resuspended in 200 µl PBS, and 10 µl Proteinase K, 4 µl RNAse A and 200 µl buffer AL (Qiagen 51304) were added per pellet. RNAse A was added to make sure that only genomic DNA was isolated. Samples were pulse-vortexed for 15 seconds and then incubated at 56^{o}C for 10 minutes. After a brief spin, 200 µl 100% ethanol (Sigma-Aldrich, 51976) were added to the samples and they were pulse-vortexed for 15 seconds. The mixture was then transferred to a QIAamp mini spin column and centrifuged at 6,000 x *g* for 1 minute. After discarding the flow-through, the spin column was centrifuged again in a clean 2 ml tube at 6,000 *x g* for 1 minute. Per tube, 500 µl buffer AW1 were added and centrifugation was repeated as above. Flow-

through was discarded, 500 µl AW2 were added onto the columns and they were centrifuged at full-speed for 1 minute. Columns were then placed in clean 1.5 ml Eppendorf tubes, 200 µl of AE buffer (Qiagen 51304) were added and after a 5-minute incubation at 20° C, the columns were centrifuged at 7,000 x *g* for 1 minute. DNA was eluted in AE buffer for subsequent storage at -20° C.

For the DNA acid hydrolysis step, the protocol was adapted from Kok et al (322). One µg of DNA was transferred to a 1.5 ml Eppendorf tube. Samples were moved into a hood with nitrogen blow-down dryer and exposed to nitrogen gas of 5 psi pressure at 50°C (lids open). After approximately 30 minutes or when all moisture was removed, the nitrogen prongs were removed and 100 µl formic acid (Sigma-Aldrich, F0507) were added to the dried pellets. Samples were then incubated for 3 hours at 130°C in a fume hood with the shield down. At this point, a lot of attention was paid to health and safety as heated formic acid is a potential risk. To avoid tube lids from opening during the high temperature phase, multiple spare heat blocks were placed on top of the tubes. After the incubation, tubes were allowed to completely cool down, before they were safe to be handled. Once cooled down, tubes were vortexed and spun down. They were then returned to the heater and dried again with nitrogen gas at 45°C, until all moisture was removed. Once dry, 25 µl dH_2O were added to the pellets and the tubes were vortexed and spun down. After 15 minutes at 20° C, 100 µl ice-cold LCMS-grade methanol (62.5%)/acetonitrile (37.5%) solution were added. Samples were vortexed and spun at 4°C for 15 minutes. Supernatant was transferred to LCMS tubes.

LCMS was performed by the Maddocks lab using a method published by Newman et al (323). Bases from hydrolysed DNA were analysed on a Dionex Ultimate 3000 LC system coupled to a Q Exactive mass spectrometer (Thermo Scientific). Chromatographic separation was achieved using a Sequant ZIC-pHILIC column (2.13150 mm, 5 mm) (Merck) with elution buffers (A) and (B) consisting of 20 mM $(NH_4)_2CO_3$, 0.1% NH_4OH in H_2O and acetonitrile, respectively. The LC system was programmed to maintain a flow rate of 200 ml/min with the starting condition at 80% (A), which linearly decreased to 20% (A) over 10 minutes, followed by washing and re-equilibration steps (20%–80% [A]) over 7 minutes. Ionization of

the analytes occurred in a heated electrospray ionization (HESI) probe fitted to the mass spectrometer that operated in negative ion mode over a mass range between 75 and 200 m/*z* at a resolution of 70,000. Thermo LCquan software was used to identify and analyse the nucleotides. For quantification of total DNA methylation, the peak area for methyl-cytosine m+0 was divided by peak area for cytosine. Examples of chromatogram peaks are shown in figure 2.1 below.

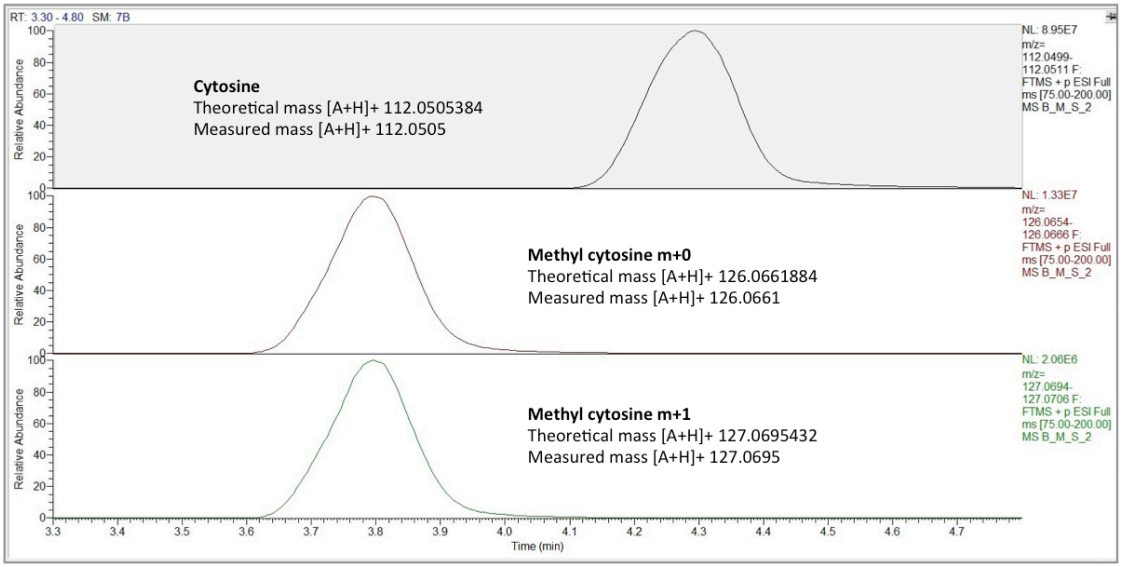

Figure 2.1: Chromatogram peaks for unmodified and methylated cytosine. Adapted from Maddocks et al, 2016, Mol Cell. Shown here after permission granted by O. Maddocks.

2.3.9 Immunohistochemistry

All the immunohistochemistry procedures, after tumour retrieval and storing in formalin, were performed by the histology department at CRUK Beatson. Immunohistochemical (IHC) staining for CD3, CD8, NKp46, F4/80 and Foxp3 was performed on 4 µm formalin fixed paraffin embedded (FFPE) sections, which had previously been heated in the oven at 60C° for 2 hours. IHC staining for CD3, CD8 and F4/80 was performed on a Leica Bond Rx Autostainer and staining for NKp46 and Foxp3 was performed on an Agilent Autostainer Link48.

The appropriate FFPE sections were loaded on the Leica Bond Rx autostainer. The CD3 and CD8 sections underwent epitope retrieval using Leica ER2 (AR9640) retrieval buffer for 20 minutes at 95°C. The F4/80 sections underwent enzymatic digestion using Leica Enzyme 1 (AR9551) for 5 minutes at 37°C. The antibodies were used at previously optimised dilutions (table 2.5) using Vector's Rat ImmPRESS (MP-7404) kit to bind to the antibody. Liquid DAB (Agilent, UK; K3468) was used to visualise the antibody-antigen complex. Sections were counterstained on board the autostainer, dehydrated in increasing concentrations of alcohol and then taken through 3 changes of xylene prior to sealing a glass coverslip using DPX mountant for microscopy.

FFPE sections for NKp46 and Foxp3 investigation underwent manual dewaxing through xylene, graded alcohol and then washed in tap water before undergoing heat-induced epitope retrieval (HIER). For FoxP3, HIER was performed on an Agilent PT module where the sections were heated to 98°C for 25 minutes in PT module 1 buffer (Thermo, UK), whereas for NKp46, HIER was performed at 97°C for 20 minutes using Flex High pH retrieval buffer (Agilent, UK). After epitope retrieval, sections were rinsed in Tris Buffered saline with Tween (Tbt, Menarini, UK) prior to being loaded onto the autostainer. The sections then underwent peroxidase blocking (Agilent, UK), washed in Tbt before application of appropriate antibody at a previously optimised dilution for 40 minutes (table 2.4). The sections were then washed in Tbt before application of rabbit EnVision (Agilent, UK; K4003) secondary antibody for FoxP3 and goat ImmPRESS antibody (Vector, UK; MP-7405) for NKp46, for 35 minutes. Sections were rinsed in Tbt before applying Liquid DAB (Agilent, UK) for 10 minutes. Haematoxylin Z (CellPath, UK) was used to counterstain the nuclei in Scott's tap water substitute. The sections were then washed in water, dehydrated in increasing concentrations of alcohol and taken through 3 changes of xylene prior to sealing with a glass coverslip using DPX mountant for microscopy.

The stained sections were then digitally captured on a Leica SCN400f slide scanner and image analysis was performed using HALO software (Indica Labs).

Mouse antigen	Supplier	Cat. No	Dilution
CD3	Abcam	ab16669	1/100
CD8	Thermo	14/9766	1/500
NKp46	R & D systems	af2225	1/200
F480	Abcam	ab6640	1/200
FoxP3	Cell Signalling	12653	1/200

Table 2.5: Antibodies used for immunohistochemistry staining.

Using the HALO software, firstly, non-malignant areas of tissue were manually excluded (figure 2.2). Following exclusion of the benign tissue areas, the slides were digitally analysed for the protein of interest using the CytoNuclear analysis tool v1.6 (example in figure 2.3). The slides were then automatically scored using the histoscore method as described by Kirkegaard et al (324). This algorithm is embedded in HALO software and after grading the staining intensity as negative (0), weakly stained (1), moderately stained (2) and strongly stained (3), it uses the formula below to calculate a histoscore value ranging between 0 and 300:

sum of (1 x % cells stained 1) + (2 x % stained 2) + (3 x % stained 3)

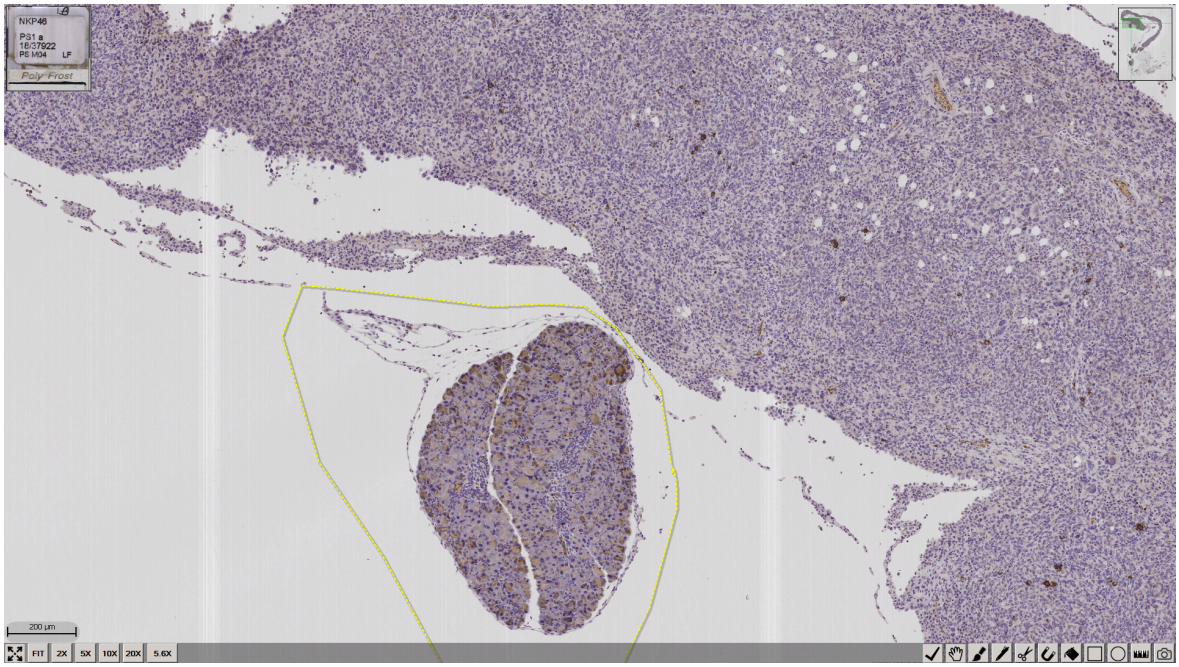

Figure 2.2: IHC showing manual exclusion of non-malignant tissue

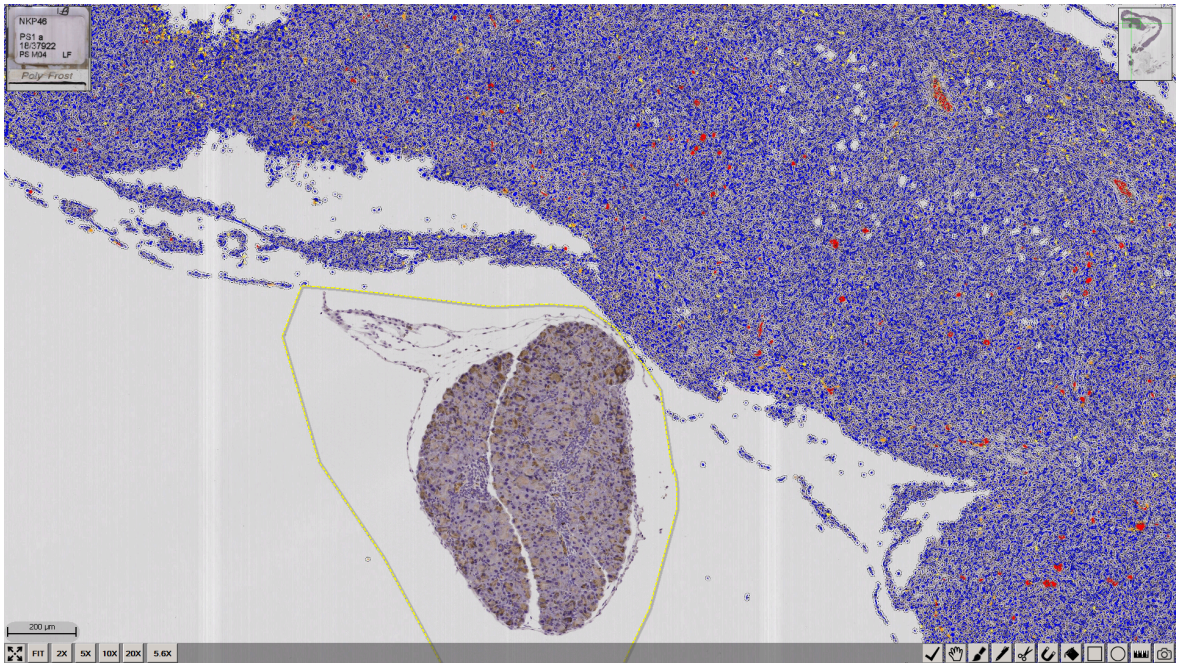

Figure 2.3: Example of the staining algorithm using CytoNuclear v1.6. Protein of interest stained (red colour) only in the malignant tissue areas. Nuclei are stained as blue.

2.4 Gene expression analysis

2.4.1 RNA extraction from cell lines and murine tumours

For cultured cells, 6-well Corning plates were used for the desirable length of time. At endpoint, medium was aspirated and cells were washed with PBS twice. After PBS washing, 350 µl RLT lysis buffer (Qiagen, 79216) were added to the wells and mixed thoroughly. Plates were now either stored at -20^{0}C or the lysate was transferred into a new eppendorf for RNA extraction as per Qiagen RNAeasy Mini kit protocol described below.

For RNA extraction from murine tumours, the weight of tumour was first determined. This was measured at the time of tumour harvesting. Tumours of less than 20 mg were immersed in 350 µl RLT with 143 mM of ß-mercaptoethanol (Sigma Aldrich, M3148), in 2 ml screw cap tubes (Star Lab, E1420-2340). For tumours between 20-30 mgs, 600 µl the same solution were used; this protocol was optimised for tumours less than 30 mg so when tumours were bigger than this size, they were cut to an approximate size of < 30mg after being placed on a cold metal block surrounded by dry ice (to ensure that they will remain frozen). Either one 2.8 mm ceramic bead or two 1.4 mm ceramic beads (Precellys, CKmix) were added in the tubes per tumour and then tumours were homogenised in a Precellys homogeniser at 2,000 x *g* for 2 periods of 30 seconds. The lysate was then centrifuged for 3 minutes at 16,000 x *g* (in a small rotor) and the supernatant was transferred to a new Eppendorf tube. Following this, the RNAeasy mini kit protocol below was followed, as per cultured cells.

One volume of 70% ethanol was added to the lysates, either from cultured cells or homogenised tumours, and pipetted gently up and down to mix. A maximum of 700 µl were transferred to an RNA binding column collection tube. The column was centrifuged for 30 seconds at 8,000 x *g* and then the flow-through discarded. Following this, 350 µl RW1 buffer were added to the column, the column was centrifuged for 30 seconds at the same speed and the flow-through again discarded. A master mix of DNase solution was made up (70 µl RDD buffer and 10 µl DNase stock) (RNase-free DNase set, Qiagen, 79254). 80µl mix were

pipetted directly onto the column and incubated for 15 minutes at 20°C. Following this, 350 µl buffer RW1 were added, centrifuged at 8,000 x *g* for 30 seconds and the flow-through discarded. Two steps of adding 500 µl RPE buffer followed, after which the columns were centrifuged for 30 seconds at step one and for 2 minutes at step two, at 8,000 x *g*, and the flow-through was discarded. The column was then placed in a new 2 ml tube and centrifuged for 1 minute at 16,000 x *g* (in a small rotor) to dry the membrane. Columns were then transferred to 1.5 ml RNase-free Eppendorf tubes. At that point, 40-50 µl RNase-free dH_2O were directly pipetted onto the column and RNA was eluted by centrifugation at 16,000 x *g* for 2 minutes. RNA was quantified using the NanoDrop 2000 spectrophotometer (Thermo Scientific, Wilmington, DE, USA), aliquoted and stored at -80°C.

2.4.2 Complementary DNA (cDNA) synthesis for reverse transcription quantitative polymerase chain reaction (RT-qPCR)

Prior to cDNA synthesis, RNA concentration was determined by NanoDrop spectrophotometer, alongside with measuring absorbance at 260 nm and 280 nm. Only samples with 260/280 ratios of approximately 2 were used for downstream cDNA synthesis. The High-capacity cDNA reverse transcription kit (ThermoFisher, 4368814) was used. The kit components and RNA samples were thawed on ice. A 2x reverse transcriptase (RT) master mix was prepared including 2 µl 10x RT buffer, 0.8 µl 25 x dNTP Mix (100 mM), 2 µl 10x RT Random Primers and 1 µl MultiScribe™ Reverse Transcriptase per sample (50 U/µL) to make a total of 5.8 µl. This was supplemented with 4.2 µl nuclease-free H2O (NF-H_2O) to a total of 10 µl. A master mix was also prepared without reverse transcriptase for a non-reverse transcriptase control (NRT). Both mastermixes were vortexed and centrifuged. A volume of RNA corresponding to 100 ng – 1000 ng (equal among samples but may vary across different experiments depending on the concentration of eluted RNA achieved) and NF-H_2O to a total of 10 µl were prepared and pipetted into qPCR tubes. Then, 10 µl the mastermix above were added per RNA sample. For the no template control (NTC), nuclease-free

H_2O was added instead of RNA. Samples were vortexed and centrifuged prior to loading onto the thermocycler (Applied Biosystems). The thermocycler was adjusted to the following settings:

1. 25°C for 10 minutes
2. 37°C for 120 minutes
3. 85°C for 5 minutes
4. 4°C (infinite hold)

cDNA produced in the reaction above was stored at -20°C prior to RT-qPCR reaction.

2.4.3 Reverse transcription quantitative PCR (RT-qPCR)

The transcribed cDNA, primers and iTaqTM Universal probes supermix (BioRad, 1725131) were thawed on ice. Hard-Shell 96-well PCR plates (Bio-Rad, HSP9631) were used. Into each well, 2 µl cDNA (amount varied between 10-100 ng between experiments but equal between samples) were mixed with 10 µl iTaqTM Universal probes supermix (containing dNTPs, iTaq DNA polymerase, $MgCl_2$, enhancers, stabilizers, and ROX normalization dyes), 7 µl NF-H_2O and 1 µl respective primer pair (table 2.6), to make a total of 20 µl. The PCR plate was sealed with adhesive Microseal B seal (BioRad MSB1001), centrifuged and loaded onto a CFX96 Real Time System (BioRad).

The following settings were applied:

1. 2 minutes 50°C
2. 10 minutes 95°C
3. 40 cycles of (15 seconds at 95°C and 1 minute at 60°C)

Fold change of gene expression was calculated using the method published by Livak et al (325). Firstly, the CT value of the gene of interest was subtracted from the CT value of the housekeeping/reference gene (ΔC_T). Following this, the $\Delta\Delta C_T$ was calculated by subtracting the ΔC_T of the gene of interest from the ΔC_T of the reference gene. The foldchange value was then calculated by converting the $\Delta\Delta C_T$ from a log2 scale to a linear scale using the following formula:

Fold change = $2^{(-\Delta\Delta C_T)}$

2.4.4 Chemokine/cytokine gene expression array

The RT^2 ProfilerTM PCR array for mouse chemokines/cytokines (Qiagen PAMM-150ZA, 330231) was used to examine changes in chemokine expression under different conditions. Plate format E384 was used; it consists of 4 replicates of a 96-well plate layout and it was used for 4 different conditions in this case.

Gene symbol	Exon spanning region	Cat No (all primers supplier by ThermoFisher)
Actb (mouse)	2-3	Mm02619580_g1
ACTB (human)	1-3	Hs01060665_g1
Cxcl10 (mouse)	1-2	Mm00445235_m1
CXCL10 (human)	1-2	Hs00171042_m1
18S ribosomal RNS (Rn18s, mouse)	-	Mm03928990_g1
GAPDH (human)	6-8	Hs02786624_g1
RANTES (CCL5, human)	1-2	Hs00982282_m1
Rantes (Ccl5, mouse)	1-2	Mm01302427_m1
MIP3b (Ccl19, mouse)	1-2	Mm00839966_g1
MCP-5 (Ccl12, mouse)	1-2	Mm01617100_m1
Stat1 (mouse)	20-21, 23-24	Mm01257286_m1
CXCL11 (human)	1-2	Hs00171138_m1
MIP-3a (CCL20, human)	2-3	Hs00355476_m1

Table 2.6: Primers pairs used for single-gene RT-qPCR

cDNA was synthesised using a different protocol than the one described above, to adhere with the instructions of the RT^2 ProfilerTM PCR (Qiagen) protocol. Using the RT^2 First Strand kit (Qiagen, 330401), 400 ng of RNA were transcribed into cDNA. Firstly, genomic DNA was eliminated by mixing 400 ng of RNA with 2 µl Buffer GE and adding NF-H_2O to a total of 10 µl. The DNA elimination mix was incubated for 5 minutes at 42ºC and then immediately placed on ice. A reverse transcription mix was prepared by mixing 4 µl 5 x buffer BC3, 1 µl control P2, 2 µl RE3 RT mix and 3 µl NF-H_2O to a total of 10 µl for each sample. This was added to the 10 µl genomic elimination mix, mixed gently and spun down. The reverse transcription mix was then incubated at 42ºC for 15 minutes and then immediately incubated at 95ºC for 5 minutes. At the end of the reaction, 82 µl NF-H_2O were added to the mix and the samples were either stored at -20ºC or used for the downstream PCR, as below.

For the RT-qPCR reaction, RT^2 SYBR Green ROX mastermix was used (Qiagen, 330520). For each sample, a PCR component mix was prepared (650 µl 2 x RT^2 SYBR Green plus 102 µl cDNA as transcribed above and 548 µl NF-H_2O) and pipetted into a reservoir. With the use of a multi-channel pipette, 10 µl the PCR component mix were added to each well of the 96-well plate replicate of the 384-well plate, with the use of different coloured 384EZLoad covers to aid pipetting.

The plate was firmly sealed with Optical Adhesive film and centrifuged for 1 minute at 260 x *g*. It was then loaded onto an AB7900 HT real time cycler and processed with the below settings:

1. 10 minutes at 95˚C
2. 40 cycles of (15 seconds at 95˚C and 1 minute at 60˚C)

Due to the complexity of data, the Qiagen online tool PCR Array data analysis Web portal was used for analysis of the results (326). The list of genes tested can be found in Appendix 1.0. The C_T cut-off was set to 38 and the data were automatically normalised to the Bmp4 and Cntf gene expression by the software; the software automatically selects an optimal set of internal control genes

derived from the full array. These are identified as the ones with the most stable expression during the experiment. Their CT values are geometrically averaged and used for the $\Delta\Delta C_T$ calculations (see Appendix 1.0 for more details).

2.4.5 Library preparation for Next Generation sequencing (NGS) of RNA

RNA from murine tumours was extracted as per 2.4.1. RNA integrity was calculated using automated electrophoresis in an Agilent 2200 TapeStation. An RNA ladder was prepared by mixing 5 µl RNA sample buffer (Agilent, 5067-5577) with 1 µl RNA ladder (Agilent, 5067-5578). Then, 1 µl the RNA samples was mixed with 5 µl RNA sample buffer and all samples were vortexed at 2,000 rpm for 1 minute. Samples were then heated at 72°C for 3 minutes and then placed on ice for 2 minutes. Samples were then spun down briefly and then inserted in an Agilent 2200 TapeStation and run on an RNA screen-tape (Agilent, 5067-5576). The electropherograms and RIN values were reviewed and only samples with RIN values > 7 were chosen for downstream library preparation.

Ribosomal RNA (rRNA) depletion

Library preparation for total RNA sequencing was performed using the New England Biolabs protocol. Firstly, 250 ng of extracted RNA in 12 µl were used in the ribosomal RNA (rRNA) depletion step (NEBNext, E6350). A mix of 1 µl NEBNext rRNA depletion solution was mixed with 2 µl probe hybridization buffer and the total volume was added to the 12 µl each RNA sample. Samples were then placed in a thermocycler and a program was run as follows with the lid set to 105°C:

1. 2 minutes at 95 °C
2. 95°C to 22°C at a pace of 0.1°C per second
3. 5 minutes at 22°C

The samples were spun down and then moved forward to the RNA ribonuclease H digestion step to degrade the hybridised RNA-rRNA. A master mix of 2 µl

NEBNext RNase H, plus 2 µl RNase H reaction buffer and 1 µl NF-H_2O was prepared in ice. This was then added to the 15 µl RNA sample from the previous step. The samples were mixed by pipetting 10 times, then spun down and placed in a thermocycler and incubated at 37^oC for 30 minutes. After incubation, samples were immediately placed on ice.

The next step was DNase digestion whereby DNA probes are degraded by DNase I. A mix of 5 µl DNase I reaction buffer, plus 2.5 µl RNase-free DNase I and 22.5 µl NF-H_2O was prepared and added to the 20 µl the RNA sample from the previous step. The total 50 µl sample was incubated at 37^oC for 30 minutes and then immediately spun down and placed on ice.

Following this, the RNA was purified with nucleic acid purification beads (Sera-Mag Magnetic Carboxylate Modified Particles, GE 44152105050250). Beads were vortexed vigorously to resuspend and then 2.2 x (110 µl) volume was added to the sample from the DNase reaction step. Samples were mixed well by pipetting and incubated on ice for 15 minutes. They were then transferred to a magnetic stand and allowed to rest for 5 minutes or until the solution became clear. Supernatant was carefully removed while the samples were still on the magnet and then the beads were washed twice with 500 µl 70% ethanol, again without removing the tubes from the magnet. After the second wash, all liquid was removed carefully, making sure that there was no ethanol left behind. Lids were then left open to dry the beads for a few minutes, and then the tubes were removed from the magnet. Whilst beads were still looking dark and glossy, 10 µl NF-H_2O were added and pipetted up and down. Tubes were allowed to rest for a few minutes before being returned to the magnet. Whilst tubes were still on the magnet, 8 µl RNA were eluted in NF-H_2O from the supernatant and transferred to another tube, making sure that the beads were not disturbed. At this point, RNA was either stored at -80^oC or the experiment continued to downstream library preparation.

Library construction

Following rRNA depletion, the sequencing library was constructed using the NEBNext Ultra™ II Directional Library prep kit for Illumina (E7760S). For the RNA fragmentation step, 5 µl rRNA-depleted RNA were mixed with 4 µl NEBNext First Strand synthesis reaction buffer and 1 µl random primers. The sample was mixed thoroughly and then placed in a thermocycler at 94°C for 20 minutes (incubation time optimised in advance). After incubation, samples were immediately placed on ice.

The fragmented RNA was then subjected to First Strand cDNA synthesis. Whilst still on ice, 10 µl the fragmented and primed RNA were mixed with 8 µl NEBNext strand specificity reagent and 2 µl NEBNext First Strand synthesis Enzyme mix and mixed by pipetting. The sample was then incubated in a cycler with the following protocol:

1. 10 minutes at 23°C
2. 15 minutes at 42°C
3. 15 minutes at 70°C
4. Hold at 4°C

The entire product of the first strand synthesis was then mixed with 8 µl NEBNext 2nd strand synthesis reaction buffer containing dUTP, 4 µl NEBNext 2nd strand synthesis enzyme mix and 48 µl NF-H_2O. The samples were mixed thoroughly and were incubated for 1 hour at 16°C with the lid open.

The second strand cDNA synthesis product was then purified using 1.8 x the sample volume of the magnetic beads (i.e. 144 µl). The DNA-bead mixes were allowed to incubate for 5 minutes at 20°C and then placed on a magnet. After the solution became clear, the same process of purification as earlier was followed. After the last ethanol step, 50 µl 0.1 x Tris-HCl/EDTA (TE) buffer were used to elute the DNA from the beads.

To prepare an End Prep of cDNA library reaction mix, the 50 µl cDNA above were mixed with 7 µl NEBNext Ultra II End Prep reaction buffer and 3 µl NEBNext Ultra

II End Prep enzyme mix. The samples were then incubated in a thermal cycler as follows:

1. 30 minutes at 20°C
2. 30 minutes at 65°C
3. Hold at 4°C

To proceed to the Adaptor Ligation step, the NEBNext adaptor was diluted from 5 x in Adaptor ligation buffer on ice and 2.5 µl the diluted adaptor were added to the End-Prepped DNA plus 1 µl NEBNext ligation Enhancer and 30 µl NEBNext Ultra II ligation mastermix. The sample was pipetted up and down to mix thoroughly and then incubated at 20°C for 15 minutes. After this, 3 µl the USER enzyme were added to make a total volume of 96.5 µl, mixed thoroughly and incubated for another 15 minutes at 37°C.

The ligation reaction product was purified using magnetic beads one more time, with a volume of 87 µl beads (0.9 x of the sample). At the end of the purification, DNA was eluted in 15 µl 0.1 x TE buffer.

For the final step of library construction, DNA was amplified by PCR enrichment. The adaptor-ligated DNA was mixed with 25 µl NEBNext Ultra II Q5 mastermix, 5 µl universal PCR primer (i5 primer) and 5 µl 10 µM index (barcoded) primer (i7 primer, NEBNext multiplex oligos for Illumina index primers set 1 and set 2 (E7335S and E7500S, see Appendix 2.0 for more details on primers). Different barcoded primers were used for different samples to allow for accurate identification during sequencing. Samples were placed in a thermocycler and the PCR reaction below was performed:

1. 1 cycle of 30 seconds at 98°C
2. 9 cycles of 10 seconds at 98°C and 75 seconds at 65°C
3. 5 minutes at 65°C

The cycle number for step 2 was determined based on the amount of input RNA and following optimisation done prior to processing the tumour samples of interest.

Lastly, DNA was purified one last time with 0.9x magnetic beads (45 µl) as described already. At the end of purification, DNA was eluted in 20 µl 0.1x TE buffer. All samples were then subjected to quality control using 1 µl DNA per sample on the Agilent D5000 Screen Tape System. DNA samples were mixed with 10 µl D5000 sample buffer each (Agilent, 5067-5589). Similarly, 1 µl the DNA ladder was mixed with 10 µl D5000 sample buffer. The samples and the ladder were vortexed, spun down and then transferred to an Agilent 2200 TapeStation where they were subjected to automated electrophoresis using D5000 Screen Tapes (Agilent 5067-5588). DNA was quantified using the Qubit dsDNA high sensitivity assay kit (Thermofisher, Q32854).

Samples with electropherograms showing a single DNA peak between 200-300 bp size were then subjected to next generation sequencing (NGS). All samples were pooled to an equal concentration of 10 nM in 150 µl before sequencing.

The amplified library was sequenced on the Nova6000 SP flow cell (Illumina) with a paired-end sequencing strategy. Read length was 50 base pairs with an expected 50 million read pairs per sample. The precise methodology of RNAseq analysis will be described in more depth in Chapter 5.

2.5 Chromatin Accessibility Profiling - Assay for Transposase Accessible Chromatin using Sequencing (ATAC-seq)

To assess chromatin configuration in murine tumours, the Assay for Transposase-Accessible chromatin sequencing (ATAC-seq) was performed using a protocol designed specifically for frozen tumours (Omni-ATAC protocol) (327). This protocol was optimised for frozen tumours derived by the ID8 cell line by me. A variety of buffers were prepared prior to the experiment (stable solutions) or fresh on the day of nuclei extraction (unstable solutions).

Frozen tumours (20 mg – 30 mg) were placed in 1 ml ice-cold 1 x unstable homogenization buffer (HB, table 2.7) in a glass Dounce homogeniser (Sigma-Aldrich, D8938). Tumours were allowed to thaw and sink to the bottom of the

dounce. Then, the tissue was dounced with pestle A with 10 strokes and pestle B with 20 strokes. Large chunks of tissue were "cleared" by centrifuging at 100 x *g* for 1 minute at 4ºC and after centrifugation, 400 µl the lysate were mixed with 400 µl the 50% iodixanol mix to give a final concentration of 25% iodixanol (table 2.8). Following this, 600 µl 35% iodixanol mix were placed at the bottom of a 2 ml safe-lock tube (VWR, 0030120094). Without mixing layers, 600 µl 29% iodixanol mix were placed on the top of the 30% mix and finally, 800 µl the 25% iodixanol also containing the tumour lysate were added on top. To maximise nuclei yield, one more aliquot of 400 µl the lysate was added to a second tube with an iodixanol gradient. The tubes were centrifuged in a swinging bucket centrifuge at 4,000 x *g* for 20 minutes and with the brake off.

6 x Homogenisation Buffer Stable Master Mix			
Reagent	**Final Conc.**	**Fold Dilution (x)**	**Vol for 100 mL**
1 M $CaCl_2$	30 mM	33.33	3 mL
1 M Mg $(Ac)_2$	18 mM	55.56	1.8 mL
1 M Tris pH 7.8	60 mM	16.67	6 mL
H_2O			89.2 mL
6 x Homogenisation Buffer – unstable solution			
			Volume per sample
6 x Homogenization Buffer Stable	6x	1	636.3
100 mM PMSF	0.1 mM	1000	0.7
14.3 M ß-mercaptoethanol	1 mM	14300	0.05
50x Roche protease inhibitor	1x	50	13
1 x Homogenisation Buffer - unstable solution			
6 x Homogenization Buffer Ustable	1x	6	166.7
1 M Sucrose	320mM	3.13	319.5
500 mM EDTA	0.1mM	5000	0.2
10% Nonidet	0.10%	100	10
H_2O			503.6

Table 2.7 Omni-ATAC protocol buffers (Nonidet was purchased from Roche, 11332473001).

Following centrifugation, the top 1,100 µl the iodixanol gradient were aspirated, in order to reach within approximately 300 µl the nuclear band. After this, 400 µl containing the nuclear band were transferred to a fresh tube. For quantification, 10 µl the nuclei band solution were mixed with 10 µl trypan blue stain 0.4% (ThermoFisher, 15250061) and 8 µl the mix were transferred onto a disposable counting slide (Immune Systems, BVS100). All nuclei stained with trypan blue were taken into account. At this point, 20,000 nuclei were transferred in 500 µl ATAC-RSB reagent (10 mM Tris-HCl pH 7.4, 10 mM NaCl, 3 mM $MgCl_2$ and 0.1% (v/v) Igepal 630 in 100 ml H_2O).

Solutions for Iodixanol gradient			
50% Iodixanol Solution			
Reagent	**Final Conc**	**Fold Dilution (x)**	**Vol per sample (ul)**
6 x Homogenisation Buffer Unstable	1x	6	66.67
60% Iodixanol	50%	1.2	333.33
29% Iodixanol Solution			
6 x Homogenization Buffer Unstable	1x	6	100.00
1 M Sucrose	160mM	6.25	96.00
60% Iodixanol Solution	29%	2.07	289.86
H_2O			114.14
35% Iodixanol Solution			
6 x Homogenization Buffer Unstable	1x	6	100.00
1 M Sucrose	160mM	6.25	96.00
60% Iodixanol Solution	35%	1.71	350.88
H_2O			53.12

Table 2.8 Solutions for Iodixanol gradient. Conc=concentration

Igepal 630 is octylphenylpolyethylene glycol and was bought from Sigma (I8896). The mix of nuclei and ATAC-RSB was centrifuged at 600 x *g* for 10 minutes at 4°C. The supernatant was aspirated carefully; reagents and transposase (Tn5) were added to the invisible nuclear pellet as per table 2.9. The mix was incubated for 30 minutes at 37°C at 400 rpm in an Eppendorf Thermomixer comfort incubator. The incubation time was determined after optimisation. Following incubation, samples were placed on ice and the MiniElute PCR purification kit (Qiagen, 28004) was used to clean up the DNA fragments.

Five volumes of buffer PB were added to the transposase reaction product and placed in a MinElute column. The column was centrifuged for 1 minute at 17,900 x *g* at 20°C. The flow-through was discarded and 750 µl buffer PE were added onto the column. The column was centrifuged again at the same conditions and the flow-through was discarded. One more centrifugation was performed with the column in a clean 2 ml tube to completely dry the membrane and then the column was placed in a clean 1.5 ml Eppendorf tube. To elute DNA, 10 µl buffer EB (Tris-HCl, pH 8.5) were added to the column and left to stand for 1 minute. DNA was eluted in 10 µl following one last centrifugation as above. DNA was stored at -20°C or used for down-stream library construction immediately.

Omni-ATAC ATAC-seq reaction mix	20 µl reaction	Supplier	Product code
2 x TD buffer	10	Illumina Tagment DNA buffer	15027866
Transposase (100nM)	0.5	Nextera Tagment DNA enzyme I	15027916
PBS	6.6		
1% Digitonin	0.2	Promega	G9441
10% Tween-20	0.2		
dH_2O	2.5		

Table 2.9 Transposase (Tn5) reaction solution.

The purified, transposed DNA was transferred into 0.2 ml PCR tubes and mixed with 10 µl dH_2O, 25 µl NEBNext High-Fidelity 2 x PCR mastermix (NEB, M0541S), 2.5 µl Universal customed PCR primer 1 and 2.5 µl customised index (barcoded) PCR primer 2 (all customised from Sigma, see Appendix 3.0). The customised primers were designed as described by Buenrostro et al (328).

The mix was incubated in a thermocycler with the program (ATAC1) below:

1. 1 cycle of 5 minutes at 72°C and 30 seconds at 98°C
2. 5 cycles of 10 seconds at 98°C, 30 seconds at 63°C and 1 minute at 72°C

For the quantification of how many extra PCR cycles are needed for further library amplification, a test RT-qPCR was performed. Five µl the already amplified DNA were mixed with 5 µl NF-H_2O, 5 µl NEBNext High-Fidelity 2 x PCR mastermix, 5 µl 100x SYBR Green I (BioRad, 1708880) and 0.4 µl each primer (universal and barcoded as described above). The qPCR was run with the settings (ATAC2) below:

1. 30 seconds at 98°C
2. 20 cycles of 10 seconds at 98°C, 30 seconds at 63°C and 1 minute at 72°C

When the test qPCR was complete, and in order to calculate the additional number of further cycles needed, the linear Relative Fluorescence Units (RFU) *vs* cycle was plotted and the cycle number that corresponds to one-third of the maximum fluorescent intensity was determined (n). This number (n) was the number of the additional cycles of PCR needed to minimally amplify the library and thereby reduce GC and size bias. An example of how this n number was determined is shown in figure 2.4. The remaining 45 µl the DNA product were again incubated using the ATAC1 protocol above, where the 5 cycles were substituted by n cycles.

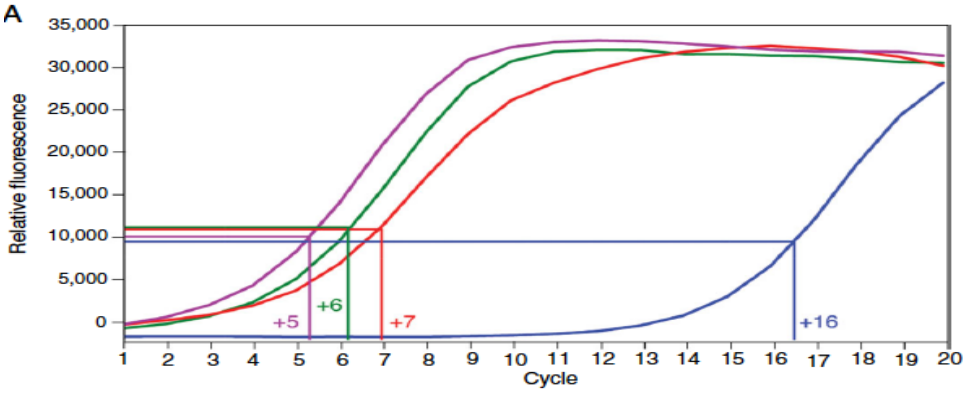

Figure 2.4: Plot depicting way to estimate the ideal number of extra PCR cycles needed for four ATAC sequencing libraries. Adapted from Buenrostro et al (329).

Following the final amplification, the DNA fragments underwent bead clean-up as described in section 2.4.5 with the Sera-Mag Speed Carboxyl beads. The beads were added at a ratio of 1.8x times the DNA sample volume (81 µl) and at the end of the clean-up, DNA was eluted in 20 µl dH_2O. Quality control was performed by assessing the electropherogram appearance on an Agilent 2200 TapeStation as described in section 2.4.5 and quantification was done using Qubit dsDNA high sensitivity assay kit. The amplified library was sequenced on a Nova6000 S1 flow cell (Illumina) with a paired-end sequencing strategy. Read length was 50 base pairs. The precise methodology of ATACseq analysis will be described in more depth in Chapter 5.

2.6 In vivo experiments

2.6.1 Animal husbandry

Animal experiments were carried out in accordance with the U.K. Home Office Animal (Scientific Procedures) Act 1986, under the project licence 70/0845 at CRUK Beatson, Glasgow and project licences 70/7997 and PA780D61A for experiments performed at Imperial College, London. All mice used in the experiments described in this thesis were 6-7 weeks old, wild-type C57BL/6 females, purchased from Charles River. Animals were allowed to acclimatise for

at least 7 days before being handled or subjected to any experimental procedures. Signs that required termination by Schedule 1 included: weight loss of 20% or more, ascites equivalent to full term pregnancy, reduced/slow activity, pale feet and visible symptoms of distress such as hunching, piloerection, closed eyes and isolation from cage mates. Additional animal husbandry was provided by technical staff in the animal facilities of either CRUK Beatson, Glasgow or Imperial College, London.

2.6.2 Tumour inoculation and endpoint

ID8 cell line derivatives were washed, trypsinised, resuspended in complete medium and counted. Pellets were washed once in PBS and resuspended at 25 x 10^6 cells/ml in 37°C PBS. Cells were then injected intraperitoneally (IP) in a volume of 200 µl (5x10^6 cells per mouse) as previously described (319). Specific drug treatments are described in the appropriate results chapters. During the initial 3-4 weeks, mice were weighed once a week. Approximately 5-6 weeks after inoculation of tumour cells, mice started developing abdominal swelling due to ascites and were subsequently weighed 2-3 times per week, or more frequently if there was welfare concern. In experiments that aimed to delineate survival, the endpoint was determined by the signs described in 2.6.1. All those making decisions about humane endpoints were blinded to the treatment groups.

2.6.3 Murine blood sampling

For in vivo experiments performed at the CRUK Beatson Institute, blood sampling was permitted via mouse cardiac puncture after performing Schedule 1 termination. Full blood count analysis was obtained using a Procyte Dx® Haematology Analyzer (IDEZZ Laboratories).

2.6.4 Harvesting of tumour samples

Tumour sample harvesting process was previously optimised by the McNeish lab. Following Schedule 1 termination, the abdominal skin was removed, and a small incision was made just below the xiphisternum. The mouse was then rapidly inverted on top of a 50 ml Falcon tube and any ascites was decanted. If no ascites was present during harvesting (the case in exploratory experiments), the peritoneal cavity was first washed with 5 ml chilled FACS buffer (0.5% FBS, 2 mM EDTA in PBS), the mouse was gently agitated and then inverted to decant any peritoneal fluid present through a small incision. Ascites was placed on ice until further processing.

Upon dissecting the peritoneum, multiple sites of disease were observed as described in figures 2.5 and 2.6. Peritoneal deposits were too small to harvest but the omental and/or the porta hepatis tumours were placed in ice-cold PBS, snap-frozen in dry ice, or placed in 10% Neutral Buffered Formalin (NBF, Sigma-Aldrich HT501128). If tumours were placed in formalin, formalin was replaced with 70% ethanol after 24 hours. When tumours were snap-frozen, they were stored at -80°C.

All samples (ascites, tumours, spleens) were measured/weighed before stored or used in downstream experiments. Mouse ascites that was not analysed immediately, was centrifuged at 260 x g for 5 minutes and the supernatant was aspirated and stored at -80°C. The remaining cell pellet was treated with 5 ml 1 x Red Blood Cell Lysis buffer (BioLegend, 420301, made 1x in dH_2O) for 10 minutes at 20°C. To neutralise, 5 ml PBS were added, and the tube centrifuged again at 260 x g. After the second centrifugation, supernatant was discarded, and the cell pellets were cryopreserved in freezing medium as described in section 2.1.

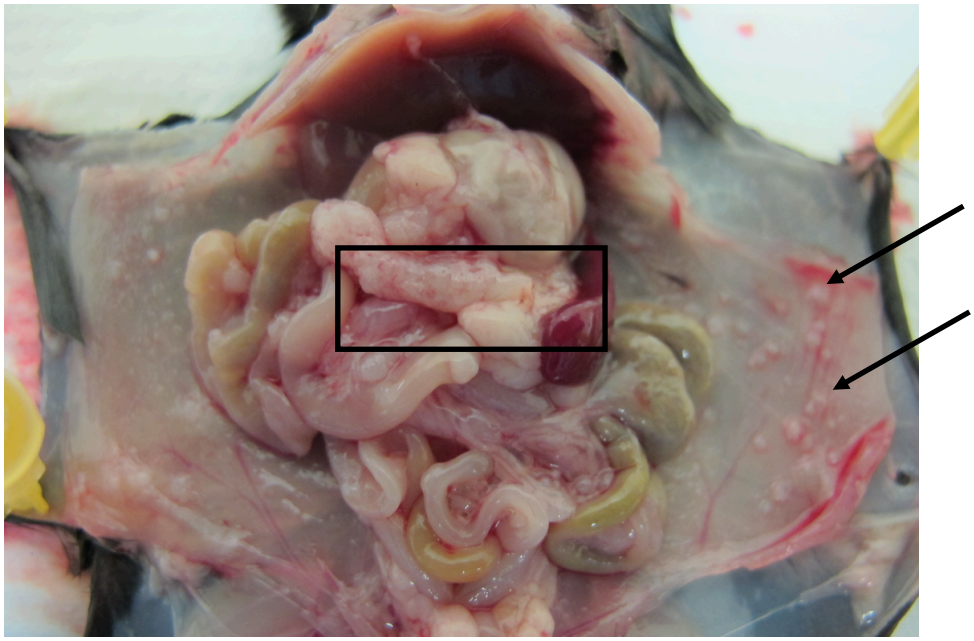

Figure 2.5: Peritoneal cavity of a wild-type C57BL/6 mouse bearing ID8 *Trp53*$^{-/-}$ tumours – omental and peritoneal deposits. Mouse is bearing an omental tumour (box) and peritoneal deposits on the visceral aspect of the peritoneum (arrows).

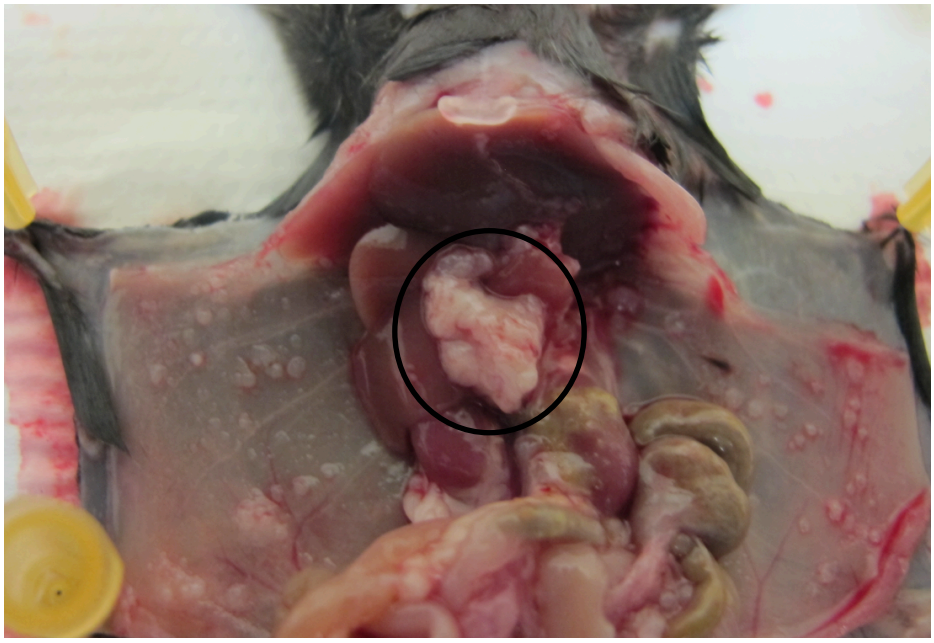

Figure 2.6: Peritoneal cavity of a wild-type C57BL/6 mouse bearing ID8 *Trp53*$^{-/-}$ tumours; porta hepatis deposit. The deposit situated below the liver (circle) – stomach and mesentery have been removed.

2.7 Flow cytometry following in vivo work

2.7.1 Tumour digestion

Tumour digestion and downstream flow cytometry protocol was created and optimised by Dr Sarah Spear, McNeish lab. Aliquots of stock 100x collagenase (Sigma, C7657) and 100x dispase (Gibco, 17105041) were prepared prior to tumour harvesting. Tumours in ice-cold PBS were chopped into small pieces with a sterile scalpel before being transferred into 5 ml RPMI medium in a 50 ml falcon tube. Collagenase and dispase were added at 1 x and tumours were incubated on a shaker at 37°C. After 20 minutes, 50 µl 0.5 M EDTA were added to quench the enzymes. The tumour solution was then passed through a 70 µm sterile filter (Easystrainer, Greiner bio-one, 542 070). Tumour pieces were mashed with a 1 ml syringe plunger onto the filter and washed through with RPMI medium, creating a single cell suspension in the new falcon tube. The suspension was then centrifuged in a pre-chilled large rotor centrifuge at 260 x *g*, resuspended in 1 ml complete RPMI medium (section 2.1) and counted in an automated cell counter (Invitrogen, Countess II). 2 x 10^6 cells per sample were then plated in 100 µl volume, in clear V-bottom plate wells (Thermo Scientific,735-0184), for further antibody staining. If the cell count was insufficient, equal numbers of cells between samples were plated instead, depending on the lowest concentration of cells present in a tumour. A small aliquot from each sample was always preserved for staining control samples [unstained controls, cell viability controls and fluorescence-minus-one controls (FMO)]. When mouse ascites was also stained for flow cytometry, the above cell seeding conditions were used after performing red blood cell lysis, as described in section 2.6.4.

2.7.2 Antibody staining

After plating cells derived from tumour digestion in V-bottom plate wells, the plate was centrifuged at 260 x *g* for 5 minutes at 4°C (henceforth all centrifugation steps will be at these settings). Supernatant was decanted and 50

µl mouse FcR II/III block were added per well (BD Biosciences, 553142, diluted 200x in FACS buffer) to block non-specific binding of immunoglobulin to Fc receptors. Cells were resuspended using a multichannel pipette and incubated at 4ºC for 15 minutes. After incubation with FcR block, 50 µl the antibody mastermix (table 2.10 and table 2.11) or FMO mix, diluted in FACS buffer, were added to respective wells and incubated at 4°C for 30 minutes. Each antibody concentration/dilution had already been optimised in the McNeish lab. Wells were then washed with 100 µl FACS buffer and the plate was centrifuged. Supernatant was decanted by gentle inversion and 50 µl Zombie Yellow fixable viability dye (diluted 1:200 PBS) were added per sample and the plate was incubated at 4ºC for 20 minutes. Samples were then washed with 100 µl FACS buffer and centrifuged again before fixation with 100 µl 2% NBF diluted in FACS buffer. The samples were finally incubated in NBF at 4°C for 20 minutes and then washed with FACS buffer and centrifuged again before resuspension in 200 µl FACS buffer and transfer to flow cytometry tubes. Samples were kept at 4°C for no longer than 1-2 days before analysis at the flow cytometer.

For interrogation of intranuclear markers (such as FoxP3), after staining with extracellular markers, the True-Nuclear Transcription factor buffer (Biolegend 424401) was used. A Fixation (Fix) buffer provided by the kit was used instead of formalin at the step described above. Cells were incubated with 100 µl Fix buffer at 20ºC (1x made up by diluting the 4x concentrate with Fix Diluent) for 20 minutes. Wells were then washed with 1x Permeabilisation buffer (made by diluting the 10x Perm buffer in PBS) and then resuspended in the intranuclear antibody/fluorochrome (diluted in 1x Perm) and incubated for 30 minutes at 20ºC. Wells were then washed with 1x Perm buffer and then washed again in FACS buffer at 20ºC, before resuspending in 200 µl FACS buffer in flow cytometry tubes.

2.7.3 Intra-tumoural T cell stimulation and staining for flow cytometry

When the intracellular abundance of chemokines was tested via flow cytometry, an aliquot of tumour-derived cells was plated in clear non-treated U-bottom plate (SLS,3879) after tumour digestion (as described in 2.7.1). After plating the cells, a cocktail of phorbol 12-myristate 13-acetate (PMA) and ionomycin (eBioscience, 00-4970) was used to stimulate the immune cell populations into secreting chemokines. The 500x stock was used at 2 µl/ml concentration in immune cell medium (medium recipe described in section 2.1). One hour after addition of the stimulation, a 500x protein transport inhibitor cocktail (eBioscience, 00-4980) was added at 1 x, to achieve intracellular retention of the secreted chemokines. After 4 hours of incubation with the inhibitor cocktail, the cells were transferred to a V-bottom plate and the staining protocol as described in 2.7.2 was followed. After the formalin fixation step, the plate was washed once in FACS buffer and once in permeabilisation buffer (10 x Perm buffer diluted to 1 x with dH_2O, Biolegend, 421002). Both washes were performed at 20°C. Cells were then stained with intracellular antibodies diluted in perm buffer and incubated for 20 minutes at 20°C. The plate was washed with 1 x perm buffer and then washed again in FACS buffer before resuspending in 200 µl FACS buffer in flow cytometry tubes. The gating strategy for intracellular chemokines is demonstrated in Appendix 9.0.

Marker	Fluorochrome	Dilution	Clone	Company	Code
CD45	Pacific Orange	1 in 20	30-F11	Life Technologies	MCD4530
CD11b	BUV 737	1 in 300	M1/70	BD Biosciences	6245992
Ly6G	Brilliant Violet 785	1 in 50	1A8	Biolegend	127645
Ly6C	Alexa Fluor 647	1 in 1500	HK1.4	Biolegend	128010
F4/80	PE	1 in 50	REA126	Miltenyi	130-102-943
MHC II	FITC	1 in 50	M5/114.15.2	Miltenyi	130-102-910
CD86	PE/Cy7	1 in 20	GL-1	Biolegend	105014
CD8a	Brilliant Violet 650	1 in 80	53-6.7	Biolegend	100742
PDL-1 (CD274)	Brilliant Violet 421	1 in 300	10F.9G2	Biolegend	124315
CD3	PerCP-Cy5.5	1 in 150	17A2	Biolegend	100217
CD19	APC/Fire 750	1 in 300	6D5	Biolegend	115557
Fixable viability dye	Similar to PE/Texas Red	1 in 200		Biolegend	423110

Table 2.10: Antibody-fluorochrome flow cytometry panel for BD FORTESSA cytometer

2.7.4 Compensation

UltraComp compensation beads (Life Technologies, 01-2222-42) were used prior to the experiments as single-color compensation control. One drop containing both a positive and a negative population was mixed with 1 µl each fluorochrome and incubated at 4ºC for 15 minutes. After incubation, 1 ml FACS buffer was added and the tubes were centrifuged at 500 x *g* for 4 minutes. FACS buffer supernatant was removed and 200 µl fresh FACS buffer were added to each tube of beads. The bead samples were run (at least 5,000 events) prior to analysing the true samples in order to correct for emission spill over between flow cytometry channels.

2.7.5 Flow cytometry analysis

Flow cytometry was performed on either a BD Fortessa (BD Biosciences, CRUK Beatson Institute) or on a Cytek Aurora cytometer (LMS/NIHR Imperial Biomedical Research Centre Flow Cytometry Facility). For each sample, a maximum of 500,000 events were captured and analysed with FlowJo software (LLC, 2006-2018). Immune cell populations were analysed either as an absolute number of cells per tumour weight (cell number per well and tumour weight were all recorded before antibody staining process) or as percentages of the wider cell population they belong to. This was further optimised by using counting beads during analysis at the flow cytometer (ThermoFischer, CountBright Absolute counting beads, C36950); the method used to quantify cell populations will be clearly stated in each experiment described, in the respective chapter.

The identification of cell populations via flow cytometry was done with the following markers/stains: Zombie Red or Green fixable viability dye which penetrates dead cells and helps to exclude them, CD45 marker for all lymphocytes (330), CD11b for cells of myeloid lineage (331) and CD19 for B cells (332). CD3 marker was used to capture T lymphocytes (333) from the CD19 and CD11b double-negative pool. $CD8^+$ cytotoxic and $CD4^+$ helper T lymphocytes were selected with their respective markers from the $CD3^+$ pool (334). From the $CD11b^+$ pool of cells, the triple negative cells for markers Ly6G, Ly6C and SiglecF were captured as a population containing macrophages and dendritic cells. Of those, macrophages were selected as $F4/80^+$ and $MHCII^-$, whereas dendritic cells were further selected for being positive for $MHCII^+$ and $CD11c^+$ marker (335-337) and negative for F4/80.

2.8 Drug Screening

Methodology of medium-throughput screening of a panel of novel epigenetic probes, provided by the Structural Genomics Consortium, will be described in Chapter 3.

Marker	Fluorochrome	Dilution	Clone	Company	Code
Myeloid pool					
CD45	Alexa Fluor 532	1 in 100	30-F11	ThermoFisher	58-0451-82
Ly6G	Alexa Fluor 700	1 in 200	1A8	Biolegend	127622
Ly6C	Brilliant Violet 605	1 in 100	HK1.4	Biolegend	128036
MHC II	Brilliant Violet 510	1 in 200	M5/114.15.2	Biolegend	107636
CD206	Brilliant Violet 711	1 in 100	C068C2	Biolegend	141727
CD80	APC/Fire750	1 in 100	16-10A1	Biolegend	104740
CD86	Brilliant Violet 785	1 in 100	GL-1	Biolegend	105043
F4/80	PE	1 in 50	BM8	Biolegend	123110
CD11b	eFluor450	1 in 100	M1/70	ThermoFisher	48-0112-82
SiglecF	FITC	1 in 50	REA798	Miltenyi	130-112-178
CD11c	PerCP/Cy5.5	1 in 100	N418	Biolegend	117328
PD-1 (CD279)	Brilliant Violet 605	1 in 100	29F.1A12	Biolegend	135220
Cxcr3	PE/Dazzle 594	1 in 100	Cxcr3 - 173	Biolegend	126534
Lymphocyte pool					
CD8a	Alexa Fluor 700	1 in 400	53-6.7	Biolegend	100730
CD19	PerCP/Cy5.5	1 in 200	6D5	Biolegend	115534
CD4	FITC	1 in 400	RM4-5	Biolegend	100510
CD44	PE	1 in 200	IM7	Biolegend	103024
CD62L	Brilliant Violet 785	1 in 100	MEL-14	Biolegend	104440
CD49b (DX5)	PE/Cy7	1 in 100	DX5	Biolegend	108916
NK1.1	APC	1 in 100	PK136	Biolegend	108710
Cxcr3	Brilliant Violet 510	1 in 100	Cxcr3 - 173	Biolegend	126528
PD-L1 (CD274)	Brilliant Violet 421	1 in 100	10F.9G2	Biolegend	124315
FOXP3	Alexa Fluor 647	1 in 50	MF-14	Biolegend	126408

Marker	Fluorochrome	Dilution	Clone	Company	Code
Lymphocyte stimulation pool					
Perforin	PE	1 in 50	S16009A	Biolegend	154306
TNFa	APC	1 in 50	MP6-XT22	Biolegend	506308
IFNγ	Brilliant Violet 510	1 in 50	XMG 1.2	Biolegend	505842
Granzyme B	PE/Cy7	1 in 50	QA16A02	Biolegend	372214
Viability Dye					
Zombie yellow	Similar to BV570	1 in 300		Biolegend	423104

Table 2.11: Antibody-fluorochrome flow cytometry panel for Cytek Aurora cytometer

2.9 Statistical Analysis

All statistical analysis was performed by me, unless otherwise stated in the text in chapter 5. All data are expressed as the mean, and error bars represent standard deviation of the mean (SD). Statistical tests were performed using Prism v7.0 (GraphPad, San Diego, CA).

Data normality was tested with D'Agostino-Pearson, Shapiro-Wilk or Kolmogorov-Smirnov tests. Differences between two group means were analysed using a Student's *t*-test or Mann-Whitney test. Wilcoxon test was used for comparison between paired non-parametric data. For differences between more than two groups, one-way ANOVA was used with Dunnett's test for multiple comparisons.

Differences in median survival were calculated using log-rank (Mantel-Cox) test. A p value ≤0.05 (*) was considered significant. The level of statistical significance is indicated using asterisks (*p<0.05, **p<0.01, ***p<0.001, ****p<0.0001).

Quantification of protein levels as measured with Western blot were analysed using the image analysis tool Image J (338).

Chapter 3. Screening novel epigenetic compounds

3.1 Introduction and aims

The intersection between epigenetics and immunity has been investigated for a long time, with the main focus being on the roles of DNA methylation and histone acetylation (257, 339). Modifiers targeting these mechanisms were the first epigenetic drugs to be developed and approved by the US Food and Drug Administration (FDA) and the European Medicines Agency (EMA) for use in patients with cancer. DNA methyltransferase (DNMT) inhibitors, such as azacytidine and decitabine are cytidine analogues that, when given at low doses, are incorporated into DNA where they block the catalytic function of DNMTs (340, 341). This leads to the gradual degradation of DNMTs and eventually widespread DNA hypomethylation, which has been extensively studied in patients with haematological malignancies (342, 343). DNA hypomethylation also plays a role on immune pathways by de-repressing immune-stimulatory genes, such as tumour-associated antigens (264, 344-346), genes involved in the interferon pathway (312, 313, 347) and more specifically, chemokines (282, 284). On the other hand, inhibitors of histone deacetylation (HDACi) lead to the accumulation of hyperacetylated histones and therefore alter the chromatin state into a conformation that is more accessible to transcription (348-351). Targeting histone acetylation in cancer cells allows for the de-repression of genes involved in immune response with mechanisms that may be overlapping with DNMTs (352). Treatment with HDACs stimulates translation of antigens in melanoma (353), expression of MICA and MICB in hepatocellular carcinoma (354) and trigger chemokine production and immune-mediated tumour regression in several tumour models (283, 355).

I hypothesized that other epigenetic modifications, aside from DNA methylation and histone acetylation, could be involved in regulation of immunity, either separately or in combination with each other, in ovarian cancer. I wished to examine if immunogenicity could be augmented via alternative epigenetic mechanisms in a murine ovarian cancer model that represents a disease, characteristically resistant to immunotherapy. To this end, I utilised a library of epigenetic probes designed and provided by the Structural Genomics Consortium (356) that consisted of probes against histone methyltransferases and demethylases, bromodomains, histone acetylases and deacetylases, oxoglutarate oxygenase, methyl-lysine binders and arginine deiminases (Table 3.1).

I chose levels of the chemokine CXCL10 as the read out following treatment of tumour cells with the SGC library, primarily because of the previously described associations between the intra-tumoural presence of CXCL10 and the development of an immunoreactive tumour microenvironment (68), and improved prognosis in patients with ovarian cancer (188). CXCL10, as part of the CXCL9/CXCL10/CXCL11 and CXCR3 axis, is involved in immune cell migration, differentiation and activation (357-359) and has been found to have anti-tumour effects both via immunostimulatory and angiostatic pathways (360). When CXCL10 was overexpressed in the syngeneic ovarian cancer ID8 model (*Trp53* proficient clones), tumour regression was observed with evidence of reduced tumour vasculature via IHC and a concomitant increase in the intra-tumoural expression of immunostimulatory genes (198). CXCR3 receptor presence has been found to be critical in the ability of cytotoxic lymphocytes to achieve tumour infiltration (361). Specifically human NK cells that are expanded ex vivo express higher levels of CXCR3 receptor and consequently demonstrate an enhanced ability to migrate towards CXCL10-producing melanoma tumours (166). Importantly, Chow et al showed that in melanoma models, the presence of CXCR3 system is imperative for tumour response to PD-1 blockade and without it, a functional $CD8^+$ T cell response cannot be elicited (362). For all the above reasons, as well as the fact that CXCL10 emerged as a technically easy to detect marker in my assays, I decided to use it as the readout of my medium throughput drug screening.

Probe Name	Family	Target
LAQ824	HDAC - class I, IIa, IIb	HDAC 1/p21 promoter activation
UNC0638	Methyltransferase	G9a, GLP
A-366	Methyltransferase	G9a (EHMT2), GLP
PFI-4	Bromodomains	BRPF1B
SGC0946	Methyltransferase	DOTL-1
UNC0642	Methyltransferase	G9a, GLP
GSK343	Methyltransferase	EZH2
GSK2801	Bromodomains	BAZ2A/2B
IOX2	Oxyglutarate oxygenase	PHD2
NI-57	Bromodomains	BRPF1, BRPF2, BRPF3
LLY507	Methyltransferase	SMYD2
GSK484	Arginine deiminase	PAD-4
PFI-3	Bromodomains	SMARCA, PB1
UNC1215	Methyl-lysine binder	L3MBTL3
I-CBP112	Bromodomains	CREBBP, EP300
BAZ2-ICR	Bromodomains	BAZ2A, BAZ2B
SGC 707	Methyltransferase	PRMT3
MS049	Methyltransferase	PRMT4,6
NVS-1	Bromodomains	CECR2
KDOAM25	Demethylase	KDM5
GSK591	Methyltransferase	PRMT5
BAY-598 (S-4)	Methyltransferase	SMYD2
OICR9429	Methyltransferase	WDR5
A196	Methyltransferase	SUV420 H1/H2
MS023	Methyltransferase	Type I PRMTs
IOX1	Oxyglutarate oxygenase	pan-2-OG
OF-1	Bromodomains	BRPF1, BRPF2, BRPF3
IBRD9	Bromodomains	BRD9
LP99	Bromodomains	BRD9/BRD7
SGC-CBP30	Bromodomains	CREBBP, EP300
PFI-2	Methyltransferase	SETD7
BI-9564	Bromodomains	BRD9/BRD7
GSK-LSD1	Demethylase	LSD-1
C646	HAT	p300/CBP
Bromosporine	Bromodomains	Pan-Bromodomain
PFI-1	Bromodomains	BRD2, BRD3, BRD4, BRDT (BET)
(+) JQ1	Bromodomains	BET (BRD2-4 and BRDT)
GSK-J4	Histone Demethylase	JMJD3/UTX
CI-994	Histone deacetylase	HDAC - class I
UNC1999	Methyltransferase	EZH2

Table 3.1: SGC library probes list; as available in May 2017

3.2 SGC library screening optimisation

3.2.1 Decitabine as a positive control

Prior to carrying out the SGC library screening, I used decitabine to confirm that the upregulation of IFNγ-inducible chemokine CXCL10 observed by other researchers in other cell lines/systems (282, 284) can also be seen in our *Trp53*$^{-/-}$ ID8 mouse line. If so, decitabine could be used as a positive control for the SGC library screening.

Decitabine (5-Aza-2'-deoxycytidine, Sigma A3656) was stored in aliquots of 10 mM in DMSO in -20^{o}C to -80^{o}C. Initial experiments focused on identifying the right dose and duration of treatment, in order to find the optimal conditions of confidently detecting CXCL10 protein.

The optimal dose and duration of decitabine treatment was tested initially in a 6-well plate setting (figure 3.1). Although there was a clear effect on also upregulating *Cxcl9*, one of the other chemokines acting on CXCR3 axis, its detection via ELISA was not possible. Doses between 200 nM–500 nM for 72 hours were considered favourable, whereas higher doses were cytotoxic. In order to confirm that the increase of CXCL10 was a consequence of demethylation and not a stress response, I performed cell cycle analysis to confirm that cells were still undergoing division whilst being treated under these conditions with decitabine. Figure 3.2(a) shows the gating strategy on untreated cells after 72 hours of cell culture.

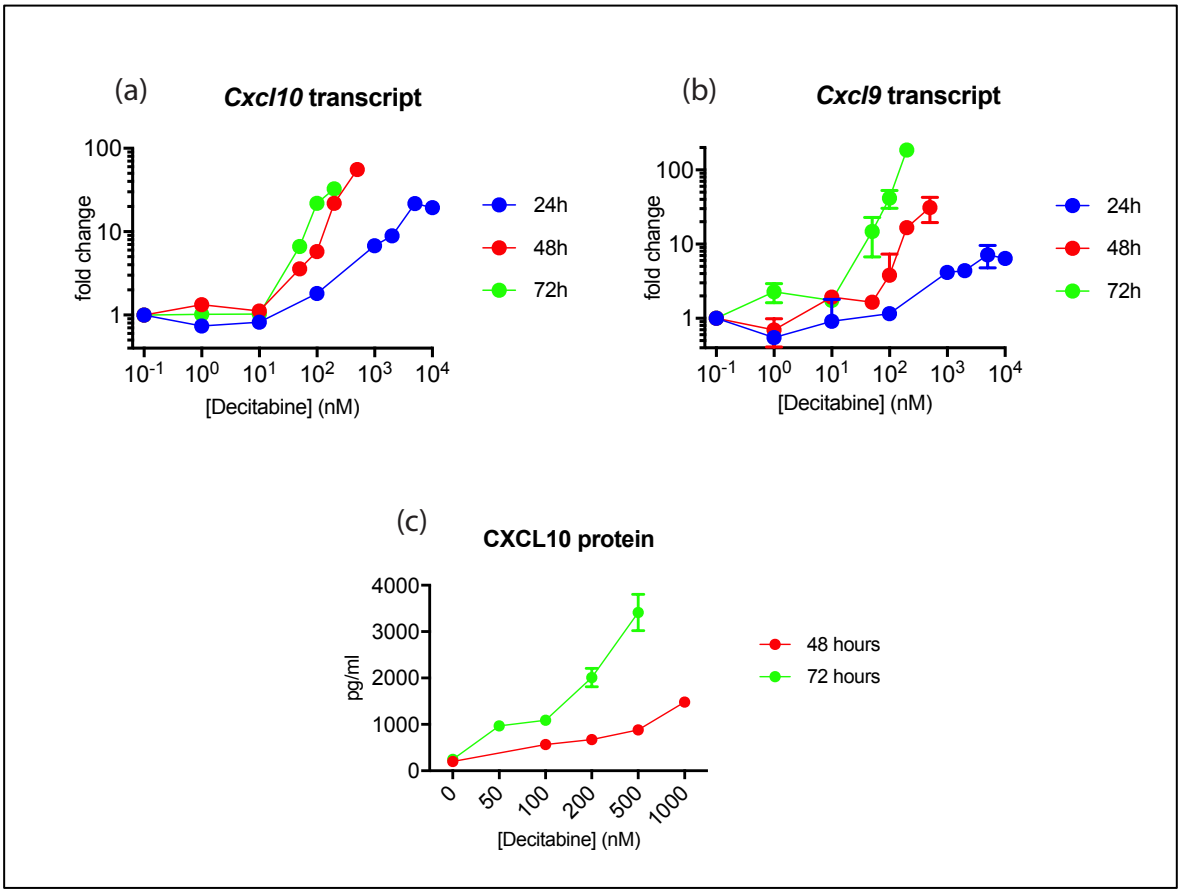

Figure 3.1: Cxcl10 transcript and protein levels following decitabine treatment. ID8 *Trp53*$^{-/-}$ cells (10^5 cells/well) were seeded in 6 well plates and treated with variable doses of decitabine as depicted on the graphs and then *Cxcl10 and Cxcl9* mRNA was measured using RT-qPCR. CXCL10 protein level was measured by ELISA in 3.1c. (For some points, the error bars are shorter than the height of the symbol. In these cases, Prism simply does not draw the error bars).

BrdU, an analog of the DNA precursor thymidine, is incorporated into newly synthesised DNA and can be used to quantify cells in S phase. All concentrations of decitabine caused a significant reduction in S phase, with a concomitant increase in cells in G2/M phase (Figure 3.2 b). In addition, as seen in figure 3.3 decitabine induced morphological change (cells have higher signal in both forward and side scatter). Nonetheless, I concluded that 200 nM decitabine allowed sufficient cell division to be used in subsequent experiments as positive control.

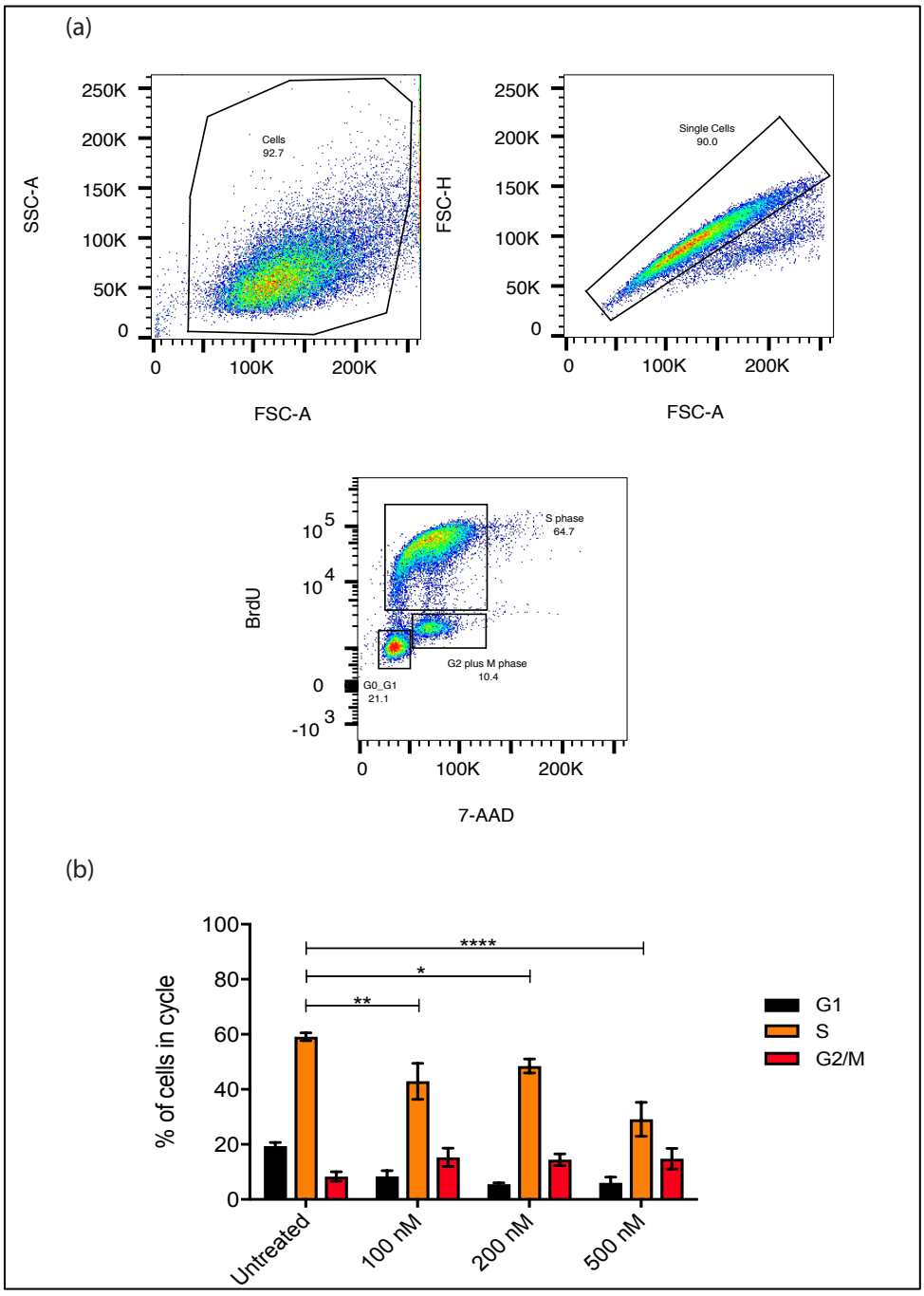

Figure 3.2: Cell cycle BrdU assay. (a) Gating strategy for cell cycle analysis of untreated ID8 *Trp53*$^{-/-}$ cells. 10^5 cells/well were in culture for 72 hours and then stained with 10 μM of BrdU and 10 μl of 7-AAD; (b) percentages of ID8 *Trp53*$^{-/-}$ cell populations in each cycle, after 72-hour treatment with variable doses of decitabine, as show on the graph. Cells were plated in technical replicates of four (n=4). One-way ANOVA with Kruskal-Wallis test and multiple comparisons for S phase was performed and shown here. Bars represent median and error bars represent standard deviation.

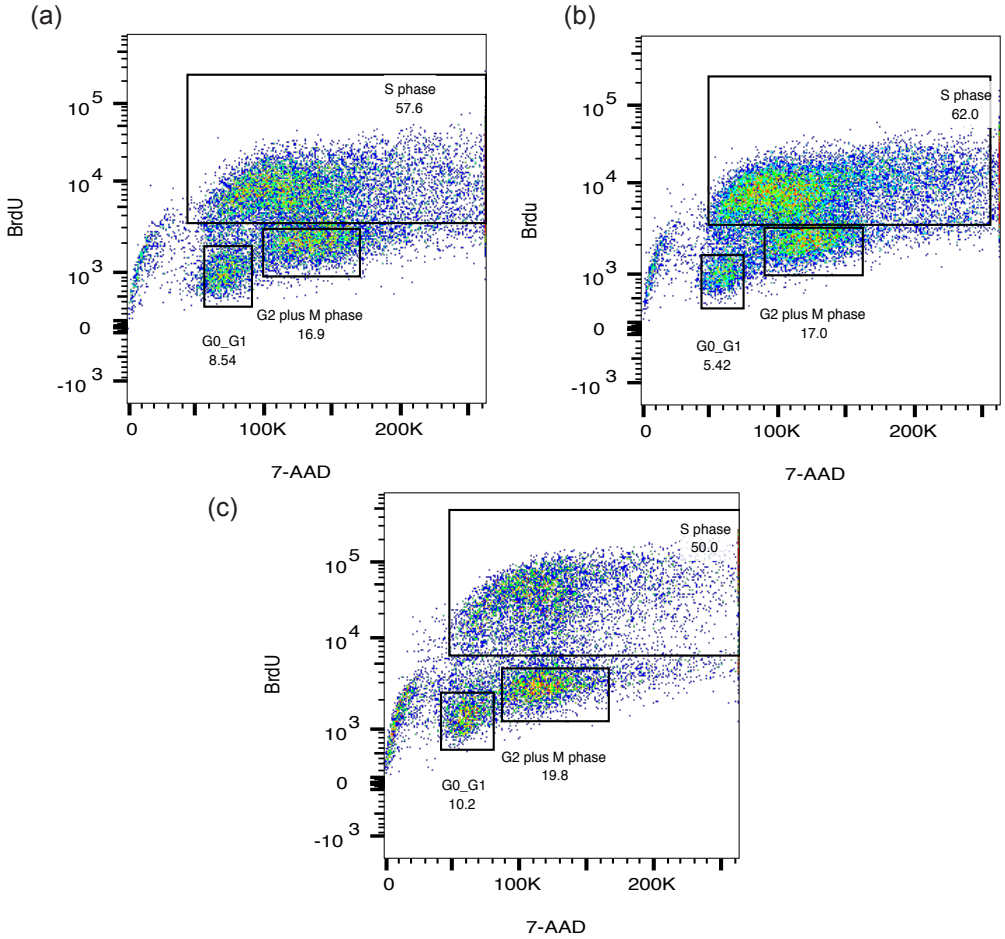

Figure 3.3: Cell cycle analysis following decitabine treatment. Representative plots of cell cycle analysis in cultured ID8 cells treated with decitabine for 72 hours at (a) 100 nM (b) 200 nM and (c) 500 nM dose. The flow graphs shown here are the ones closest to the median percentage of each population; performed in replicates of three.

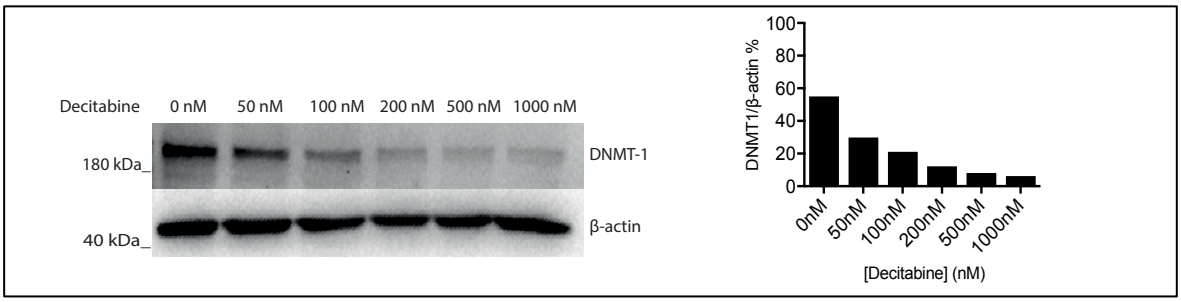

Figure 3.4: Western blot for DNMT1 protein following decitabine. ID8 *Trp53*$^{-/-}$ cells were treated with variable doses of decitabine and protein was extracted after 72 hours. DNMT1 protein was blotted and quantified by Image J software. Results of 1 sample (n=1) shown here.

200 nM decitabine resulted in the passive degradation of DNMT-1 (figure 3.4) as well as whole-genome hypomethylation (figure 3.5) as confirmed by the reduction of methyl-cytosine/cytosine ratio, measured by LCMS. Although treatment with decitabine resulted in DNA hypomethylation earlier than 72 hours, I concluded that 72h treatment duration would be an appropriate timepoint for the SGC library screening given the paucity of prior data on the SGC compounds.

I then optimised cell density for conducting the SGC library screening in 384-well plates. Adequate detection of CXCL10 protein by ELISA was the aim of this optimisation. Cells were plated in 50 µl at densities 250 - 4,000 cells/well of a 384-well black polypropylene (flat-bottom) plate on day -1. On day 0, decitabine was added at a concentration of 200 nM and supernatant was harvested on day 3 for immediate analysis by ELISA. Results from this ELISA (figure 3.6) suggested that 2 x 10^3 cells/well was a suitable concentration for subsequent experiments.

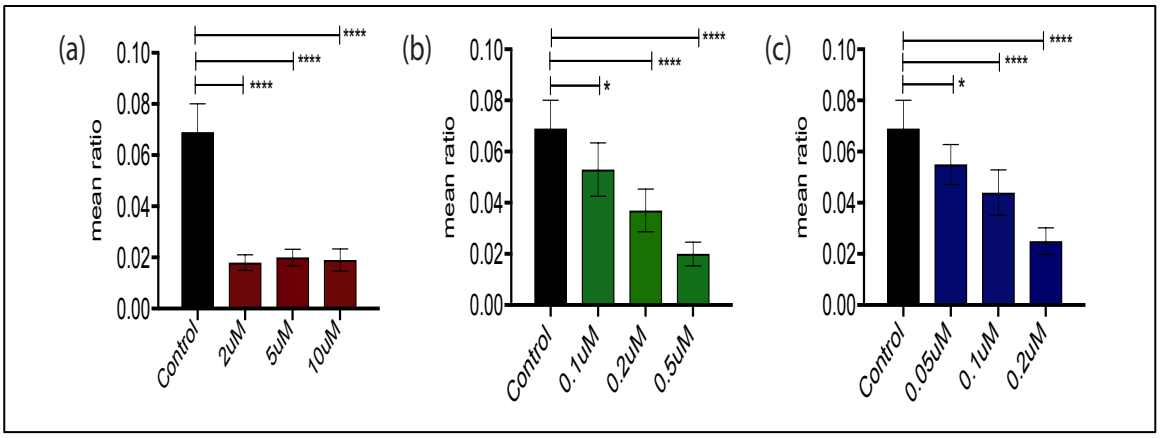

Figure 3.5: Liquid chromatography mass spectrometry following decitabine treatment. Methylcytosine/cytosine ratio after treatment with variable doses of decitabine for (a) 24 hours, (b) 48 hours and (c) 72 hours, as measured by LCMS. Each bar represents median of 5 biological replicates (n=5) and mean differences have been compared with one-way ANOVA and Dunnett's multiple comparison test. Error bars represent standard deviation.

3.2.2 Optimisation of SGC library drugs doses

Trp53$^{-/-}$ ID8 cells were seeded at a density of 2x10^3 cells per well in 384-well plates using an XRD-384 automated reagent dispenser (FluidX112 Ltd), at a volume of 47.5 µl per well, on day -1. The SGC library drugs were already aliquoted in barcoded master plates at 10 mM in DMSO (maintained and handled by the Screening Facility scientist, Lynn McGarry).

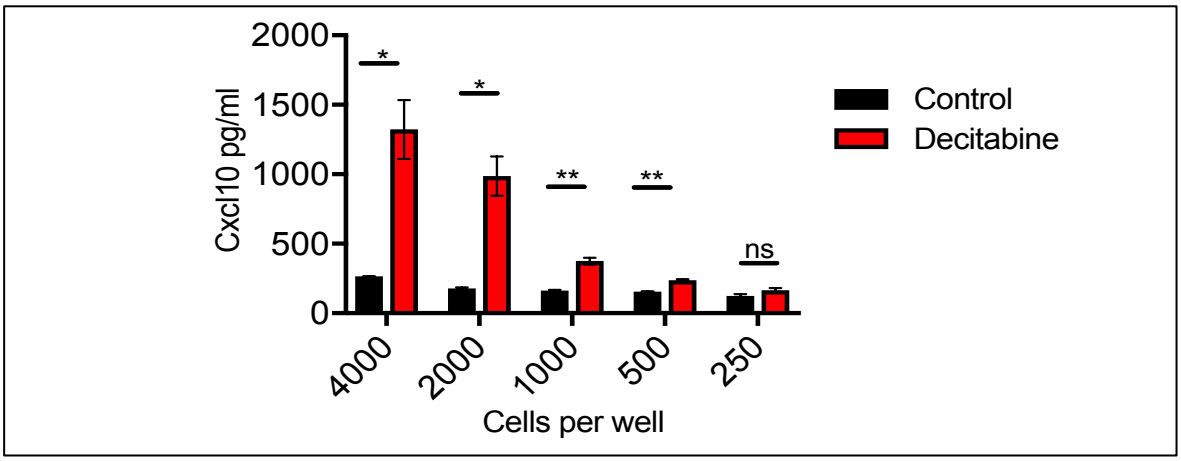

Figure 3.6: CXCL10 ELISA following decitabine treatment. Optimisation of cell density for 384-well drug screening via CXCL10 detection. Variable cell densities were seeded on day 0 and treated with 200 uM of decitabine, or control, on day 1. ELISA was performed on cell supernatant on day 3. Bars represent triplicates; error bars represent standard errors; medians of control *vs* decitabine per condition were compared using Mann-Whitney test, assuming data is not normally distributed.

On day 0, the drugs were diluted 1:50 into ID8 medium (see 2.1.1) in intermediate plates, to a concentration of 200 μM, using the JANUS G3 MDT automated workstation (Perkin Elmer). They were then added at a 2.5 μl volume onto two 384-well plates containing the cells, as per the format on figure 3.7, again using the JANUS workstation. On figure 3.8, the exact concentration gradient of drug per well is depicted in a 96-well format. The outer wells were not used to avoid edge effects.

After 72-hour incubation, plates were fixed and stained with 4′,6-diamidino-2-phenylindole (DAPI, ThermoFisher D1306). Using the XRD-384 automated reagent dispenser and Matrix WellMate disposable tubing cartridges (ThermoFischer, 201-3001), 50 μl 8% formaldehyde were added to the 50 μl medium per well. Plates were then incubated for 20 minutes at 20ºC. Formaldehyde was then safely decanted, and the wells were washed with 100 μl PBS.

After decanting the PBS, 80 μl DAPI/Tx-100 (DAPI 0.25 μg/ml and Tx-100 0.1%) were added per well and the plates were allowed to rest in the dark for 1 hour at 20ºC. After incubation, plates were transferred and read at 10x magnification in an Operetta high-content imaging system (Perkin Elmer) where nuclei were counted. The results were expressed as percentage loss of viability, relative to the DMSO wells. They are represented in figures 3.9 – 3.12. Imaging of one of the replicates of the two 384-well plates is shown in figures 3.13 and 3.14.

Given that my aim was to identify a non-cytotoxic dose that would induce an epigenetic effect on viable and actively dividing cells, I decided that 1 μM was an appropriate starting dose for CXCL10 screening, for most of the SGC probes. For GSK-J4 and LAQ-824 that were evidently more cytotoxic than the other probes, I chose 0.5 μM and 0.1 μM, respectively, and the dose for my positive control, decitabine, remained as 0.2 μM.

(a)

	1	2	3	4	5	6	7	8	9	10	11	12	13	14	15	16	17	18	19	20	21	22	23	24
A													DMSO	DMSO										
B													DMSO	DMSO										
C			(+) JQ1	BI-9564	(+) JQ1	BI-9564	(+) JQ1	BI-9564	(+) JQ1	BI-9564	(+) JQ1	BI-9564		DMSO	(+) JQ1	BI-9564	(+) JQ1	BI-9564	(+) JQ1	BI-9564	(+) JQ1	BI-9564	(+) JQ1	BI-9564
D			GSK484	IOX2	GSK484	IOX2	GSK484	IOX2	GSK484	IOX2	GSK484	IOX2	DMSO	DMSO	GSK484	IOX2	GSK484	IOX2	GSK484	IOX2	GSK484	IOX2	GSK484	IOX2
E			A-366	Bromospo rine	A-366	Bromospo rine	A-366	Bromospo rine	A-366	Bromospo rine	A-366	Bromospo rine			A-366	Bromospo rine	A-366	Bromospo rine	A-366	Bromospo rine	A-366	Bromospo rine	A-366	Bromospo rine
F			GSK591	KDOAM25	GSK591	KDOAM25	GSK591	KDOAM25	GSK591	KDOAM25	GSK591	KDOAM25	DMSO	DMSO	GSK591	KDOAM25	GSK591	KDOAM25	GSK591	KDOAM25	GSK591	KDOAM25	GSK591	KDOAM25
G			A196	GSK-J4	A196	GSK-J4	A196	GSK-J4	A196	GSK-J4	A196	GSK-J4		DMSO	A196	GSK-J4	A196	GSK-J4	A196	GSK-J4	A196	GSK-J4	A196	GSK-J4
H			I-CBP112	LLY507	I-CBP112	LLY507	I-CBP112	LLY507	I-CBP112	LLY507	I-CBP112	LLY507	DMSO	DMSO	I-CBP112	LLY507	I-CBP112	LLY507	I-CBP112	LLY507	I-CBP112	LLY507	I-CBP112	LLY507
I			BAY-598	GSK-LSD1	BAY-598	GSK-LSD1	BAY-598	GSK-LSD1	BAY-598	GSK-LSD1	BAY-598	GSK-LSD1			BAY-598	GSK-LSD1	BAY-598	GSK-LSD1	BAY-598	GSK-LSD1	BAY-598	GSK-LSD1	BAY-598	GSK-LSD1
J			IBRD9	C646	IBRD9	C646	IBRD9	C646	IBRD9	C646	IBRD9	C646	DMSO	DMSO	IBRD9	C646	IBRD9	C646	IBRD9	C646	IBRD9	C646	IBRD9	C646
K			BAZ2-ICR	GSK2801	BAZ2-ICR	GSK2801	BAZ2-ICR	GSK2801	BAZ2-ICR	GSK2801	BAZ2-ICR	GSK2801			BAZ2-ICR	GSK2801	BAZ2-ICR	GSK2801	BAZ2-ICR	GSK2801	BAZ2-ICR	GSK2801	BAZ2-ICR	GSK2801
L			IOX1	LP99	IOX1	LP99	IOX1	LP99	IOX1	LP99	IOX1	LP99	DMSO	DMSO	IOX1	LP99	IOX1	LP99	IOX1	LP99	IOX1	LP99	IOX1	LP99
M			Staurospo rine	GSK343	Staurospo rine	GSK343	Staurospo rine	GSK343	Staurospo rine	GSK343	Staurospo rine	GSK343			Staurosporine	GSK343	Staurospo rine	GSK343	Staurospo rine	GSK343	Staurospo rine	GSK343	Staurospo rine	GSK343
N			Dac	Dac	Dac	Dac	Dac	Dac	Dac	Dac	Dac	Dac	DMSO	DMSO	Dac	Dac	Dac	Dac	Dac	Dac	Dac	Dac	Dac	Dac
O													DMSO	DMSO										
P													DMSO	DMSO										

(b)

	1	2	3	4	5	6	7	8	9	10	11	12	13	14	15	16	17	18	19	20	21	22	23	24
A													DMSO	DMSO										
B													DMSO	DMSO										
C			MS023	CI-994	MS023	CI-994	MS023	CI-994	MS023	CI-994	MS023	CI-994		DMSO	MS023	CI-994	MS023	CI-994	MS023	CI-994	MS023	CI-994	MS023	CI-994
D			PFI-4	UNC0638	PFI-4	UNC0638	PFI-4	UNC0638	PFI-4	UNC0638	PFI-4	UNC0638	DMSO	DMSO	PFI-4	UNC0638	PFI-4	UNC0638	PFI-4	UNC0638	PFI-4	UNC0638	PFI-4	UNC0638
E			MS049	OICR9429	MS049	OICR9429	MS049	OICR9429	MS049	OICR9429	MS049	OICR9429	DMSO	DMSO	MS049	OICR9429	MS049	OICR9429	MS049	OICR9429	MS049	OICR9429	MS049	OICR9429
F			SGC 707	UNC0642	SGC 707	UNC0642	SGC 707	UNC0642	SGC 707	UNC0642	SGC 707	UNC0642	DMSO	DMSO	SGC 707	UNC0642	SGC 707	UNC0642	SGC 707	UNC0642	SGC 707	UNC0642	SGC 707	UNC0642
G			NI-57	PFI-1	NI-57	PFI-1	NI-57	PFI-1	NI-57	PFI-1	NI-57	PFI-1	DMSO	DMSO	NI-57	PFI-1	NI-57	PFI-1	NI-57	PFI-1	NI-57	PFI-1	NI-57	PFI-1
H			LAQ824	UNC1215	LAQ824	UNC1215	LAQ824	UNC1215	LAQ824	UNC1215	LAQ824	UNC1215	DMSO	DMSO	LAQ824	UNC1215	LAQ824	UNC1215	LAQ824	UNC1215	LAQ824	UNC1215	LAQ824	UNC1215
I			NVS-1	PFI-2	NVS-1	PFI-2	NVS-1	PFI-2	NVS-1	PFI-2	NVS-1	PFI-2		DMSO	NVS-1	PFI-2	NVS-1	PFI-2	NVS-1	PFI-2	NVS-1	PFI-2	NVS-1	PFI-2
J			SGC-CBP30	UNC1999	SGC-CBP30	UNC1999	SGC-CBP30	UNC1999	SGC-CBP30	UNC1999	SGC-CBP30	UNC1999	DMSO	DMSO	SGC-CBP30	UNC1999	SGC-CBP30	UNC1999	SGC-CBP30	UNC1999	SGC-CBP30	UNC1999	SGC-CBP30	UNC1999
K			OF-1	PFI-3	OF-1	PFI-3	OF-1	PFI-3	OF-1	PFI-3	OF-1	PFI-3	DMSO	DMSO	OF-1	PFI-3	OF-1	PFI-3	OF-1	PFI-3	OF-1	PFI-3	OF-1	PFI-3
L			SGC0946	Olaparib	SGC0946	Olaparib	SGC0946	Olaparib	SGC0946	Olaparib	SGC0946	Olaparib	DMSO	DMSO	SGC0946	Olaparib	SGC0946	Olaparib	SGC0946	Olaparib	SGC0946	Olaparib	SGC0946	Olaparib
M			Staurospo rine	1	Staurospo rine	2	Staurospo rine	3	Staurospo rine	4	Staurospo rine	5	DMSO	DMSO	Staurosporine	6	Staurospo rine	7	Staurospo rine	8	Staurospo rine	9	Staurospo rine	10
N			Dac	Dac	Dac	Dac	Dac	Dac	Dac	Dac	Dac	Dac	DMSO	DMSO	Dac	Dac	Dac	Dac	Dac	Dac	Dac	Dac	Dac	Dac
O													DMSO	DMSO										
P													DMSO	DMSO										

Figure 3.7: SGC drug library screening layout. Format of the 384-well plates containing cells treated with the SGC library at concentrations 20 nM - 10 µM, as per format in figure 3.8. $2x10^3$ ID8 *Trp53*$^{-/-}$ cells were plated on day 0 and treated with the SGC library or decitabine on day 1 (Dac = decitabine). Each plate was tested in triplicate.

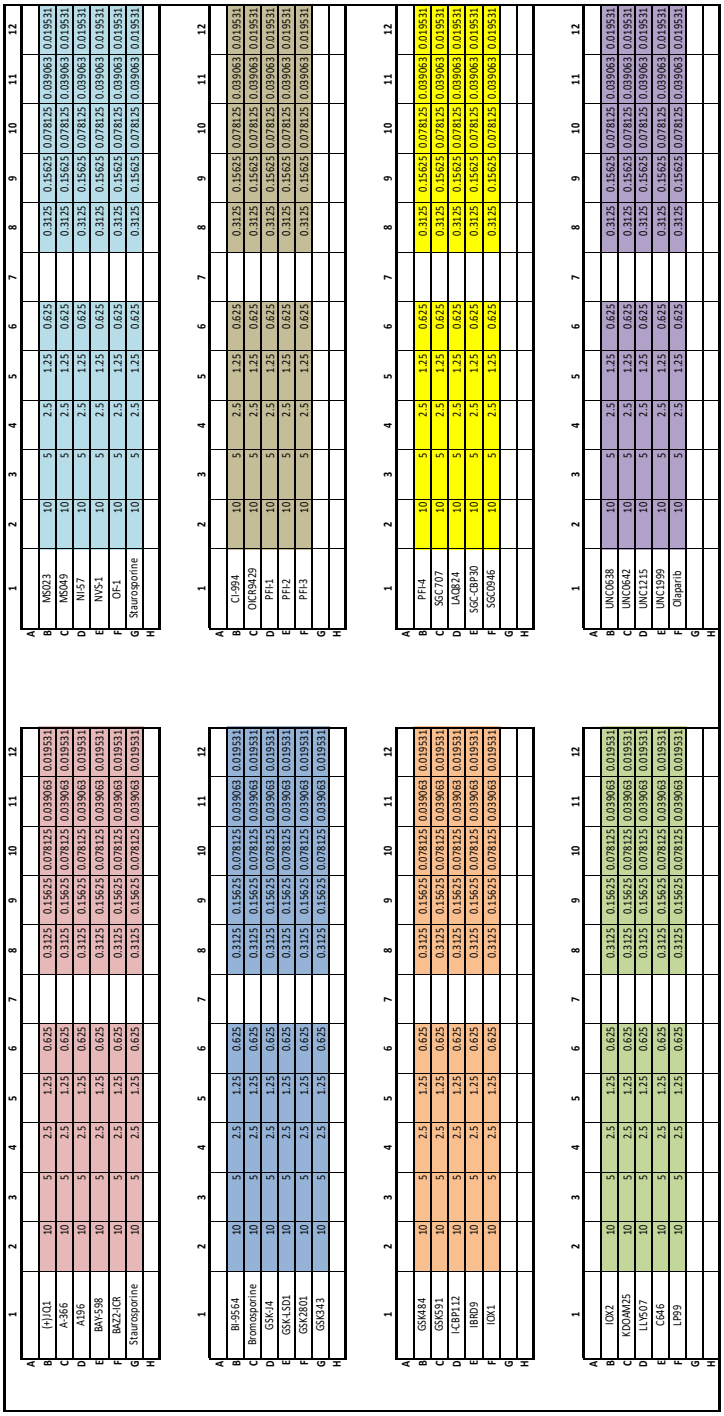

Figure 3.8: SGC drug library concentrations gradient layout. Format of the 384-well plates containing cells treated with the SGC library at concentrations 20 nM - 10 µM, as per layout in figure 3.7. 2x10^3 ID8 *Trp53*$^{-/-}$ cells were plated on day 0 and treated with the SGC library or decitabine on day 1 (Dac = decitabine). Each plate was tested in triplicate. Staurosporine was included in the library as a positive control for cell death. Note that Olaparib is not an epigenetic probe but it was also included in the SGC library and therefore tested.

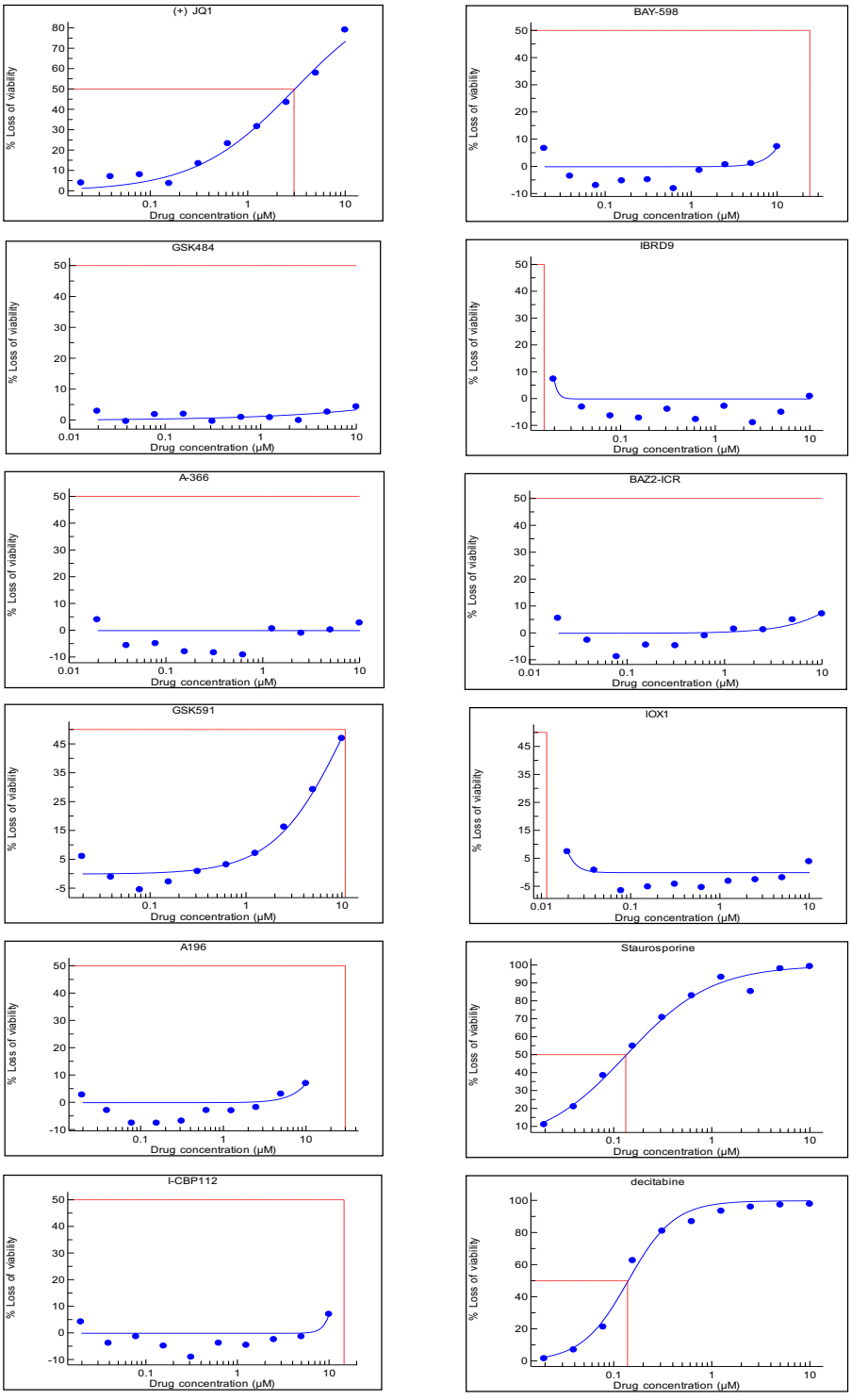

Figure 3.9: Drug-response curves, drugs 1-12. 2x10^3 ID8 *Trp53*$^{-/-}$ cells were plated on day 0 and treated with the SGC library on day 1, at concentrations 20 nM - 10 μM. Loss of viability is shown here, as measured by DAPI stained nuclei in treated wells relative to DMSO controls (n=3).

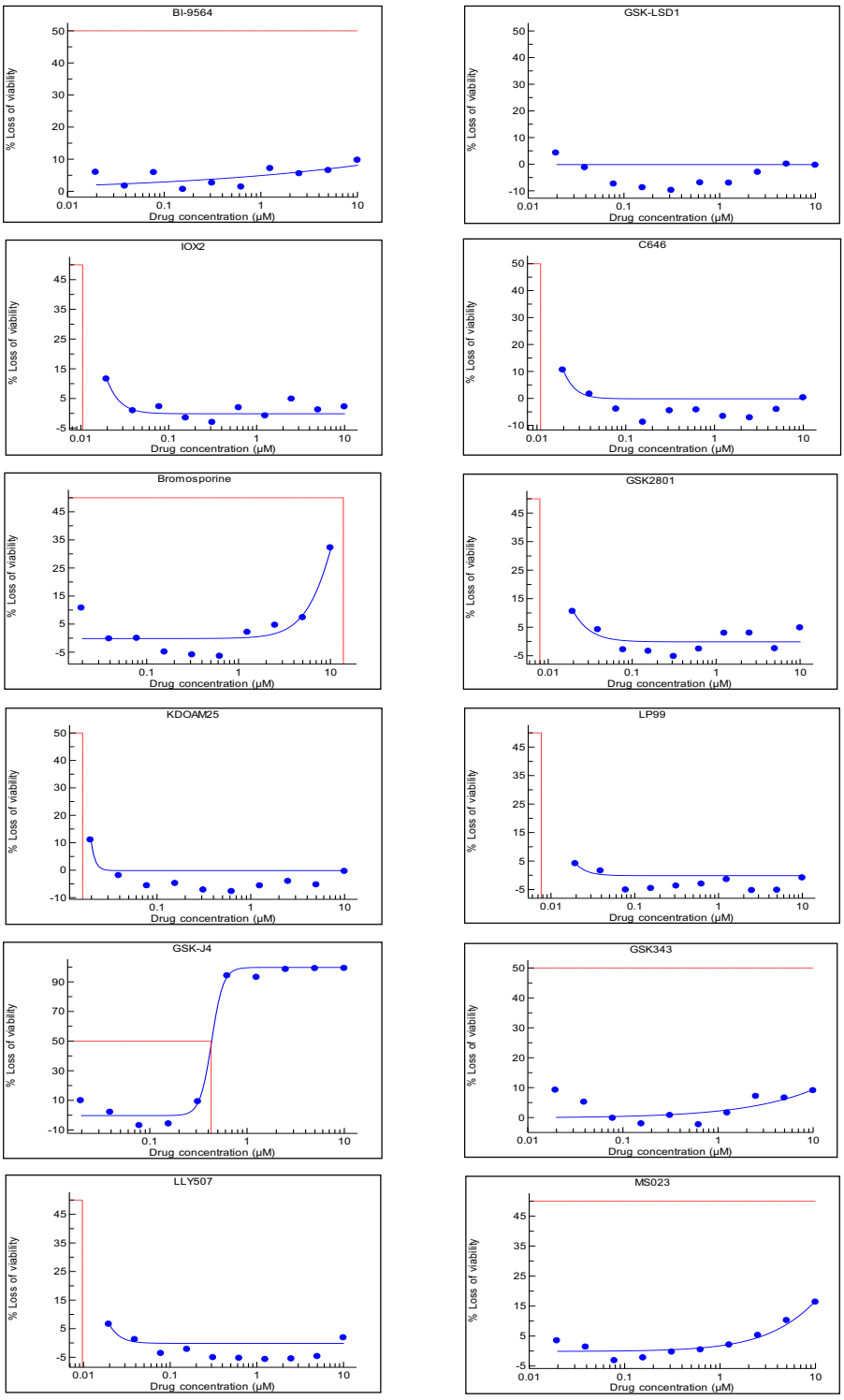

Figure 3.10: Drug-response curves, drugs 13-24. 2x10^3 ID8 *Trp53*$^{-/-}$ cells were plated on day 0 and treated with the SGC library on day 1, at concentrations 20 nM - 10 μM. Loss of viability is shown here, as measured by DAPI stained nuclei in treated wells relative to DMSO controls (n=3).

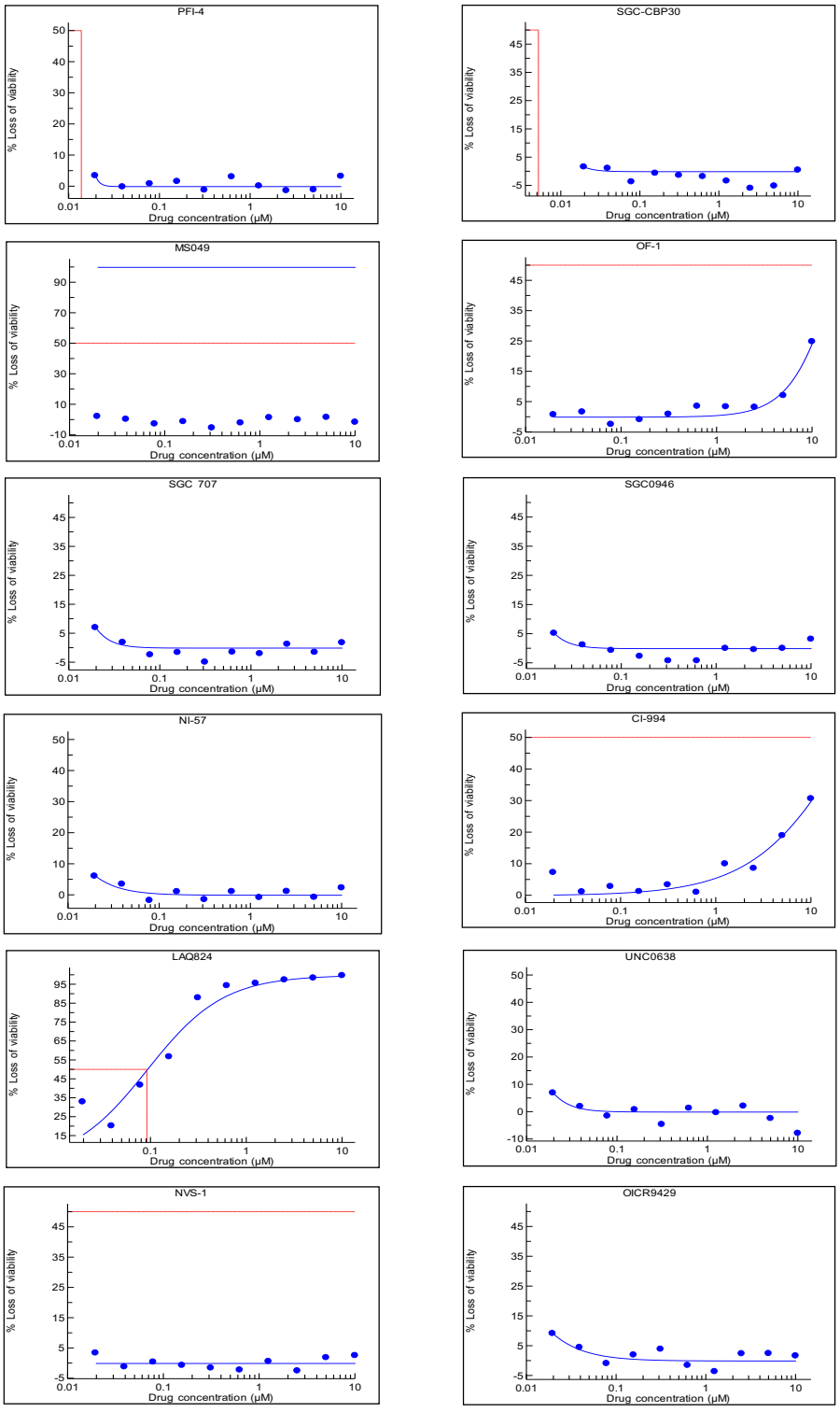

Figure 3.11: Drug response curves 25-36. 2x10^3 ID8 *Trp53*$^{-/-}$ cells were plated on day 0 and treated with the SGC library on day 1, at concentrations 20 nM - 10 μM. Loss of viability is shown here, as measured by DAPI stained nuclei in treated wells relative to DMSO controls (n=3).

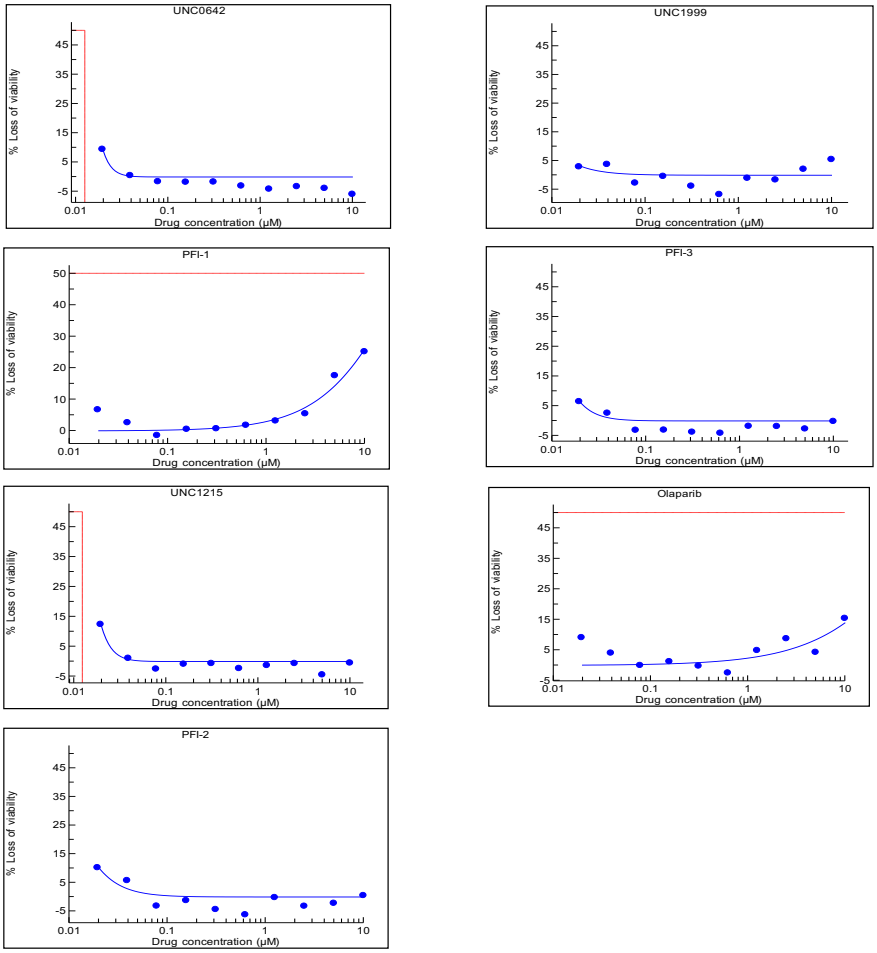

Figure 3.12: Drug-response curves, drugs 36-43. 2x10^3 ID8 *Trp53*$^{-/-}$ cells were plated on day 0 and treated with the SGC library on day 1, at concentrations 20 nM - 10 μM. Loss of viability is show here, as measured by DAPI stained nuclei in treated wells relative to DMSO controls (n=3).

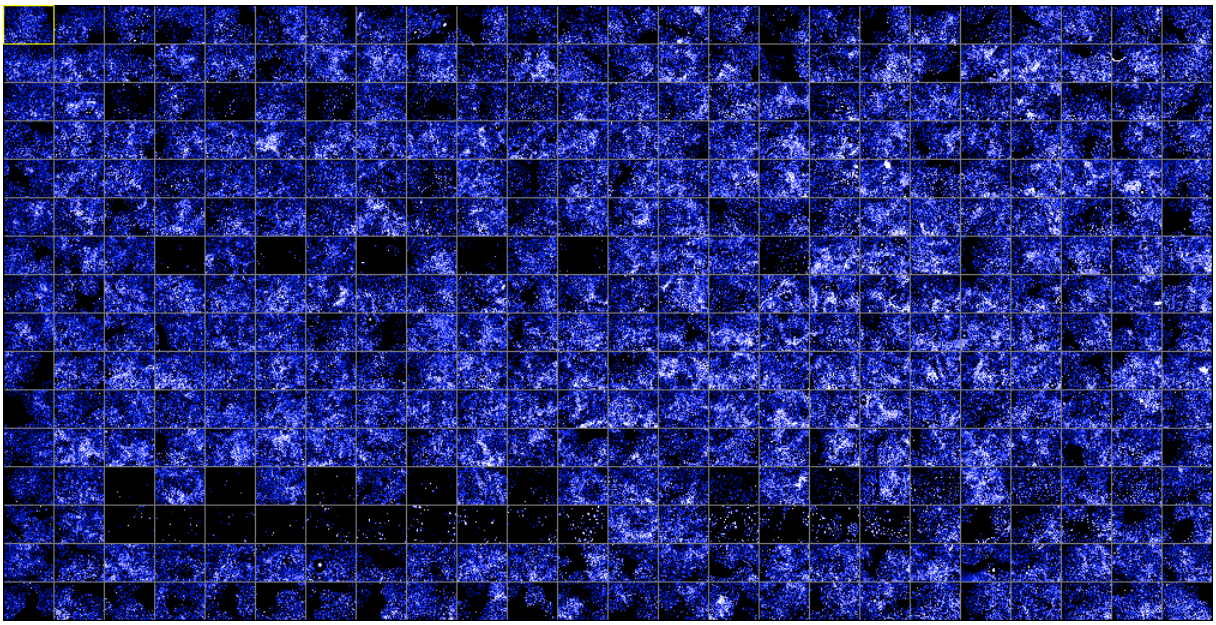

Figure 3.13: Imaging of plate (a) from figure 3.7 using the high-content imaging system, Operetta. 2x10^3 ID8 *Trp53*$^{-/-}$ cells were plated on day 0 and treated with the SGC library on day 1, at concentrations 20 nM - 10 μM. After 72 hours of treatment, nuclei were stained with DAPI (only one replicate shown here). Plates were then visualised in a high-throughput microscope.

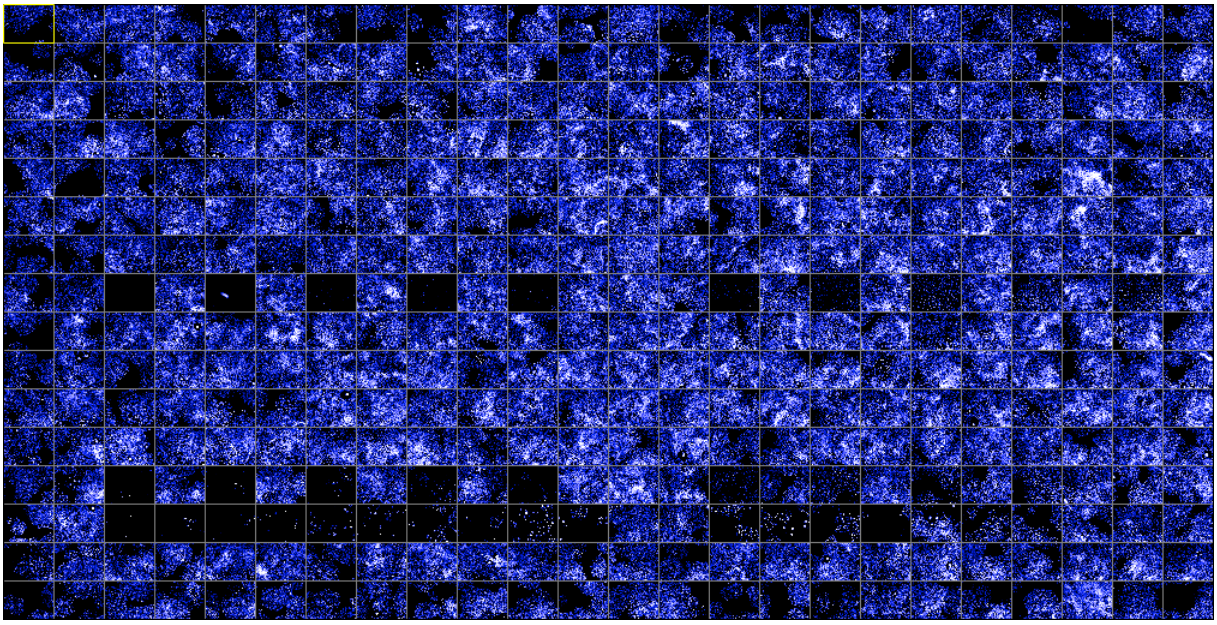

Figure 3.14: Imaging of plate (b) from figure 3.7 using the high-content imaging system, Operetta. 2x10^3 ID8 *Trp53*$^{-/-}$ cells were plated on day 0 and treated with the SGC library on day 1, at concentrations 20 nM - 10 μM. After 72 hours of treatment, nuclei were stained with DAPI (only one replicate shown here). Plates were then visualised in a high-throughput microscope.

CXCL10 ELISA screening was then performed. In the first screen, there was no positive signal for any of the probes other than HDAC inhibitor LAQ824 (figure 3.15a and 3.15b). This was not surprising as the effect of histone deacetylation on immunostimulatory pathways has been extensively described by others (231, 347, 363-365). Subsequently, I decided to screen the epigenetic probes in the presence of IFNγ as CXCL10 is an IFNγ target gene (366). I initially optimised IFNγ dose and schedule (figure 3.16). Pilot experiments indicated that CXCL10 production was greater when 1000 pg/ml IFNγ was added at the same time as decitabine (figure 3.16b), rather than 24h earlier (figure 3.16a). Thus, in all subsequent experiments, IFNγ was added with the test drug.

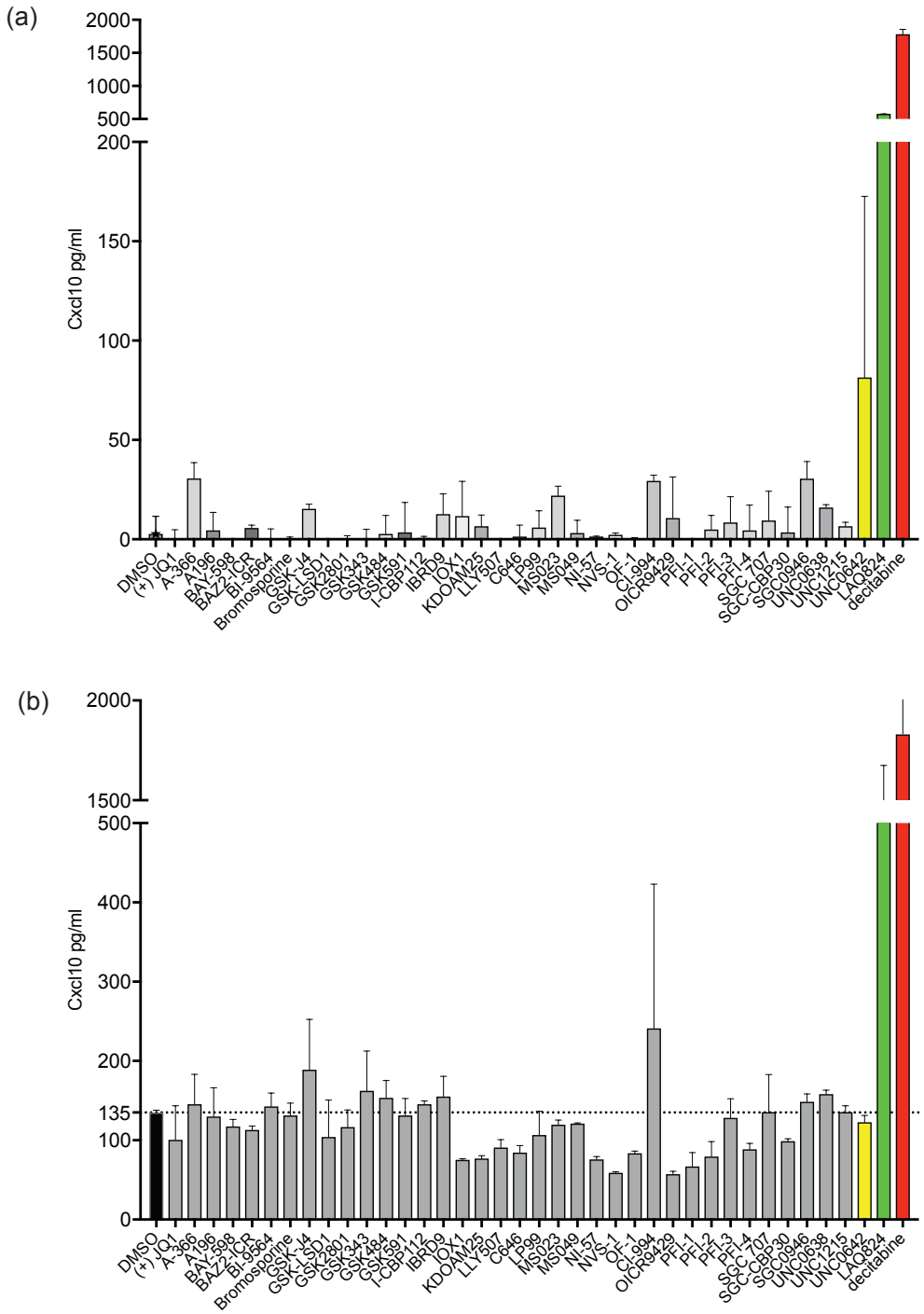

Figure 3.15: CXCL10 ELISA drug library screening. SGC library screening for CXCL10 by ELISA, tested in triplicates. 2x10^3 ID8 *Trp53*$^{-/-}$ cells were plated on day 0 and treated with the SGC library on day 1. All drugs were tested at dose 1 μM, apart from decitabine 0.2 μM, LAQ824 0.1 μM and GSK-J4 0.2 μM. (a) daily drug-containing medium change and (b) daily drug addition in pre-existing medium.

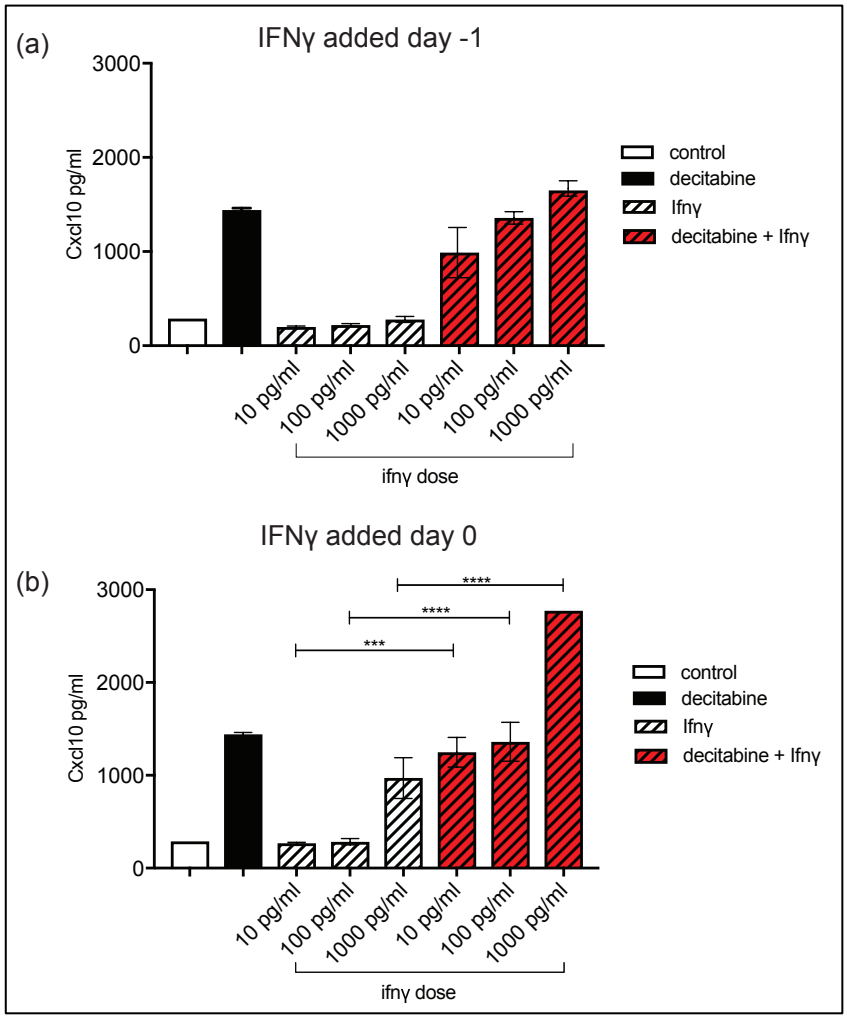

Figure 3.16: Optimisation of CXCL10 ELISA following IFNγ stimulation. (a) IFNγ on variable doses (as per graph) added the day before decitabine treatment (0.2 μM) or (b) the same day as decitabine. Experiment performed in 384-well setting. Every bar represents the median of triplicates and errors represent standard deviation; one-way ANOVA with Kruskal Wallis performed to compare conditions of interest in (b).

3.3 SGC library screening

Upon repeating the drug screening with IFNγ stimulation, I observed that some probes potentially had a synergistic effect with IFNγ (figure 3.17a). Comparing mean CXCL10 following treatment with the SGC library probes to the mean of IFNγ stimulation alone by one-way ANOVA did not reveal a statistically significant increase in CXCL10. However, some probes appeared to produce a stronger effect when compared to IFNγ alone. As a next step, I retested ten probes at two concentrations (figure 3.17b and figure 3.17c).

The greatest increase was observed with 10 μM of UNC0642, an inhibitor of G9a (EHMT2) and G9a-like protein (GLP, otherwise known as EHMT1) histone methyltransferases (367). G9a and GLP are SET-domain-containing proteins that form heteromeric complexes and mediate methylation of lysine 9 and lysine 27 on histone 3 (H3K9/H3K27), and thereby regulate gene transcription (368-374). Methylation of H3K9 and H3K27 are thought to represent marks of repressed chromatin and gene silencing (372). G9a is enzymatically more stable in a G9a/GLP complex, when compared to being expressed alone, and G9a/GLP heterodimer (henceforth referred to as G9a) is vital for multiple cellular processes (370). BIX-01294 was the first described G9a methyltransferase inhibitor (375). Since then, several other G9a inhibitors have been described, including A-366, UNC0638 and UNC0642, all of which were included in the SGC library (376-378). UNC0638 has weak in vivo properties (367, 379) and A-366, although it resulted in a modest increase in CXCL10 in the initial screening, was not selected for the smaller 10-drug screening. However, at

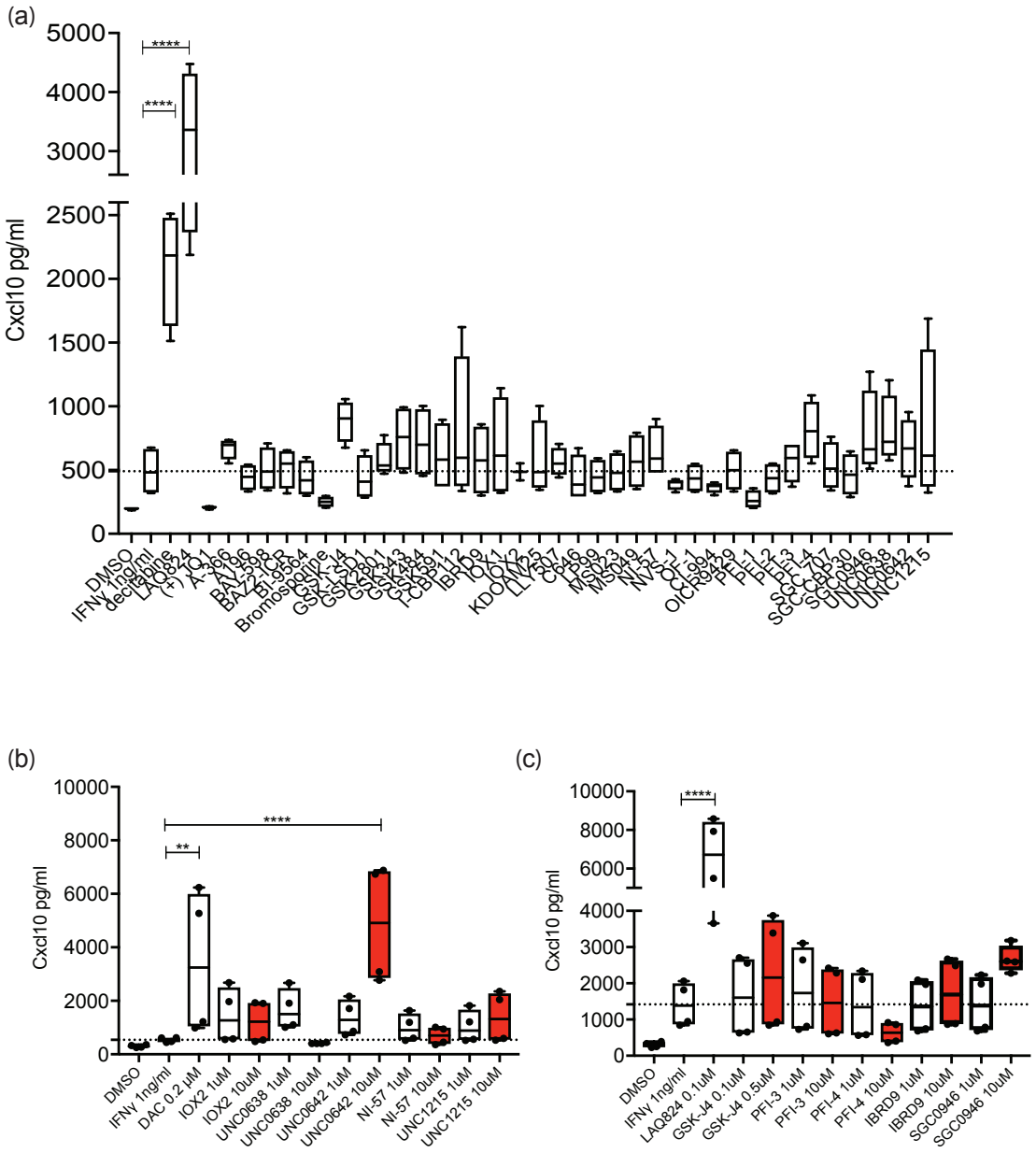

Figure 3.17: CXCL10 ELISA drug library screening with IFNγ stimulation (a) Screening of 38 epigenetics drugs at a single dose of 1 μM (apart from decitabine 0.2 μM, LAQ824 0.1 μM and GSK-J4 0.2 μM). (b) and (c) show repeat screening of 10 selected drugs at doses 1 μM and 10 μM, with decitabine (b) and LAQ824 (c) as positive controls, respectively. (b) and (c) represent separate experiments. One-way ANOVA with Dunnett's multiple comparison test was used to compare all means to the mean of IFNγ stimulation alone; non-significant results by ANOVA are not shown.

the time when these experiments were conducted, UNC0642 was more widely described in the literature (380, 381) and I, therefore, decided to investigate G9a inhibition further with UNC0642.

3.4 Screening validation and combination treatment with G9a/EZH2 inhibition

To validate the screening findings and establish the UNC0642 dose in vitro, I measured *Cxcl10* mRNA following UNC0642 treatment, which confirmed the transcriptional upregulation (figure 3.18a) alongside the protein increase seen during screening.

G9a, as critical mediator of both H3K9 and H3K27 methylation (369, 374), also cooperates closely with Enhancer of zeste homolog 2 (EZH2) (382). EZH2 is a major catalytic component of the epigenetic machinery Polycomb Repressive Complex 2 (PRC2), and is vital in mediating methylation of H3K27 (383-385). H3K9 and H3K27 colocalise on the genome (386-389). In addition, Mozzetta et al showed that there is functional interdependence between the PRC2 machinery and H3K9 methyltransferases, with EZH2 recruitment and activity relying heavily on the presence of G9a. The exact mechanism of G9a – EZH2 interaction is still largely unknown, but interestingly, Coward et al have showed that in idiopathic pulmonary fibrosis, knocking down G9a significantly reduces EZH2 and its respective methylation mark on H3K27 on the CXCL10 promoter region, and conversely, knocking down EZH2 reduces G9a's methylation mark on H3K9 on the CXCL10 promoter (390).

The above observations led me to investigate the effect of combining G9a and EZH2 inhibition on our tumour model. To this end, I used the EZH2 inhibitor UNC1999 (provided to me by the Adams lab, Sigma-Aldrich, SML0778) alone and

in combination with UNC0642. In addition, I tested the novel dual G9a/EZH2 inhibitor, HKMTI-1-005, which was designed and validated at Imperial College by the Fuchter lab (Department of Chemistry, Imperial College London) and a previous PhD student in the Robert Brown group, Dr Ian Green (391, 392). On the grounds that both enzymes contain a SET domain and that the histone binding pockets of histone methyltransferases are chemically very similar, the Fuchter lab created a compound library of BIX-01294 derivatives that was thereafter screened for simultaneous EZH2 target inhibition. Overall, HKMTI-1-005 was found to have the most favourable characteristics out of all hits and was selected as the hit compound. HKMTI-1-005 was kindly provided to me by the Fuchter lab for all the experiments described in this thesis. This compound is protected under the patent WO/2013/140148 (393).

RT-qPCR and ELISAs confirmed that the combination of UNC0642 and UNC1999 has an additive effect on both the *Cxcl10* transcript and protein levels (figure 3.18b and 3.18d) and that the dual inhibitor, HKMTI-1-005, follows the same pattern (figure 3.18c and 3.18e). Moreover, Western blot analysis showed that the inhibitors downregulated their primary targets, H3K9me2 for UNC0642, H3K27me3 for UNC1999 and both H3K9me2 and H3K27me3 for the dual inhibitor, HKMTI-1-005. These HKMTI-1-005 results are in keeping with previous results published by Curry et al (381).

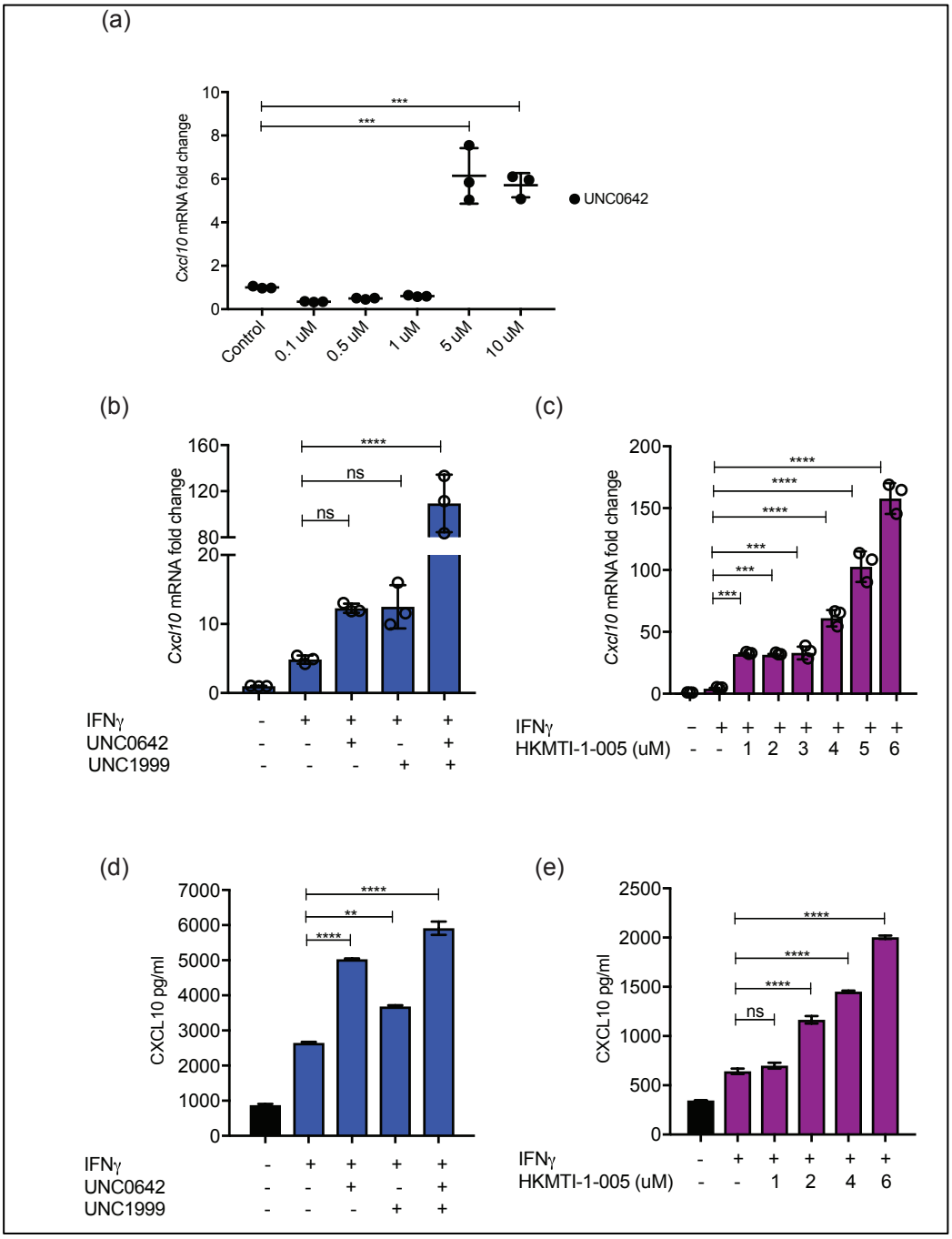

Figure 3.18: *Cxcl10* RT-qPCR and ELISA. (a) *Cxcl10* mRNA with variable doses of UNC0642, (b) synergistic effect of combining UNC0642 (5 μM) with UNC1999 (2 μM) on *Cxcl10* mRNA and (c) *Cxcl10* mRNA following treatment with the dual G9a/EZH2 inhibitor, HKMTI-1-005 (d) CXCL10 protein level following combination treatment with UNC0642 and UNC1999 and (e) CXCL10 protein level following treatment with the dual G9a/EZH2 inhibitor, HKMTI-1-005. Mean comparisons were performed using one-way ANOVA and Dunnett's multiple comparisons test. UNC0642= G9a inhibitor, UNC1999=EZH2 inhibitor.

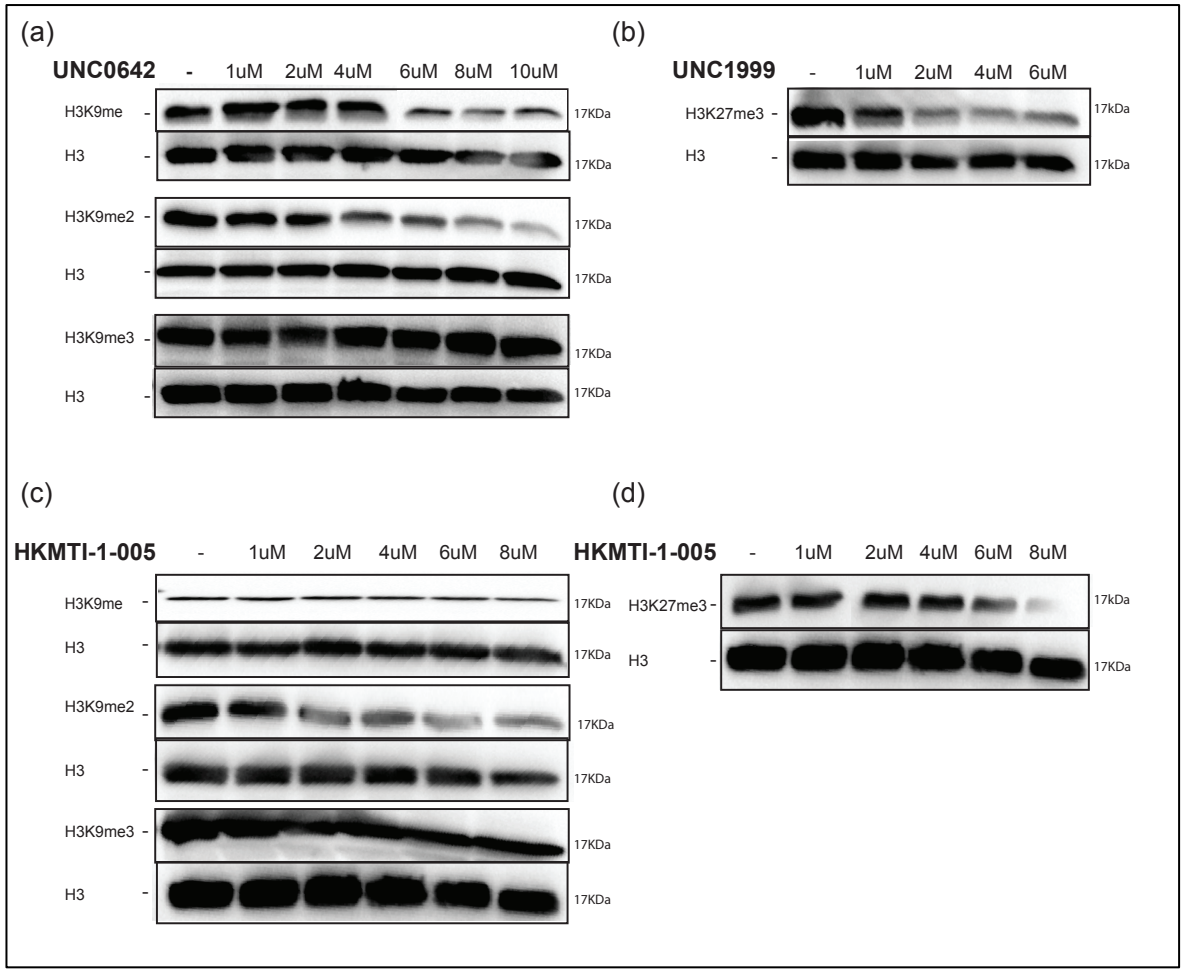

Figure 3.19: Western blot analysis following inhibition of G9a, EZH2 and combination G9a/EZH2. Western blot analysis for H3K9 methylation marks with UNC0642 (a) and HKMTI-1-005 (c) and H3K27me trimethylation for UNC1999 (b) and HKMTI-1-005 (d). Histone H3 was used as a loading control. Protein electrophoresis was performed for each methylation mark and its respective loading control on separate gels, given that both the size of H3 and the size of the methylated mark were both approximately 17kDa.

In order to elucidate the effect of G9a inhibition as well as the combined G9a/EZH2 inhibition on the overall chemokine gene expression, I also performed an 84-gene chemokine/cytokine RT-PCR array panel comparing IFNγ stimulated cells with cells that had additionally been treated with either UNC0642 or HKMTI-1-005 (figure 3.20). List of genes tested, as well as the quality control of this analysis, can be found in Appendix 1.0.

The array results confirmed that dual G9a/EZH2 inhibition has a more potent effect on chemokine expression than G9a inhibition alone. *Cxcl10*, *Cxcl9* and *Ccl5* genes were statistically significantly upregulated amongst others (figure 3.20c and Appendix 4.0). CCL5, previously known as RANTES, is involved in both innate and adaptive immunity and leucocyte trafficking, as well as positively regulating the interactions between T cells and dendritic cells (394-396). In cancer, CCL5 has been associated with favourable response to immunotherapy in melanoma (397, 398), longer survival in lung adenocarcinoma (399) and the presence of cytotoxic T lymphocytes in ovarian cancer (192). CXCL9 and CXCL10, as discussed before, have a well-described anti-tumour immunostimulatory role with CXCL9 having been associated with improved outcomes in ovarian cancer (68, 149, 188, 400)

Neither treatment with G9a inhibitor nor HKMTI-1-005 upregulates *Il-1* or *Il-18*, chemokine genes that have been extensively associated with cell death (401, 402). HKMTI-1-005 results in a non-statistically significant log2fold change of -1.2 for *Il-1a* and -0.7 for *Il-1b*, respectively; the log2fold change for *Il-18* was -5.6 ($p<0.05$). Similarly, UNC0642 led to the reduction of both *Il-1a* (log2fold change of -2.05) and *Il-1b* (log2fold change -0.7), although both of these were statistically non-significant. As with HKMTI-1-005, *Il-18* transcription was downregulated (log2fold change -2.1, $p<0.05$) with UNC0642 treatment. Both these cytokines are instrumental in stimulating a potent immune response following sterile cell death with the production of pro-inflammatory chemokines that can recruit phagocytes (403, 404).

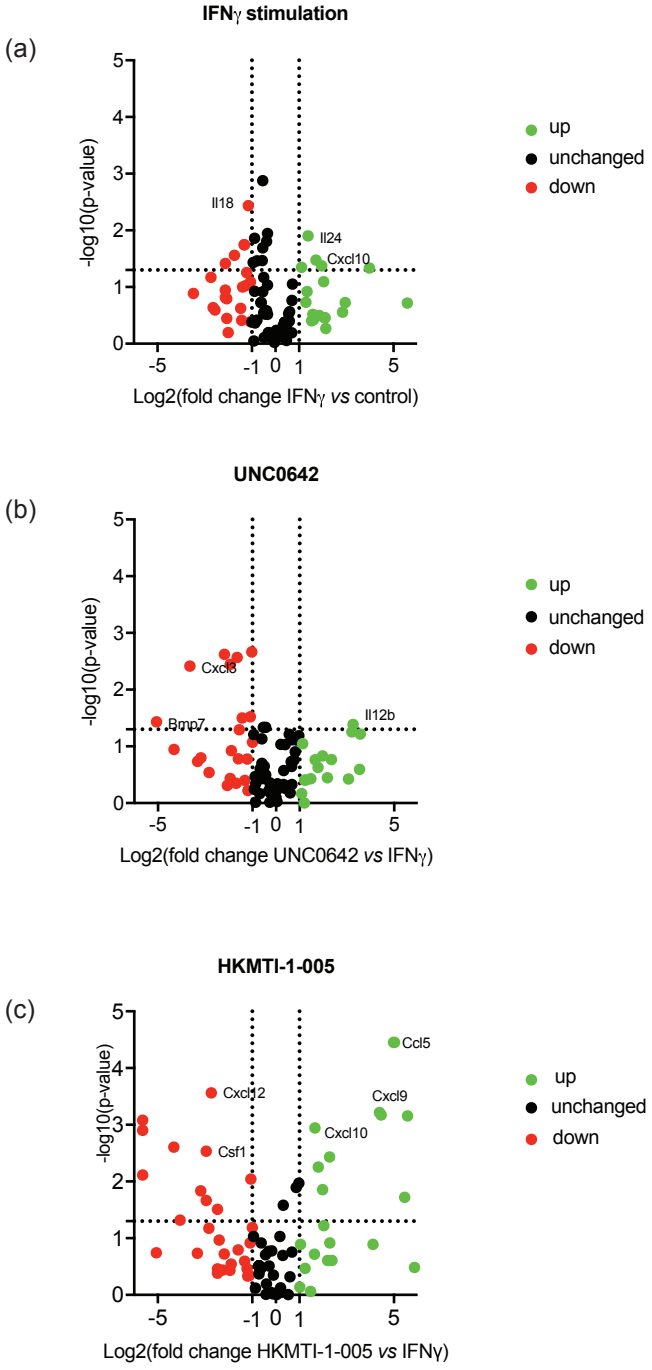

Figure 3.20: Chemokine/cytokine array following G9a or G9a/EZH2 inhibition. ID8 *Trp53*$^{-/-}$ cells were treated for 48 hours with control or 1 ng/ml IFNγ, or 1 ng/ml IFNγ plus 5 μM UNC0642 or 1 ng/ml IFNγ plus 6 μM of HKMTI-1-005. The experiment was performed in triplicates and each replicate was tested on a different plate. Details on analysis in methods 2.4.4 and Appendix 1.0.

3.5 Validation on human samples and established human cell lines

I sought to investigate if the effect of dual-blockade of G9a/EZH2 (with HKMTI-1-005) on murine cells is also observed on human cells. I used epithelial cells derived from 5 patients with ovarian high-grade serous carcinomas as well as the 3 established ovarian cancer cell lines, OVCAR3, OVCAR4 and Kuramochi.

Patient samples were derived and processed as described in method 2.1.1. In work done previously in the McNeish lab, this methodology yields cells with mutant *TP53* in almost 100% of the cases (6/7 patients previously tested had mutant *TP53*; sequencing was not possible in the negative patient due to insufficient DNA). The genomic characterisation of the current seven patients presented here is still on-going at the time of writing this thesis (sequencing data awaited). Basic clinical characteristics of the patients can be found in Appendix 19.0.

In the primary patient samples, G9a/EZH2 inhibition overall augmented the transcription of *Cxcl9* (p=0.01), *Cxcl11* (p=0.01) and *Ccl5* (p=0.03) with a lesser effect on *Cxcl10* (p=0.15) and *Ccl20* (p=0.10) (figures 3.21a/b/c/d/e). All 3 established human cell lines showed a statistically significant increase in *Cxcl10* transcription with Kuramochi possibly being the most responsive (figure 3.21f).

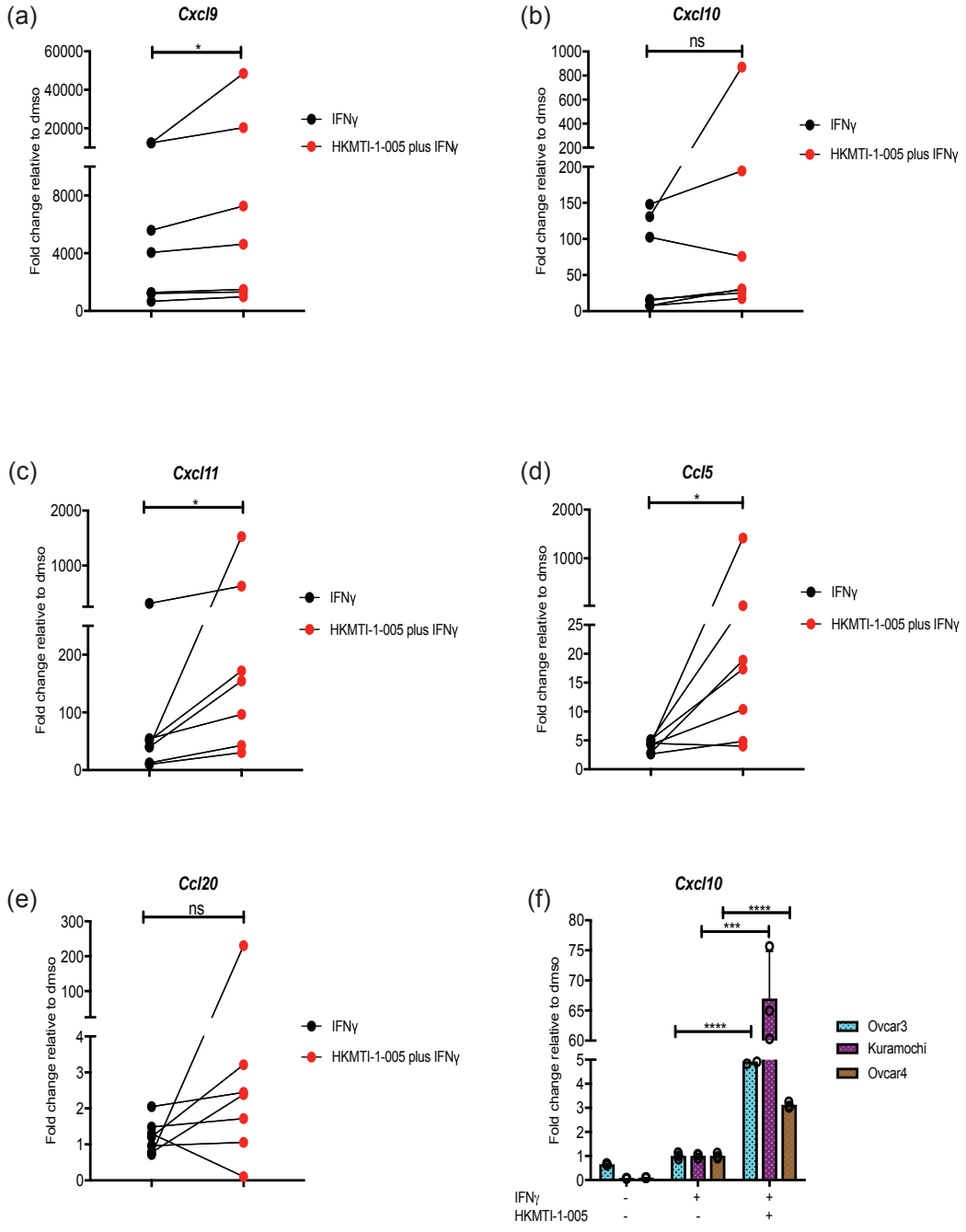

Figure 3.21: Chemokine gene expression on human samples.
(a) – (e) Chemokine gene expression on human ascites derived cultures. Each dot represents one patient, groups were compared using the Wilcoxon matched-pair test as data was paired and non-parametric. Graph (f) demonstrates *Cxcl10* transcription changes in OVCAR3, OVCAR4 and Kuramochi human cell lines; comparisons were made using Mann-Whitney test. Each bar represents n=3 and error bars represent standard deviation.

3.6 Discussion

The experiments described in this chapter show that inhibition of G9a, the histone methyltransferase that primarily mediates methylation of H3K9, induces the upregulation of CXCL10 in a *Trp53*$^{-/-}$ deficient ID8 cell line, at both mRNA and at protein level. This was discovered through screening a library of novel epigenetic probes, curated by the Structural Genomics Consortium (SGC) and it was a novel observation, in the context of cancer, at the time of writing this thesis. For this to be possible, the assay required lengthy optimisation; decitabine was used as a positive control, at a dose and duration that was thought to be only weakly cytotoxic. Cell number seeding was optimised for adequate CXCL10 detection and treatment dose was also titrated to avoid cell death. Finally, the dose and timing of IFNγ stimulation required optimisation. The result that G9a modifies *Cxcl10* transcription adds to prior knowledge that chemokine regulation is under the epigenetic control of DNA methylation and histone deacetylation.

The effect was observed using a dose of UNC0642 that was not cytotoxic (figure 3.12), which would support the hypothesis that tumour cells are releasing CXCL10, not as a result of cell stress and death, but secondary to a direct or indirect drug effect on gene transcription.

EZH2, the histone methyltransferase that orchestrates PRC2-mediated trimethylation of H3K27, is known to be involved in regulating gene expression of immune cells with critical effects on differentiation of T lymphocytes and Natural Killer (NK) cells (276, 285, 293, 405) as well as the activation of macrophages (298, 300). More recently, the co-dependence of EZH2 and G9a was delineated by Mozzetta et al (382) and this has led to efforts of discovering pharmacological inhibitors that target both enzymes simultaneously, with HKMTI-1-005 being the first one described (381). Following the SGC library screening, I used individual G9a or EZH2 inhibitors, as well as their combination

and observed an additive effect on CXCL10 upregulation, which was also confirmed with treatment with HKMTI-1-005.

As previously mentioned, HKMTI-1-005 was developed at Imperial College London, following a BIX-01294 derivative library screening, by the Fuchter group. The library was initially tested via RT-qPCR, for the re-expression of genes known to be silenced in an EZH2-dependent manner, such as KRT17 and FBXO32 (406) and the hits HKMTI-1-005, HKTMI-1-011 and HKMTI-1-022 emerged. Following on from this, HKMTI-1-005 was found to inhibit the transfer of a tritium-labelled methyl group from S-adenosyl methionine (SAM) to a biotinylated H3 [1-25] peptide (normally mediated by G9a) at a much lower dose than the other hits (391). An enzymatic assay investigating the ability of HKMTI-1-005 to inhibit EZH2 function by testing for the transfer of methyl group from SAM to biotinylated H3 [21-44] confirmed that HKMTI-1-005 abrogates EZH2 activity too (392).

To consolidate our knowledge on the effect of HKMTI-1-005 on chemokines, treatment of *Trp53*$^{-/-}$ deficient ID8 cells showed an additive effect on *Cxcl10*, *Cxcl9* and *Ccl5* transcripts, in an 84-chemokine array. These are known to be potent attractant of lymphocytes, NK cells and dendritic cells and to have been associated with anti-tumour immune response and favourable patient survival. Results from this array confirmed that treatment with either UNC0642 or HMKTI-1-005 does not elicit the release of cell-death associated chemokines. Damaged cells release danger-associated molecular patterns (DAMPs) and these DAMPs in combination with caspase-1 and other proteins can form into multiprotein complexes that are referred to as inflammasomes. This, in turn, results in the activation of caspase-1 and subsequent cleavage of the prodrome forms of IL-1 and IL-18 into their active forms (407). IL-1-dependent signalling triggers the up-regulation of secondary inflammatory cytokines such as G-CSF, TNFα and IL-6 in order to facilitate the removal of damaged cells and perpetuate the inflammatory response (402-404, 407, 408). Therefore, the lack of *Il-1* and *Il-18* increase would support that the upregulation of *Ccl5*, *Cxcl9* and *Cxcl10*, is

unlikely to be a sequela of cell stress and death, but rather an effect on the production of specifically these, important for lymphocyte trafficking, chemokines.

Moreover, treatment of human cell lines and human samples with the dual inhibitor revealed a similar trend. The immortalised cell lines were chosen after review and consideration of the literature on the molecular subclassification of epithelial ovarian cancer. Ovarian HGSC is characterised by gene copy number variations and almost universal *TP53* mutations (66, 68, 72). Work on established human lines has showed that a great discordance exists between lines regularly used in literature as ovarian HGSC models and the molecular characteristics of the actual human disease, as defined in human tumour samples. Based on work from Beaufort et al and Domcke et al on collating morphological and genetic characteristics of widely used lines for *in vitro* work, I decided to test OVCAR3, Kuramochi and OVCAR4 cell lines. All these lines harbour *TP53* mutations and moreover their copy number alterations profile correlates best with that of human tumours (409, 410). Additionally, the Kuramochi cell line has a *BRCA2* mutation and amplification of *MYC* and *KRAS;* whereas the OVCAR3 cell line has amplified *CCNE1* and *C11orf30* genes.

All the above justified investigating the dual inhibitor *in vivo,* in order to elucidate if the upregulation of chemokines has the potential to stimulate an immune response in immunocompetent mice bearing ID8 tumours.

Chapter 4. Combined G9a/EZH2 inhibition versus G9a inhibition alone; therapeutic role and its effect on the tumour immune microenvironment

Chapter 4 Results

4.1 Introduction and aims

Following the experiments described in chapter 3, I sought to investigate whether combined inhibition of G9a and EZH2 methyltransferases is a viable therapeutic target in an ovarian cancer model, compared to G9a inhibition alone. A further hypothesis was that G9a/EZH2 blockade could alter the tumour microenvironment and that could contribute to its anti-tumour effect.

The role of G9a histone methyltransferase has been investigated in various cancer types and contexts. In ovarian cancer, G9a is highly expressed in metastatic lesions when compared to the primary tumour and patients' prognosis is worse when their tumours overexpress G9a (411). In the same study, it was observed that G9a regulates genes related to the migrating potential of ovarian cancer cells and when G9a was depleted, cells were less able to resist anoikis or achieve anchorage-independent growth (411). Moreover, a global increase of H3K9me2 and G9a was observed in ovarian cancer patient-derived tumour cells and immortalised human lines that had developed resistance to treatment with PARP inhibitors; conversely, pharmacological or genetic disruption of G9a restored sensitivity to PARP inhibition via altering the way that G9a-mediated gene regulation aids cancer cells restore DNA damage (412). Furthermore, G9a has been implicated in promoting resistance to gemcitabine in the pancreatic cancer cell line PANC-1, as evidenced by reversal of resistance when G9a is inhibited and, as with ovarian cancer, G9a overexpression is associated with poorer outcomes for patients with pancreatic cancer (413). In hepatocellular carcinoma (HCC), G9a has been found to silence tumour-suppressor genes such as *RARES3* and therefore promote HCC development and metastasis (414). Another observation in HCC suggests that G9a is involved in epithelial-mesenchymal transition via mediating methylation of H3K9 at the promoter of *E-cadherin* (415). An association of G9a with tumorigenesis, tumour aggressiveness and poor patient survival have not only been observed in ovarian, pancreatic cancer and HCC (414-416), but also in colorectal cancer (417), gastric cancer (418), hepatobiliary tract cancers (419), bladder cancer (420) and breast

cancer (421, 422). G9a is thus involved in a variety of cellular processes (379). Based on my observation that pharmacological inhibition of G9a results in upregulation of a chemokine paramount to the immune response, I next wished to investigate G9a inhibition *in vivo*.

The oncogenic role of EZH2 histone methyltransferase is more widely recognised than that of G9a methyltransferase, with a great amount of work focusing specifically on epithelial ovarian cancer (240). EZH2 and its partner SUZ12 are overexpressed in epithelial ovarian cancer when compared to healthy ovarian or fallopian tube epithelium and they promote tumour proliferation (423) This denotes an important role of the PRC2 complex in the development and maintenance of disease (240). Asides from the role in mediating chemokine expression and therefore regulating Th1 immunity against tumours in an ovarian cancer mouse model that I have already described (282), EZH2 directs expression of transforming growth factor-ß1 (TGF-ß1) and E-cadherin, thereby controlling cancer cell migration and invasion (424). Moreover, Rizzo et al observed that EZH2 depletion with siRNA knockdown leads to loss of ovarian cancer stem cells and reduces anchorage-independent growth resulting in tumour regression (425). Asides from migration and phenotypic changes, EZH2 is implicated in ovarian cancer angiogenesis pathways; vascular-endothelial growth factor (VEGF) directly stimulates expression of EZH2, which in turns mediates gene silencing of the antiangiogenic factor vasohibin 1 (vash1). EZH2 silencing in ovarian cancer-associated endothelial cells reactivates *vash1* and results in tumour regression (426).

Increased levels of EZH2 that correlate with tumour progression and aggressiveness have also been observed in melanoma, breast, prostate and endometrial cancers (427-429). In *BRCA1* related triple-negative breast cancers with either *BRCA1* mutations, *BRCA1* promoter methylation or *BRCA1*-like copy number profile, EZH2 is overexpressed and this increase correlates with sensitivity to chemotherapy, potentially identifying a therapeutic pathway that can be very pertinent to ovarian cancer too (430). In melanoma, targeting EZH2 reactivated tumour suppressor genes with a direct effect on tumour growth (431) but perhaps even more interestingly, EZH2 was found to promote

inactivation of immunogenicity. EZH2 deficiency restores the immunogenicity of melanoma cells and synergises with immunotherapy in achieving significant tumour regression (432).

At the time of writing this thesis, the inhibition of both enzymes had only been investigated in the context of tumour cell killing in breast cancer cell lines (381). On the basis of all the above evidence, I decided to investigate the effect of dual G9a/EZH2 blockade on the tumour immune microenvironment.

4.2 Combined G9a/EZH2 inhibition confers better survival when compared to G9a inhibition alone

I first sought to investigate whether UNC0642 (G9a inhibitor) or HKMTI-1-005 (dual G9a/EZH2 inhibitor) had an effect on survival of C57BL/6 mice bearing *Trp53*$^{-/-}$ ID8 tumours.

For UNC0642, there were only two publications reporting its use *in vivo*, at the dose of 5 mg/kg (367, 380). At 5 mg/kg, G9a was sufficiently inhibited in adult mice and a preliminary test here in 3 mice confirmed that treatment with 5mg/kg UNC0642 was well-tolerated.

For HKMTI-1-005, previous *in vivo* work undertaken by Crown Bioscience UK Ltd on behalf of Imperial College (study director Simon Jiang, unpublished data; OVCAR3 ovarian cancer xenografts in SCID mice), indicated that 20 mg/kg was the best tolerated dose (relevant data in Appendix 5.0). The T max for 5 mg/kg HKMTI-1-005 in these studies highlighted the need for twice daily dosing and, although intravenous regimen achieved the best bioavailability, it was felt to be technically difficult and potentially harmful for the animals (Appendix 6.0). Therefore, the IP regimen of 20 mg/kg twice daily was taken forward. On pharmacokinetic simulation analysis, this dose achieved concentrations lower than the dose that caused 50% growth inhibition (GI50) in cell lines in vitro

(Appendix 7.0), but as already mentioned, doses higher than 20 mg/kg were not tolerated *in vivo*. Moreover, the focus was more on the immunostimulatory effect rather than its cytotoxic/cytostatic properties. To remove drug exposure bias, I treated mice for the same duration with each drug, i.e. 2 weeks of either 5 mg/kg UNC0642 or 20 mg/kg HKMTI-1-005 (figure 4.1).

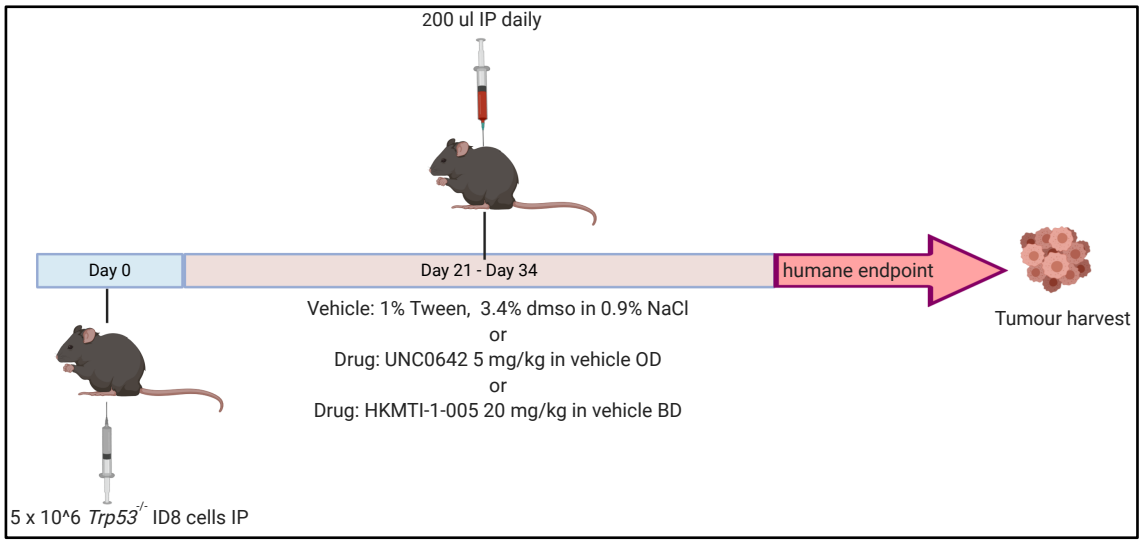

Figure 4.1: Schematic of survival experiment with either vehicle, UNC0642 or HKMTI-1-005 (n=12 per cohort). Each drug (stored in DMSO) was reconstituted with vehicle (1% Tween in 0.9% NaCl) just before dosing. Dose was calculated based on the median weight of mice. In the control group treatment, the maximum equivalent of DMSO concentration found in the drug treatment was added, for consistency. OD: once daily, BD: twice daily.

Results from this initial survival experiment showed that HKMTI-1-005 significantly prolongs mice survival compared both to vehicle (52 days *vs* 45 days, p<0.0001) and UNC0642 (52 days *vs* 49, p=0.01), and at endpoint, mice bore less ascites than vehicle-treated animals (3.7 ml *vs* 5.6 ml, p=0.003, figure 4.2c). Tumours weighed less in the HKMTI-1-005 treated group (157 mg *vs* 177.9 mg, p=0.4) but this was not statistically significant (figure 4.2b). Mice treated with HKMTI-1-005 had higher haemoglobin than vehicle-treated (7.8 g/dL *vs* 4.3 g/dL, p=0.003), but other haematological parameters were not statistically different, including the prognostic factor neutrophil/lymphocyte ratio (433) (figure 4.2d-4.2g). Treatment with UNC0642 led to a moderate but significant prolongation of survival (49 days *vs* 45 days, p=0.0009). Both ascites volume and tumour weight were decreased with treatment, but this decrease did not reach statistical significance (ascites 4.6 ml *vs* 5.6 ml, p=0.09 and tumour weight 160.5 mg *vs* 177.9 mg, p=0.5). The haematological parameters of the mice treated with UNC0642 were no different to the vehicle group, at endpoint.

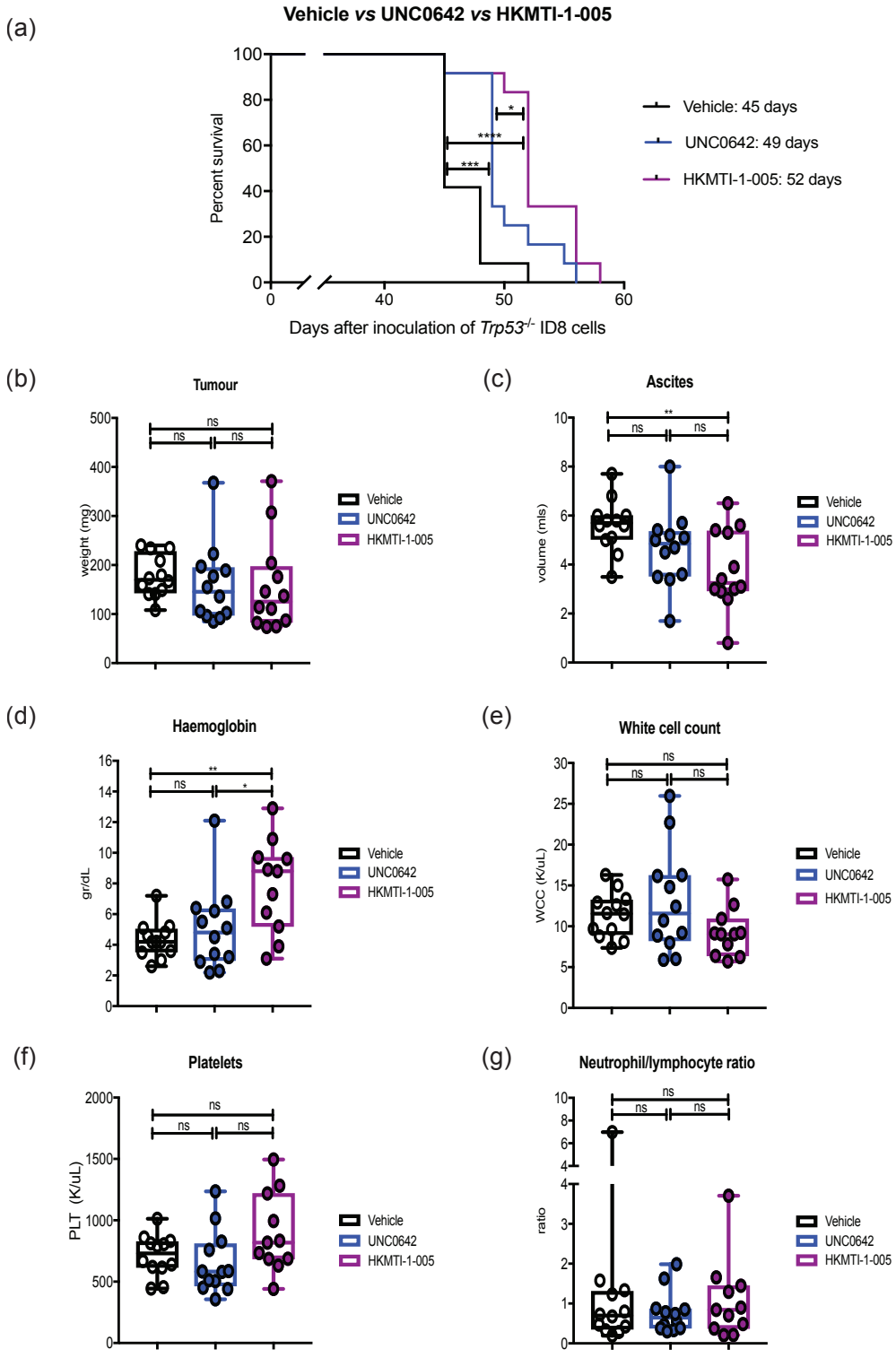

Figure 4.2: Results of survival experiment with treatment with either vehicle, UNC0642 or HKMTI-1-005 for 14 days. (a) Survival curves for mice treated with vehicle (n=12), 5 mg/kg UNC0642 (n=12) or 20 mg/kg HKMTI-1-005 (n=12) as per schedule on figure 4.1. Curves were compared using the Log-rank Mantel-Cox test. Tumour weights (b) and ascites volume (c) when mice reached humane endpoint; comparisons were made using one-way ANOVA and Dunnett's multiple comparison test. Haematological parameters as measured at endpoint in (d), (e), (f) and (g). One-way ANOVA with Dunnett's multiple comparison test used for comparison between groups.

4.3 G9a inhibition does not alter the immune microenvironment

I sought to investigate if G9a inhibition, alone, had an impact on the composition of immune populations in *Trp53*$^{-/-}$ ID8 tumours. To this end, mice were treated with UNC0642 and their tumours harvested immediately and 72 hours after last treatment (figure 4.3a). A striking initial observation was that the mice treated with UNC0642 had significantly less ascites than the untreated cohort (0.145 ml *vs* 0.430 ml, p=0.04, figure 4.3b). Tumour deposits harvested from porta hepatis, were subjected to digestion and flow cytometry, as described in methods section 2.7 and the results were analysed in a BD Fortessa flow cytometer (gating strategy figure 4.4 and figure 4.5).

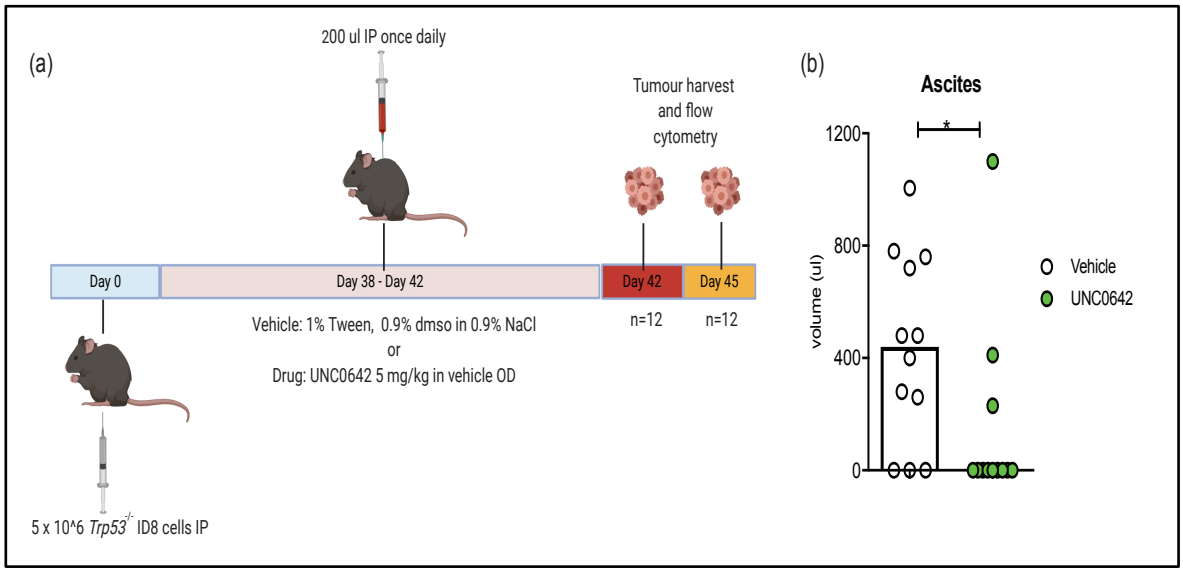

Figure 4.3: (a) Schematic of exploratory experiment with UNC0642 and ascites volume results after treatment. UNC0642 dose was 5 mg/kg (n=12 per cohort). Tumours were harvested straight after the last drug dose (n=6 control and n=6 treatment) and 72 hours after last dose (n=6 control and n=6 treatment). OD: once daily. (b) Ascites volume (n=12 per cohort), bar in the vehicle group represents the median as data was non-parametric, Mann-Whitney test was used for comparison.

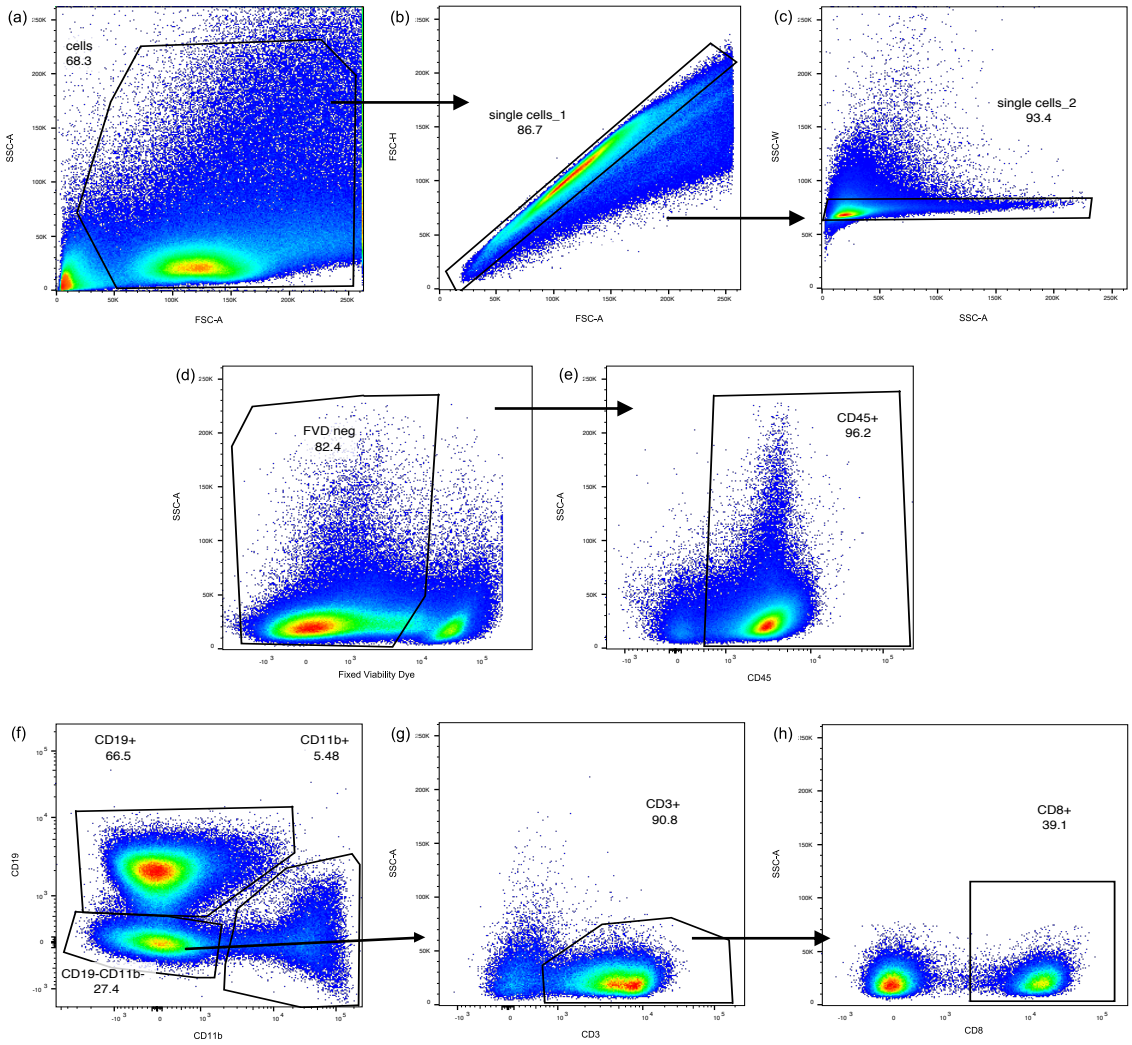

Figure 4.4: Gating strategy for flow-assisted sorting of immune cells from murine tumour deposits - lymphoid population. (a) gate on entire cell population, excluding cell debris; (b) and (c) gates on single cells, excluding dublets; (d) gate on Zombie Red negative cells to exclude dead cells (Zombie red positive cells); (e) gate on CD45 positive cells that represent all immune cells. (f) gates on $CD19^{+}CD11b^{-}$ cells to identify B cells, gate on $CD11b^{+}$ cells to identify myeloid-derived cells and gate on $CD19^{-}CD11b^{-}$ double negative cells, from which $CD3^{+}$ are gated in (g) and $CD8^{+}$ cells in (h).

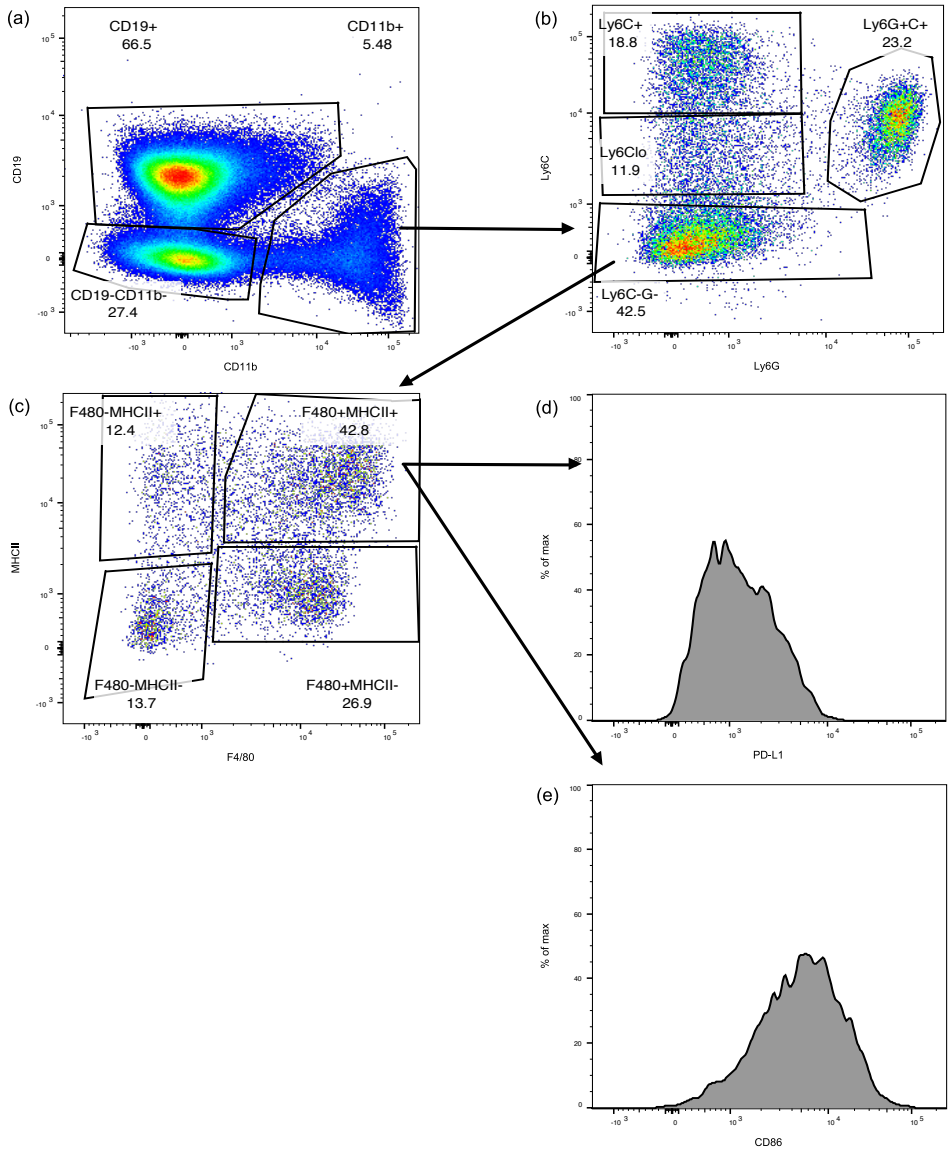

Figure 4.5: Gating strategy for flow-assisted sorting of immune cells from murine tumour deposits - myeloid population. (a) Gate on $CD11b^{+}$ $CD19^{-}$ myeloid-derived cells, further characterised with Ly6G and Ly6C antibody staining in (b); $Ly6G^{+}Ly6C^{+}$ cells define the myeloid-derived suppressor cells, whereas $Ly6C^{+}$ $Ly6G^{-}$ cells define the population of monocytes. $Ly6G^{-}Ly6C^{-}$ double negative cells from (b) were then characterised with F4/80 and MHCII antibody staining to identify the tumour-associated macrophages, as $F4/80^{+}MHCII^{+}$ and the dendritic cells as $F4/80^{-}MHCII^{+}$ in (c). For both macrophages and dendritic cells, the geometric mean of PD-L1 and CD86 cell markers was calculated to characterise their expression specifically on the cell surface of these sub-populations.

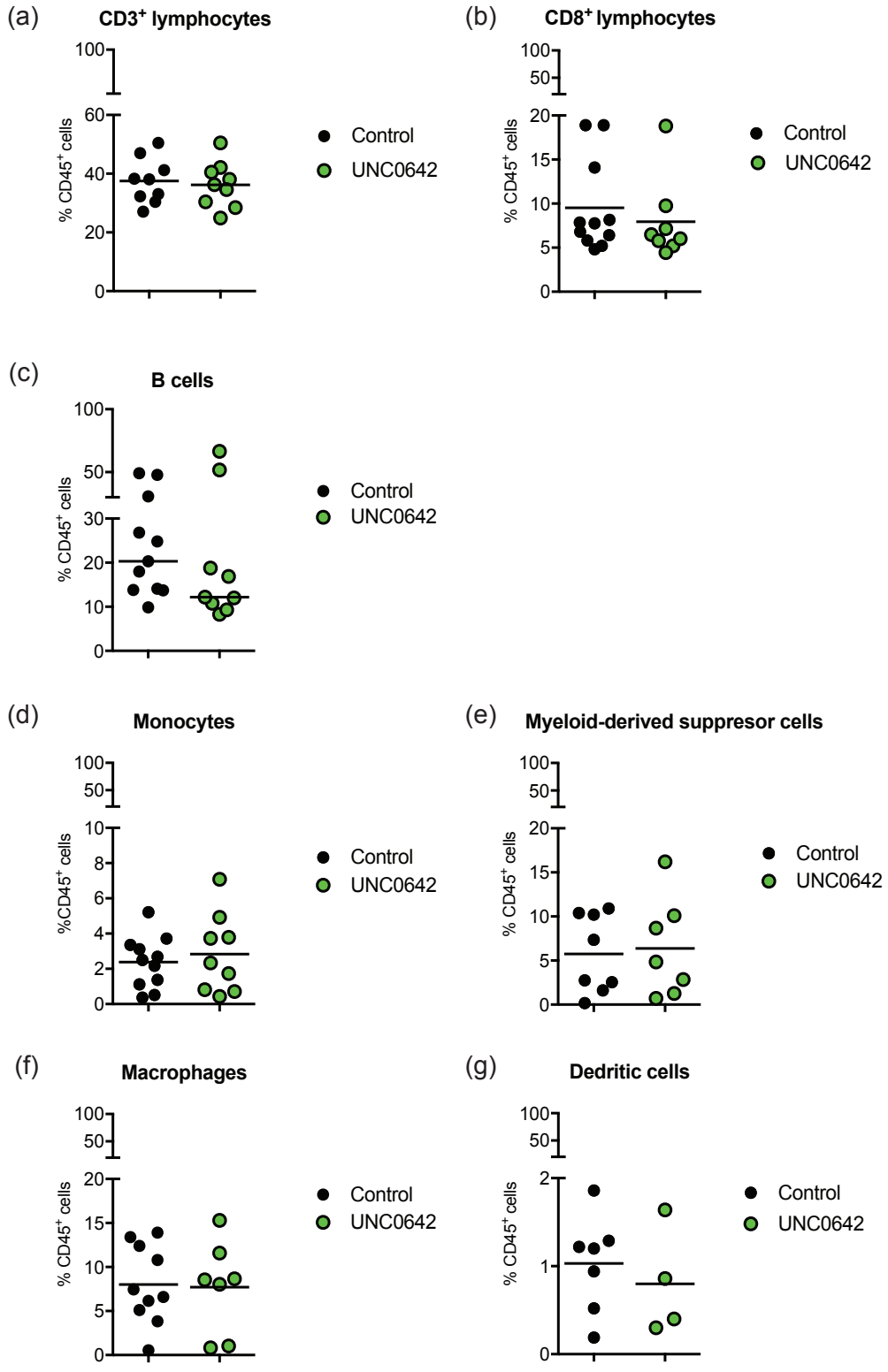

Figure 4.6: Immune cell population frequency following G9a inhibition treatment, as per schedule on graph 4.3. Immune cell population frequency expressed as percentages within the entire $CD45^+$ cell population. Gates that contained <200 events were not included in the analysis. Lines represent the mean and each dot represents one mouse; mean comparisons were made using Student's *t*-test. None of the results reached statistical significance.

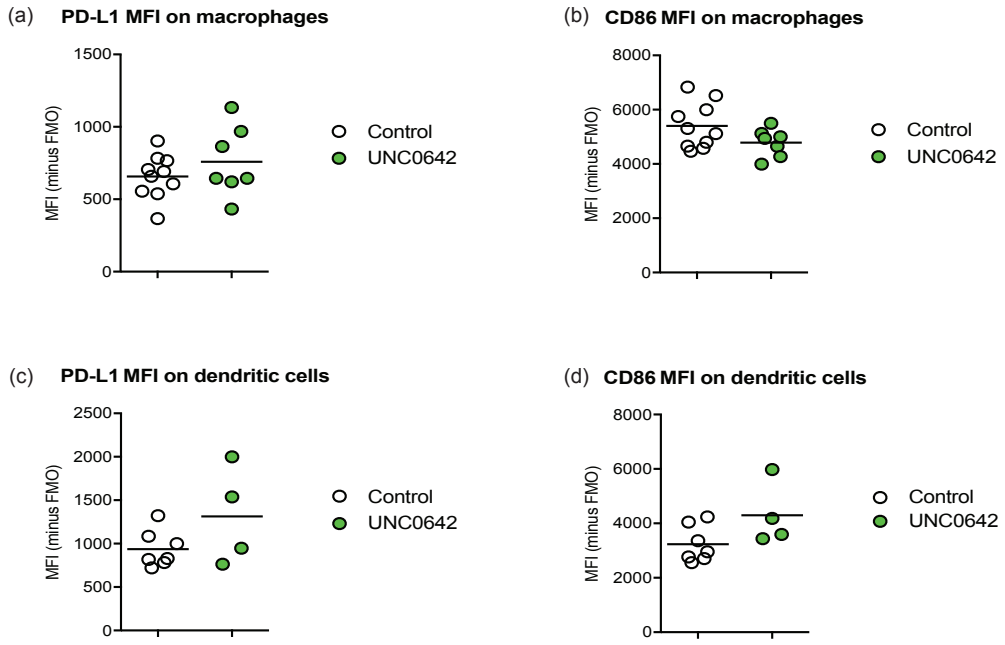

Figure 4.7: Geometric mean fluorescence (MFI) of markers PD-L1 and CD86 on macrophages and dendritic cells, following G9a inhibition. Geometric mean fluorescence (MFI) of PD-L1 marker was measured on macrophages (a) and dendritic cells (c) and the MFI of CD86 on macrophages (b) and dendritic cells (d). MFI of the fluorescence-minus-one sample was subtracted from each sample. Gates that contained <200 events were not included in the analysis. Lines represent the mean and each dot represents one mouse; mean comparisons were made using Student's *t*-test.

Overall, analysis of the immune cell populations in tumours treated with UNC0642 did not show any significant change when compared to untreated tumours. Percentages of both lymphoid and myeloid populations remained on the whole unchanged with treatment. With regards to the expression of PD-L1 and CD86 on macrophages and dendritic cells, as markers of inhibition and activation, respectively, I observed a trend towards stronger expression of CD86 on dendritic cells (MFI 4298 ± 583 *vs* 3234 ± 254, p=0.08). The expression of PD-L1 was also moderately increased (MFI 1313 ± 282 *vs* 937 ± 80, p=0.13) without it being statistically significant. Dendritic cells express CXCR3 (359) and through the CXCR3/CXCL10 axis can amplify and maintain lymphocyte activation (359, 362, 434-437), therefore the moderate increase of CD86 on the surface of dendritic cells could signify an activated state (438). Nevertheless, this did not correlate with any difference in the abundance of cytotoxic lymphocytes in the tumour microenvironment of UNC0642-treated mice.

4.4 Combined G9a/EZH2 inhibition modulates the tumour immune microenvironment

4.4.1 Flow cytometry - porta hepatis tumour deposit

I then endeavoured to examine the tumour immune microenvironment after blocking both G9a and EZH2 with HKMTI-1-005. Mice were treated as per regimen in figure 4.8a. Once again, a complete inhibition of ascites development was observed in the treatment cohort (0% *vs* 44%, $p<0.0001$, figure 4.8b). The whole tumour burden was defined as the sum of omental and porta hepatis deposits weights (figure 4.8c/d/e). The results show inhibition of tumour growth in the treatment group as evident by the absence of ascites and the reduced tumour weight (whole tumour burden weight 104 mg *vs* 138 mg, $p=0.02$).

The porta-hepatis tumours were subjected to flow cytometry, with additional surface markers (table 2.9) to allow for more accurate characterisation of the immune cell populations. With regards to the lymphoid populations, some interesting changes were observed. The number of $CD3^+$ cells within the tumour was overall increased with HKMTI-1-005 (44.1 $x10^6$ cell/g *vs* 16.3 $x10^6$ cell/g, $p=0.01$) with an increase in both $CD8^+$ (20.7 $x10^6$ cell/g *vs* 4.9 $x10^6$ cell/g, $p=0.16$) and $CD4^+$ (23.5 $x10^6$ cell/g *vs* 3.8 $x10^6$ cell/g, $p=0.001$) subpopulations (figure 4.9a). Similarly, B cells were increased with HKMTI-1-005 (37 $x10^6$ cell/g vs 6 $x10^6$ cell/g, $p=0.001$). Natural killer (NK) cells and Natural Killer T lymphocytes (NKT) populations, defined as $CD3^-DX5^+$ and $CD3^+DX5^+$, were unchanged between treated and vehicle cohorts.

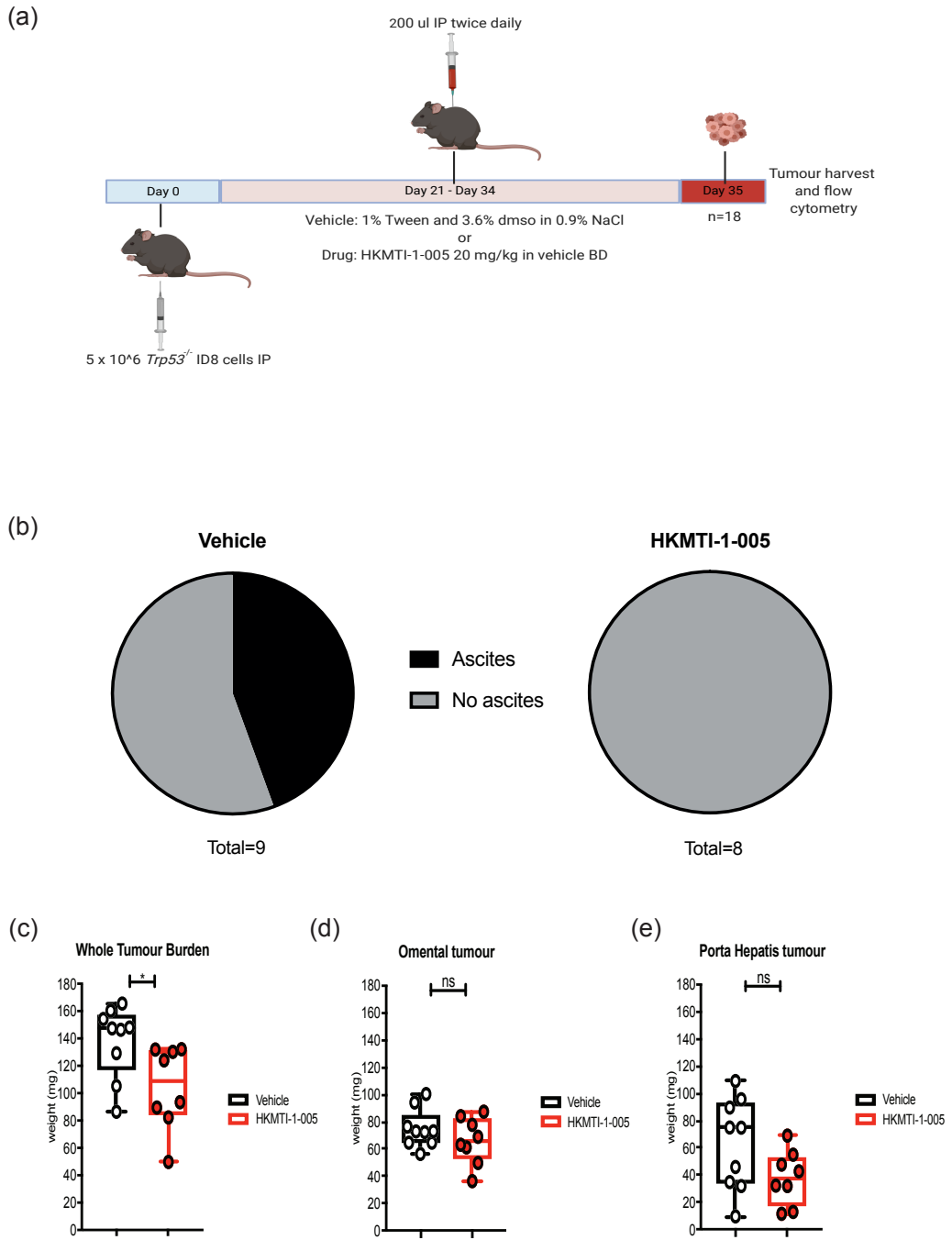

Figure 4.8: Exploratory experiment following treatment with the dual G9a/EZH2 inhibitor, HKMTI-1-005. (a) Treatment schedule. Note that initial mice number was n=18, however, one mouse in the treatment group was eliminated due to injury on day of 1 of injections. (b) Ascites in vehicle *vs* treatment groups. Tumour weights expressed as whole tumour burden (c) and their break-down to omental tumour weight (d) and porta hepatis tumour weight (e). Means were compared with Student's *t*-test, error bars represent standard deviation.

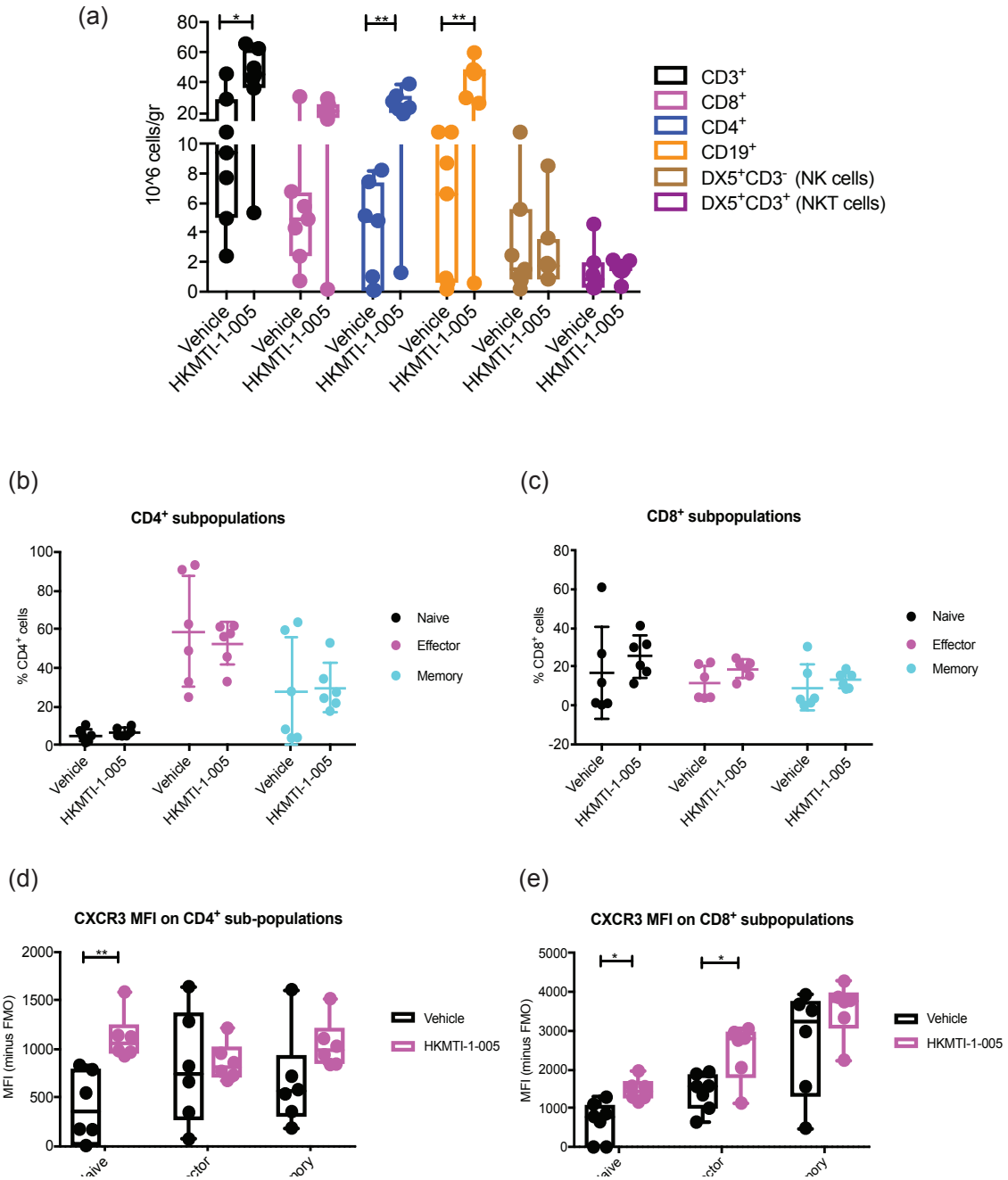

Figure 4.9: Flow cytometry results following 2 weeks of HKMTI-1-005 treatment. (a) Changes in $CD3^+$, $CD8^+$, $CD4^+$, $CD19^+$, $CD3^-DX5^+$ and $CD3^+DX5^+$ populations, normalised to tumour weight. (b) and (c) naïve/effector and memory subpopulations of $CD4^+$ and $CD8^+$ cells, expressed as percentages of their respective populations. (d) CXCR3 expression on $CD4^+$ naïve, effector and memory cells. (e) CXCR3 expression on $CD8^+$ naïve, effector and memory cells. Error bars represent standard deviation and comparisons were done using Student's *t*-test.

When looking specifically into $CD4^+$ and $CD8^+$ cell populations with CD44 and CD62L markers for identification of naïve ($CD44^-CD62L^+$), effector ($CD44^+CD62L^-$), and memory ($CD44^+CD62L^+$) cells, I did not observe any significant differences in this experiment (figure 4.9b, figure 4.9c and appendix 8.0). Nevertheless, naïve $CD4^+$ cells and naïve and effector $CD8^+$ cells had increased expression of CXCR3, the receptor for CXCL10, after treatment with HKMTI-1-005 (figure 4.9d and figure 4.9e). Representative flow plots of a treated and an untreated mouse for $CD4^+$, $CD8^+$ and B cell populations are shown in figure 4.10a and 4.10b.

The most noticeable and statistically significant increase in CXCR3 expression was observed on the NK cells (MFI 2011 ± 297 *vs* -344.5 ± 215, $p<0.0001$), as shown in figures 4.10c and 4.10d.

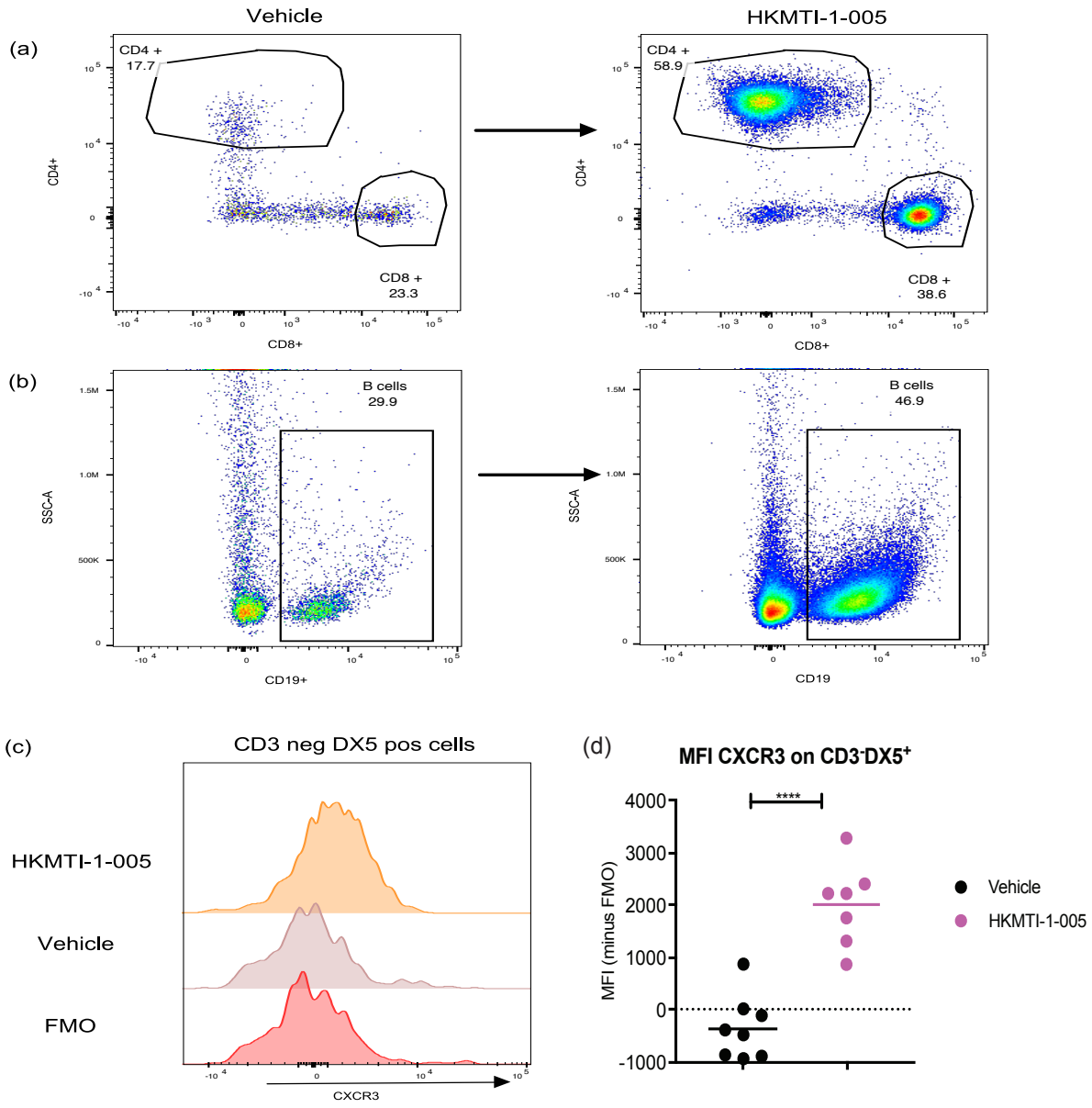

Figure 4.10: Flow cytometry plots and CXCR3 expression on NK cells following HKMTI-1-005 treatment. Representative flow plots showing differences between a mouse receiving vehicle and a mouse receiving HKMTI-1-005 with respect to $CD4^+$, $CD8^+$ (a) and B cells (b). (c) representative histogram showing CXCR3 fluorescence on fluorescence-minus-one (FMO), vehicle and HKMTI-1-005 samples, on NK cells. (d) Mean CXCR3 fluorescence on NK cells. Note that gates with <200 events were excluded from the analysis, hence the sample discrepancy between vehicle and treated. Some fluorescence values for the vehicle group are negative as they were subtracted by the average (minus FMO) fluorescence; the minus-FMO sample contains a mixture of all samples and therefore can have a higher value than some of the vehicle samples.

Analysis of the intracellular chemokine content of $CD8^+$ cells by flow cytometry did not show any statistically significant differences between vehicle and HKMTI-1-005 treated mice (figure 4.11a and gating in Appendix 9.0).

To characterise the composition of myeloid populations, my planned gating strategy was different to that described in figure 4.5. Access to a Cytek Aurora flow cytometer allows the use of fluorochromes combinations that could not be simultaneously used with the BD FORTESSA, which allowed me to add new cell surface markers. Therefore, after identification of $Ly6G^-Ly6C^-$ cells within the $CD11b^+$ population, I used Siglec-F marker to exclude Siglec-F positive eosinophils. Then, within the Siglec-F negative population, I defined $F4/80^+MHCII^+$ cells as tumour-associated macrophages (TAMs) and the $F4/80^-$ $MHCII^+$ population as dendritic cells, but only if the latter were also positive for CD11c marker (Appendix 10.0). Following this, I also quantified the MFI of CD80, CD86, CD206 and PD-L1 on TAMs and dendritic cells.

However, in this experiment as well as subsequent ones, it became apparent that a significant number of the $F4/80^+MHCII^+$ cells, which are traditionally described as TAMs, retain a high expression of Ly6C in the HKMTI-1-005 treated cohort (figure 4.11b; right panel). This was not observed in the vehicle group (figure 4.11c; right panel). Thus, although the literature suggests that macrophages lose Ly6C expression as they differentiate from $Ly6C^+$ monocytes to TAMs when entering the tumour microenvironment (170, 439, 440), it became apparent that excluding $Ly6C^+$ cells as non-TAMs would lead to flawed results in my experiment. Therefore, when quantifying TAMs in my *in vivo* experiments with HKMTI-1-005 treatment, I did not gate out the Ly6C positive cells as per my initial gating methodology. Their precise phenotype therefore is $CD11b^+Ly6G^-$ $SinglecF^-F4/80^+MHCII^+$ (figure 4.11b/c).

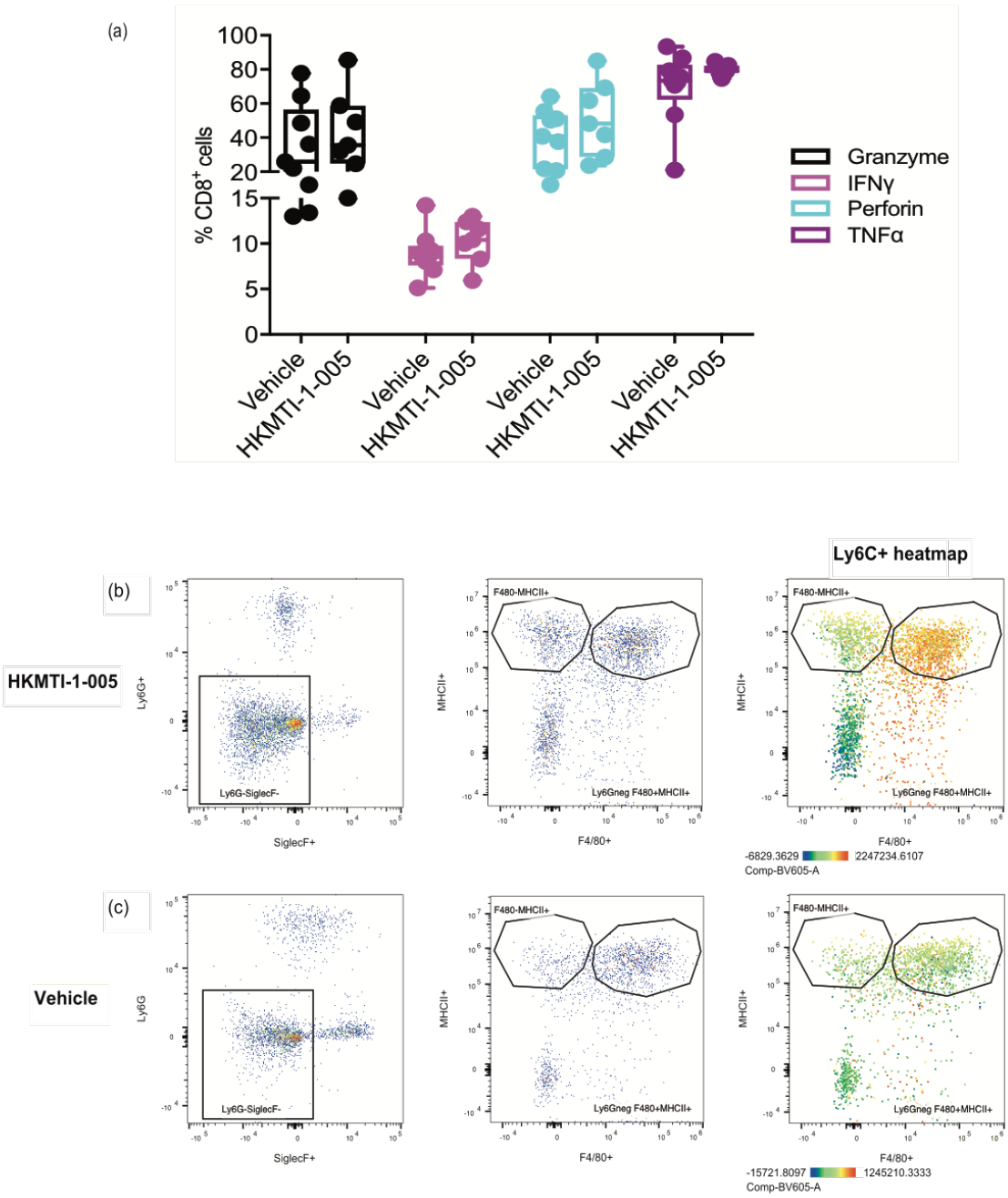

Figure 4.11: Results of intracellular chemokine content and myeloid cell gating strategy following HKMTI-1-005 treatment. (a) Graph showing percentages of $CD8^+$ cells positive for intracellular stain for granzyme-B, IFNγ, perforin and TNF-α chemokines. Means of treated and untreated cohorts were compared with Student's *t*-test; results were statistically not significant. (b) Gating on $Ly6G^-SiglecF^-$ double negative cells and Ly6C stain superimposed on $F4/80^+MHCII^+$ cells showing that this population is retaining Ly6C expression in the treated group, compared to untreated group (c).

There were no statistically significant differences in the number of TAMs and DCs within tumours in treated and untreated mice (figure 4.12a, 4.12c). However, Ly6C positive macrophages were significantly increased in the treated cohort (1.7 x10^6 cell/g vs 0.2 x10^6 cell/g, p=0.008; figure 4.12b) supporting the observation that macrophages retain Ly6C expression only in tumours treated with HKMTI-1005. Moreover, these TAMs had higher expression of CD86 (MFI 14091 ± 385 *vs* 10864 ± 364, p=0.0004) and lower expression of CD206 (MFI 5377 *vs* 6830, p=0.009), highlighting that treatment also has an effect on the activation status of macrophages (figure 4.12e). Similarly, dendritic cells had differential marker expression with treatment; CD80 expression was moderately decreased (MFI 4327 ± 70 *vs* 5250 ± 370, p=0.01) whereas CD86 was increased (MFI 13555 ± 405 vs 8838 ± 1484, p=0.006) (figure 4.12f).

PD-L1 expression showed an increasing trend in both TAMs and DCs, although this did not reach statistical significance for either. There was a striking increase in PD-L1 expression on non-immune ($CD45^-$) cells within tumour deposits with HKMtI-1-005 (MFI 507.9 ± 838.7 *vs* -3530 ± 291.6, p=0.0005; figure 4.12d). Although the tumour microenvironment contains a variety of $CD45^-$ cells, a large proportion are tumour cells, suggesting that HKMTI-1-005 treatment increases PD-L1 expression on malignant cells.

Immunohistochemistry confirmed there were more $CD3^+$ cells (H-score 20.4 *vs* 14.8, p=0.09) in the HKMTI-1-005 treatment group, as seen in flow cytometry. Moreover, NK cells were increased (H-score 3.8 *vs* 2.8, p=0.08) in the treated tumours, whereas immunosuppressive FoxP3 cells (H-score 9.6 *vs* 13.1, p=0.36) were decreased. However, none of these results reached statistical significance (figure 4.13).

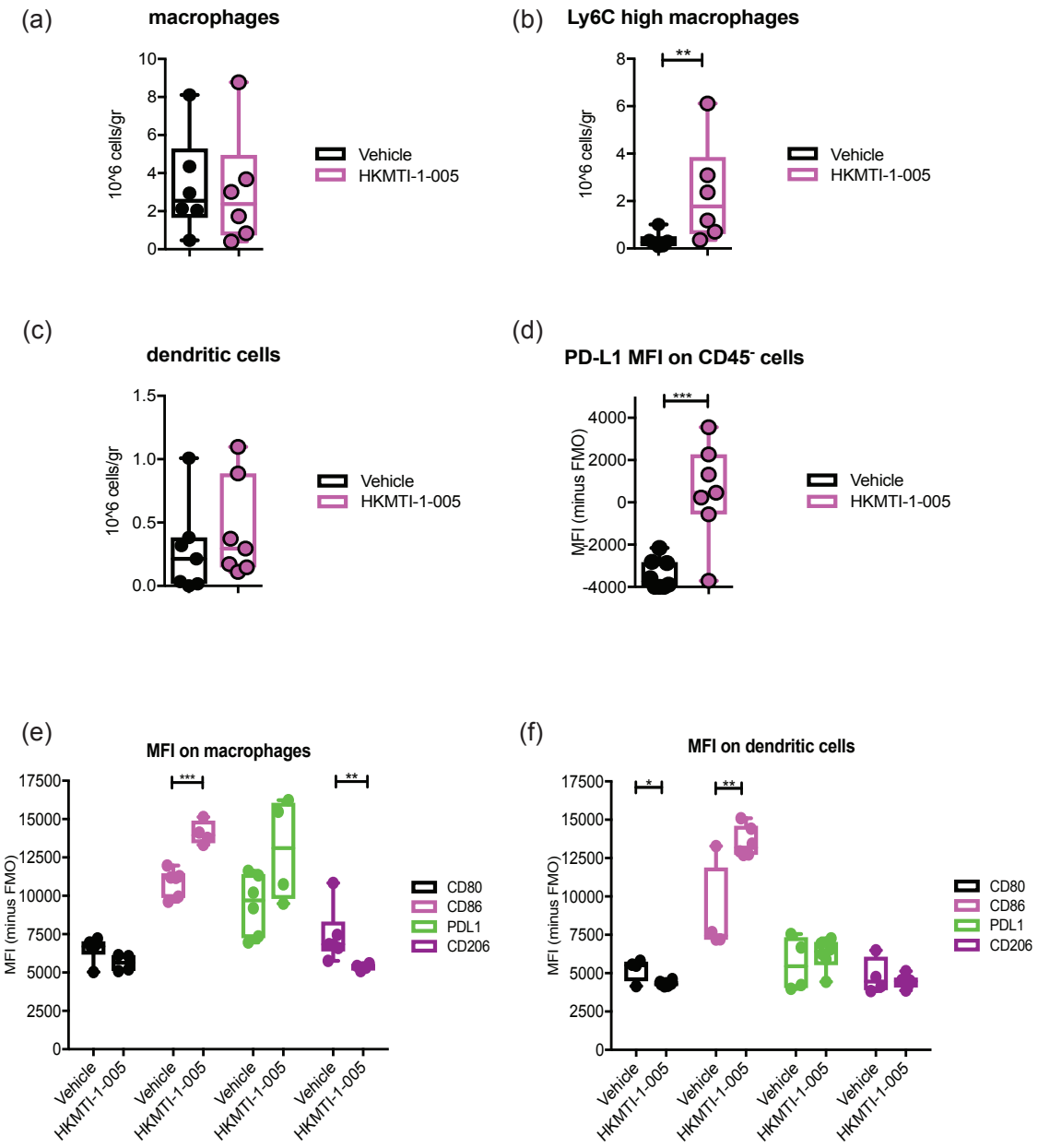

Figure 4.12: Flow cytometry results following HKMTI-1-005 treatment- myeloid populations and receptor expression. Flow cytometry analysis showing number of TAMs (a) and DCs (c) normalised to tumour weight; showing number of Ly6C$^+$ TAMs in tumours (b); (d) PD-L1 MFI on CD45$^-$ cells as a proxy for tumour cells. MFI for markers CD80, CD86, PD-L1 and CD206 on TAMs (e) and DCs (f). For statistical comparisons: Student's *t*-test used for PD-L1 MFI on CD45$^-$ cells, CD86 on TAMs, CD86 and CD80 on DCs. Mann-Whitney test used for Ly6C$^+$ TAMs and CD206 on TAMs. Each dot represents one mouse and differences between cohorts are due to the arbitrary cut-off of >200 events/gate in order to include mouse in the analysis.

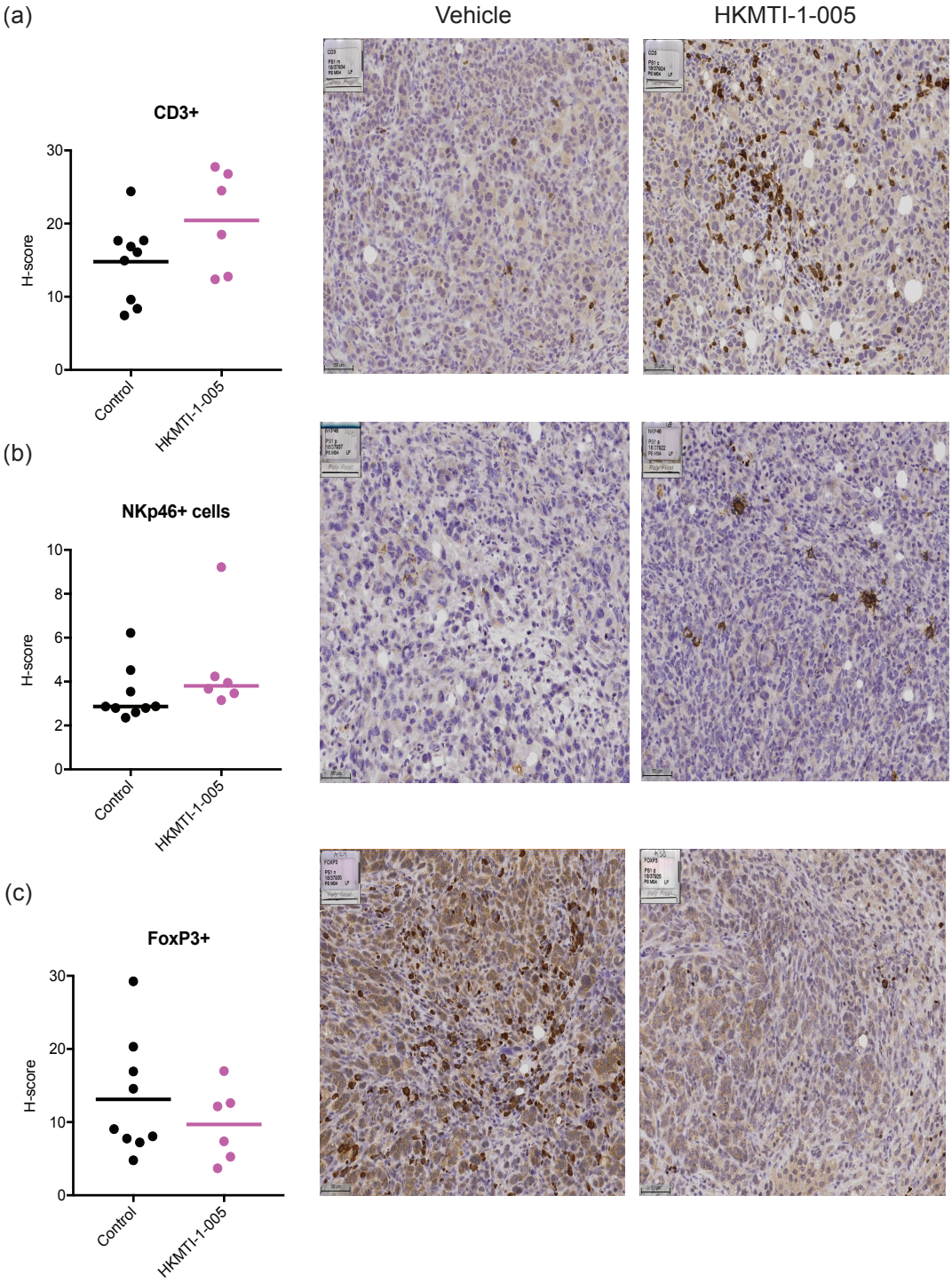

Figure 4.13: Immunohistochemistry following HKMTI-1-005 treatment. Immunohistochemistry on omental tumours of vehicle *vs* HKMTI-1-005 treated mice for $CD3^+$ (a), $NKp46^+$ (b) and $FoxP3^+$ (c) stains. Histoscore (H-score) calculated with HALO software. Statistical comparisons done with Student's *t*-test for $CD3^+$ and $FoxP3^+$ stains and Mann-Whitney test for $NKp46^+$ stain.

4.4.2 Flow cytometry - porta hepatis and omental tumour deposits

In the subsequent experiment, I firstly wanted to confirm results of the previous experiment (4.2.1) and secondarily investigate potential differences between sites of disease, namely omental tumour and the porta hepatis deposits. The methodology was identical to the one described in figure 4.8a. Porta hepatis tumours are smaller than the omental tumours, which limited the amount of tumour material available for flow cytometry analysis.

In this experiment, the overall $CD3^+$ population did not change in either porta hepatis or omental deposits (figure 4.14a) and, in contrast to previous results, B cells (3.1 $x10^6$ cell/g *vs* 8.9 $x10^6$ cell/g, p=0.005) and $CD4^+$ cells (3.2 $x10^6$ cell/g *vs* 5.3 $x10^6$ cell/g, p=0.04) decreased with treatment in both disease sites (figure 4.14b, 4.14c). The decrease of $CD4^+$ cells could at least partially be explained by a decrease in the $CD4^+FoxP3^+$ cells (0.9 $x10^6$ cell/g *vs* 2.2 $x10^6$ cell/g, p=0.02; figure 4.16a).

$CD8^+$ cells were significantly decreased in the porta hepatis (6.8 $x10^6$ cell/g *vs* 28.6 $x10^6$ cell/g, p=0.02) but not in the omental deposits (2.3 $x10^6$ cell/g *vs* 2.2 $x10^6$ cell/g, p=0.87; figure 4.14d). Nevertheless, the NK cells ($CD3^-DX5^+$) increased in both porta hepatis (10.4 $x10^6$ cell/g *vs* 4.2 $x10^6$ cell/g, p=0.01) and omental deposits (4.0 $x10^6$ cell/g *vs* 2.3 $x10^6$ cell/g, p=0.09; figure 4.14e), whereas the NKT cell population remained unchanged (figure 4.14f).

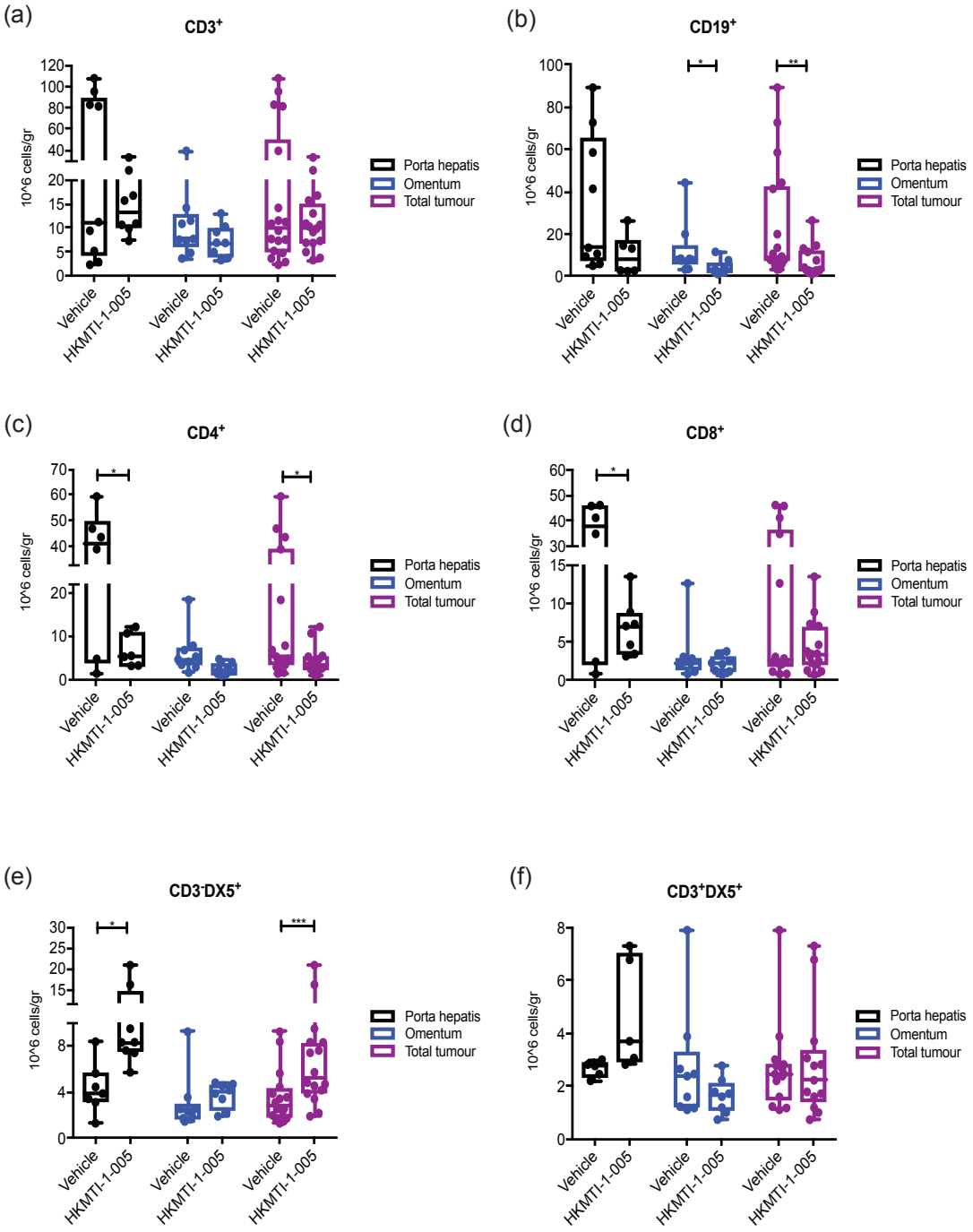

Figure 4.14: Flow cytometry results at porta hepatis and omental tumours after treatment with HKMTI-1-005 – lymphoid populations. Flow cytometry analysis showing $CD3^+$ (a), $CD19^+$ (b), $CD4^+$ (c), $CD8^+$ (d), NK (e) and NKT (f) cells in untreated *vs* treated mice, in porta hepatis, omental deposit and as a total in both disease sites. Mann-Whitney test was used for all comparisons apart from comparisons of omental $CD4^+$ and porta hepatis $CD19^+$, $CD8^+$, $CD4^+$, $CD3^+DX5^+$, $CD3^-DX5^+$, where Student's *t*-test was used. Error bars represent standard deviation.

Within the $CD4^+$ population, the percentages of naïve, effector and memory cells did not change significantly (figure 4.15a, 4.15c, 4.15e). However, in the porta hepatis deposit, I observed an increase in effector $CD8^+$ cells (66.7% *vs* 37.1%, p=0.03; figure 4.15f) with a concomitant decrease of naïve $CD8^+$ (3.2% *vs* 14.0%, p=0.03) and memory $CD8^+$ cells (28.3% *vs* 42.9%, p=0.04) (figure 4.15b, figure 4.15d).

Interestingly, the $CD3^+$ population in both anatomical sites had higher expression of CXCR3 in the HKMTI-1-005 treated tumours (MFI 2729 ± 394 *vs* 838 ± 265, p=0.0003), both $CD4^+$ (MFI 2341 ± 173 *vs* 1099 ± 165, p<0.0001) and $CD8^+$ (3959 ± 239 *vs* 2097 ± 264, p<0.0001) populations (figure 4.16b-4.16d). An increase in CXCR3 expression was also observed in the NK cells (1507 ± 100 vs 440 ± 152, p<0.0001; figure 4.16e).

HKMTI-1-005 treatment had no effect in the production of IFNγ and TNFα (figure 4.17a and 4.17d) but a significant increase was observed in granzyme-b positive $CD8^+$ cells in both the porta hepatis and the omental deposits (65.1% vs 27.2%, p<0.0001; figure 4.17b). Interestingly, although the perforin secreting $CD8^+$ cells were increased with treatment in the porta hepatis, these were decreased in the omental deposit (figure 4.17c).

I characterised the TAM population again using the gating approach as described on figure 4.11b. These were significantly more numerous with HKMTI-1-005 in the porta hepatis deposit (15.4 $x10^6$ cell/g *vs* 3.2 $x10^6$ cell/g, p=0.002) but not in the omental deposit (6.3 $x10^6$ cell/g *vs* 7.4 $x10^6$ cell/g, p=0.34) (figure 4.18a).

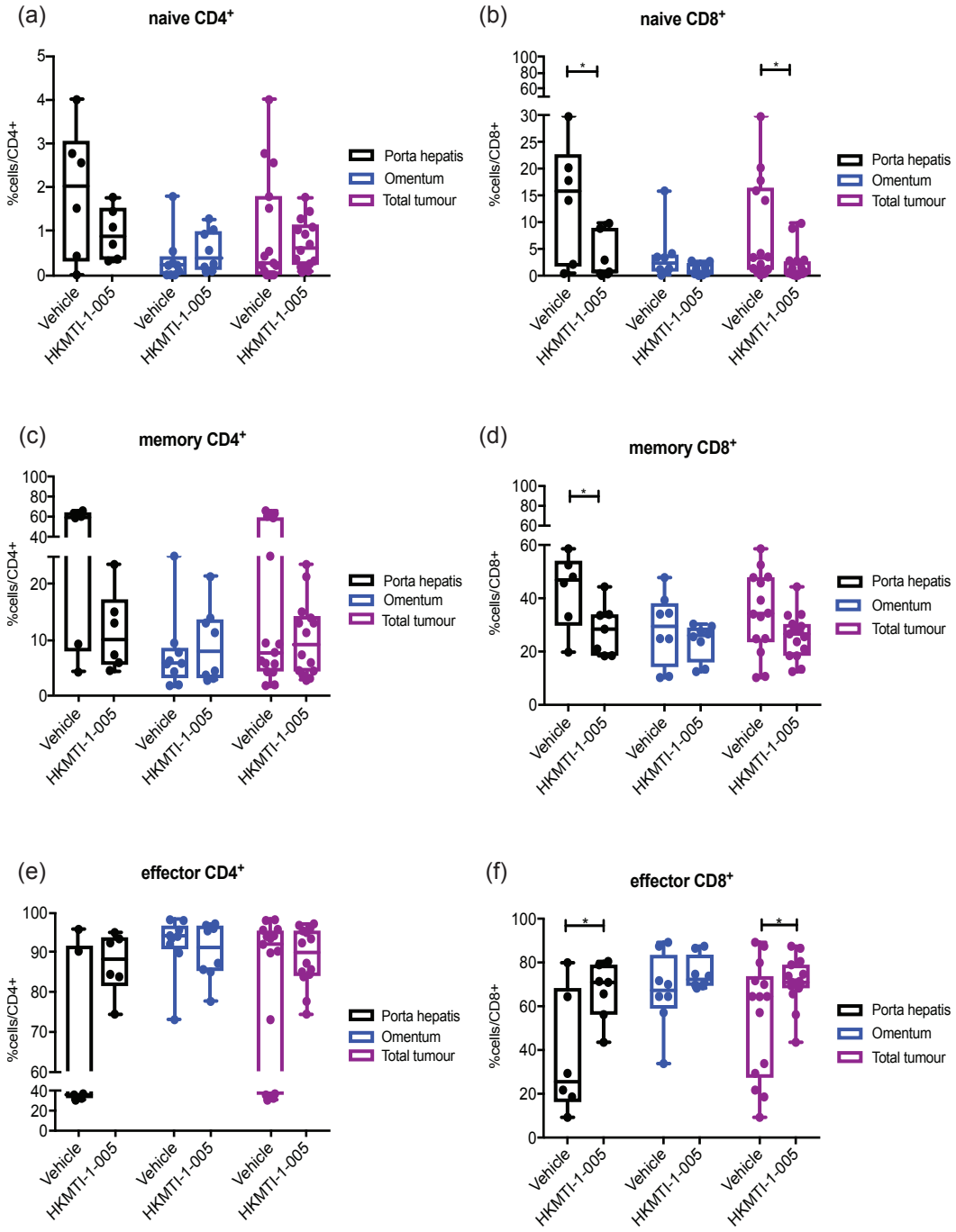

Figure 4.15: Flow cytometry results at porta hepatis and omental tumours after HKMTI-1-005 treatment – lymphoid subpopulations. Flow cytometry analysis of $CD4^+$ naïve (a), memory (c) and effector (e) cells; flow cytometry analysis of $CD8^+$ naïve (b), memory (d) and effector (f) cells. With regards to statistically significant results, Student's *t*-test was used for porta hepatis naïve, memory and effector $CD8^+$ cells, as well as total tumour effector $CD8^+$ cells. Mann-Whitney test was used for the total tumour naïve $CD8^+$ cells. Error bars represent standard deviation.

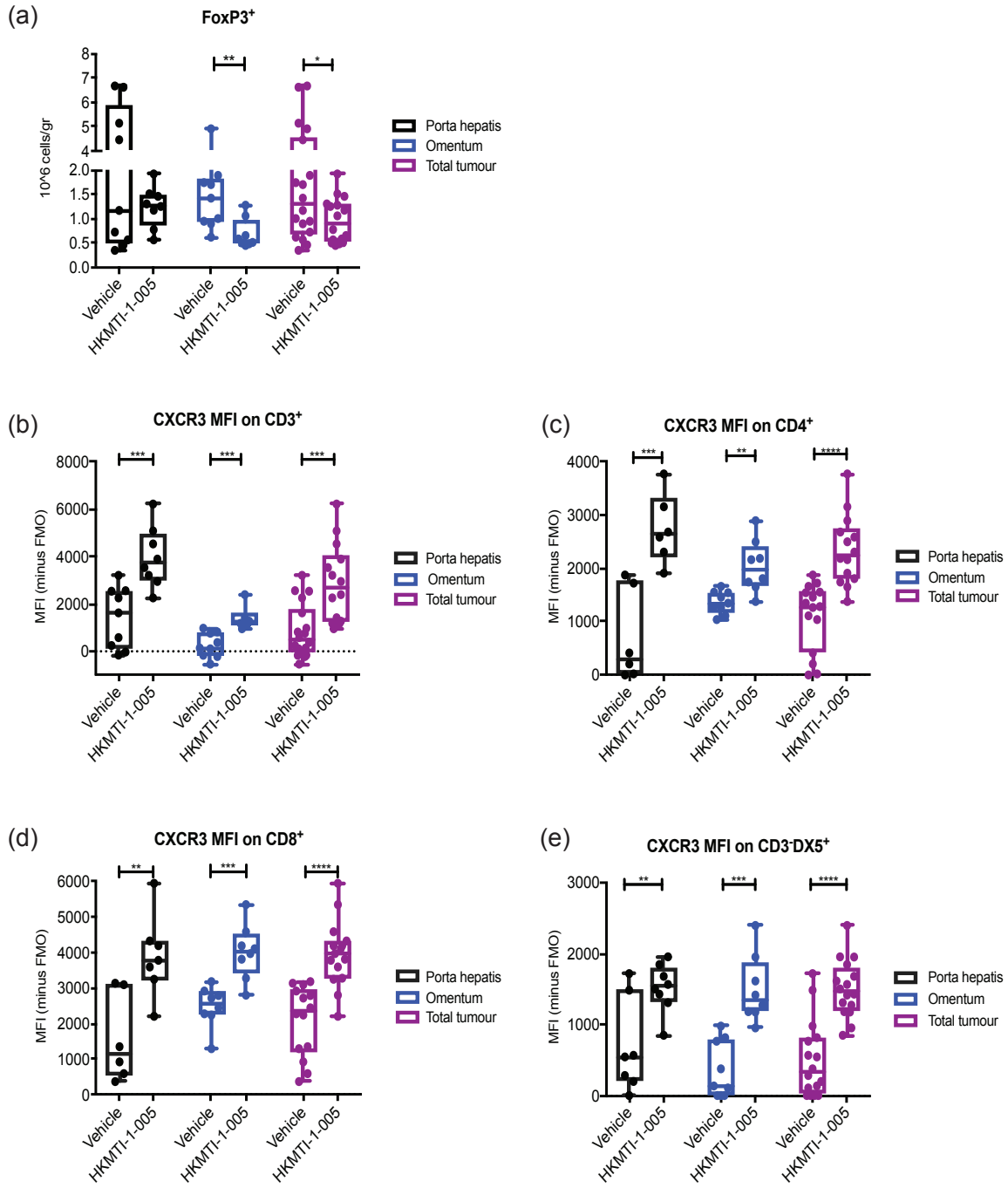

Figure 4.16: Flow cytometry results at porta hepatis and omental tumours after treatment with HKMTI-1-005 – T regs and CXCR3 expression on lymphoid populations. (a) flow cytometry analysis of intranuclear FoxP3 stain on $CD4^+$ cells. Mann Whitney test was used for omental $FoxP3^+$ and Student's *t*-test for the total tumour $FoxP3^+$. CXCR3 MFI quantification on $CD3^+$ (b), $CD4^+$ (c), $CD8^+$ (d) and $CD3^-DX5^+$ (e) cells. Student's *t*-test was used for all comparisons. Error bars represent standard deviation. Tregs= T regulatory cells.

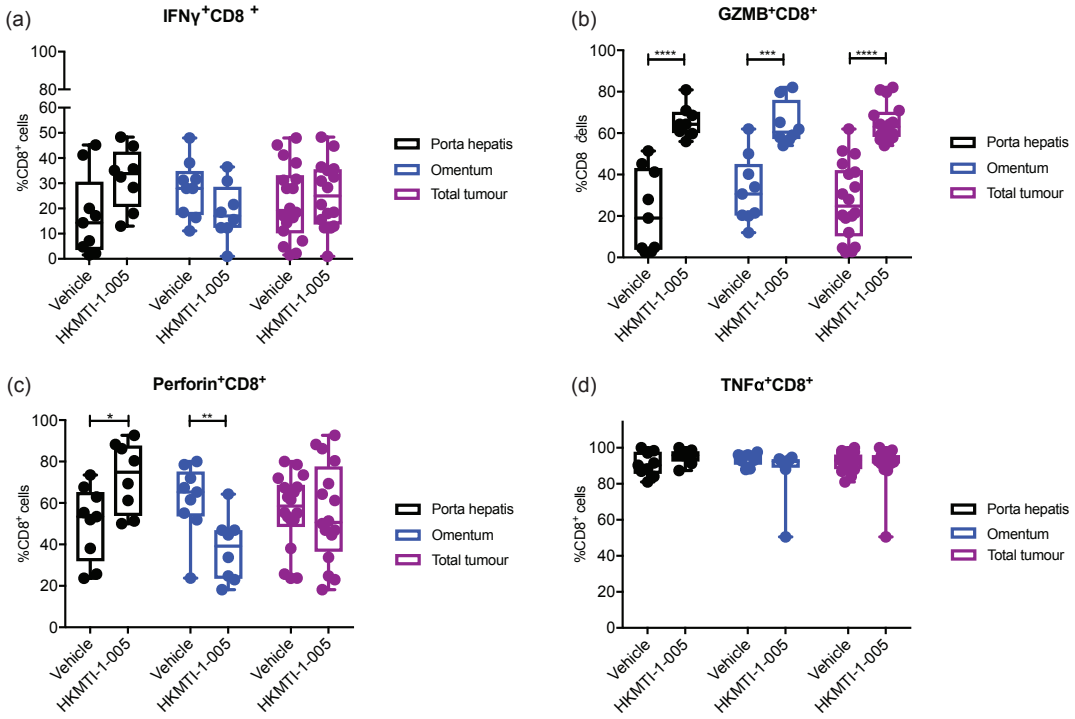

Figure 4.17: Flow cytometry results at porta hepatis and omental tumours after treatment with HKMTI-1-005; intracellular chemokine content. Percentages of $CD8^+$ cells stained positive for IFNγ (a), granzyme B (b), perforin (c) and TNFα (d) in porta hepatis deposit, omental deposit and total tumour. Student's *t*-test was used for all comparisons apart from the omental and total tumour $TNFα^+$ $CD8^+$ cells. Error bars represent standard deviation.

Interestingly, once again, the majority of TAMs in HKMTI-1-005 treated tumours retained their Ly6C expression (7.9 x10^6 cell/g *vs* 0.6 x10^6 cell/g, p<0.0001), confirming the previous observation (figure 4.18c). DCs were increased in the porta hepatis (7.8 x10^6 cell/g *vs* 0.8 x10^6 cell/g, p=0.01 and also showed a trend towards increase in the omental deposit (2.5 x10^6 cell/g *vs* 1.7 x10^6 cell/g, p=0.10) (figure 4.18b).

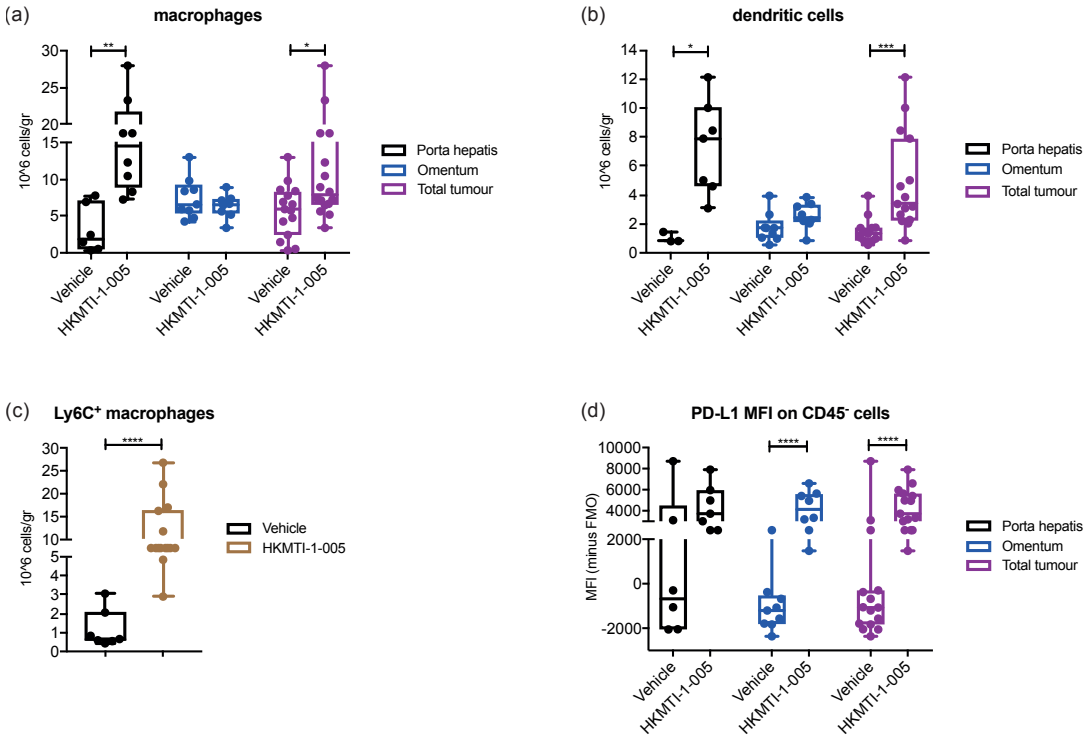

Figure 4.18: Flow cytometry results at porta hepatis and omental tumours after treatment with HKMTI-1-005; myeloid populations. Flow cytometry results for TAMs (a) and DCs (b) in porta hepatis deposit and omental deposit in untreated *vs* HKMTI-1-005 treated tumours. In (c), Ly6C$^+$ TAMs are compared between untreated/treated; events from both sites of disease have been averaged due to low event rate. MFI of PD-L1 ligand on surface of CD45$^-$ cells is shown in (d); some MFI values are negative as they were subtracted by the average (minus FMO) fluorescence value, which could in some occasions have a higher value. Mann Whitney test was used for all comparisons apart from porta hepatis TAMs and PD-L1 on CD45$^-$ cells and omental TAMs, DCs and PD-L1 on CD45$^-$ cells, where student's *t*-test was used. Error bars represent standard deviation.

In TAMs, I observed an upregulation of CD86 in the porta hepatis (MFI 25783 ± 1102 *vs* 19891 ± 1665, p=0.009) and a decrease in CD206 in the omental deposit (MFI 5220 ± 508 *vs* 7620 ±626, p=0.01), as seen before (figure 4.19b and 4.19c). Consistent with the prior experiment, PD-L1 expression was increased in both disease sites (MFI 23354 *vs* 11079, p<0.0001) (figure 4.19d).

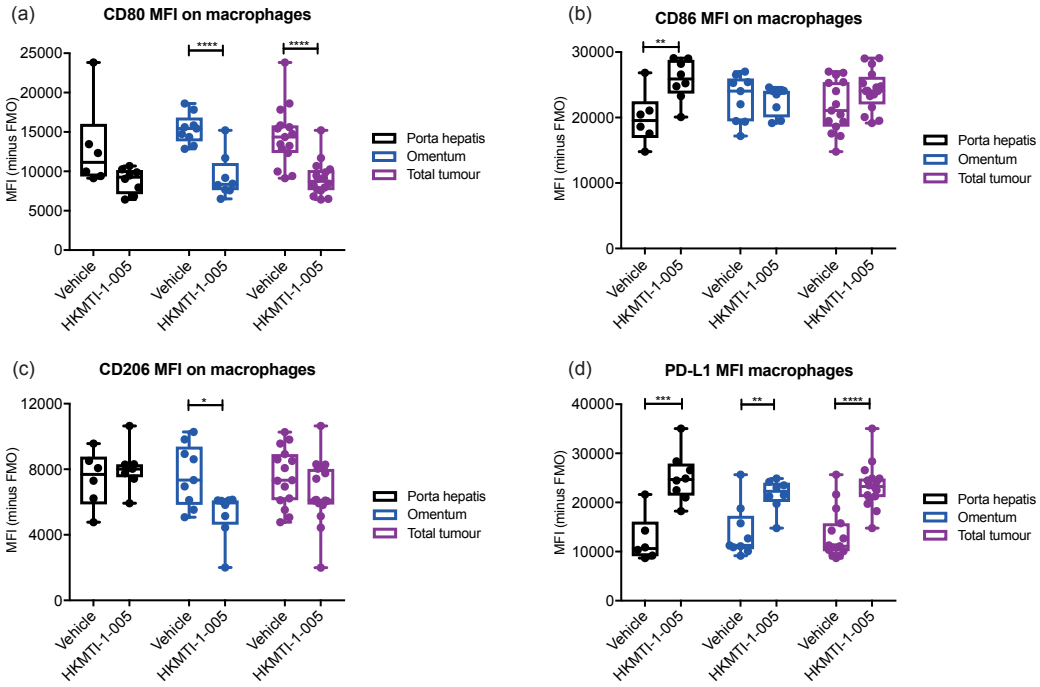

Figure 4.19: Flow cytometry results at porta hepatis and omental tumours after treatment with HKMTI-1-005; cell membrane markers on myeloid cells - macrophages. Quantification of TAMs receptor expression for CD80 (a), CD96 (b), CD206 (c) and PD-L1 (d) between treated/untreated in porta hepatis and omental deposits. Student's *t*-test was used for all comparisons apart from total tumour PD-L1 and omental CD86 MFI, for which Mann-Whitney test was used instead.

Unexpectedly, CD80 did not follow the upward trend of CD86 receptor; on the contrary, it was decreased in the omental deposit with treatment (MFI 9321 ± 999 *vs* 15397 ± 636, p<0.0001) (figure 4.19a).

In DCs, the changes seen reflected some of the changes seen in TAMs, with CD86 expression being higher with treatment in the omental deposit (MFI 22251 ± 1140 *vs* 15808 ± 647, p=0.0001) and CD206 showing a trend in being lower in both disease sites (MFI 4291 ± 284 *vs* 5192 ± 247, p=0.02) (figure 4.20b and 4.20c).

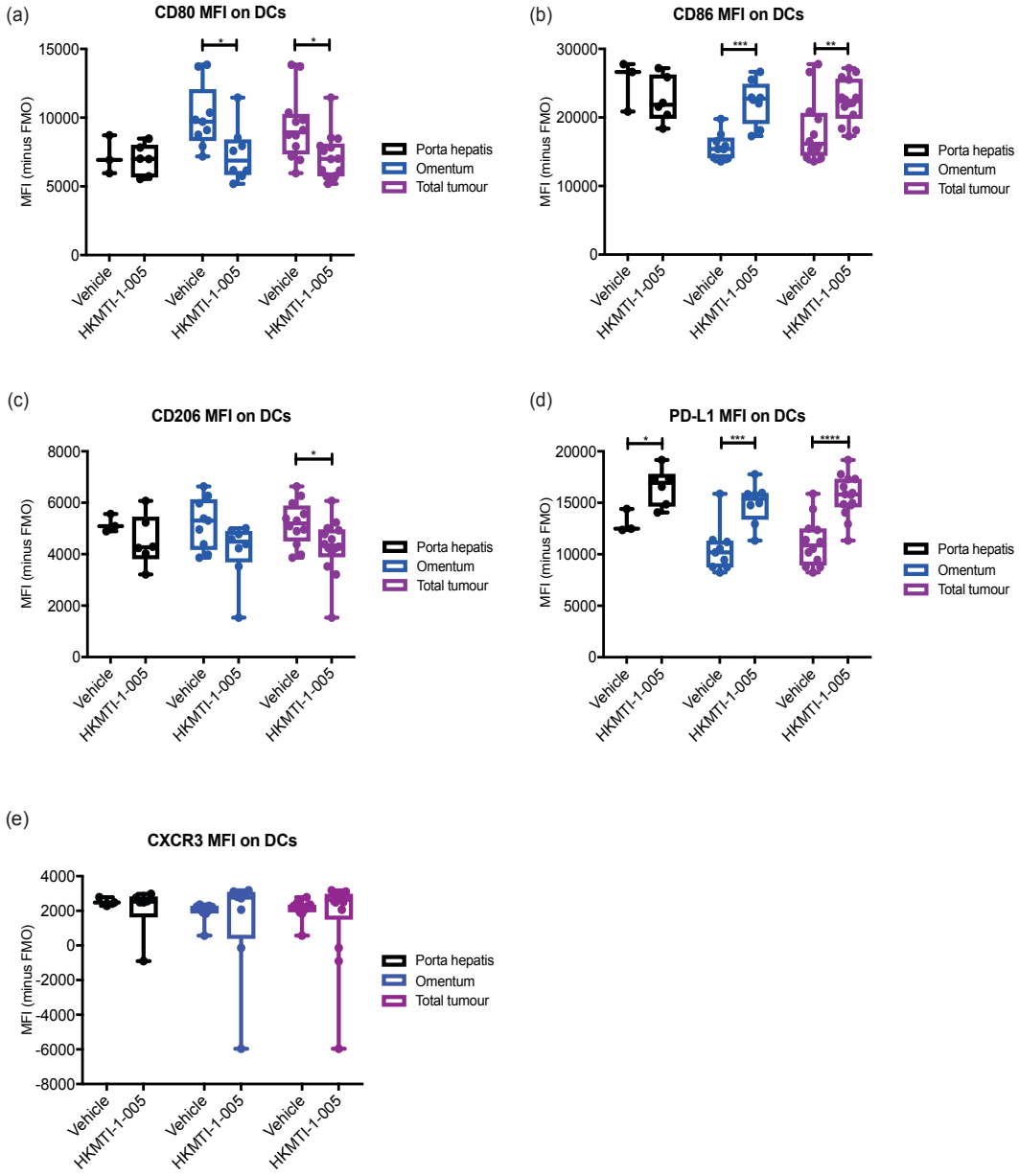

Figure 4.20: Flow cytometry at porta hepatis and omental tumours after treatment with HKMTI-1-005; cell membrane markers on myeloid cells – dendritic cells. Quantification of DCs receptor expression for CD80 (a), CD96 (b), CD206 (c), PD-L1 (d) and CXCR3 (e) between treated/untreated in porta hepatis, omental deposits and in total. Student's *t*-test was used for all mean comparisons apart from the comparison of CXCR3 for both sites, where Mann-Whitney test was used.

As seen in TAMs, CD80 expression decreased (MFI 7173 ± 444 *vs* 9341 ± 705, p=0.01; figure 4.20a) with treatment, whereas PD-L1 expression was significantly increased in all disease sites (MFI 15620 ± 542 *vs* 11141 ± 676, p<0.0001; figure 4.20d). Interestingly, the expression of CXCR3 which showed an overall increase in the lymphoid population, was not increased in the surface of DCs (figure 4.20e). PD-L1 expression in non-immune cells ($CD45^-$ cells was again significantly increased with treatment (MFI 3721 *vs* -1075, p<0.0001; figure 4.19d).

4.4.3 Flow cytometry - spleen and peritoneal wash

Given the significance of the peritoneal cavity in the dissemination of ovarian HGSC, I sought to investigate if HKMTI-1-005 treatment modulates the immune cellularity of the peritoneal fluid. Previous experiments showed that HKMTI-1-005 results in complete inhibition of ascites development. Therefore, I characterised immune cells in the peritoneal cavity by performing a peritoneal lavage. Moreover, I investigated potential changes within the murine spleen, as an important secondary lymphoid organ where lymphocyte storage and priming occurs. Because of the changes that I had previously observed on NK cells, I characterised them more thoroughly and introduced NK1.1 cell surface marker during flow cytometry analysis. NK cells were defined as $CD3^-DX5^+NK1.1^+$.

The treatment regimen used in this experiment is described in figure 4.8a. At the end of treatment, the peritoneal wash and spleens were subjected to flow cytometry, whereas the omental tumours were used for next-generation sequencing (described in Chapter 5).

Once again, $CD3^+$, $CD8^+$ and $CD19^+$ populations were overall unchanged and the $CD4^+$ population was decreased (0.01 $x10^6$ cell/g *vs* 0.02 $x10^6$ cell/g, p=0.01; figure 4.21a) in the treatment cohort. I observed that, as with tumour deposits, NK cells were increased with HKMTI-1-005 treatment (0.03 $x10^6$ cell/g *vs* 0.01 $x10^6$ cell/g, p=0.006; figure 4.21a) and the immunosuppressive population of

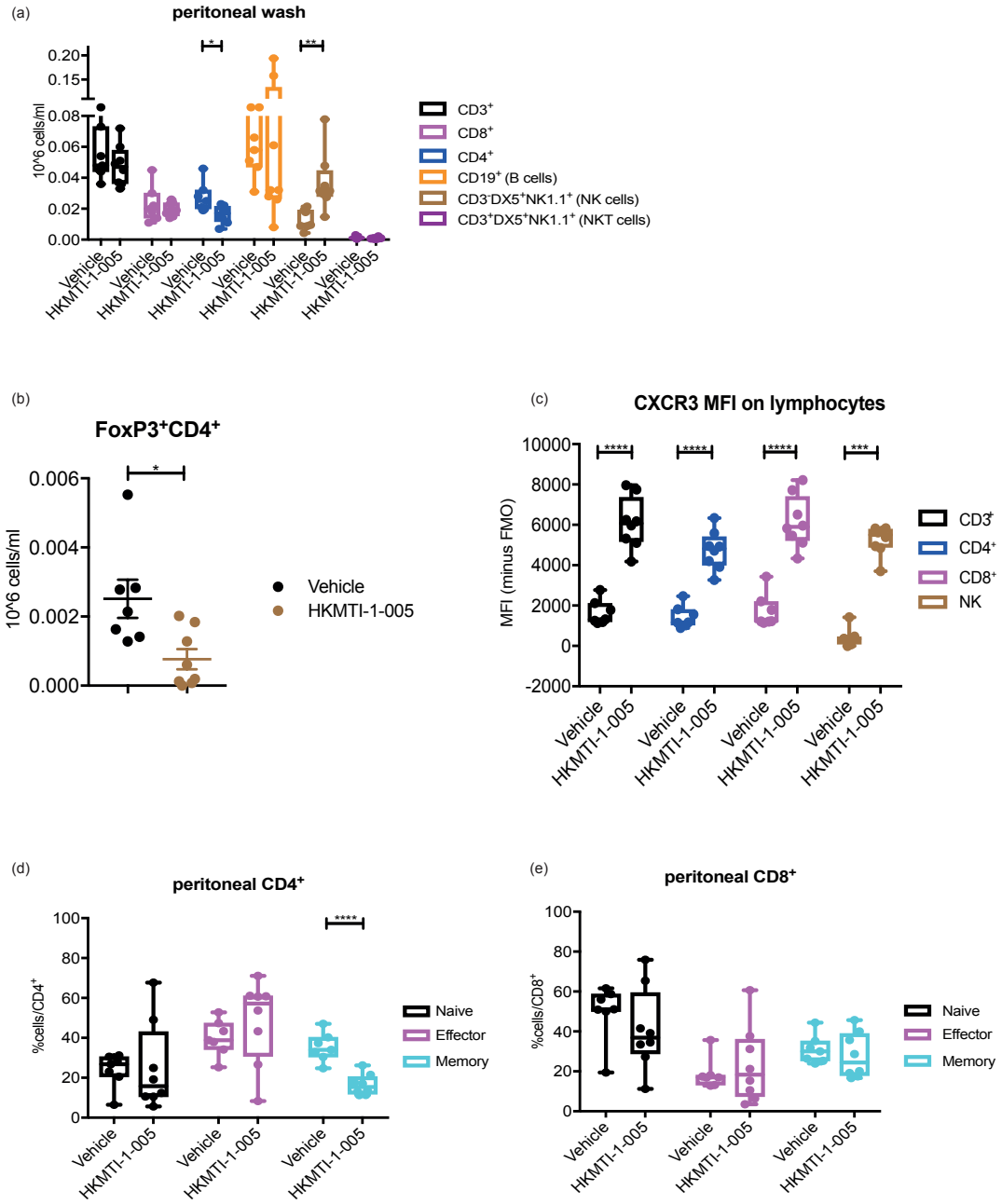

Figure 4.21: Flow cytometry results in peritoneal wash after treatment with HKMTI-1-005 – cell populations, CXCR3 expression and lymphoid subpopulations. Quantification of lymphocyte population (a) and FoxP3$^+$CD4$^+$ cells (b) in the peritoneal wash; means were compared with student's *t*-test. (c) CXCR3 MFI on CD3$^+$, CD4$^+$, CD8$^+$ and NK cells in the peritoneal wash; student's *t*-test was used for all comparisons apart from NK cells, where Mann-Whitney test was used. (d) and (e) show the naïve, effector and memory sub-populations of CD4$^+$ and CD8$^+$ cells; Student's t-test was used for all comparisons apart from naïve and effector peritoneal CD8$^+$ cells.

FoxP3$^+$CD4$^+$ cells were decreased (7 x10^2 cell/g *vs* 25 x10^2 cell/g, p=0.01; figure 4.21b).

As previously observed, HKMTI-1-005 increased expression of CXCR3 receptor on CD3$^+$ (MFI 6087 ± 453 *vs* 1653 ±231, p<0.0001), CD4$^+$ (MFI 4738 ± 339 *vs* 1438 ± 210, p<0.0001), CD8$^+$ (6144 ± 459 *vs* 1746 ± 318, p<0.0001) and NK cells (MFI 5509 *vs* 343, p=0.0003) (figure 4.21c).

Overall, treatment did not have an effect on the naïve, effector or memory phenotype of CD8$^+$ cells in the peritoneal cavity (figure 4.21e). CD4$^+$ memory cells, however, were decreased with treatment (16.4% *vs* 35.2%, p<0.0001), with the rest of the sub-populations remaining widely unchanged (figure 4.21d). There was no increase in the intracellular content of IFNγ, granzyme B or perforin chemokines in cytotoxic CD8$^+$ cells (figure 4.22a), however, the IFNγ-containing NK cells were significantly more in the peritoneal cavity of treated mice (62.5% ± 3.9 *vs* 27.5% ± 7.2, p=0.001; figure 4.22b) compared to untreated.

I observed a new population of MHCII medium TAMs that I had not observed in the tumour deposit flow analysis (figure 4.11b). Therefore, I analysed these two population separately as MHCII high and MHCII medium expression (MHCII^{high} and MHCII^{med}) and looked into whether they maintain the Ly6C marker. There was an increase in the number of MHCII^{med} macrophages with HKMTI-1-005 treatment (0.1 x10^6 cell/g ± 0.02 *vs* 0.01 x10^6 cell/g ± 0.001, p=0.0009; figure 4.22a), whereas the MHCII^{high} TAMs remained unchanged. Irrespective of the expression of MHCII marker, peritoneal macrophages, once again, remained highly positive for Ly6C, as seen in tumour deposits. (Ly6C$^+$MHCII^{high} 0.07 x10^6 cell/g ± 0.013 *vs* 0.01 x10^6 cell/g ± 0.002, p=0.001 and (Ly6C$^+$MHCII^{med} 0.13 x10^6 cell/g *vs* 0.002 x10^6 cell/g, p=0.0003) (figure 4.22d and 4.22f).

In the spleen, the numbers of main lymphocyte populations were not altered with treatment (figure 4.23a). However, the naïve and effector CD4$^+$ subpopulations increased significantly with HKMTI-1-005 treatment (naïve 12.8% ± 1.7% *vs* 7.7% ± 0.3%, p=0.01; effector 21.6% ± 0.7% *vs* 18.2% ± 0.3%, p=0.002),

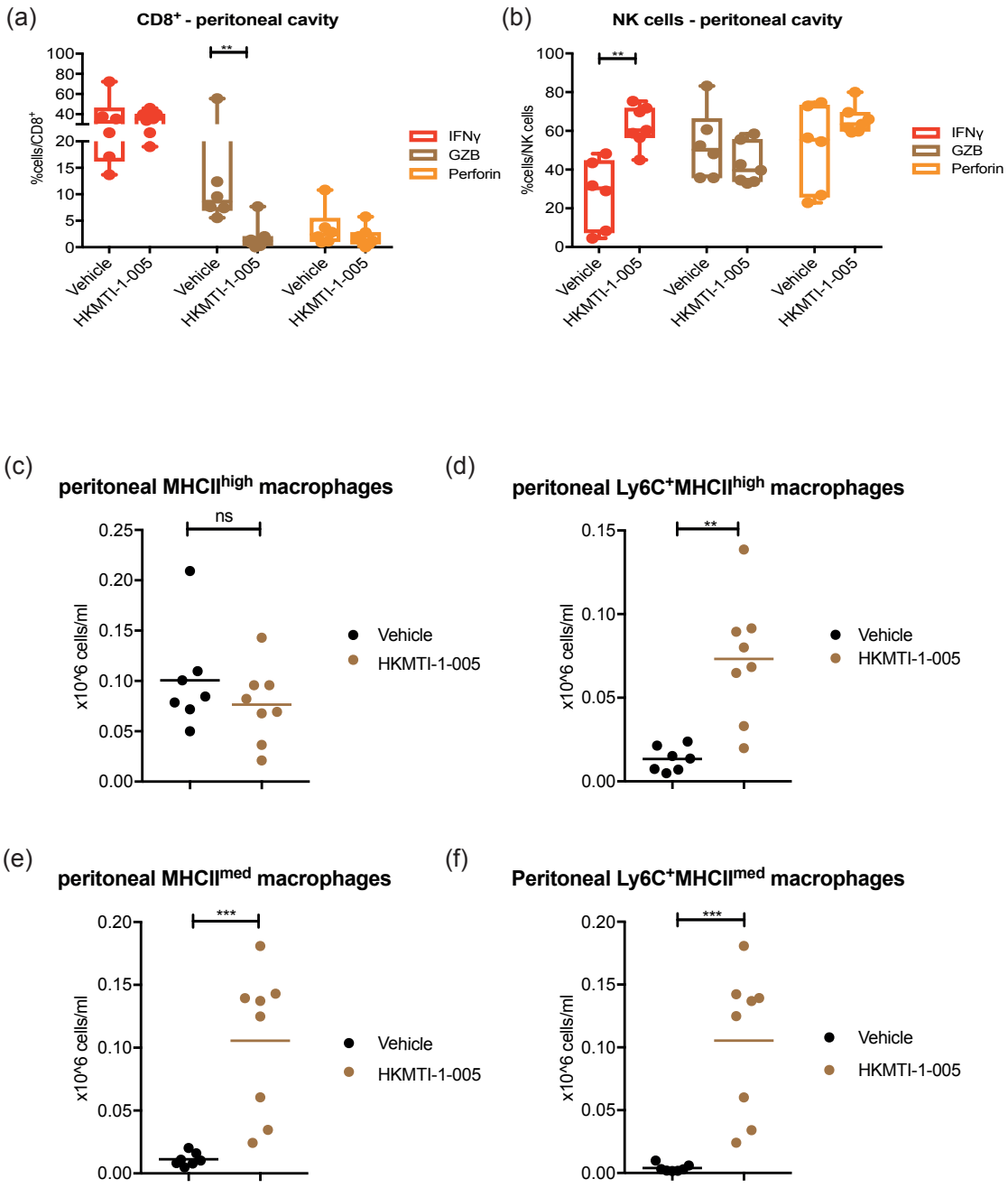

Figure 4.22: Flow cytometry results in peritoneal wash after treatment with HKMTI-1-005; intracellular chemokines, Ly6C and MHCII on macrophages. Quantification of the chemokine-containing CD8⁺ (a) and NK (b) cells in the peritoneal wash; Student's *t*-test was used for all comparisons apart from granzyme-B containing CD8⁺ cells, where Mann-Whitney test was used. (c), (d), (e) and (f) quantification of TAM sub-populations in the peritoneal wash; all comparisons were made by Student's *t*-test, apart from (f) where Mann-Whitney test was used.

whereas memory $CD4^+$ decreased (64.4% ± 1.7% *vs* 73.6% ± 0.6%, p=0.0005) (figure 4.23b). Moreover, the effector $CD8^+$ population increased significantly with treatment (3.55% *vs* 2.46%, p=0.009; figure 4.23c).

Overall, the $CD8^+$ population found in the spleen had more cells containing IFNγ (22.1% *vs* 18.1%, p=0.01) and perforin (10.2% ± 0.9% *vs* 5.9% ± 0.8%, p=0.004), (figure 4.23d), and the NK cells contained more granzyme-B (58.4% ± 2.5% *vs* 43.9% ± 3.9%, p=0.007; figure 4.23e).

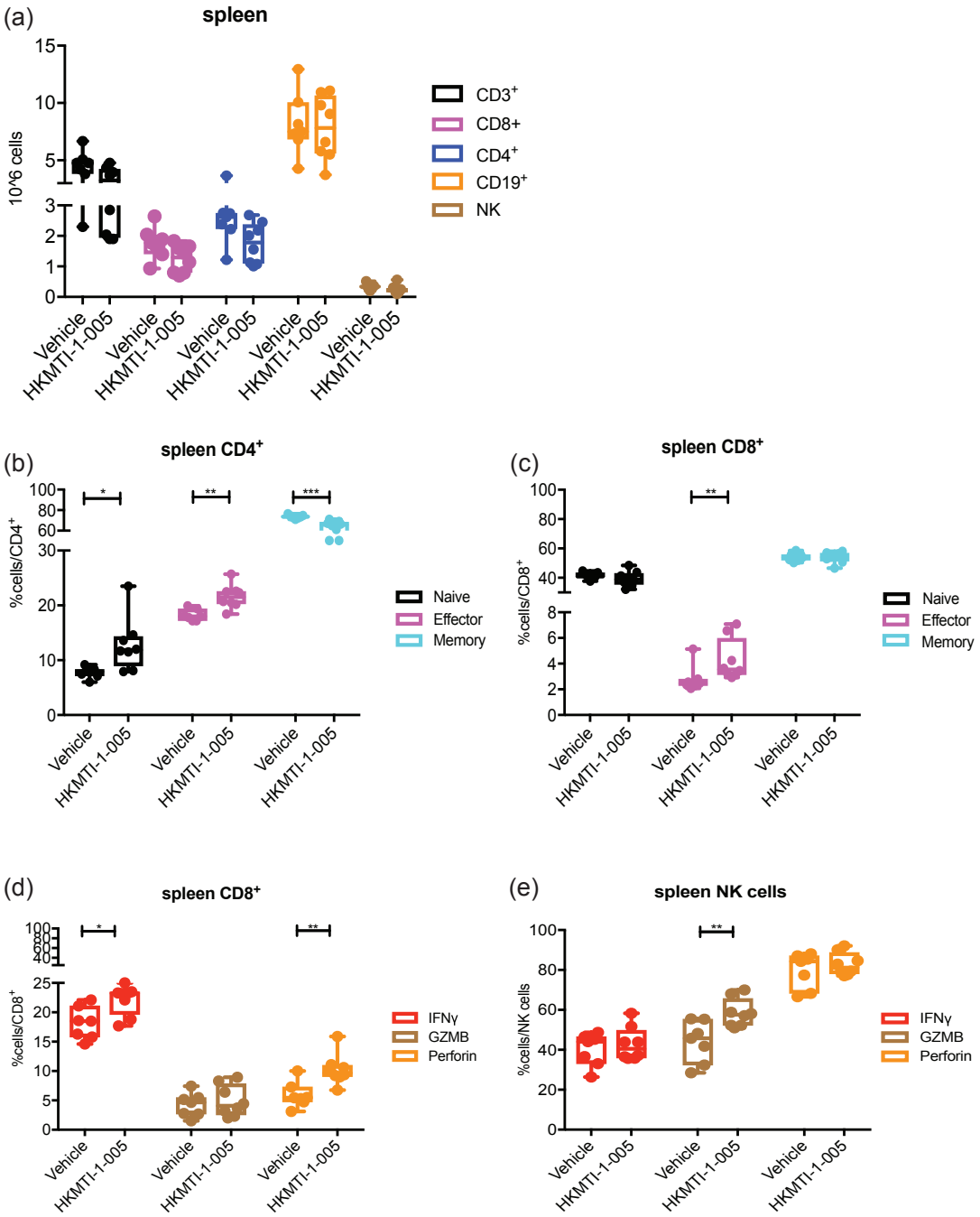

Figure 4.23: Flow cytometry results in the spleen after treatment with HKMTI-1-005; cell populations, lymphoid subpopulations and intracellular chemokines. Quantification of $CD4^+$ (a) and $CD8^+$ (b) naïve, effector and memory sub-populations in the spleen. All mean comparisons were done with Student's t-test, apart from the effector $CD8^+$ cells mean which were compared with the Man-Whitney test. Percentages of chemokine-containing $CD8^+$ (c) and NK cells (d) in the spleen for IFNγ, granzyme-B and perforin; Student's *t*-test was used for all mean comparisons.

4.4.4 Chemokine production *in vivo*

I next investigated if the changes seen in chemokines *in vitro* with HKMTI-1-005 treatment were also observed *in vivo*. I also wanted to see if the upregulation of CXCR3 by flow cytometry *in vivo* is accompanied with an increase in its ligands CXCL9 and CXCL10. RT-qPCR in omental tumours treated with HKMTI-1-005 (described in figure 4.8a), showed an increase in *Cxcl10* (fold change 2.9 ± 0.3 *vs* 1.2 ± 0.2, p=0.0003). Additionally, I observed a significant increase in *Ccl5* (fold change 3.4 *vs* 0.9, p=0.0019) and a trend for HKMTI-1-005 to increase *Ccl12* (fold change 1.8 *vs* 0.9, p=0.11) and *Ccl19* (fold change 1.6 ± 0.3 *vs* 1.2 ± 0.2, p=0.3), chemokines which were also significantly elevated *in vitro* (figure 4.24).

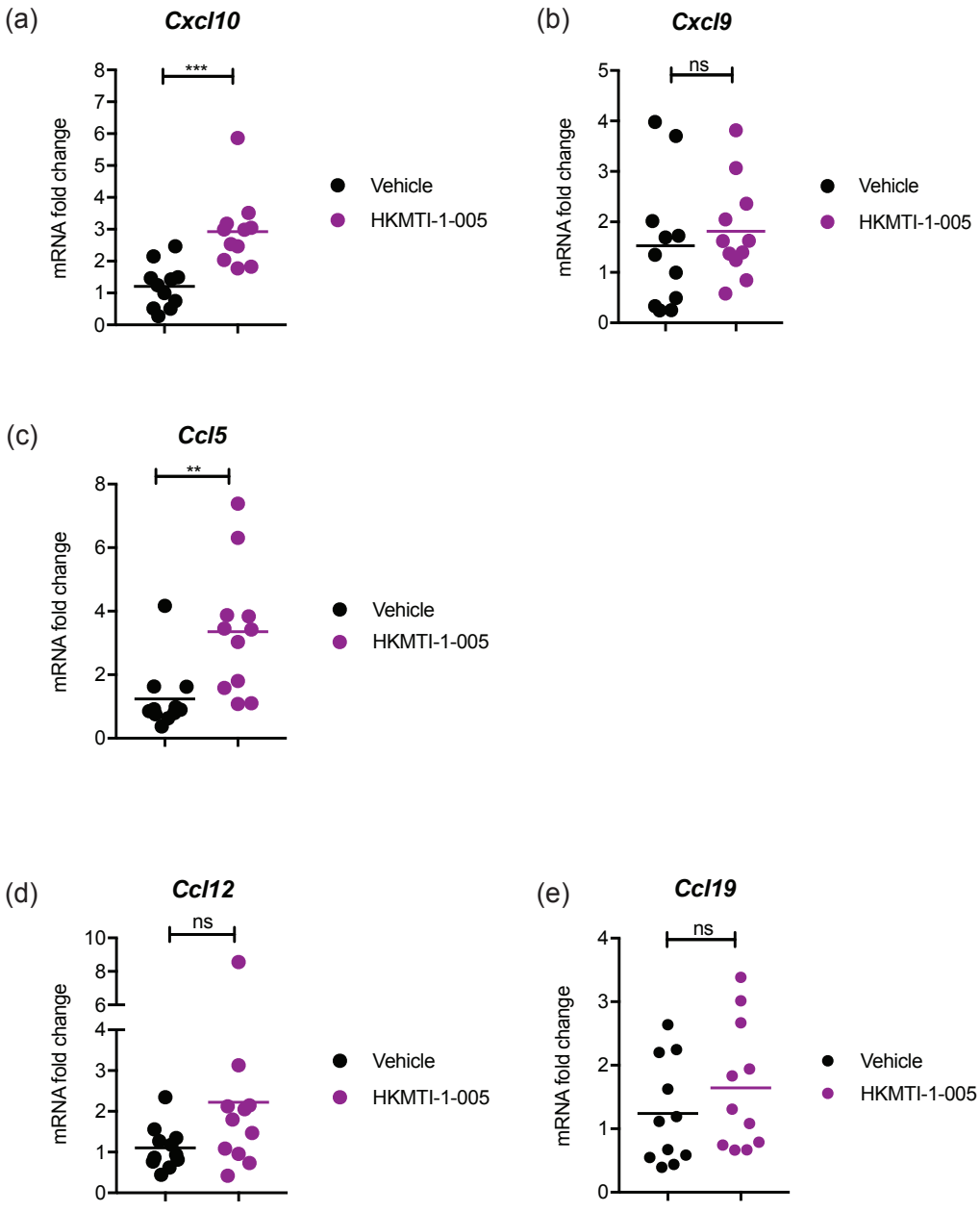

Figure 4.24: Intratumoral chemokine expression after treatment with HKMTI-1-005; RT-qPCR for *Cxcl10* (a), *Cxcl9* (b), *Ccl5* (c), *Ccl12* (d) and *Ccl19* (e) genes in omental tumours of untreated and HKMTI-1-005-treated mice (n=11 per cohort). Each dot represents one mouse. Student's t-test was used for comparing *Cxcl10, Cxcl9* and *Ccl19* chemokines. Mann-Whitney test was used for comparing *Ccl5* and *Ccl12* chemokines.

4.5 Dual G9a/EZH2 inhibition combined with either PD-1 blockade or cisplatin treatment *in vivo*

4.5.1 HKMTI-1-005 upregulates PD-L1 expression on tumour cells *in vitro*; it reduces tumour burden but does not confer survival advantage when combined with PD-1 blockade *in vivo*

In vitro, treatment with HKMTI-1-005 upregulated the expression of PD-L1 on IFNγ stimulated *Trp53*$^{-/-}$ ID8 cells, by flow cytometry (MFI 1946 *vs* 180, p<0.0001; figure 4.25a and 4.25b), confirming the results in the CD45^{-} cell population of mouse tumour deposits *in vivo* (figure 4.12d and 4.18d). RT-qPCR confirmed that *PD-L1* transcript is maximally upregulated in IFNγ stimulated *Trp53*$^{-/-}$ ID8 cells after 24 hours (fold change 54.2 ± 1.7 *vs* 21.3 ± 1.0, p<0.0001; figure 4.25c).

On the basis that HKMTI-1-005 modulated the immune microenvironment in tumour deposits and it also upregulated PD-L1 expression *in vitro*, I next combined HKMTI-1-005 with PD-1 blockade, to examine the effect of the combination treatment on survival of mice bearing *Trp53*$^{-/-}$ ID8 tumours.

The anti-PD1 antibody (clone RMPI-14, BioXcell, BE0146) was kindly provided by Dr Roxburgh's lab. The treatment regimen involved starting HKMTI-1-005 one week before the anti-PD-1 antibody (figure 4.25d). Mice were then allowed to reach humane endpoint. In order to comply with the principles of 3Rs, I decided to not repeat treatment with HKMTI-1-005 alone in this experiment, given that this had been done before.

Median survival did not differ between the three treatment cohorts (median survival 45 days for all groups, p=0.49; figure 4.26a). There was a trend for reduction of hazard ratio with the combination of anti-PD1 plus HKMTI-1-005 (HR 0.71, 95% CI 0.19-2.5) but this was not statistically significant. Interestingly, 2 mice in the combination cohort had prolonged survival, with one of them

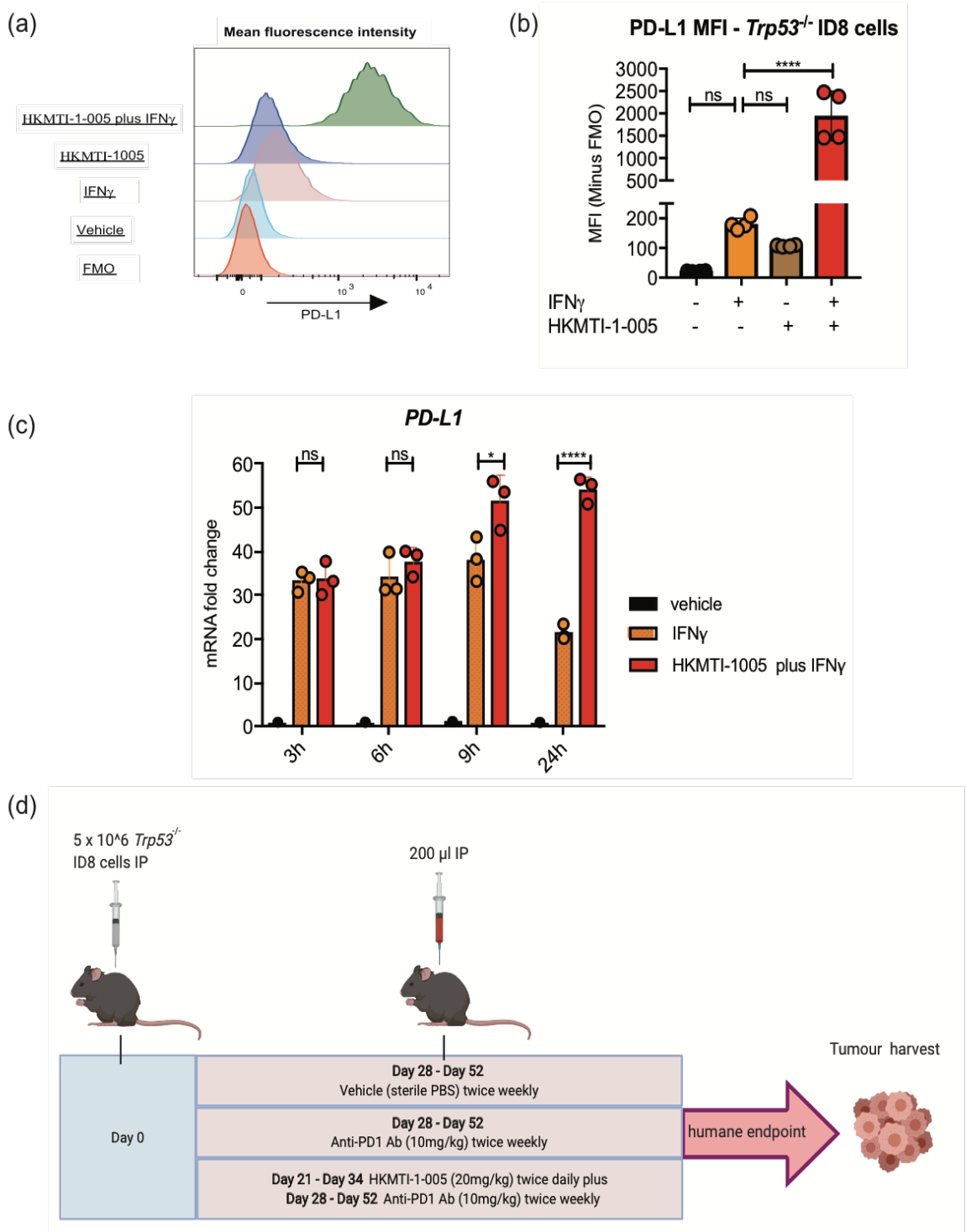

Figure 4.25: PD-L1 on ID8 *Trp53*$^{-/-}$ cells *in vitro* and schematic of *in vivo* experiment with PD1 antibody plus HKMTI-1-005 treatment. (a) Representative histogram of PD-L1 MFI (n=1) and (b) Quantification of PD-L1 MFI on *Trp53*$^{-/-}$ ID8 cells, (n=4), means compared with one-way ANOVA (c) RT-qPCR for *PD-L1* on *Trp53*$^{-/-}$ ID8 cells at various timepoints, (n=3). Student's *t*-test used for all comparisons apart from the 6-hour comparison between IFNγ and HKMTI-1-005/IFNγ, where Mann-Whitney test was used. Error bars reflect standard deviation. (d) Treatment regimen in survival experiment comparing vehicle to anti-PD1 mAb and the combination of anti-PD1 mAb plus HKMTI-1-005. MFI: mean fluorescence intensity; mAb: monoclonal antibody.

surviving for 59 days and the other mouse surviving for 85 days (7 and 33 days after the end of anti-PD1 treatment, respectively). Both mice had developed tumour deposits when examined at endpoint.

The volume of ascites did not differ significantly between cohort (figure 4.26b), but the total tumour weight for the combination group was significantly lower than the group receiving anti-PD1 antibody alone (175.6 mg *vs* 277.1mg, p=0.007; figure 4.26c) and also lower than the vehicle group (175.6mg *vs* 256.2mg, p=0.04). This was due to a significant reduction in omental tumour weight in the combination group; in the porta hepatis, only a trend to reduction was observed (figure 4.26e and 4.26d). Blood results at endpoint did not show any significant differences between cohorts (Appendix 11.0).

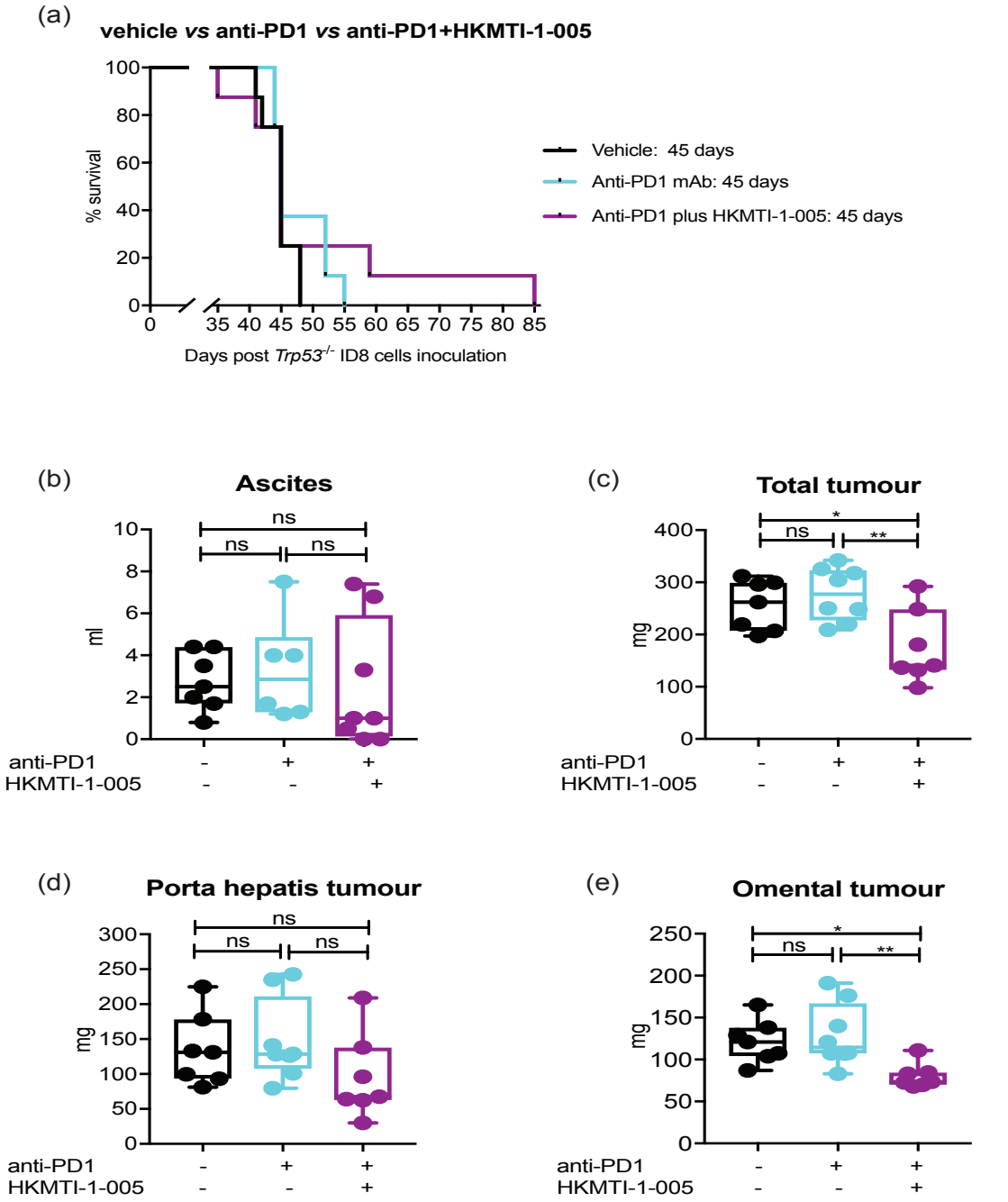

Figure 4.26: Results of *in vivo* survival experiment with anti-PD1 plus HKMTI-1-005 treatment (a) Survival curves of mice treated with vehicle or anti-PD1 Ab or anti-PD1 Ab plus HKMTI-1-005 (n=8 per group). Median survival did not differ between groups, using the Log-rank test for comparison. (b) ascites volume and (c) total tumour weight at humane endpoint. Break-down of total tumour weight in porta hepatis (d) and omental deposit (e). All comparisons in (b), (c), (d) and (e) were made with ordinary one-way ANOVA and Tukey's multiple comparison test. Each dot represents one mouse and error bars represent standard devation. Discrepancies between group numbers in ascites and tumour graphs are related to technical problems of harvesting tumour/ascites at endpoint.

4.5.2 Adding HKMTI-1-005 to cisplatin treatment does not result in additional tumour regression

Thereafter, I examined the combination of HKMTI-1-005 with a platinum compound (cisplatin), which has been the standard of care in ovarian HGSC for decades. My hypothesis was that tumour cell death caused by cisplatin could release tumour-associated antigens, which in turn could increase antigenicity and enhance the immunostimulatory effect of HKMTI-1-005. Recently emerging data from patient samples show that neo-adjuvant chemotherapy with platinum induces Th1 immune responses and reduces Treg in ovarian tumours (441). Given that this animal experiment was conducted in a new animal unit and that I was using a new batch of the HKMTI-1-005 compound, I decided to include a new cohort of HKMTI-1-005 treated mice in order to re-evaluate the median survival (figure 4.27a).

Surprisingly, in this experiment, HKMTI-1-005 did not confer a survival advantage and the mice treated with HKMTI-1-005 had a median survival of only 1.5 days longer than vehicle (51.5 days *vs* 50 days, p=0.42; figure 4.27b). Cisplatin extended median survival to 71 days which was significantly different than vehicle or HKMTI-1-005 and in keeping with the survival advantage seen before in this model (442). Adding HMTI-1-005 to cisplatin did not achieve a significant prolongation (72 days *vs* 71 days, p=0.01; figure 4.27b), in terms of median survival. However, it reduced the hazard ratio to 0.25 (95% CI 0.07-0.89, Mantel-Haenszel test, p=0.01). This indicates that there is an effect on reducing the risk of death, when compared to cisplatin alone. Ascites was not statistically different between groups. Nevertheless, the combination of cisplatin with HKMTI-1-005 resulted in a significant reduction in total tumour weight, when compared to vehicle (45.5 mg *vs* 80.9 mg, p=0.01; figure 4.27d). Tumour weight in the combination treatment overall follows the same reducing trend in porta hepatis and omental deposit (figure 4.27e and figure 4.27f), however, rather disappointingly, this is not different than the tumour reduction achieved by cisplatin or HKMTI-1-005 monotherapy alone.

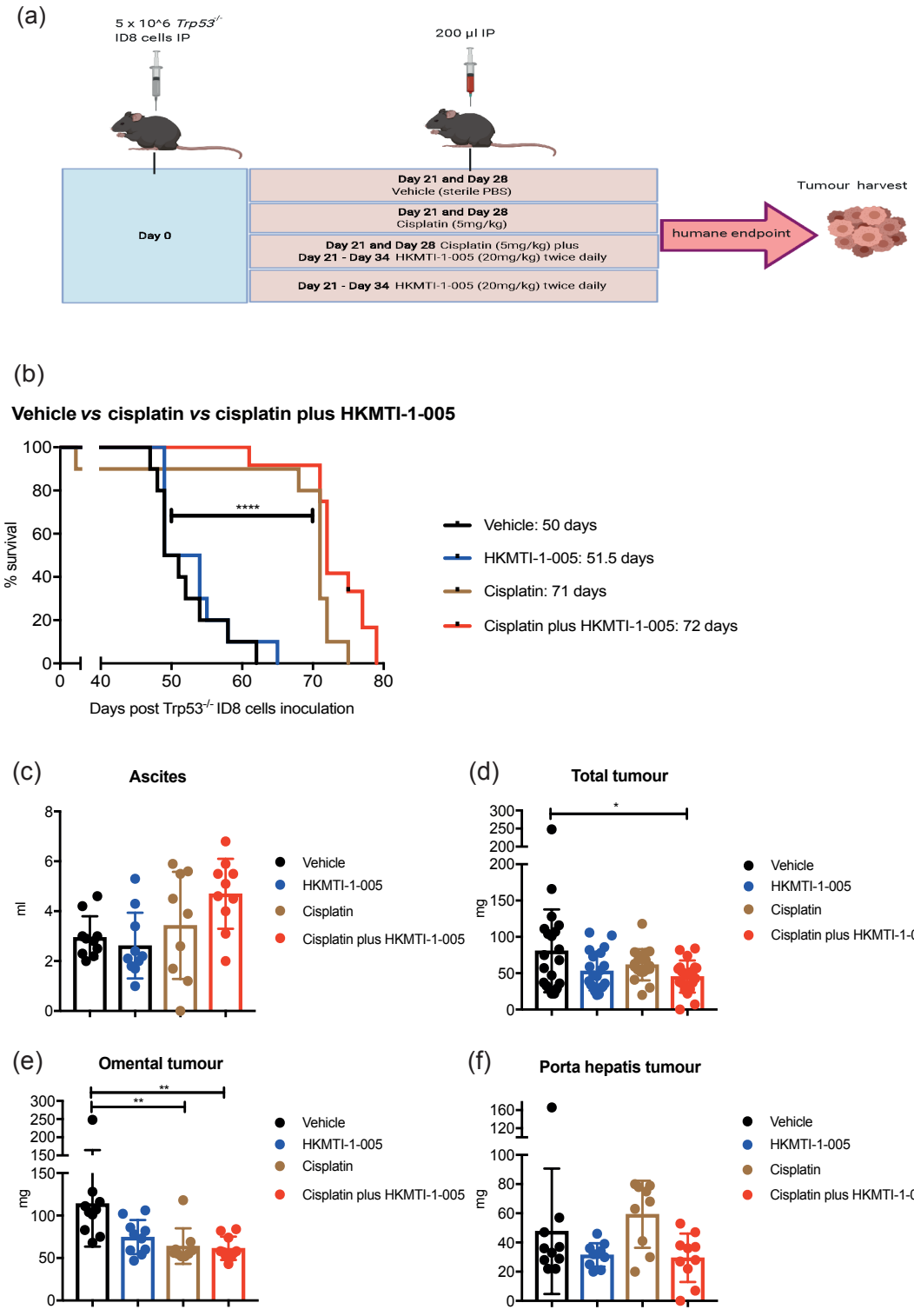

Figure 4.27: Survival experiment with cisplatin plus HKMTI-1-005 treatment. (a) Schematic of treatment regimen and experiment methodology, (n=10 mice per group), (b) Survival curves of mice treated with vehicle, HKMTI-1-005, cisplatin or cisplatin plus HKMTI-1-005; note that one event occuring as early as 31 days in the cisplatin group relates to one mouse which was culled due to toxicity (weight loss> 20% from baseline); this was not included in the survival analysis. Median survival was compared using the Log-rank test. (c) ascites volume and (d) total tumour weight at humane endpoint between the four groups. Break-down of total tumour weight in omental (e) and porta hepatis deposit (f). Comparisons in (c) and (d) were made using the Kruskal-Wallis test

Figure 4.27: Survival experiment with cisplatin plus HKMTI-1-005; continued. And Dunn's multiple comparisons test, whereas in (e) and (f), using ordinary one-way ANOVA and Tukey's multiple comparisons test. Differences that were statistically non-significant are not annotated on this graph. Each dot represents one mouse; discrepancies between group numbers in ascites and tumour graphs are related to technical problems in harvesting tumour/ascites at endpoint.

4.6 NK cell depletion in vivo

Given that the changes seen in the NK cell population with HKMTI-1-005 treatment were more consistent across experiments and sites (see figures 4.13b, 4.14e, 4.21a, 4.22b and 4.23e), I next investigated the effect of NK cell depletion on the activity of HKMTI-1-005 *in vivo*. My hypothesis was that, if HKMTI-1-005 does indeed induce an immune-related anti-tumour effect via NK cell activation, then this would be obliterated when NK cells are depleted.

To deplete murine NK cells *in vivo*, I used a monoclonal antibody (mAb) against NK1.1 (clone PK136, BioXcell, BE0036) and an IgG2a mAb as isotype control. In order to adhere to the 3Rs principles, the HKMTI-1-005 cohort is common between this experiment and the experiment with cisplatin treatment (section 4.5.2).

To determine whether NK depletion was achieved, flow cytometry was performed at three different timepoints: after the first 2 loading doses of anti-NK1.1 mAb in murine blood and spleen (figure 4.29a/4.29b), at the trough timepoint of the weekly regimen in blood (i.e. one day before the regular anti-NK1.1 mAb dose; figure 4.29c) and in the tumour/ascites at endpoint (figure 4.30). Results confirmed that treatment with anti-NK1.1 mAb depleted NK cells in all samples, at all three timepoints.

As depicted in figure 4.28b, there were no statistically significant differences between the median survival of the 4 groups (IgG2a median survival 52 days *vs* HKMTI-1-005 51.5 days *vs* anti-NK1.1 mAb 51 days *vs* HKMTI-1-005 plus anti-NK1.1 mAb 55.5 days, p=0.92).

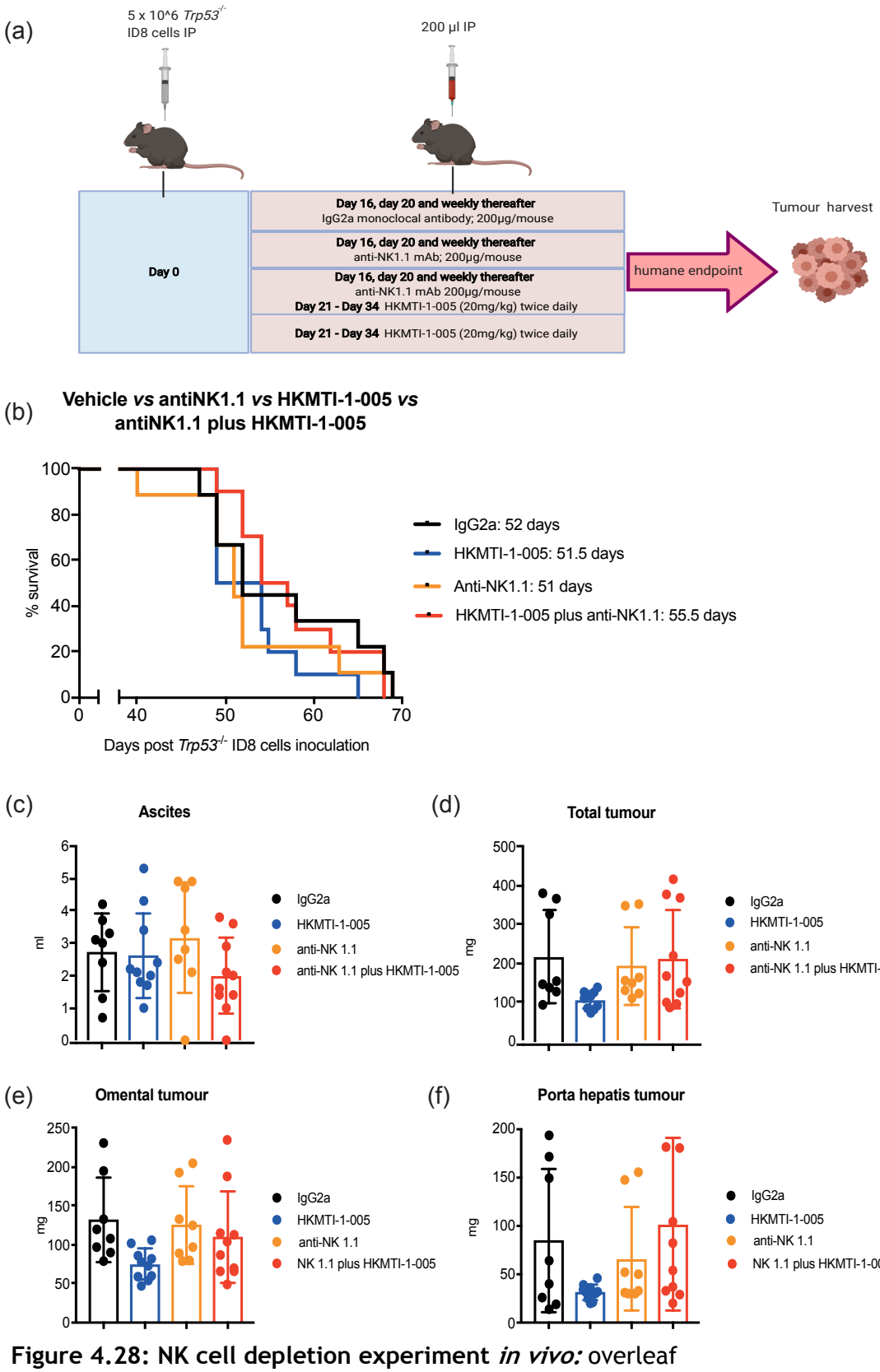

Figure 4.28: NK cell depletion experiment *in vivo:* overleaf

Figure 4.28: NK cell depletion experiment *in vivo* (a) Schematic of treatment regimen and experiment methodology, (n=10 mice per group), treatment as per graph; note that 1 mouse from each group of IgG2a and anti-NK1.1 mAb treatment were culled before starting HKMTI-1-005 treatment to perform flow cytometry on their spleens and confirm NK cell depletion; these mice were not included in the survival analysis (b) Survival curves of mice treated with IgG2a isotype control, HKMTI-1-005, anti-NK1.1 mAb or anti-NK1.1 mAb plus HKMTI-1-005; median survival was compared using the Log-rank test; none of the comparisons were statistically significant. (c) ascites volume and (d) total tumour weight at humane endpoint between the four groups. Break-down of total tumour weight in omental (e) and porta hepatis deposit (f). All comparisons in (c), (d), (e), (f) were made using ordinary one-way ANOVA and Tukey's multiple comparisons test. Differences that were statistically non-significant are not annotated on this graph. Each dot represents one mouse; discrepancies between group numbers in ascites and tumour graphs are related to technical problems in harvesting tumour/ascites at endpoint.

Similarly, there were no statistically significant differences in tumour burden, both in term of ascites volume and total tumour weight at humane endpoint. However, there was a clear trend for HKMTI-1-005 to inhibit tumour growth compared to treatment with either IgG2a, anti-NK1.1, or the combination of HKMTI-1-005 and anti-NK1.1 mAb (106.2mg *vs* 216.1mg, p=0.11; *vs* 191.1mg, p=0.29; *vs* 210.3mg, p=0.11). This could signify that NK cell depletion inhibits the HKMTI-1-005 mediated anti-tumour effect. However, these results are not statistically significant and furthermore, they are not supported by the survival results of this experiment.

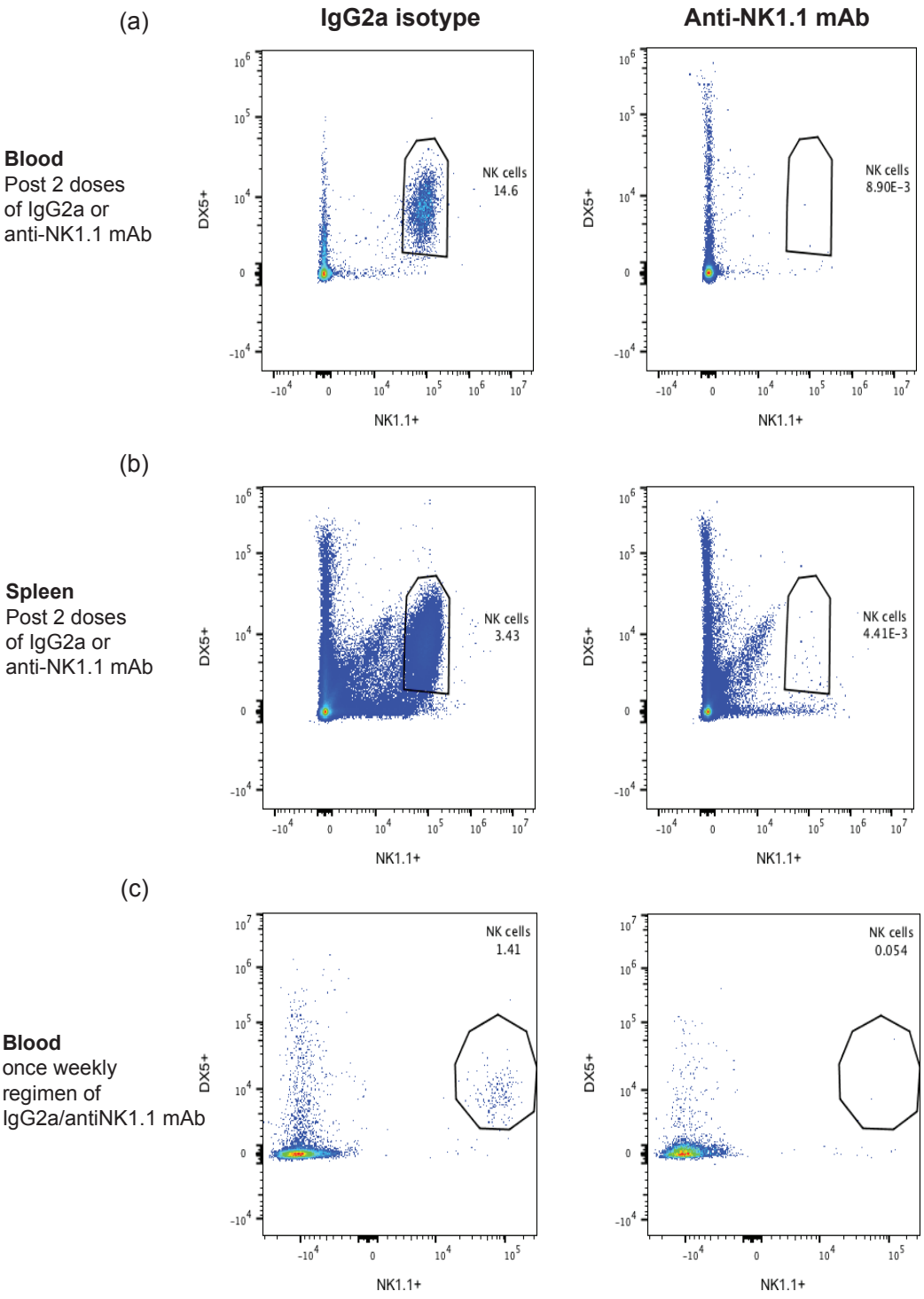

Figure 4.29: Confirmation of NK cell depletion by flow cytometry - blood and spleen. Flow cytometry for NK cell population, defined as double positive for $DX5^{+}NK1.1^{+}$ (n=1) between treatment with IgG2a isotype control (left panel) and anti-NK1.1 mAb (right panel) in blood (a) and spleen (b) after the first 2 loading doses (day -5 and day -1 before HKMTI-1-005 treatment) of IgG2a or anti-NK1.1 mAb. (c) NK cell population (n=1) between treatment with IgG2a and anti-NK1.1 mAb in blood during the weekly IgG2a/anti-NK1.1 mAb regimen; sample taken 24h before dosing. mAb=monoclonal antibody.

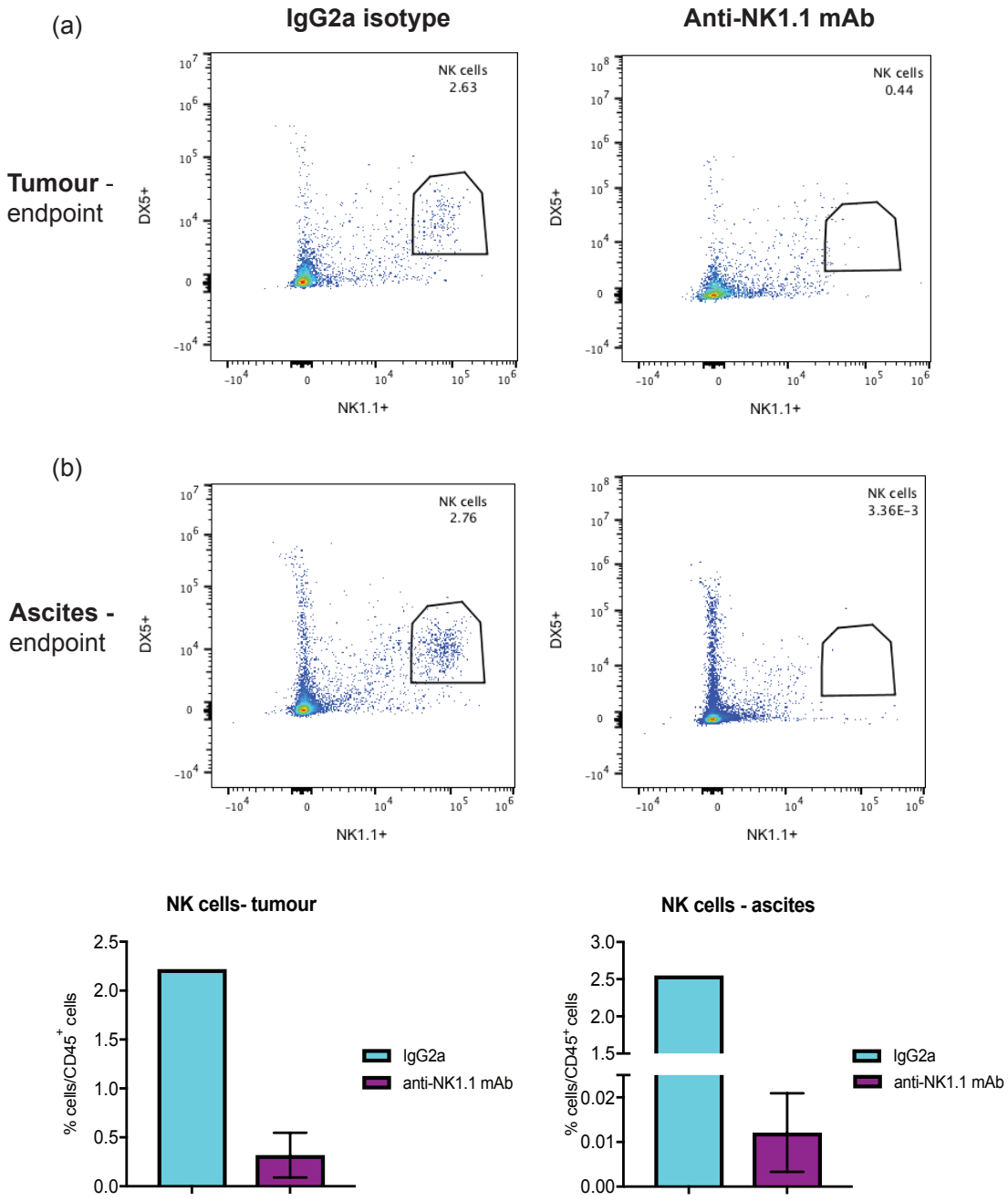

Figure 4.30: Confirmation of NK cell depletion by flow cytometry - tumour and ascites. Flow cytometry for NK cell population, defined as double positive for $DX5^{+}NK1.1^{+}$ (n=1) between treatment with IgG2a isotype control (left panel) and anti-NK1.1 mAb (right panel) in mouse tumour (a) and mouse ascites (b) at humane endpoint. (c) graphic representation of the average NK cell percentages, relative to the total $CD45^{+}$ population. Error bars represent standard deviation. Note that there is no error bar for the IgG2a cohort as n=2.

4.7 Discussion

After showing that G9a and EZH2 histone methyltransferases are involved in suppressing chemokine pathways in both murine and human ovarian cancer (chapter 3), I sought to investigate the effect of their inhibition on the tumour immune microenvironment and the survival of mice bearing *Trp53*$^{-/-}$ ID8 tumours. Results confirm that dual inhibition of G9a and EZH2 result in a moderate, albeit statistically significant prolongation of survival (1 week), which is superior to the one achieved with G9a inhibition alone.

Although G9a inhibition with UNC0642 resulted in a better survival compared to vehicle, flow cytometry analysis of intra-tumoral immune cell populations after a 5-day treatment did not show any meaningful differences or trends. This may

be due to the different treatment durations between the flow cytometry exploratory experiment (5-day treatment) and the survival experiment (2-week treatment).

At the time of conducting both these experiments, we knew that the dose of 5mg/kg was sufficient to inhibit G9a *in vivo* (367, 380). However, the optimum treatment duration had not been defined. Nevertheless, I considered the prolongation of survival by 3 days not to be supportive of conducting further experiments with UNC0642, and for this reason, my focus was transferred to dual inhibition of G9a and EZH2 with HKMTI-1-005.

Based on preliminary simulation PK studies with HKMTI-1-005, the dose used in all the *in vivo* work (20mg/kg) was not above the *in vitro* GI_{50} dose. This means that treatment would generate drug levels that are lower that a cytostatic/cytotoxic threshold. Despite this, HKMTI-1-005 had a favourable outcome on survival *in vivo* and this reinforces the hypothesis that HKMTI-1-005 inhibits tumour growth via immune clearance, rather than direct tumour cell killing.

The flow cytometry results, despite their variability, point towards changes that could mediate this immune clearance with HKMTI-1-005 treatment. I observed

an increase in cytotoxic chemokine producing NK cells across sites, an increase in effector $CD8^+$ cells and DCs and a reduction in immunosuppressive Tregs.

With treatment, CXCR3 was ubiquitously overexpressed in lymphocytes and CD86 in myeloid cells. Overall, we see an immunostimulatory microenvironment described by immune priming, T cell activation/cytotoxicity and eventually tumour growth inhibition.

With regards to the lymphocyte population, an increase in the total $CD3^+$ population, including both $CD8^+$ and $CD4^+$ cells, was initially observed in the porta hepatis deposit of *Trp53*$^{-/-}$ ID8 tumours. However, when this was re-tested in both porta hepatis and omental deposits, it was not confirmed. Instead, an increase in the effector $CD8^+$ subpopulation (with concomitant decrease in naïve $CD8^+$ cells) was observed which was accompanied by an increase in granzyme B producing $CD8^+$ cells. It is likely that the results of the initial experiment represent an earlier phase of the immune cycle when we observe increased overall numbers of $CD4^+$ and $CD8^*$ populations without the phenotypic change to effector/memory subtype having happened yet, hence the absence of high chemokine content. On the contrary, results of later experiments represent a phase where, despite the unchanged numbers of $CD8^+$ overall, an increase in the effector subpopulation is observed, with a higher content of intracellular chemokines and hence a higher cytotoxic potential. Interestingly, the $CD4^+$ population overall showed a downward trend across later experiments, which could only partially be explained by a reduction in $FoxP3^+$ population. Nevertheless, even a small reduction in the $FoxP3^+$ fraction of $CD4^+$ cells indicates that treatment with HKMTI-1-005 impedes immunosuppression in the tumour microenvironment.

The lymphocyte population that perhaps followed a more consistent trend across sites (porta hepatis or omental deposits and peritoneal wash) was that of NK cells. I initially defined NK cells as $CD3^-DX5^+$ cells, however through the course of the experiments and with the ability to include additional flow cytometry markers, I later on defined them as $CD3^-DX5^+NK1.1^+$. NK cells showed an increase in absolute number in porta hepatis deposit, omental deposit and peritoneal

wash. When examined for their chemokine content, the peritoneal NK cells contained more IFNγ and had a moderate increase in perforin content. In the spleen, their numbers were not altered, but they contained more granzyme-B and there was a trend for higher content of IFNγ and perforin too. The observed effects on the NK cell population would be in keeping with previous evidence that EZH2 is involved in NK cell lineage differentiation and that blocking EZH2 enzymatic activity contributed to NK cell maturation and cytotoxicity (293).

The expression of CXCR3 on the lymphoid population was undoubtedly increased with HKMTI-1-005, across sites of disease and sites of sampling. Enrichment of CXCR3 on lymphocyte surface happens as lymphocytes undergo a phenotypic switch from naïve to effector populations and it mediates their trafficking whilst maintaining lymphocyte activation (358, 435, 443-446). Notably, although CXCR3 is also expressed by DCs (359, 447-449), treatment with HKMTI-1-005 led to an increase of CXCR3 only on the surface of lymphocyte surface. This coupled with the increase of the CXCR3 ligand, CXCL10, indicates that the CXCR3-CXCL10 axis is activated in the tumour microenvironment, as well as in the peritoneal fluid, following treatment with HKMTI-1-005.

In addition to *Cxcl10*, there was a trend for increase in *Ccl19* which is involved in lymphocyte chemotaxis (394, 450) and has been found to increase in response to adoptive cell therapy in mice bearing tumours in a melanoma model (451). Perhaps even more importantly, I observed a statistically significant increase of *Ccl5* transcript which is a potent attractant of cytotoxic lymphocytes (394, 452), is linked directly to anti-tumour effects (453) and is associated with “immune hot” tumours with favourable outcomes (144, 450, 454-457).

The changes in lymphocyte subpopulations in the spleen of mice treated with HKMTI-1-005 are interesting. The spleen, a secondary lymphoid organ, is frequently being used as a reflection of the immune microenvironment at the effector site (in this case the intraperitoneal deposits), although this role is yet undefined. Nevertheless, given the technical complexities of harvesting peripheral lymph nodes in mice, I decided to test the immune profile of spleens in order to see if it supplements the intra-tumoral findings. Once again, the

overall population numbers are in balance with or without treatment, but we observe a moderate increase in the effector $CD8^+$ subpopulation and more IFNγ and perforin containing $CD8^+$ cells overall; a finding also present in the tumour following HKMTI-1-005 treatment. Similarly, the NK cells have a higher content of chemokines, as seen in the peritoneal fluid. Interestingly, Sckisel et al recently showed that changes in the immune cell composition of murine spleens can accurately reflect the changes in peripheral sites and that following treatment with IL-2 in mice, spleen $CD8^+$ lymphocytes undergo phenotypic changes as defined by CD44 and CD62L expression (458).

With regard to the myeloid population, the more striking finding after treatment with HKMTI-1-005 was that the tumour-associated macrophage (TAM) population, classically described as $CD11b^+F4/80^+MHCII^+$, retains the expression of Ly6C marker. TAMs are characterised by remarkable plasticity and consensus on their exact differentiation states is hard to find in the literature. However, it is widely recognised that TAMs derive from the large population of $CCR2^{high}Ly6C^+$ inflammatory monocytes which constantly contributes to the pool and that Ly6C expression gradually reduces as TAMs differentiate within the tumour (170, 439, 440, 459). It is therefore conceivable that HKMTI-1-005 blocks this differentiation. Stromnes et al observed that $Ly6C^{high}$ TAMs are associated with an increase in the intra-tumoral infiltration by TCR-engineered T cells and their survival (460). We could hypothesise that retaining Ly6C expression is consistent with a tumour-suppressing phenotype and given that EZH2 and its enzymatic activity has been previously linked to the monocyte-to-macrophage differentiation (298), we can conclude that HKMTI-1-005 leads to a block on this switch from $Ly6C^+$ to $Ly6C^-$ phenotype which could be favourable. This maintenance of Ly6C marker presence on TAMs was also observed in TAMs found in the peritoneal wash. Interestingly though, these TAMs seem to have a lower MHCII expression in the peritoneal fluid, something I did not observe in the intra-tumoral cells. Movahedi et al have showed that TAMs with lower MHCII expression are more frequently found in hypoxic areas and they are associated with immunosuppressive/pro-tumour gene and protein profiles (440). This is

perhaps contradictory to the maintenance of a Ly6C positive phenotype, yet it is very interesting that this population is only present in the peritoneal fluid.

Another observation that is consistent across experiments and disease sites, is the upregulation of CD86 marker on myeloid cells following treatment. CD86 is an activation marker and it was increased with HKMTI-1-005 on both DCs and TAMs. It is rather intriguing that its partner receptor, CD80, follows the opposite direction, however, these receptors can act independently and it is believed that CD86 induces a more robust interaction between DCs and T cells (438, 461). Interestingly, the trend for CD86 to be upregulated on dendritic cells was observed with UNC0642 single treatment too.

However, in light of recently published evidence on the nature of DCs that are responsible for efficient anti-tumour responses, the relevance of reported results on DCs in this chapter, is not entirely clear. Results on the frequency and marker expression of DCs in this chapter was based on gating DCs ($MHCII^+CD11c^+$ cells) out of the pool of cells that were CD11b marker positive. Despite the recognised, long-standing uncertainty of DC lineage markers (462), there is now established evidence that conventional DCs are divided in further subtypes with distinct marker repertoire and function (337). The sub-type mostly associated with priming an antitumour cytotoxic T cell response notably expresses the CD103 marker in mouse and CD141 marker in human (463), and is CD11b marker negative. These $CD103^+$ DCs are highly dependent on the transcription factor *Batf3* (464) and are essential to the antigen presentation, T cell stimulation and trafficking in tumours (463, 465, 466). Therefore, the analysis described in this chapter perhaps describes changes in a subset of DCs, however this is not the subset of DCs that promotes anti-tumour immune priming and T cell activation. It would be extremely interesting to interrogate the flow cytometry results again by deriving the DC subset from the CD11b negative population, however this is beyond the scope of this thesis.

Following the above findings, I wanted to investigate whether these immune-related changes could, in combination with other treatments, improve the survival outcome of mice bearing *Trp53*$^{-/-}$ ID8 tumours. The hypothesis behind

combining HKMTI-1-005 with PD-1 inhibition was that we could simultaneously activate immune cell effector functions and hinder their exhaustion. Bearing in mind that inhibition of PD-1/PD-L1 axis has had modest outcomes in ovarian HGSC to date (22, 23), I embarked on combining HKMTI-1-005 with an anti-PD-1 antibody, with HKMTI-1-005 treatment starting one week earlier than the anti-PD-1 treatment, to hopefully induce a priming effect, before targeting immune cell exhaustion. Perhaps unsurprisingly, the combination did not confer any benefit when compared to PD-1 blockade alone or indeed vehicle. Admittedly, due to the technical aspects of the experiment, the number of mice treated per cohort was relatively small and this could be a limitation for this experiment. Interestingly, tumour weight was significantly less with the combination treatment compared to anti-PD-1 alone and vehicle and two out of eight mice had prolonged survival. One could argue that this is consistent with what is observed with the use of immune checkpoint inhibitors in clinic; durable but infrequent responses.

The outcome of combining HKMTI-1-005 with cisplatin was also not robustly positive. Rational behind this combination was that tumour cell killing with cisplatin would augment tumour antigenicity and that the addition of HKMTI-1-005 would contribute to T and NK cell activation. In my experiment however, despite the statistically significant reduction in HR with combination treatment, the median survival prolongation was poor. Again, the technical aspects of the experiment might have contributed to this modest result (aggressive mouse model, lack of established treatment protocol due to HKMTI-1-005 novelty).

Lastly, to test the hypothesis that HKMTI-1-005 treatment produces NK cell-mediated tumour clearance, I examined NK cell depletion *in vivo*, in combination with HKMTI-1-005 treatment. The results here between tumour volume and mice survival were discordant. Adding NK cell depletion to HKMTI-1-005 reverses the tumour regression seen with HKMTI-1-005 alone (result not statistically significant), however this was not reflected on the survival of mice.

Overall, the results here describe that HKMTI-1-005 is a tolerable treatment that leads to a modest tumour regression (see merged data on mice weight, as a

marker to general well-being, and tumour volume from all experiments combined in Appendix 12.0). Treatment led to some notable changes in the immune composition of tumour deposits, peritoneal fluid and spleen. However, adding it to conventional treatments such as immune checkpoint blockade or cisplatin did not improve outcomes in the ID8 model. My next step was to better characterise treatment effect *in vivo*, in terms of changes in transcriptome and chromatin conformation.

Chapter 5. Dissecting the pathways altered with combined G9a/EZH2 inhibition (RNAseq/ATACseq)

Chapter 5 Results

5.1 Introduction

The results of Chapter 4 showed, by flow cytometry, that immune cell composition and their receptor expression in the tumour microenvironment changes with treatment with HKMTI-1-005. To support the hypothesis that HKMTI-1-005 mediates intra-tumoral immune cell activation, I sought to investigate gene transcription changes in the tumour and correlate these with the results of flow cytometry. Although transcriptional changes in cell lines and tumours with either EZH2 or G9a inhibitors or their individual combination with DNMT inhibitors have been described by others in the literature (282, 294, 467), the effect of the combined G9a/EZH2 inhibition on tumours had not been described at the time of writing this thesis. Moreover, observing transcriptional changes in tumours after HKMTI-1-005 treatment could also act as marker of successful drug penetration.

By performing ATACseq on the same tumours, I aimed to gain an overall idea of structural chromatin changes with HKMTI-1-005 treatment. Correlation between chromatin conformation changes and gene transcription could give insight into the direct effect of HKMTI-1-005 on distinct cell populations within tumours.

In addition, I investigated how G9a/EZH2 inhibition can alter expression of endogenous retroviral sequences (ERVs) in *Trp53*$^{-/-}$ ID8 tumours. ERVs are retro-transposable elements that are "footprints" of ancient infections. They comprise approximately 8%-10% of the human and mouse genome and are usually transcriptionally silenced (468). ERV silencing is modulated by DNA (469-471) and/or histone methylation (472), which ensures that their chromatin is compacted; when expressed, these elements are able of eliciting a robust immune response (473). Recently, focus has been redirected to ERVs because of published evidence showing that their reactivation by DNA demethylation can trigger immune signalling via the intracellular dsRNA response pathways (312, 313). As well as DNA methylation, histone acetylation and demethylation have been found to have a synergistic effect with DNA demethylation in enhancing re-expression of these elements, and therefore promoting immune stimulation (347, 474). Mechanistically, Zeng et al reported that ERV RNA can induce

cytosolic pattern recognition receptors (PRRs) and thereby trigger an antiviral signalling cascade which, in turn, can elicit T-cell independent B cell activation (475). In clear cell renal carcinoma, ERVs were found to be more transcriptionally active in patients whose disease responded to immune checkpoint inhibitors and also to correlate positively with patient survival (476). Similarly, in melanoma, analysis of non-coding RNA on primary tumours and benign melanocytic lesions revealed that ERVs are significantly repressed in high-risk, poor prognosis tumours (477). Overall, ERVs are emerging as a potentially significant mediator of anti-tumour immunity by developing a state of viral mimicry.

Using the regimen described in figure 4.8a, I treated mice with HKMTI-1-005 and harvested the omental deposits at the end of treatment. Half of the tumour was dedicated to RNA sequencing (RNAseq) and the other half for ATAC sequencing (ATACseq). The methodology of library preparation -total RNA library construction for RNAseq and Omni-ATAC protocol for ATACseq- are described in detail in Materials and Methods chapter.

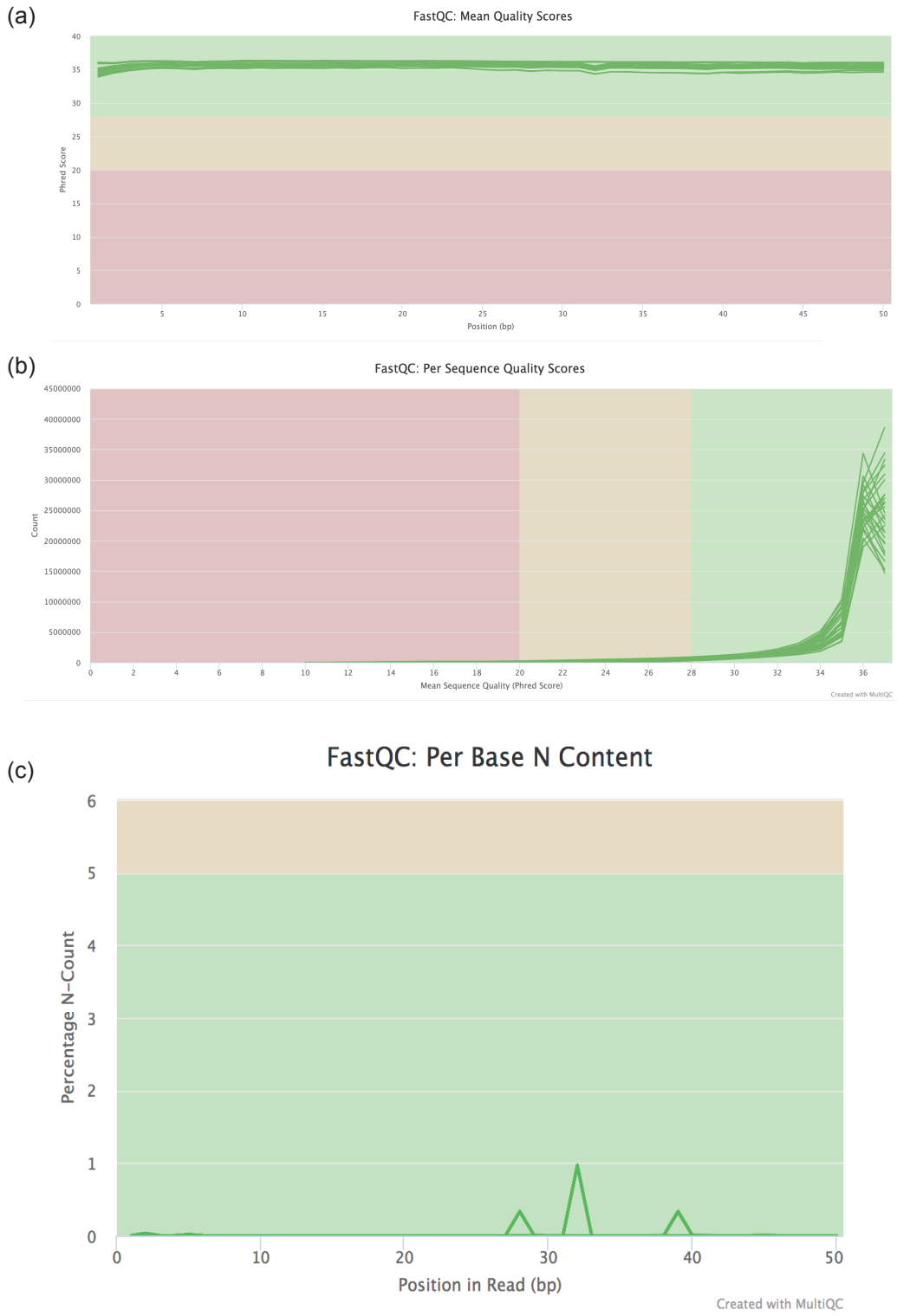

Figure 5.1: RNA sequencing quality control (a) and (b) Phred score illustrated in two ways: score of ~ 35 signifies data with sequencing accuracy between 99.9%-99.99% (n=7 per cohort). (c) Percentage of per base N-content showing N content of <1%.

Chapter 5 Results

5.2 RNA sequencing

5.2.1 Transcriptome analysis

In order to develop a library that would include non-coding regions of the genome, I decided to proceed with a total RNA library construction with ribosomal RNA depletion, as described in section 2.4.5 (478). Only extracted RNA with RIN score >7 was used in the library construction (Appendix 13.0). After library construction, the quality of DNA library was tested in an Agilent 2200 TapeStation and only samples with satisfactory, single DNA peak between 200-300bp were subjected to downstream RNAseq (Appendix 14.0). The analysis described below was conducted in collaboration with our lab's bioinformatician, Mr Hasan Mirza.

After completion of sequencing, data (n=7 vehicle and n=7 HKMTI-1-005 samples) were checked for quality control (QC) as per the parameters of the FastQC program (479). Data were found to be satisfactory, as evident by the high Phred quality score (figure 5.1a and 5.1b) and minimal per-base-N-content (figure 5.1c). The total library size for each sample is shown in figure 5.2a. There were no samples found with adapter contamination of more than 0.1%. Contamination with rRNA varied between 0.2%-16.2% (figure 5.2b); however rRNA reads were removed using the BBduk package (480). Following this, raw reads were aligned to mouse genome version GRCm38.p4 (mm10) using the STAR aligner with default parameters (figure 5.2c) (481). Raw counts were generated using the Rsubread package (482). We then checked for Differentially Expressed Genes (DEGs) using the DESeq package (483), which internally normalises the counts across samples using its median of ratios method (484).

All analyses, statistical tests, and plots were generated in R version 3.3.3 unless specified otherwise. MultiQC was used to collate data across different programs (485).

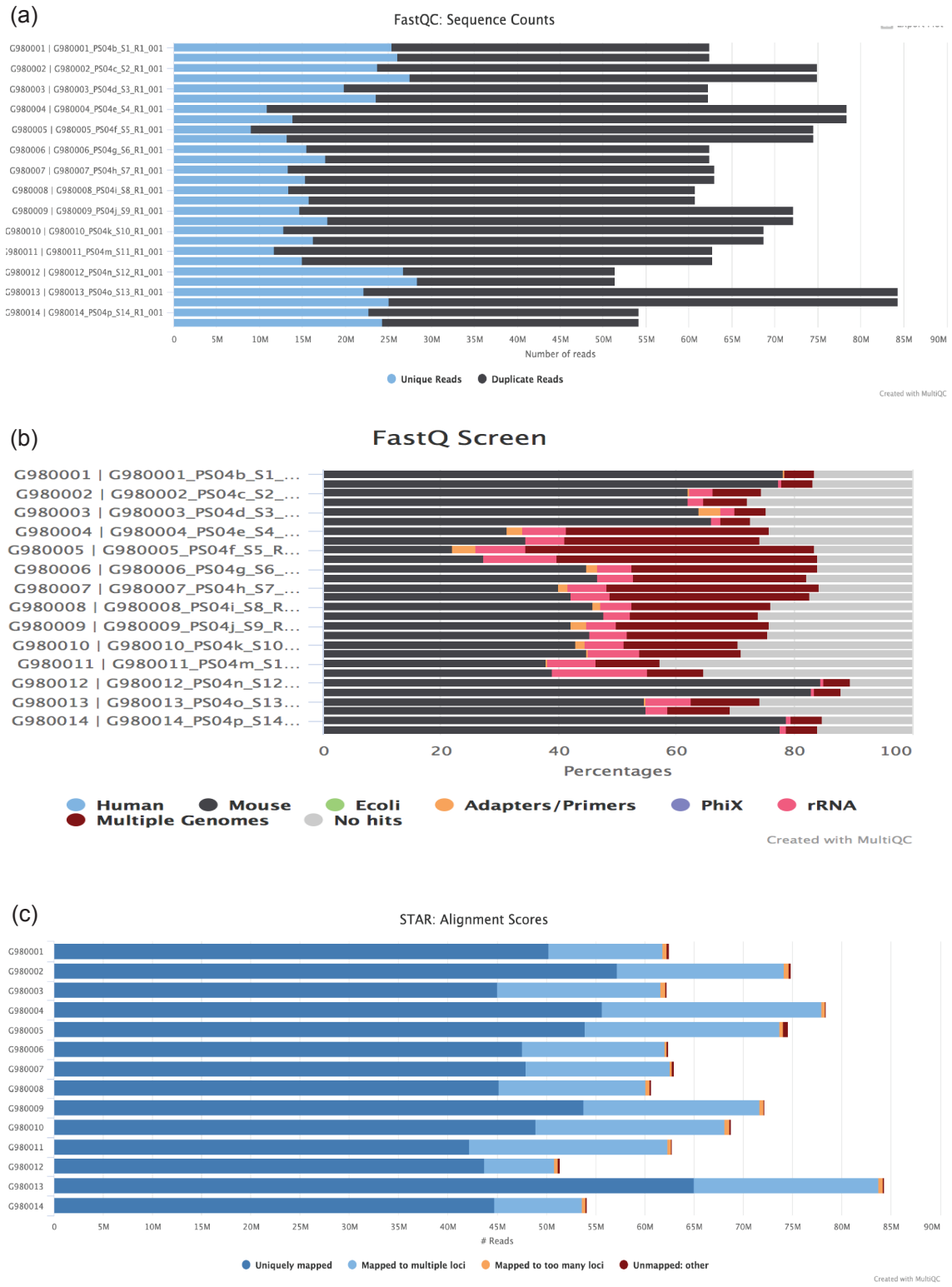

Figure 5.2: RNA sequencing quality control and library composition (a) Number of reads for all samples (n=7 per cohort) (b) genomic composition of the library and (c) alignment results using the aligner STAR showing number of reads aligned to GRCm38.p4 (mm10) version of mouse genome per sample.

In total, 1,146 genes were found to be overexpressed in the treated samples using the filtration criteria of log-2-fold change of ≥ 0 at FDR threshold of 5%. In contrast, 733 genes were downregulated with log-2-fold change of ≤ 0 at FDR threshold of 5% (figure 5.3a and 5.3b). Using Ward's hierarchical clustering method, we observe that vehicle samples cluster separately from treatment samples and within each group, DEGs mostly follow similar trends (figure 5.4a).

Following HKMTI-1-005 treatment, immunoglobulin kappa variable 2-109 was the gene showing the largest fold change (Log_2FC 4.43, FDR= 0.006) and *Gpnmb,* which encodes the type I glycoprotein GPNMB and is known to be present in ovarian cancer recurrences (486), had the most statistically significant upregulation (Log_2FC 4.39, FDR= 1.08e-116). Amongst those 1,146 upregulated DEGs were genes that had already been found to be overexpressed by single-gene qPCR or by qPCR array, including *Cxcl10* (Log_2FC 1.69, FDR<0.001), *Cxcl11* (Log_2FC 1.19, FDR<0.001) and *Ccl5* (Log_2FC 1.84, FDR= 8.33e-08). Importantly, a myriad of other immune-stimulatory genes was also upregulated, including *GzmB* (Log_2FC 2.74, FDR=3.49e-09), *Klrk1* (Log_2FC 1.15, FDR=0.016), *stat2* (Log_2FC 1.36, FDR= 1.61e-10) and *Tlr9* (Log_2FC 1.21, FDR=5.00e-05).

Type I IFN system mediators were also increased, including *Irf7* (Log_2FC 2.28, FDR=1.26e-19), *Irf9* (Log_2FC 0.68, FDR=1.79e-05) and *Irf5* (Log_2FC 0.41, FDR=0.02) (487), as well as Type I IFN inducible genes including *Oasl1* (Log_2FC 1.87, 3.61e-19), *Oas2* (Log_2FC 1.94, 5.79e-11) and *Oas3* (Log_2FC 2.22, 6.30e-11) which are involved in the antiviral defence gene network (488).

In terms of DEGs with reduced expression after treatment, *Olfr732* had the largest reduction (Log_2FC -6.13, FDR=0.038), although its relation to cancer has not been described in the literature as yet. Interestingly, the most statistically significant reduction occurred in *Marco* (Log_2FC -5.12, FDR=7.57e-24), which is a pattern-recognition receptor of the class A scavenger receptor family, expressed in TAMs. MARCO has been found to be overexpressed in the breast cancer microenvironment and to be associated with poor prognosis (489). Inhibiting MARCO reprograms macrophages to acquire an anti-tumour phenotype and to successfully obstruct tumour growth (490, 491).

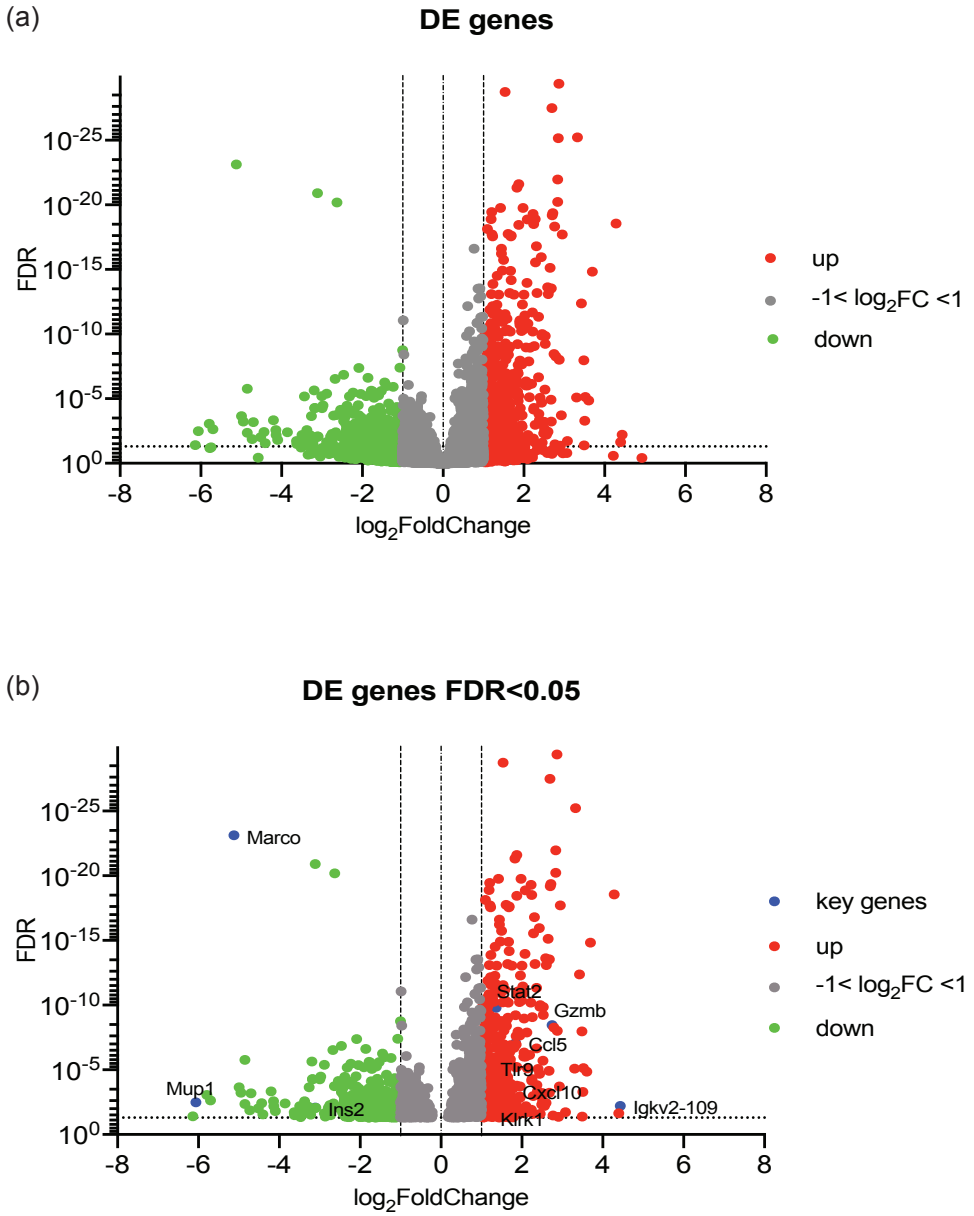

Figure 5.3: RNA sequencing- differentially expressed genes (a) Volcano plot of all differentially expressed genes between mice treated with vehicle (n=7) and HKMTI-1-005 (n=7), all FDR values included, and (b) same plot as (a) but only for genes with FDR < 0.05, along with some key genes annotated. FDR= False Discovery Rate.

For functional annotation of DEGs, we used the Database for Annotation, Visualization and Integrated Discovery (DAVID) online Functional Annotation Tool (492) with access to Gene Ontology (GO) (493, 494), REACTOME (495), and KEGG (496) databases. Gene ontology results for the Biological Processes (BP) sub-ontology showed that the most significantly upregulated pathway in the HKMTI-1-005-treated tumours was the immune pathway (GO:0002376, FE 6.9, FDR=7.43e-67), with more than 10% of the DEGs with HKMTI-1-005 treatment overlapping with the genes including in the pathway. Innate immune response (GO:0045087, FE 5.35, FDR=9.55e-41) and viral defence (GO:0051607, FE 7.36, FDR=3.12e-30) were also significantly upregulated (figure 5.4b). Compared to upregulated pathways, fewer pathways were downregulated as a response to treatment. Amongst those with FE of less than 0.5 were “positive regulation of glucose metabolic process” (GO:0010907, FE 0.07, FDR=0.00001), “positive regulation of lipid metabolic process” (GO:0045834, FE 0.06, FDR=3e-5) and “negative regulation of gluconeogenesis” (GO:0045721, FE 0.08, FDR=5e-5) (figure 5.4b). Analysis by KEGG database also revealed immune pathways being significantly changed with treatment, such as “antigen processing and presentation” (mmu04612, FE 5.4, FDR=1.11e-10), “natural killer cell mediated cytotoxicity” (mmu04650, FE 3.3, FDR=6e-5) and “cytokine-cytokine receptor interaction” (mmu04660, FE 2.6, FDR=2.51e-06) (figure 5.4c).

According to the KEGG database, none of the downregulated pathways was found to be statistically significant. We also analysed the data using the GO sub-ontologies “cellular content” (CC) and “molecular function” (MF). With regards to genes related to the cellular content (figure 5.5a), the family of lysosome genes was found to be significantly increased (GO:0005764; FE 4.69, FDR=8.1e-26), an observation also made with the KEGG database (figure 5.4c). Networks related to immunity such as the MHC class I protein complex (GO:0042612; FE 14.09, FDR=7.68e-08) and the phagocyte vesicle membrane (GO:0030670; FE 8.15, FDR=1.12e-09) were highly expressed.

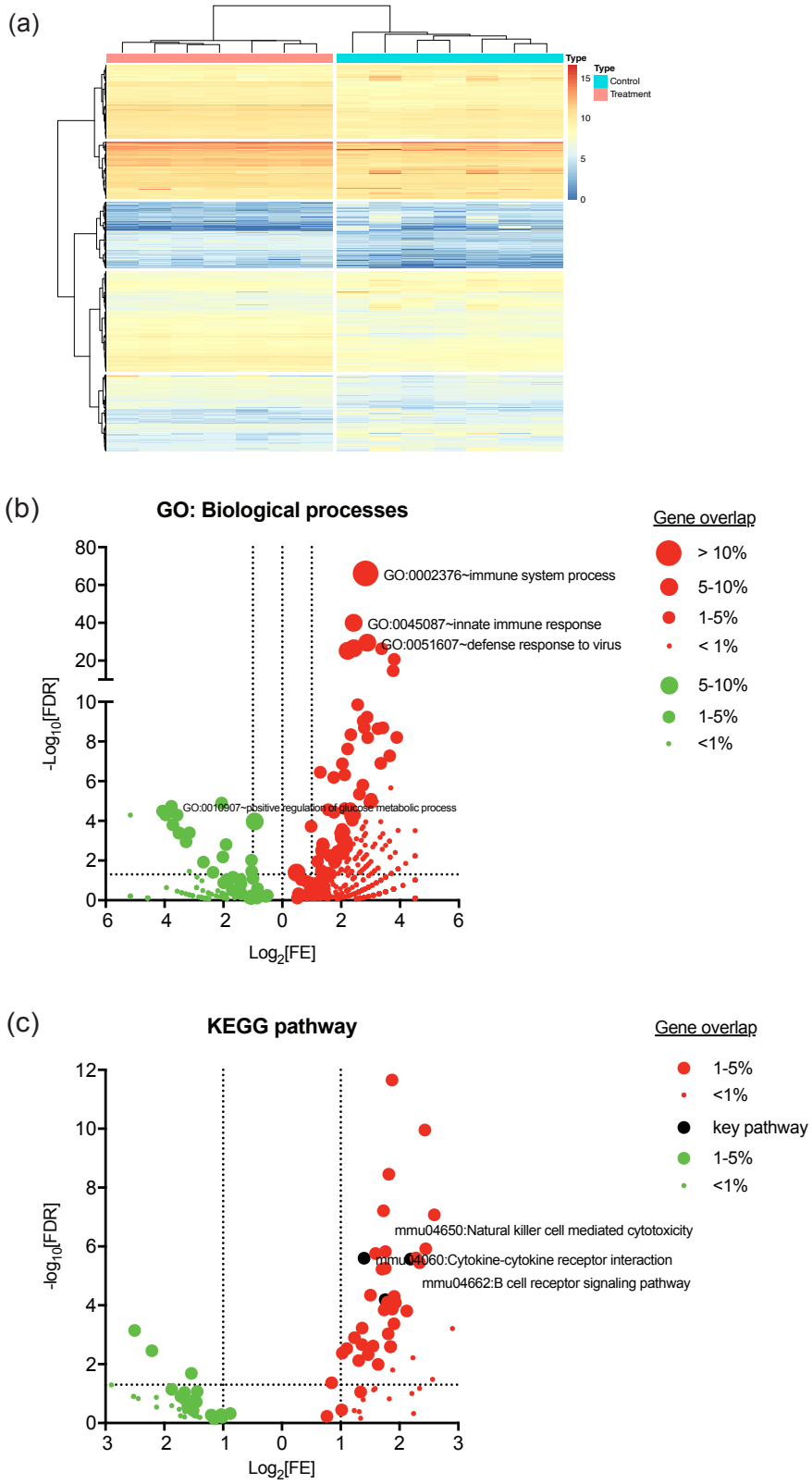

Figure 5.4: RNA sequencing hierarchical clustering and functional annotation analysis (a) Heatmap of DEGs with hierarchical clustering trees for tumours (columns) and DEGs (rows), comparing vehicle versus HKMTI-1-005 treated tumours. Red colour represents upregulation and blue colour downregulation (b) Functional annotation analysis for DEGs

Figure 5.4: RNA sequencing hierarchical clustering and functional annotation analysis, continued: results using the Gene Ontology Biological Processes database; (c) Functional annotation analysis results for DEGs using the KEGG database; DEGs= differentially expressed genes. Size of the dot represents the percentage of genes in our DEGs list that overlap with the individual pathway gene list, red colour = upregulated genes, green colour = downregulated genes, DEGs= differentially expressed genes.

In our analysis of molecular function sub-ontology (figure 5.5b), I found that GTPase activity was strongly enhanced with treatment (GO:0003924; FE 3.56, FDR=6.26e-09). Moreover, cytokine activity (GO:0005125; FE 2.66, FDR=0.0002) and cytokine receptor activity (GO:0004896; FE 5.35, FDR=0.0004) were upregulated with treatment, as was tumour necrosis factors receptor binding (GO:0005164; FE 6.84, FDR=0.0001).

I was also interested in correlating the sequencing results to relative immune cell composition. This correlation has recently become possible via the analytical tools such as CIBERSORT or EPIC (497, 498); however, these tools are designed for human, rather than murine, sequence data. We therefore decided to use the more recently developed ImmuCC tool (499) which utilises a 162-gene signature matrix to describe 10 immune cell populations. Based on ImmuCC tool, there were no significant differences in the immune cell distribution between HKMTI-1-005 treatment and vehicle groups (figure 5.6a and 5.6b).

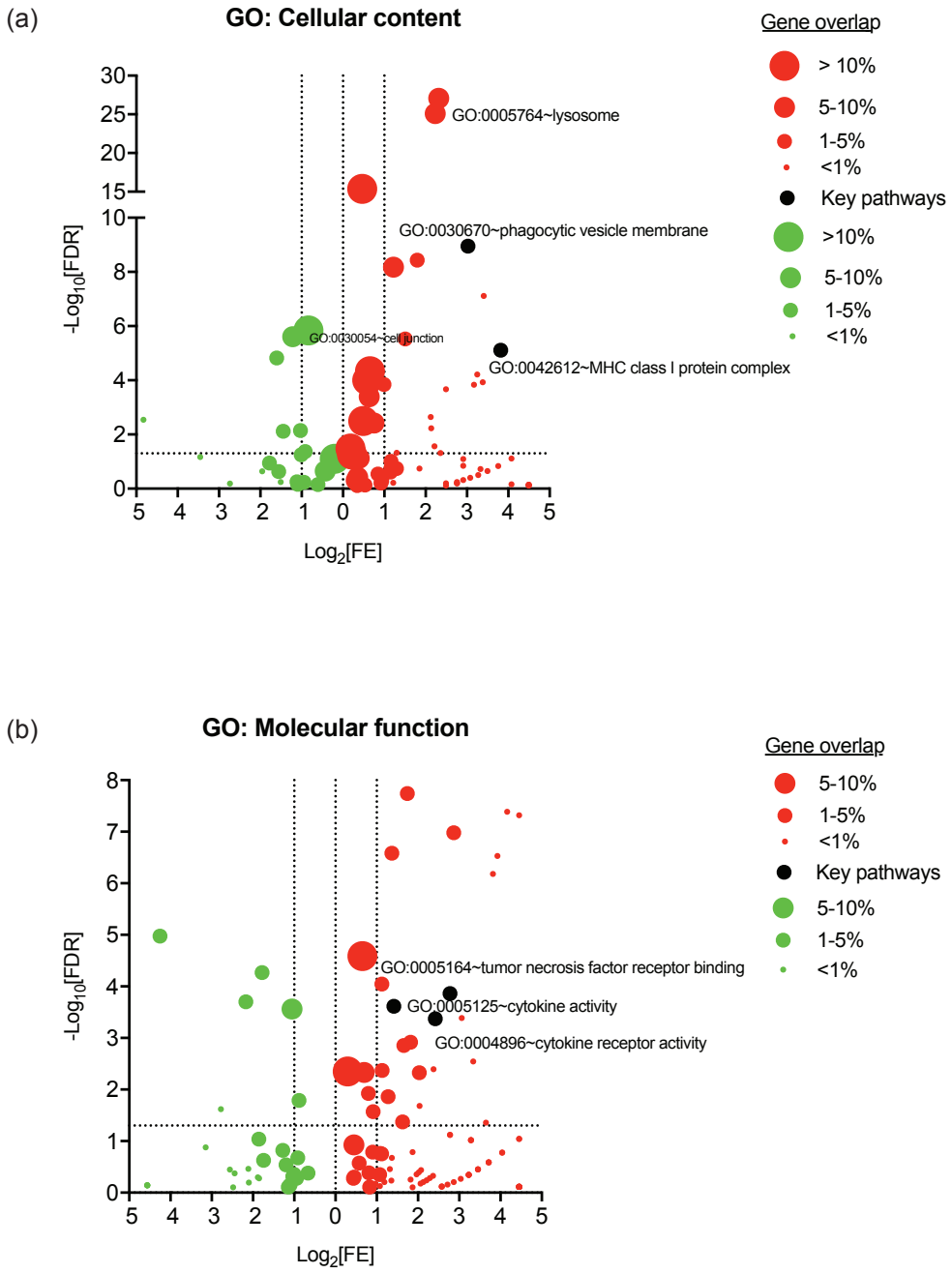

Figure 5.5: RNA sequencing - functional annotation analysis continued. Functional annotation analysis of DEGs results using the Gene Ontology Cellular Content (a) and Molecular Function (b) databases; Size of the dot represents the percentage of genes in our DEGs list that overlap with the individual pathway gene list, red colour = upregulated genes, green colour = downregulated genes, DEGs= differentially expressed genes.

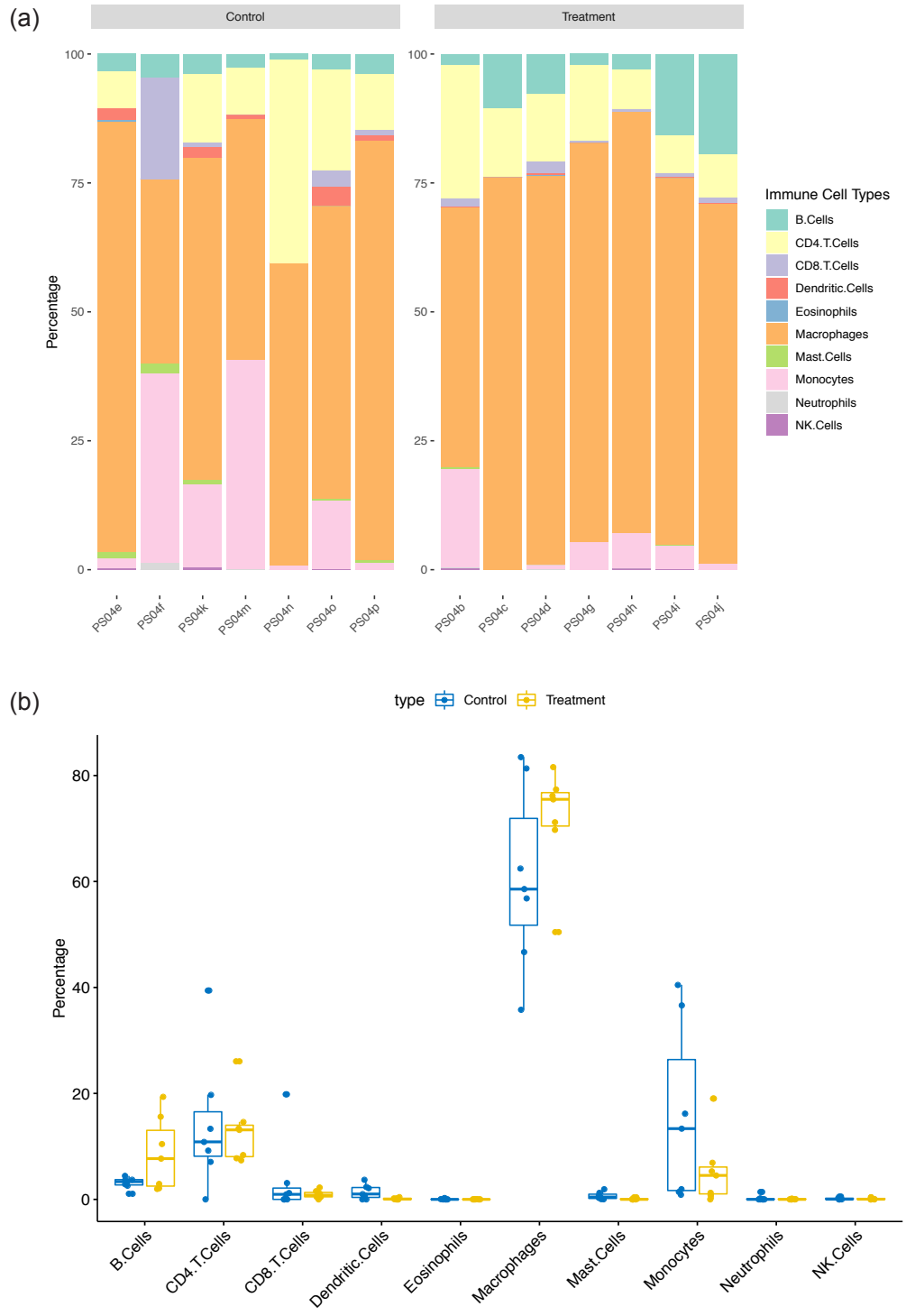

Figure 5.6: RNA sequencing- ImmuCC tool (a) Immune cell distribution in the vehicle (left panel) and treatment group (right panel) as per ImmuCC tool. (b) quantification of (a) as percentages.

Despite the ImmuCC tool results above, single sample Gene Set Enrichment Analysis (ssGSEA) showed a strong concordance between the RNAseq results and published immune-related gene signatures. ssGSEA is a variant of the original GSEA, tailored for individual samples where a separate enrichment score for a gene set is calculated for each sample (500-502). Normalised counts from DEGs from RNAseq were subjected to ssGSEA analysis using the online available R code (503). This ssGSEA enrichment score represents the degree to which the genes in a particular gene set are co-ordinately up- or down-regulated within a sample. For each gene set, these scores were normalised as z-scores to make them comparable across the samples.

Overall, 235 immune-related signatures were significantly enriched in the HKMTI-1-005 treatment group compared to vehicle (FDR<0.04) (Appendix 15.0), confirming that HKMTI-1-005 certainly modulates intra-tumoural immune networks (504). I reviewed the literature describing the generation of all these 235 signatures and specifically focused on the ones that could correspond to pathways resulting in the phenotypic changes seen with treatment, by flow cytometry. Some of them are presented in figure 5.7.

Wherry et al described some of the gene networks involved in the differentiation of virus-specific $CD8^+$ cells from effector to exhausted cells following chronic infection from lymphocytic choriomeningitis virus (505). In ssGSEA analysis, tumours treated with HKMTI-1-005 were enriched for genes that are associated with the maintenance of a $CD8^+$ effector status (figure 5.7a).Tumours were also enriched for gene pathways that reflect a phenotypic change from naive to effector $CD8^+$ cells (figure 5.7b) (505). A similar trend for treated tumours being enriched of networks relating to the differentiation from naïve to memory $CD8^+$ cells was also seen, using a different genomic profiling, produced by Sarkar et al (506) (figure 5.7e).

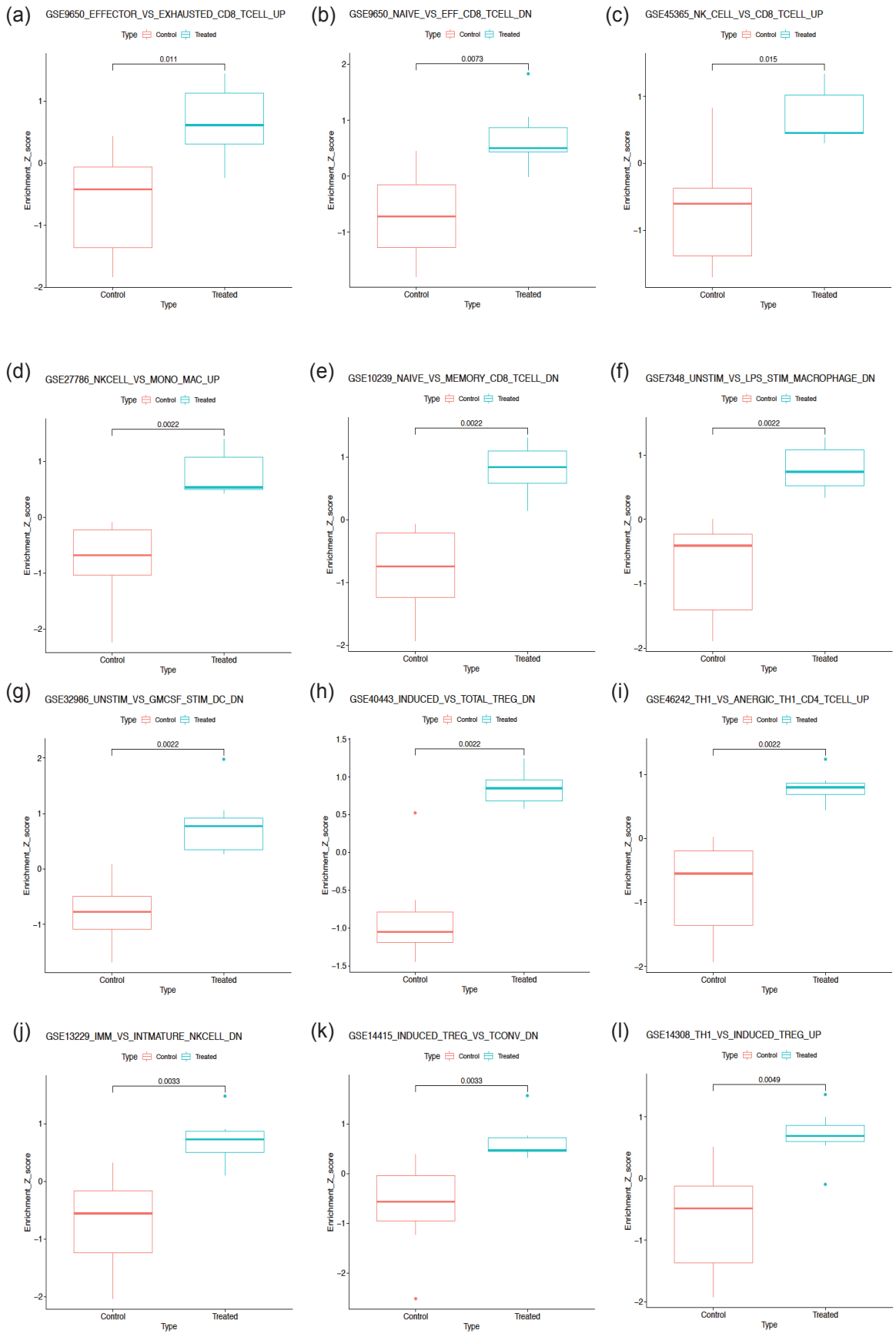

Figure 5.7: RNA sequencing; Single-sample GSEA analysis: overleaf.

Figure 5.7: RNA sequencing; Single-sample GSEA analysis (a) to (l) Box plots showing enrichment score of ssGSEA immune gene signatures (C7: immunological signatures). UP (up) or DN (down) at the end of box plot title refers to the direction relating to the first (left side) component of the title i.e. GSE9650 effector_vs_exhausted_CD8_tcell_up: in this gene signature, the gene set relating to effector CD8 cells has an upward trend. ssGSEA= single sample Gene Set Enrichment Analysis.

I also observed that NK cell gene networks that are activated as a response to type I IFN during viral infection are abundant in tumours treated with HKMTI-1-005, when compared to gene sets activated in $CD8^+CD11b^+$ dendritic cells (507) (figure 5.7c). This correlates with the increase in NK cells observed by flow cytometry, and partially by immunohistochemistry. Following microarray analysis of all haematopoietic cell lineages, purified from mature C57Bl/6 mouse bone marrow, Konuma et al categorised gene sets for individual immune cell types (508). The gene set associated with NK cells was increased in HKMTI-1-005-treated tumours (figure 5.7d). Based on an NK cell maturation signature discovered by Chiossone et al, the genomic profiling of NK cells in HKMTI-1-005 treated tumours was reminiscent to that of cells that are in a process of maturing and gaining effector functions (509) (figure 5.7j).

Induced T regulatory ($FoxP3^+$) cells are thought to be responsible for peripheral immune tolerance, associated with tumour-promoting potential, and to be different than the rest of natural T regulatory cells, found mainly in the thymus (510). In the tumours treated with HKMTI-1-005, gene networks are enriched with natural T regulatory profiles as opposed to induced T regulatory profiles, which again would support flow cytometry results of Chapter 4 (figure 5.7h). A similar trend towards a reduction in pathways involved in the differentiation and maintenance of induced T regulatory cells was also seen using gene profiling data by Haribhai et al (figure 5.7k) (511). Based on two independently published gene signatures (512, 513), Th1 immune response networks were found enhanced in HKMTI-1-005 treated tumours compared to vehicle, supporting the hypothesis that HKMTI-1-005 indeed fosters a balance towards anti-tumour immune response rather than T cell anergy (figure 5.7i and 5.7l).

Lastly, with regards to myeloid cells, I observed that HKMTI-1-005 treated tumours express macrophages gene networks that are activated following stimulation of macrophages with bacterial lipopolysaccharide (514) (figure 5.7f) and also express signatures associated with activated and mature dendritic cells (515) (figure 5.7g).

5.2.2 Endogenous Retroviruses (ERVs) analysis

Recent evidence suggests that ERVs can potentiate anti-tumour immunity when they are transcriptionally active (312, 313, 476). In addition, RNAseq results demonstrated upregulation of the "defence response to virus" pathway with HKMTI-1-005. Therefore, I decided to conduct an ERV analysis with guidance Dr Marina Natoli (Imperial College). As described in 5.2.1, RNAseq QC was performed and raw reads were aligned to mouse genome version GRCm38.p4 (mm10) using the STAR aligner with default parameters (481). A mm10 annotation for mouse endogenous viral elements was obtained from the gEVE database (516, 517). Reads were assigned to mouse ERV features using featureCount from the Rsubread package (482) with the options for reads to be multimapping and "primary only", which takes primary alignments only into account, a method adapted by Haase et al (518).

To remove low-expressing ERVs, we applied a filtration threshold whereby an ERV needed a count of at least 10 in one or more samples (in either the vehicle or treatment group) in order to be included in our analysis. The total number of ERVs detected was 61,184 but only 2,781 and 2,465 passed the filtration threshold in the control and treatment groups respectively. 2,118 ERVs were common to both groups and they were subjected to differential expression analysis using the DESeq2 package (483). Interestingly, out of these 2,118 ERVs, 51 were differentially expressed at the 5% FDR threshold with 39/51 showing a trend to be overexpressed (Log2FC $\geq$ 0).

The ERVB2 and IAP retrotransposon elements of the ERVK class were found to be the most highly transcribed in treated tumours. One of the IAP ERVK elements,

IAPEY3-int|LTR/ERVK, had a fold change of log_2FC of 2.89 (FDR= 2.40e-22) and one of ERVB2 ERVK elements had a fold change of 2.67 (FDR=2.41e-23) (figure 5.8c). On the other hand, almost all of the downregulated retrotransposon elements in HKMTI-1-005 treated tumours belonged to ERV1 class. The elements with the steepest reduction were MuRRS4-int|LTR/ERV1 (log_2FC -1.92, FDR<0.001), and MURVY-int|LTR/ERV1 (log_2FC -1.6, FDR<0.001) (figure 5.8c). The frequency of these elements in the differentially expressed list of sequences is also shown in tables in figure 5.8a and figure 5.8b. These elements represent identical sequences in different genomic loci (Appendix 16.0).

(a)

ERV class (RepBase)	Frequency
LTR/ERVK	28
LTR/ERV1	10
LINE/L1	5
LTR/ERVL	3
LTR/ERV1 (AGCGAC)n	1
LTR/ERV1 RLTR19-int	1
LTR/ERVK ERVB2_1A-I_MM	1
LTR/ERVK MERVK26-int	1
snRNA L1_Mm	1

(b)

ERV Family (RepBase)	Frequency
ERVB2_1-I_MM	8
IAPEY4_I-int	7
ERVB5_1-I_MM	3
IAPEY3-int	3
IAPEz-int	3
MuRRS4-int	3
MURVY-int	3
ETnERV2-int	2
MERVL-int	2
ETnERV-int	1
ETnERV3-int	1
L1_Mm	1
L1_Mus3	1
L1Md_A	1
L1Md_F2	1
L1VL2	1
MERV1_I-int	1
MERVL_2A-int	1
MMERGLN-int	1
MuRRS-int	1
RLTR13D5	1
RLTR26_Mus	1
RLTR4_MM-int	1
RLTR6-int	1
RodERV21-int	1
U6	1

(c)

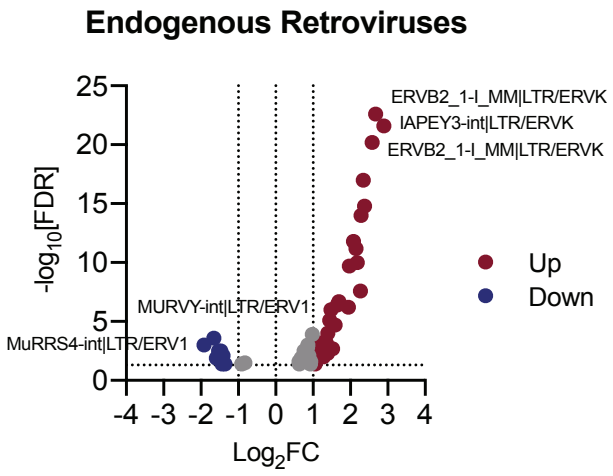

Figure 5.8: RNA sequencing; endogenous Retroviruses analysis. Tables showing the frequency of ERVs found to be differentially expressed, categorised by class (a) and by family (b). (c) Volcano plot demonstrating DE ERVs with an FDR < 0.05. ERVs=endogenous retroviruses.

5.3 ATAC sequencing

For ATACseq library construction, I followed the OmniATAC protocol by Corces et al (see section 2.5) (327). The electropherograms of samples used in downstream sequencing are shown in Appendix 17.0. ATACseq data (n=6 control and n=6 treatment samples) were checked for quality control (QC) using FastQC (1) program. The data were found to be of good sequencing quality based on the Phred scores and the per-base-N-content (figure 5.9). Adapter contamination was found at the 3' ends and these were removed using Trimmomatic tool (519), (figure 5.10a and 5.10b). Reads were aligned against the GRCm38.p4 (mm10) mouse genome with the use of BWA-MEM method (520) and post-alignment quality metrics were accessed using the qualimap program (521). Picard tools were used to mark duplicate reads (522). A very high proportion of duplicate reads was found across samples (figure 5.10c), an effect commonly seen with ATACseq library construction (verbal communication by Dr Ian Garner). During construction of my DNA library, the low starting material which required PCR overamplification probably contributed to the presence of high number duplicate reads. Such duplicates were removed before proceeding with the downstream analyses. All bam files were sorted and indexed using the samtools (523). We decided to remove one treatment sample from the downstream analysis (PS04d) (figure 5.11a and 5.11b) as it yielded a very small number of sequencing reads compared to the remainder of the cohort. Thus, we were left with n = 6 controls, and n = 5 treatment samples. Mitochondrial reads represented 0.8%-4.3% of reads and they were therefore ignored (figure 5.11c).

All analyses, statistical tests, and plots were generated in R version 3.3.3 unless specified otherwise. MultiQC was used to collate data across different programs (485).

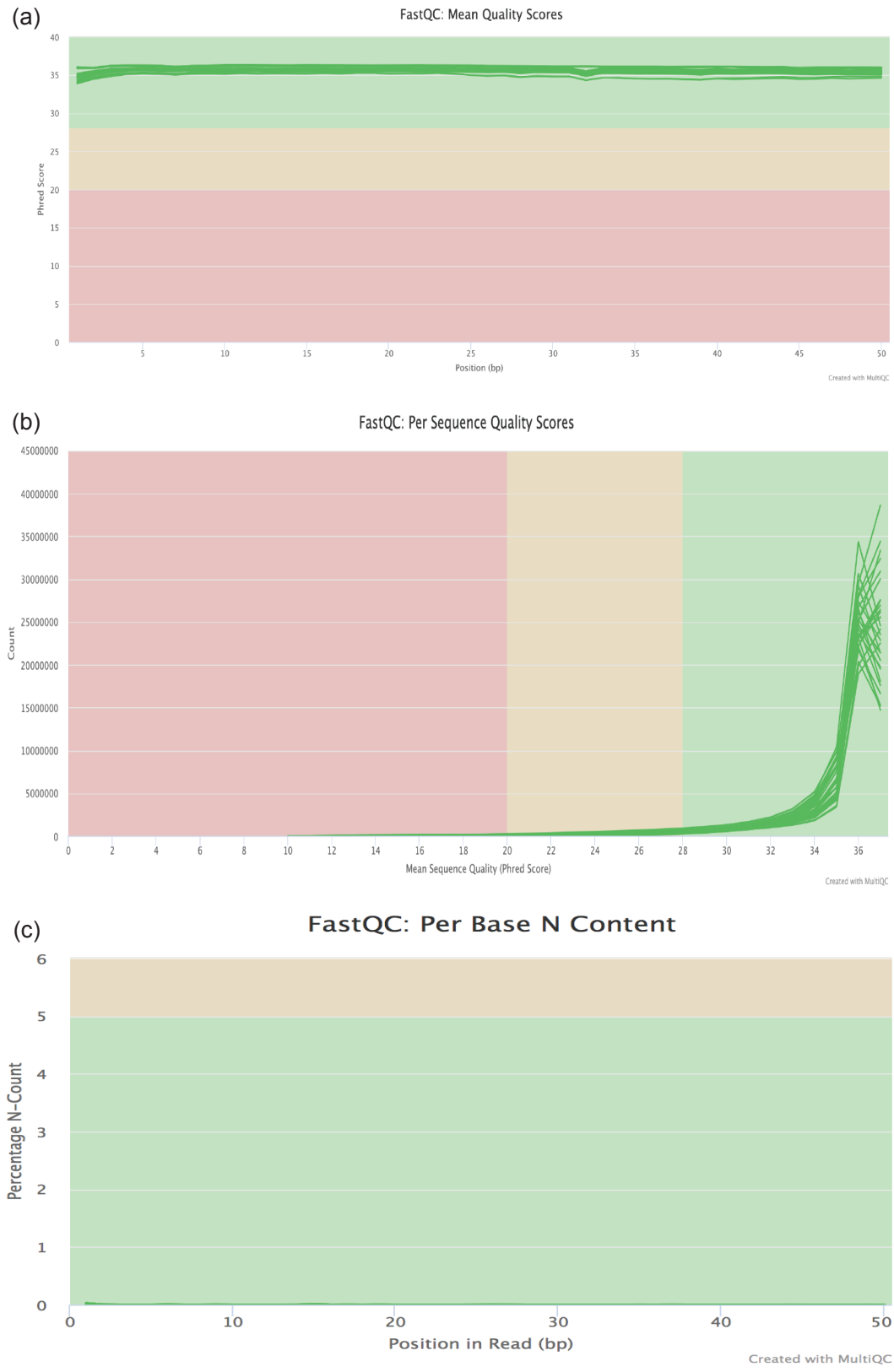

Figure 5.9: ATAC sequencing quality control (a) and (b) Phred score illustrated in two ways: score of ~ 35 signifies data with sequencing accuracy between 99.9%-99.99% (n=7 per cohort). (c) Percentage of per base N-content showing N content is essentially 0%.

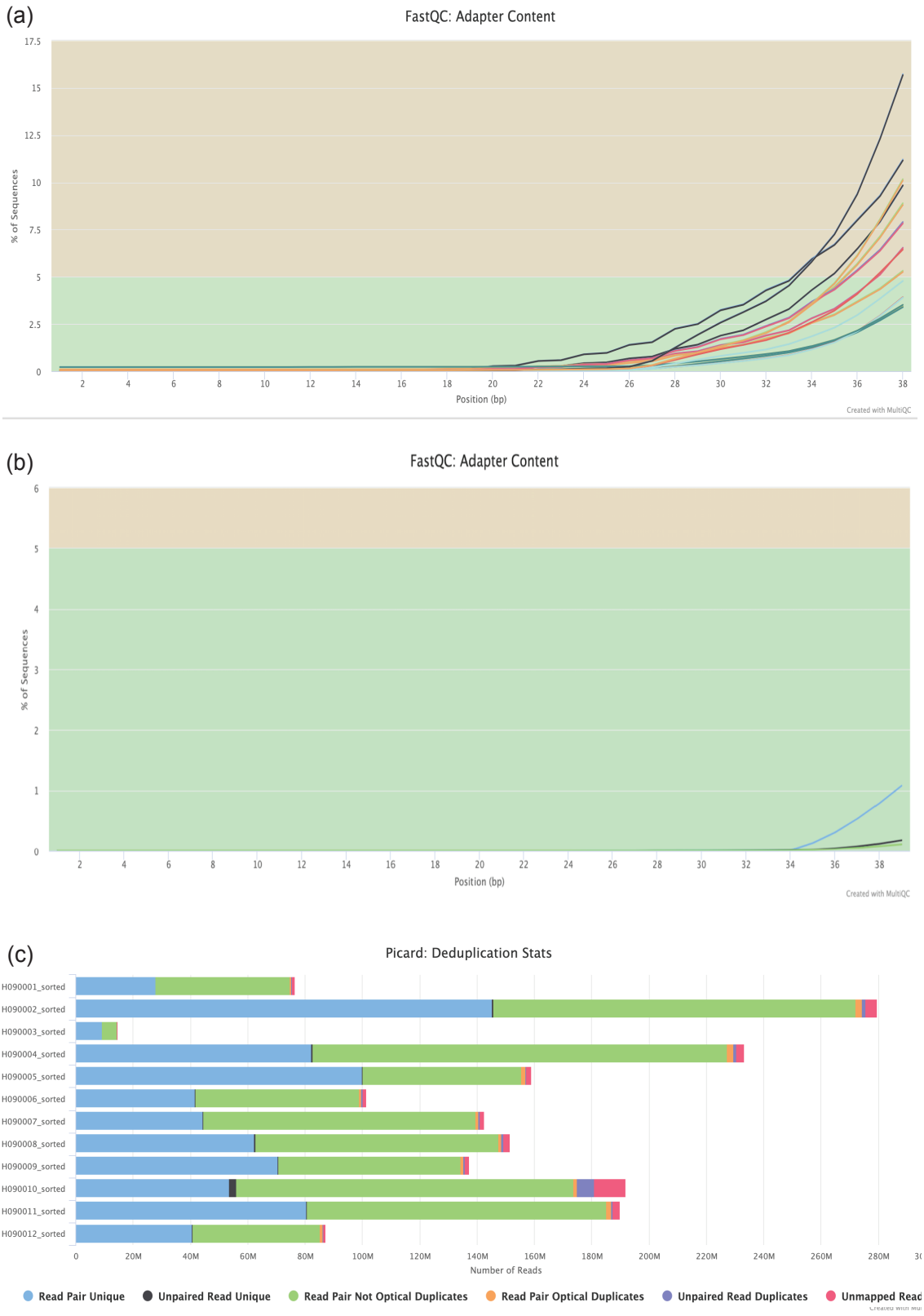

Figure 5.10: ATAC sequencing quality control and library composition. The cumulative percentage count of the proportion of the library which has been contaminated by adapter before adapter removal (a) and after adapter removal (b), using the Trimmomatic tool (519).(c) Duplication rate after library alignment.

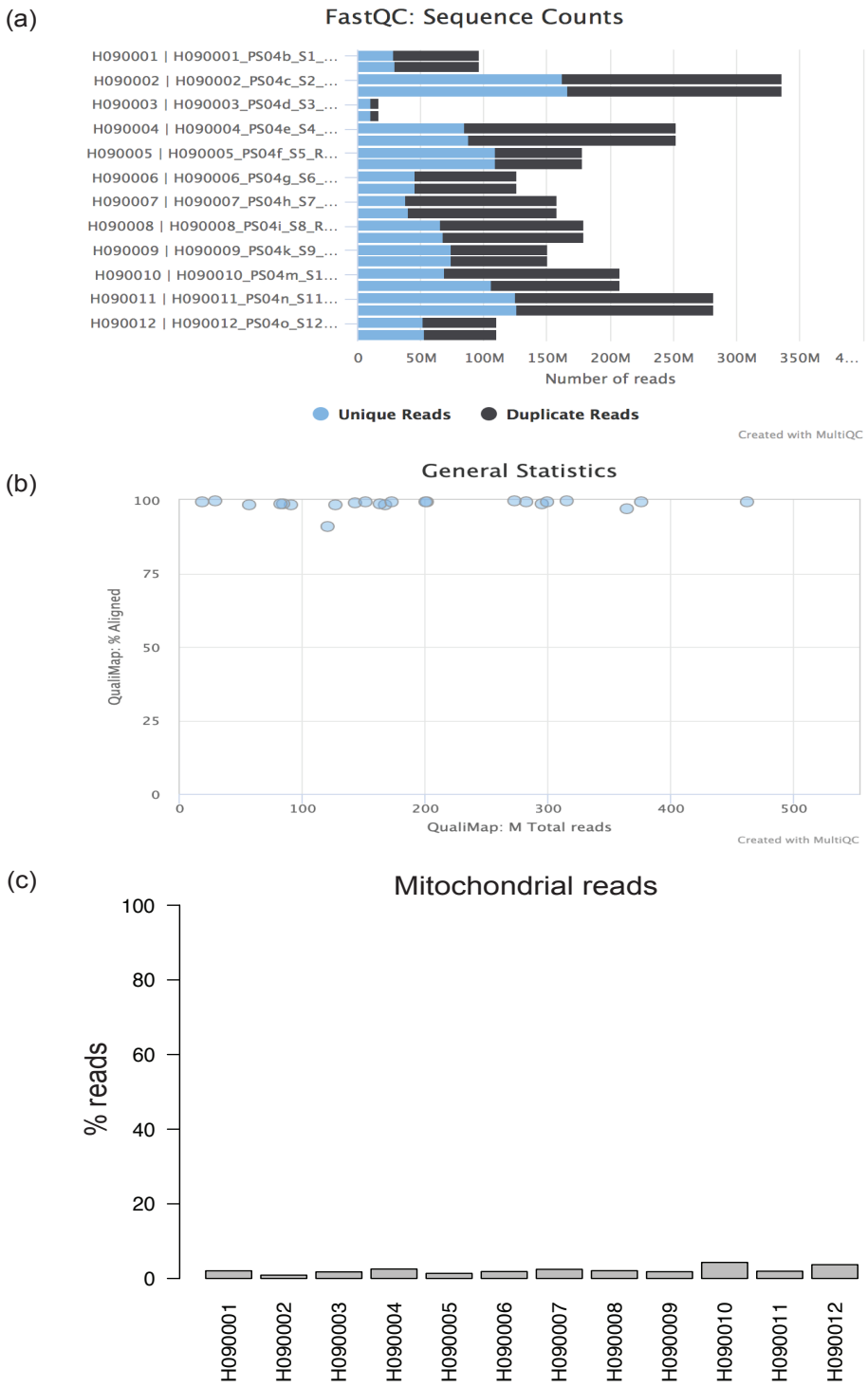

Figure 5.11: ATAC sequencing quality control - continued (a) Sequencing counts for the entire pool of samples; PS04d sample was removed from analysis, given the small number of reads yielded (b) Map of total number of reads, post-alignment, which shows two files (every sample was represented by t wo files) in the far left, having the lowest number of reads; this sample was removed from downstream analysis (c) percentages of mitochondrial reads across all samples.

The MACS2 tool was used to call peaks on all individual control and treatment samples (524). This generated narrow peak files for each sample (figure 5.12a). The average length of these peaks was <400 bp (figure 5.12b). In the absence of a matched background input for each sample, we devised again a filtration strategy whereby only those peaks that were present across all treatment samples (n = 5) - with any proportion of overlap among them - were considered to truly represent areas of open chromatin.

After application of this filtration, 88,401 consistent peaks were called in all treatment samples. These peaks were also filtered for presence in the control samples with any proportion of overlap i.e. from one base to the full peak length. While doing so, we only considered those peaks that were present in at least 50% of the control samples i.e. 3/6 control samples. Following this process, there were 74,424 consensus control peaks that matched these criteria. All consensus treatment peaks i.e. 88,401 were tested for overlap with the 74,424 consensus control peaks and any overlapping peaks were filtered out. Interestingly, approximately 71% of 88,401 had no overlap with control peaks i.e. 62,886 unique narrow peaks were found in the treatment samples that were not present in the control samples.

The true 62,886 open chromatin regions consistent across all treatment samples were annotated for known genomic markers, regulatory regions, and open reading frames of all genes including the UTR regions at both ends. Most of the peaks were found to be scattered around the genome in the intergenic regions (60%) whereas about 35% of them were found within the gene bodies and UTR regions (figure 5.12c). With the use of BEDtool v.2.29.0 software (525) and annotation from the GRCm38.p4 (mm10) database, we found that these peaks (found within gene bodies) overlapped with 7,788 known mouse genes. The majority of these (88.2%) were found to be protein-coding genes (figure 5.13a). When these genes were matched with the RNAseq data, we found 552 that were common between the differentially RNAseq 5% FDR DEGs and the list of genes associated with peak changes on ATACseq analysis (figure 5.13b).

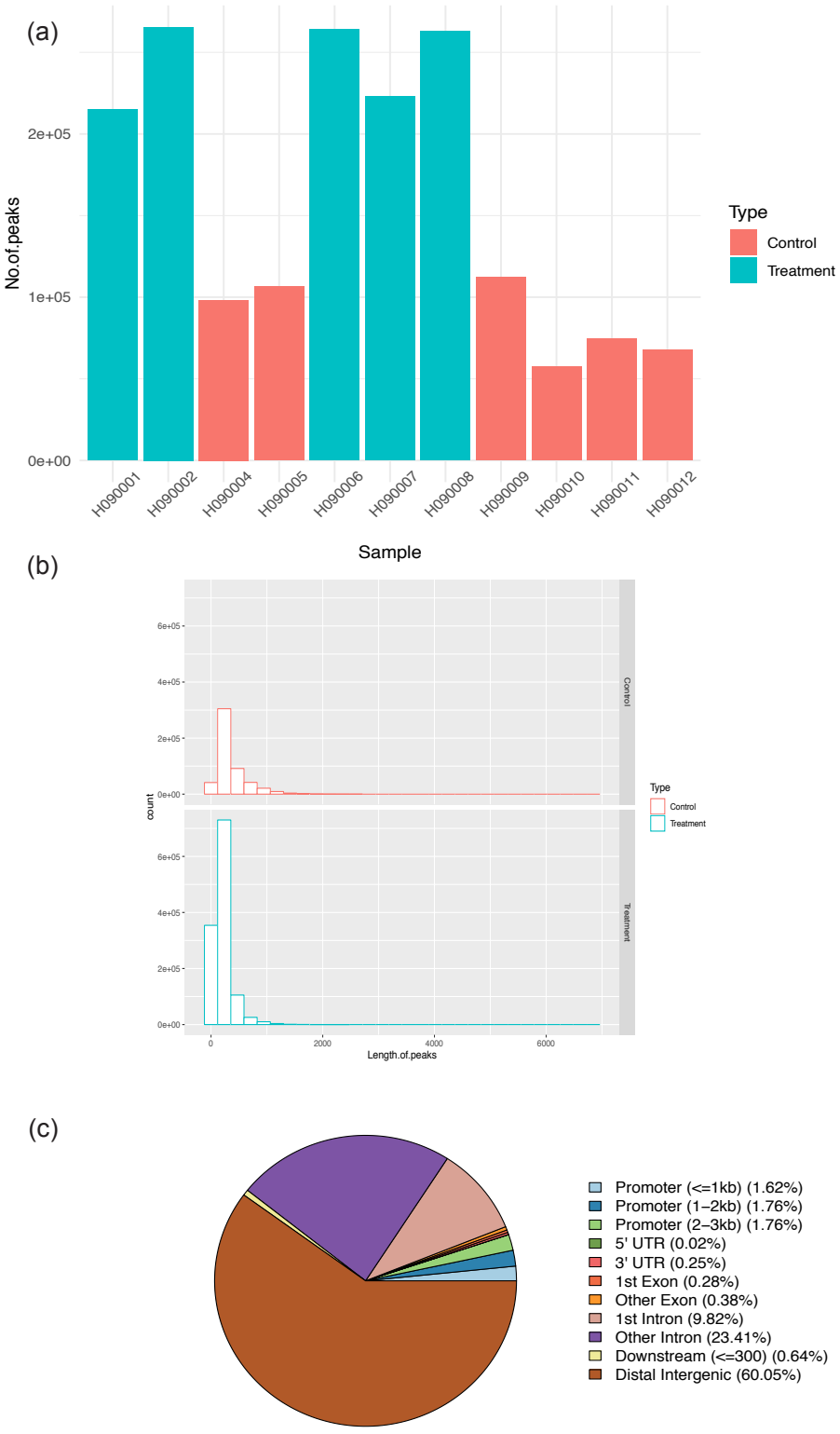

Figure 5.12: ATAC sequencing peak results. Number of ATACseq peaks per sample (a) and average length of peaks (b) found in vehicle and HKMTI-1-005 treated samples, before applying filtration criteria. (c) distribution of ATAC seq peaks across the genome in percentages. ATACseq= assay for transposase accessible chromatin using sequencing.

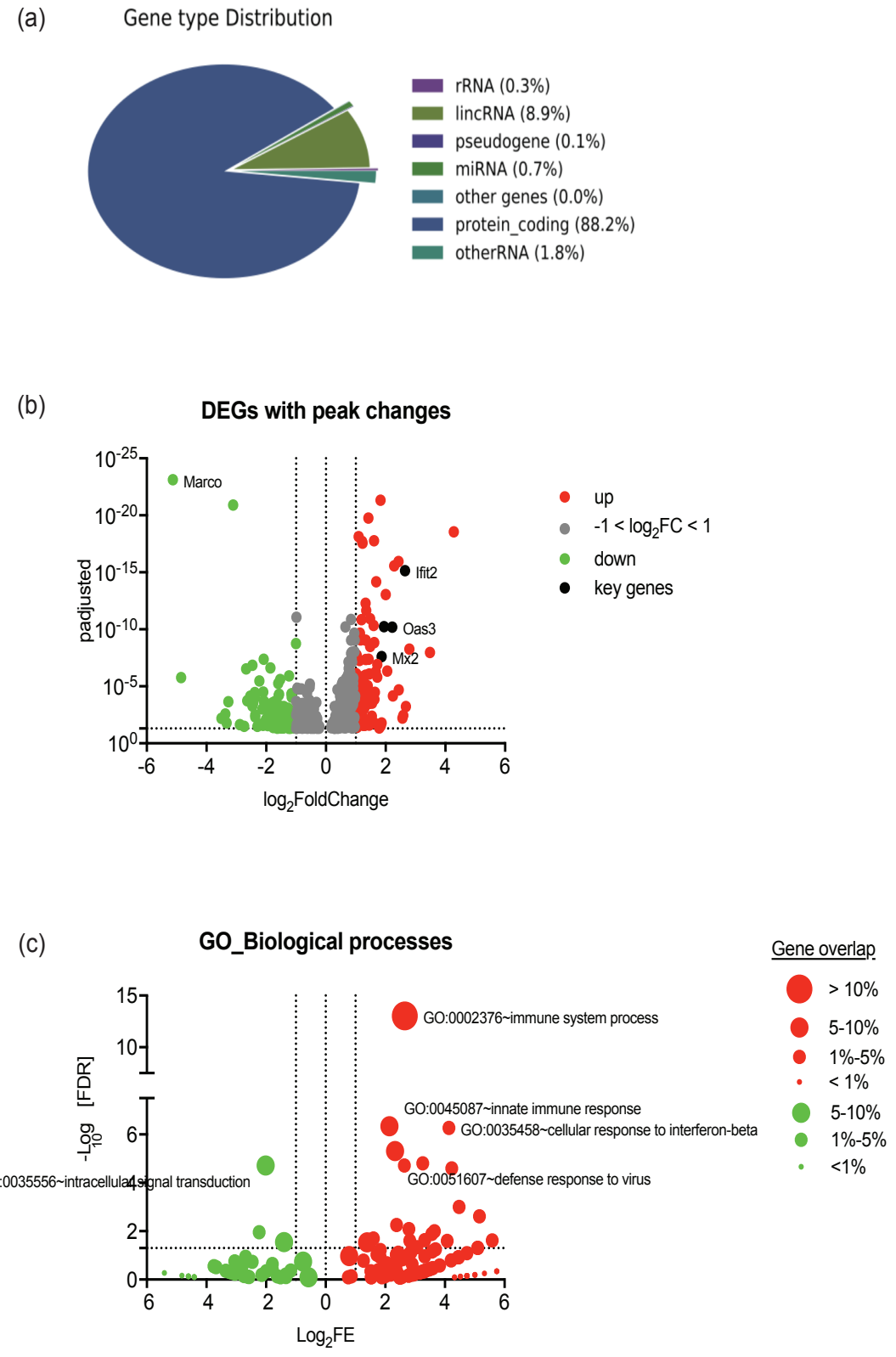

Figure 5.13: ATAC sequencing results; peak distribution and overlap between present peaks and DEGs by RNA sequencing: overleaf

Figure 5.13: ATAC sequencing results; peak distribution and overlap between present peaks and DEGs by RNA sequencing (a) Pie chart showing the distribution of gene types for the unique ATACseq peaks found, after applying filtration criteria. (b) Volcano plot showing fold change of the genes that were positive for presence of unique ATACseq peak, following HKMTI-1-005 treatment. (c) Volcano plot showing functional annotation by GO BP database of the DEGs that were positive for presence of unique ATACseq peak, following HKMTI-1-005 treatment. Size of the dot represents the percentage of genes in our DEGs list that overlap with the individual pathway gene list, red colour = upregulated genes, green colour = downregulated genes, rRNA= ribosomal RNA, lncRNA= long non-coding RNA, miRNA=microRNA, ATACseq= assay for transposase accessible chromatin using sequencing, DEGs=differentially expressed Genes, FE= fold enrichment, FDR=False Discovery Rate= p adjusted.

We then used the DAVID online Functional Annotation Tool (492) to add functional annotation on these 552 DEGs using Gene Ontology (GO) (493, 494), REACTOME (495), and KEGG (496) databases. Based on the Biological Processes sub-ontology of GO, the upregulated genes with open chromatin overlapped significantly with genes belonging to “immune system process” signatures (FDR=9.19e-14) (figure 5.13c). Amongst other significant pathways were “innate immune response” (FDR= 4.57e-06), “cellular response to IFN-β” (FDR= 5.34e-07) and “defence response to virus” (FDR= 0.001). This signifies that at least some of the intra-tumoural changes in chromatin conformation occur in genomic areas that are transcriptionally active and strongly associated with pathways of the immune system. The analysis results by the other GO sub-ontologies and the KEGG pathway are shown in Appendix 18.0.

The ERVs (n=51) that were found to be differentially expressed in treatment samples had no overlap with the ATACseq unique treatment peaks.

5.4 Discussion

The results of this chapter describe intra-tumoral changes in transcriptome and chromatin conformation after treatment with HKMTI-1-005 in *Trp53*$^{-/-}$ ID8 tumours. In terms of gene expression profiling, treated and vehicle samples separated apart very nicely, signifying a robust drug effect.

Major mediators of immune response, including *Cxcl10, Cxcl11, Ccl5, Stat2, GzmB, Tlr9* and *Klrk1* (which encodes the NK cell receptor NKG2D), were transcriptionally upregulated with treatment. Gene ontology (GO) analysis showed that the most significantly upregulated biological pathways were immune process and, more specifically, innate immune response and response to virus. Different sub-ontologies of GO confirmed that immune-related networks were overexpressed in treated tumours. Single sample Gene Set Enrichment Analysis also highlighted that tumours were enriched for gene sets associated with effector CD8^{+} cells, memory CD8^{+} cells, mature NK cells as well as stimulated macrophages and dendritic cells. By contrast, transcription networks related to induced Tregs were not enriched. Overall, these RNAseq results mirror changes seen by flow cytometry-assisted characterisation of the intra-tumoral immune cell populations.

By contrast, the ImmuCC tool results showed no significant changes between treatment and control samples. The ImmuCC tool was designed using public and experimental data and is currently the only tool available to help deconvolute immune cellular composition, based on gene expression profiling in murine systems. The design methodology of ImmuCC seems robust. However, it is not widely used yet by the scientific community and it has perhaps not been tested enough. Moreover, ImmuCC provides a crude cellular composition of the main cell types, without deciphering differentiation or activation state. Given that the flow cytometry results mainly support a change in differentiation (effector CD8^{+}) or marker expression (Ly6C on macrophages), it is perhaps unsurprising that the transcriptome changes do not necessarily reflect a change in the absolute number of immune cell populations, as defined by ImmuCC.

The differences seen in ERV transcription with treatment are extremely interesting. Expression of endogenous retro-elements is subject to epigenetic silencing (526, 527) with different mechanisms safeguarding this silencing in different cell types and stages of development and differentiation (528-530). Interestingly, H3K9me3, one of HKMTI-1-005 targets, has been established as a repressive mark on ERVs in embryonic stem cells (472, 528). ERVs can activate B cells when they present as nucleic acids intracellularly (475, 531). Moreover, ERV viral protein products can also be presented to T and B cells as antigens and induce spontaneous immune responses (532, 533). In patients with breast cancer, melanoma and testicular cancer, ERVs such as ERVH, ERVE and ERVK, were found to be overexpressed compared to normal tissue (534-538). Interestingly, antibodies against human ERVK – the same ERV that was upregulated in my RNAseq results- were found in the peripheral blood of patients with breast cancer; PBMCs from the same patients could mount an effector response after co-culture with autologous DCs that were pulsed with ERVK RNA or protein (537). T cell reactivity against ERVs has also been observed in other human cancers (534-536, 539, 540), other than breast cancer, however, there is paucity of data on murine models in the literature.

ERV analysis after HKMTI-1-005 treatment showed elements of ERVK being upregulated in different chromosomes or different locations of the same chromosome, whereas ERV1 retrotransposon was transcriptionally downregulated. Although the exact immunogenic effect of ERVK in mice has not yet been described, this increase in ERVs transcript, in conjunction with viral defence pathways being highly enriched in the treated tumours, indicates that de-repression of ERVs may be a mechanism of enhanced antigenicity following HKMTI-1-005 treatment.

We also conducted ATACseq analysis on the same tumour that the RNAseq interrogation was performed. Unsurprisingly, given the drug's mechanism of action, there were approximately 60,000 peaks of open chromatin region present in the treated tumours that were not present in the vehicle. It is worth noting that only narrow peaks were selected for the purposes of this analysis and in combination with our filtration criteria imposed on these narrow peaks, our

analysis would be described as fairly stringent. Nevertheless, out of approximately 7,800 genes found in areas of ATACseq peaks, 552 genes overlapped with DEGs found by RNAseq. Focusing on these, we once again discovered that these genes belong to immune response pathways, including innate and antiviral responses.

Interestingly, 60% of these areas of open chromatin were located in intergenic regions, a finding that lends itself to future interrogation, hypothesizing that perhaps these regions are related to enhancers/repressors that regulate gene expression remotely. We did not detect any retroelements within these areas of open chromatin and this could be a result of our relatively stringent ATACseq filtration criteria. Certainly, given the evolving role of ERVs in inducing anti-tumoral responses (312, 313, 347), it would be worthwhile re-interrogating the ATACseq results with perhaps more lenient filtration criteria and with a focus on intergenic regions. Overall, these findings confirm that HKMTI-1-005 treatment *in vivo* induces chromatin conformation changes that lead to transcriptional activation. This transcriptional activation mainly involved immune gene networks, and this would explain the changes in immune cellular composition seen in tumours by flow cytometry. One obvious question at this stage would be whether these chromatin and transcriptional changes actually occur in the tumour cells or represent immune cells in the tumour microenvironment and this question would require single-cell RNA and/or ATAC sequencing experiments to be answered. Irrespective of which cell population HKMTI-1-005 affects the most *in vivo,* the transcriptional changes seen, coupled with the functional changes observed by flow cytometry and the moderate therapeutic effect signifiy that an anti-tumour immune response takes place in the TME. Ovarian carcinoma prognosis is extremely depended on the hosts ability to mount an anti-tumour response (151, 154, 205, 541) and therefore, reinforcing local immune networks remains an important target.

Chapter 6. Concluding remarks

Chapter 6 Concluding remarks

Despite ample evidence that robust anti-tumour response is associated with improved patient survival, current immunotherapies have had disappointing results in OC, when compared to other tumour types such as melanoma, lung and renal cancers. Therefore, the need to discover ways to potentiate immune therapies for OC is critical. Recently, a lot of focus has been directed on discovering how cancer cells epigenetically alter the transcription of key immune genes, in order to achieve immune evasion. Epigenetic pathways, in contrast to many gene mutations, are "targetable" pharmacologically and therefore present actionable options for inhibition.

I started this project taking an agnostic approach to discovering novel epigenetic targets that could influence the transcription of a chemokine that is pivotal to leukocyte migration and activation. Through a medium-throughput screening, G9a histone methyltransferase emerged as a hit. In the face of growing evidence that EZH2 methyltransferase regulates immune cell fate very tightly and that it also works in conjunction with G9a, I proceeded with investigating the inhibition of both targets, G9a and EZH2, simultaneously. Dual blockade of the two targets revealed an improved therapeutic outcome and a measurable effect on reprogramming the TME to a more favourable immune cell composition. This included the presence of cytotoxic lymphocytes with effector properties, an increased frequency of natural killer cells, coupled with a reduction in immunosuppressive $CD4^+$ cells and changes in the expression of activating receptors on dendritic cells. These differences following treatment with dual G9a/EZH2 inhibition were observed at *in vivo* doses that were not above the GI_{50} dose (as tested on MDA-MB-231 and A2780 cell lines *in vitro*). This would support that combined G9a/EZH2 inhibition at sub-GI_{50} doses elicits an immunostimulatory response through means other than just cell killing. Moreover, treatment with G9a/EZH2 inhibition induced transcriptional and chromatin accessibility effects that supported the changes seen in the immune cellular composition.

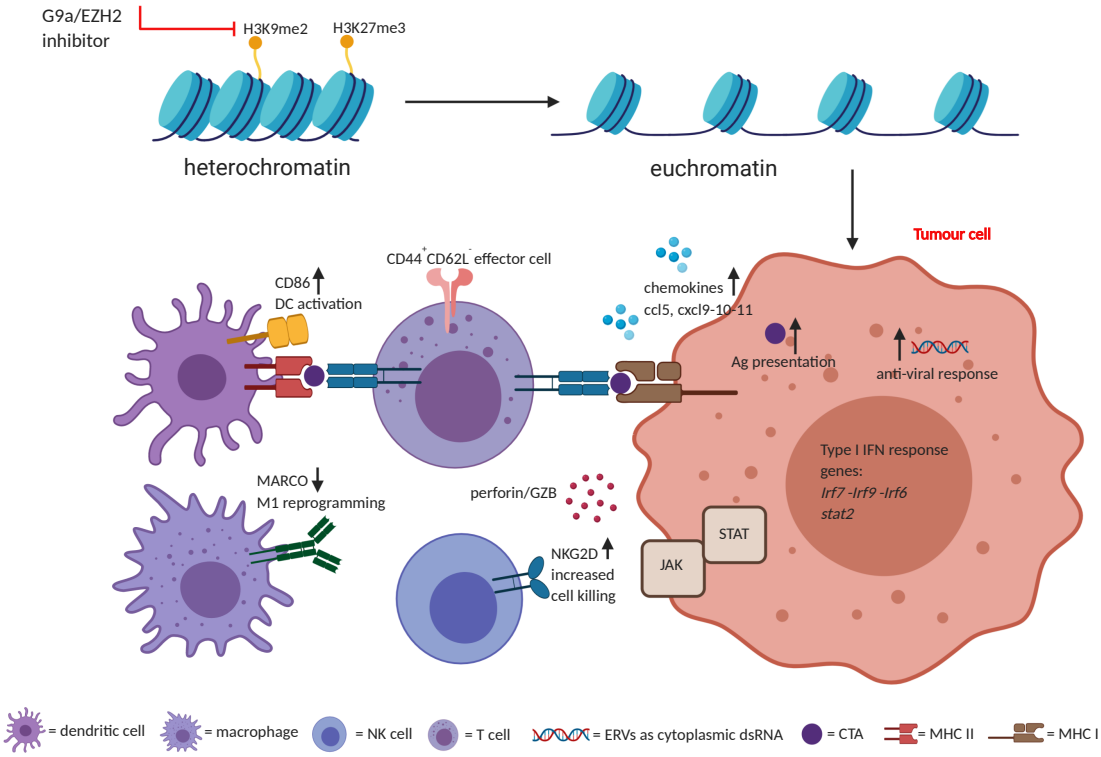

Figure 6.1: Immune related changes observed in vivo in *Trp53*$^{-/-}$ ID8 tumours, following treatment with the dual G9a/EZH2 inhibitor HKMTI-1-005. Reactivation of repressed endogenous retroviruses (ERVs) leads to the presence of double-stranded RNAs (dsRNAs) in the cytoplasm of cancer cells which in turn activates Type I IFN signalling pathways. Antigen presentation on tumour cells in increased via induction of MHC molecules expression. Tumour cells produce chemokines such as CCL5, CXCL9, CXCL10, CXCL11 which promote T cell homing and their activation to effector cells. Induction of CD86 receptor on DCs augments DC-T cell interaction and therefore T cell activation too. The reduction of MARCO receptor on macrophages has been associated with reprogramming to M1 phenotype (490, 491). The NK cell activating receptor NKG2D is increased following treatment, as well as the NK cell granzyme-B and perforin content.

Figure 6.1 summarises the most important immune-related changes observed *in vivo* following treatment with the dual G9a/EZH2 inhibitor HKMTI-1-005, as shown by flow cytometry and RNA/ATAC sequencing.

The results of the experiments described in Chapter 3 and Chapter 4 raise questions that are worthy of further exploration. Firstly, the therapeutic and immunomodulatory effects of HKMTI-1-005 need to be tested in other syngeneic

models of ovarian cancer to confirm that this effect is not specific to the ID8 model. Recently, new syngeneic models that recapitulate the TME of ovarian cancer have been produced (542). Some of these models were generated on the background of fallopian tube secretory epithelium (543) and will therefore be more representative of the human disease. Given the novelty of HKMTI-1-005, testing the reproducibility of the existing results on other mouse models will add to our observations on the safety of this compound and will help us establish a definitive treatment protocol.

Although the transcriptional results following HKMTI-1-005 treatment show concordance with the flow cytometry results, there is still uncertainty as to which cell type is the primary target of HMKTI-1-005. We know that HKMTI-1-005 treatment upregulates the secretion of chemokines CXCL9, CXCL10 and CCL5 by tumour cells *in vitro*, and this could, of course, contribute to mounting an immune response in the TME. However, our transcriptional and chromatin accessibility results on murine tumours were based on whole-tumour sequencing and therefore, do not specify which exact cell type underwent these changes the most. Single-cell sequencing following treatment with HKMTI-1-005 would be the best way forward to delineate the mechanism via which the compound exerts its function in the TME.

The contribution of ERV-K retroelements in the initiation of immune response following HKMTI-1-005 treatment should be further explored. ERV-K elements are overexpressed in ovarian tumours, when compared to normal ovaries which may of course not be the precursor tissue of origin in all cases. Furthermore, antibodies against ERV-K have been detected in the sera of OC patients in comparison to healthy controls (544). To further support the role of ERV-K in HKMTI-1-005-mediated immune stimulation, we could use ERV-K peptide to pulse autologous DCs and then perform DC-T cell co-culture to look for evidence of T cell stimulation, such as T cell proliferation, tumour cell killing and IFNγ release.

The type 1 IFN pathway, which is responsible for building anti-viral responses (545), was upregulated following HKMTI-1-005 treatment *in vivo*. This could

further support that G9a/EZH2 inhibition activates ERV expression, which in turn stimulates Type 1 IFN networks and the subsequent immune TME changes observed at the cellular level. Testing HKMTI-1-005 treatment while blocking the type 1 IFN pathway could therefore help us confirm that this is the principal mechanism of action for this compound. The transcriptional factor interferon-regulator factor 7 (IRF7), a critical step in type 1 IFN transcription, was found to be upregulated following HKMT-1-005 treatment *in vivo*. Crucially, IRF7 is principally phosphorylated by the TANK-binding kinase 1 (TBK1) (546). The McNeish lab has generated a *Tbk1*$^{-/-}$ ID8 subclone and an immediate future plan is to use HKMTI-1-005 treatment on mice harbouring *Trp53*$^{-/-}$ ID8 tumours versus *Trp53*$^{-/-}$ *tbk1*$^{-/-}$ ID8 tumours. If TBK1 deficiency reverses the immune changes seen in *tbk1* wild-type tumours, then we can be confident that HKMTI-1-005 mediates immune stimulation via the type 1 IFN pathway.

Although the effect of dual G9a/EZH2 blockade on survival and immune stimulation *in vivo* is robustly superior to G9a inhibition alone, dual blockade has not been compared to EZH2 inhibition. Experiments whereby dual inhibition is compared head-to head to single EZH2 inhibition are therefore warranted.

EZH2 is rapidly emerging as a therapeutic target in various cancers (427-429, 547-549). In OC, EZH2 regulates pathways of epithelial-to-mesenchymal transition, invasion, immune response, as well as resistance to chemotherapy (282, 425, 550-552). Novel EZH2 inhibitors, such as tazemetostat, CPI-1205, SHR2554 and PF06821497, have already entered early phase clinical trials in solid tumours and lymphomas (table 6.1). Tazemetostat, was granted FDA approval in refractory/relapsed follicular lymphoma patients with EZH2 mutations earlier this year and also showed promising results in solid tumours, like sarcoma (553). A phase 2 study on patients with relapsed/refractory lymphoma and either mutated or wild-type EZH2 showed exceptional objective responses [objective response rate 69% (95% CI 53–82%)] in the EZH2 mutated cohort and 35% (23–49%)] in the EZH2 wild-type cohort. Moreover, PFS in both patients with mutated EZH2 [13.8 months (95% CI 10.7–22.0)] and wild-type EZH2 [11.1 months (3.7–14.6)] was favourable (554).

Study title	Disease/condition	EZH2 inhibitor
Study of Tazemetostat in participants with relapsed/refractory B-cell Non-Hodgkin's Lymphoma with EZH2 gene mutation	Relapsed or Refractory B-cell Non-Hodgkin's Lymphoma	Tazemetostat
A phase II, multicenter study of the EZH2 Inhibitor Tazemetostat in adult subjects with INI1-Negative tumours or relapsed/refractory Synovial Sarcoma	Malignant Rhabdoid tumours, Rhabdoid tumours of the kidney, Atypical Teratoid Rhabdoid tumours, Selected Tumours with Rhabdoid Features, Synovial Sarcoma INI1-negative Tumours, Malignant Rhabdoid Tumour of Ovary, Renal Medullary Carcinoma, Epithelioid Sarcoma	Tazemetostat
Study of the EZH2 Inhibitor Tazemetostat in Malignant Mesothelioma	Mesothelioma, BAP1 Loss of Function	Tazemetostat
A phase 1 study of the EZH2 Inhibitor Tazemetostat in paediatric subjects with relapsed/refractory INI1-Negative tumours or Synovial Sarcoma	Rhabdoid Tumours, INI1-negative Tumours, Synovial Sarcoma, Malignant Rhabdoid Tumour of Ovary	Tazemetostat
Open-Label, multicenter, phase 1/2 study of Tazemetostat as a single agent in subjects with advanced solid tumours or with B-cell Lymphomas and Tazemetostat in combination with prednisolone in subjects with DLBCL	B-cell Lymphomas, Advanced Solid Tumours, Diffuse Large B-cell Lymphoma	Tazemetostat
A study evaluating CPI-1205 in patients with B-Cell Lymphomas	B-Cell Lymphoma	CPI-1205
ProSTAR: a study evaluating CPI-1205 in patients with metastatic castration resistant prostate cancer	Metastatic Castration Resistant Prostate Cancer	CPI-1205
Phase Ⅰ/Ⅱ study of SHR2554 in combination with SHR1701 in patients with advanced solid tumours and B-cell Lymphomas	Solid Tumour, Lymphoma	SHR2554 plus SHR1701
Testing the addition of the anti-cancer drug, tazemetostat, to the usual treatment (dabrafenib and trametinib) for metastatic melanoma that has progressed on the usual treatment	Cutaneous Melanoma, Metastatic Malignant Neoplasm in the Central Nervous System	Tazemetostat
Safety and efficacy of MAK683 in adult patients with advanced malignancies	Diffuse Large B-cell Lymphoma	MAK683 (EED inhibitor)
ORIOn-E: A Study Evaluating CPI-1205 in Patients with Advanced Solid Tumours	Advanced Solid Tumours	CPI-1205
Busulfan, Fludarabine, Donor Stem Cell Transplant, and Cyclophosphamide in treating patients with multiple myeloma or myelofibrosis	EZH2 Gene Mutation, myeloma, myelofibrosis	-
A Phase 1 study of SHR2554 in subjects with relapsed or refractory mature lymphoid neoplasms	Relapsed or Refractory Mature Lymphoid Neoplasms	SHR2554
PF-06821497 Treatment of Relapsed/Refractory SCLC, Castration Resistant Prostate Cancer, and Follicular Lymphoma	Small Cell Lung Cancer, Follicular Lymphoma, Castration Resistant Prostate Cancer, Diffuse Large B-Cell Lymphoma	PF-06821497
tazemetostat expanded access program for adults with epithelioid sarcoma	Epithelioid Sarcoma	Tazemetostat

Table 6.1: On-going early phase trials with EZH2 inhibition.

Cancer Types	Associated genes	References
	EZH2 overexpression	
Breast	*CK5*, *CK6*, *P-cadherin*, *CDKN1C*, *FOXC1*, Wnt/ß-catenin signaling, DNA repair (*RAD51*)	(428, 429, 555-559)
Prostate	*DAB2IP*, *p16*, *CDK4*, *MSMB*, *E-cadherin*, *Ras* (*KRAS*), *NF-κB* (*NFKB1*), *TIMP2*, *TIMP3*	(428, 429, 560-565)
Endometrial	*p16*, *E-cadherin*, *SFRP1*, *DKK3*, ß-*catenin*	(428, 566, 567)
Melanoma	*CDKN1A*, *DCK*, *AMD1*, *WDR19*	(236, 432, 557, 568)
Ovarian	*VASH1*	(426)
Glioblastoma	*BMPR1B*	(557, 569)
Lung	*DKK1*	(570)
Natural killer/T-cell lymphoma	*Cyclin D1*	(571)
Hepatocellular	Unknown	(572)
Bladder	Unknown	(557, 573, 574)
	EZH2 mutation (gain of function)	
Non-Hodgkin's lymphoma or melanoma	*CDKN2A*, *CDKN1A*, *BLIMP1*	(575-579)

Table 6.2: EZH2 overexpression and gain-of-function mutations in cancers and affected targets

Undoubtedly, the promising results observed in lymphoma will encourage further research in other tumour types, especially those with aberrant EZH2 (table 6.2). With regards to G9a histone methyltransferase, there is certainly preclinical evidence for its role in tumorigenicity in various cancer types (377, 420-422, 580) and studies on human samples are gradually starting to emerge (411, 416-418, 467). G9a inhibitors are currently being optimised but have not yet entered clinical development (376, 379).

The prospect of inhibiting both methyltransferases with a dual inhibitor is therefore an exciting one, as we will be able to synergistically abrogate gene networks that promote tumorigenesis, either via blocking the conventional proliferative pathways, or via re-activation of immunostimulatory signals. Given the profound toxicity that is observed with the combination immunotherapies in clinical practice (581), an attempt to augment immune checkpoint inhibition with epigenetic modifiers (as opposed to additional checkpoint antibodies), may represent a safer approach going forward. The preclinical results presented in

this thesis are perhaps modest therapeutically but provide good evidence that dual inhibition of G9a/EZH2 induces favourable changes in the tumour immune microenvironment of ovarian cancer. In retrospect, and with the knowledge that achieving a therapeutic response with current immunotherapies in ovarian cancer is challenging, it is perhaps worthwhile investigating the role of G9a/EZH2 inhibition in other tumour types too. These could, for example, be either lymphoma, where EZH2 inhibition has already showed a proven therapeutic effect (554) or cutaneous melanoma, where pre-clinically, EZH2 has been found to control adaptive resistance to immunotherapy (432).

Overall, the results of this thesis support that dual blockade of G9a/EZH2 histone methyltransferases modulates anti-tumour response and warrants further investigation towards clinical development.

Appendix

Appendix 1 – RT2 Profiler PCR Array Mouse Chemokines and Cytokines; quality control and normalisation results.

Position	RefSeq Number	Symbol	Description
A01	NM_009605	Adipoq	Adiponectin, C1Q and collagen domain containing
A02	NM_007553	Bmp2	Bone morphogenetic protein 2
A03	NM_007554	Bmp4	Bone morphogenetic protein 4
A04	NM_007556	Bmp6	Bone morphogenetic protein 6
A05	NM_007557	Bmp7	Bone morphogenetic protein 7
A06	NM_011329	Ccl1	Chemokine (C-C motif) ligand 1
A07	NM_011330	Ccl11	Chemokine (C-C motif) ligand 11
A08	NM_011331	Ccl12	Chemokine (C-C motif) ligand 12
A09	NM_011332	Ccl17	Chemokine (C-C motif) ligand 17
A10	NM_011888	Ccl19	Chemokine (C-C motif) ligand 19
A11	NM_011333	Ccl2	Chemokine (C-C motif) ligand 2
A12	NM_016960	Ccl20	Chemokine (C-C motif) ligand 20
B01	NM_009137	Ccl22	Chemokine (C-C motif) ligand 22
B02	NM_019577	Ccl24	Chemokine (C-C motif) ligand 24
B03	NM_011337	Ccl3	Chemokine (C-C motif) ligand 3
B04	NM_013652	Ccl4	Chemokine (C-C motif) ligand 4
B05	NM_013653	Ccl5	Chemokine (C-C motif) ligand 5
B06	NM_013654	Ccl7	Chemokine (C-C motif) ligand 7
B07	NM_011616	Cd40lg	CD40 ligand
B08	NM_011617	Cd70	CD70 antigen
B09	NM_170786	Cntf	Ciliary neurotrophic factor
B10	NM_007778	Csf1	Colony stimulating factor 1 (macrophage)
B11	NM_009969	Csf2	Colony stimulating factor 2 (granulocyte-macrophage)
B12	NM_009971	Csf3	Colony stimulating factor 3 (granulocyte)
C01	NM_007795	Ctf1	Cardiotrophin 1
C02	NM_009142	Cx3cl1	Chemokine (C-X3-C motif) ligand 1
C03	NM_008176	Cxcl1	Chemokine (C-X-C motif) ligand 1
C04	NM_021274	Cxcl10	Chemokine (C-X-C motif) ligand 10
C05	NM_019494	Cxcl11	Chemokine (C-X-C motif) ligand 11
C06	NM_021704	Cxcl12	Chemokine (C-X-C motif) ligand 12
C07	NM_018866	Cxcl13	Chemokine (C-X-C motif) ligand 13
C08	NM_023158	Cxcl16	Chemokine (C-X-C motif) ligand 16
C09	NM_203320	Cxcl3	Chemokine (C-X-C motif) ligand 3
C10	NM_009141	Cxcl5	Chemokine (C-X-C motif) ligand 5

Appendix 1 – RT2 ProfilerTM PCR Array Mouse Chemokines and Cytokines; quality control and normalisation results; continued.

Position	RefSeq Number	Symbol	Description
C11	NM_008599	Cxcl9	Chemokine (C-X-C motif) ligand 9
C12	NM_010177	Fasl	Fas ligand (TNF superfamily, member 6)
D01	NM_008155	Gpi1	Glucose phosphate isomerase 1
D02	NM_010406	Hc	Haemolytic complement
D03	NM_010503	Ifna2	Interferon alpha 2
D04	NM_008337	Ifng	Interferon gamma
D05	NM_010548	Il10	Interleukin 10
D06	NM_008350	Il11	Interleukin 11
D07	NM_008351	Il12a	Interleukin 12A
D08	NM_001303244	Il12b	Interleukin 12b
D09	NM_008355	Il13	Interleukin 13
D10	NM_008357	Il15	Interleukin 15
D11	NM_010551	Il16	Interleukin 16
D12	NM_010552	Il17a	Interleukin 17A
E01	NM_145856	Il17f	Interleukin 17F
E02	NM_008360	Il18	Interleukin 18
E03	NM_010554	Il1a	Interleukin 1 alpha
E04	NM_008361	Il1b	Interleukin 1 beta
E05	NM_031167	Il1rn	Interleukin 1 receptor antagonist
E06	NM_008366	Il2	Interleukin 2
E07	NM_021782	Il21	Interleukin 21
E08	NM_016971	Il22	Interleukin 22
E09	NM_031252	Il23a	Interleukin 23, alpha subunit p19
E10	NM_053095	Il24	Interleukin 24
E11	NM_145636	Il27	Interleukin 27
E12	NM_010556	Il3	Interleukin 3
F01	NM_021283	Il4	Interleukin 4
F02	NM_010558	Il5	Interleukin 5
F03	NM_001314054	Il6	Interleukin 6
F04	NM_008371	Il7	Interleukin 7
F05	NM_008373	Il9	Interleukin 9
F06	NM_008501	Lif	Leukemia inhibitory factor
F07	NM_010735	Lta	Lymphotoxin A
F08	NM_008518	Ltb	Lymphotoxin B
F09	NM_010798	Mif	Macrophage migration inhibitory factor
F10	NM_010834	Mstn	Myostatin
F11	NM_013611	Nodal	Nodal
F12	NM_001013365	Osm	Oncostatin M
G01	NM_019932	Pf4	Platelet factor 4

Appendix 1 – RT2 ProfilerTM PCR Array Mouse Chemokines and Cytokines; quality control and normalisation results; continued.

Position	RefSeq Number	Symbol	Description
G02	NM_023785	Ppbp	Pro-platelet basic protein
G03	NM_009263	Spp1	Secreted phosphoprotein 1
G04	NM_009367	Tgfb2	Transforming growth factor, beta 2
G05	NM_009379	Thpo	Thrombopoietin
G06	NM_013693	Tnf	Tumour necrosis factor
G07	NM_008764	Tnfrsf11b	Tumour necrosis factor receptor superfamily, member 11b (osteoprotegerin)
G08	NM_009425	Tnfsf10	Tumour necrosis factor (ligand) superfamily, member 10
G09	NM_011613	Tnfsf11	Tumour necrosis factor (ligand) superfamily, member 11
G10	NM_033622	Tnfsf13b	Tumour necrosis factor (ligand) superfamily, member 13b
G11	NM_009505	Vegfa	Vascular endothelial growth factor A
G12	NM_008510	Xcl1	Chemokine (C motif) ligand 1
H01	NM_007393	Actb	Actin, beta
H02	NM_009735	B2m	Beta-2 microglobulin
H03	NM_008084	Gapdh	Glyceraldehyde-3-phosphate dehydrogenase
H04	NM_010368	Gusb	Glucuronidase, beta
H05	NM_008302	Hsp90ab1	Heat shock protein 90 alpha (cytosolic), class B member 1
H06	SA_00106	MGDC	Mouse Genomic DNA Contamination
H07	SA_00104	RTC	Reverse Transcription Control
H08	SA_00104	RTC	Reverse Transcription Control
H09	SA_00104	RTC	Reverse Transcription Control
H10	SA_00103	PPC	Positive PCR Control
H11	SA_00103	PPC	Positive PCR Control
H12	SA_00103	PPC	Positive PCR Control

Data quality control (QC)	
Quality checks performed and results	
Test Performed	**Test Result**
1. PCR Array Reproducibility	All Samples Passed
2. RT Efficiency	All Samples Passed
3. Genomic DNA Contamination	All Samples Passed

Appendix 1 – RT2 ProfilerTM PCR Array Mouse Chemokines and Cytokines; quality control and normalisation results; continued.

Normalization analysis

Automatic selection from full panel

Groups	Samples	Bmp4	Cntf	Geometric Mean	Average Geometric Mean
Control Group	IFNg	21.191742	26.935425	23.89	24.05
Control Group	IFNg	21.209953	26.528824	23.72	
Control Group	IFNg	21.926346	27.47536	24.54	
Group 2	UNC0642	21.601772	26.78769	24.06	24.09
Group 2	UNC0642	21.47843	26.507425	23.86	
Group 2	UNC0642	21.993658	26.983818	24.36	
Group 3	HKMTI-1-005	21.146624	27.272264	24.01	23.87
Group 3	HKMTI-1-005	20.72649	26.189022	23.30	
Group 3	HKMTI-1-005	21.67379	27.24161	24.30	

Appendix 2 - List of primers used for NGS RNAseq

Product	Index Primer Sequence	Expected Index Primer Sequence Read
NEBNext Index 7 Primer for Illumina	5´-CAAGCAGAAGACGGCATACGAGATGATCTGGTGACTG GAGTTCAGACGTGTGCTCTTCCGATC-s-T-3´	CAGATC
NEBNext Index 12 Primer for Illumina	5´-CAAGCAGAAGACGGCATACGAGATTACAAGGTGACTG GAGTTCAGACGTGTGCTCTTCCGATC-s-T-3´	CTTGTA
NEBNext Index 13 Primer for Illumina	5´-CAAGCAGAAGACGGCATACGAGATTGTTGACTGTGACT GGAGTTCAGACGTGTGCTCTTCCGATC-s-T-3´	AGTCAA
NEBNext Index 14 Primer for Illumina	5´-CAAGCAGAAGACGGCATACGAGATACGGAACTGTGAC TGGAGTTCAGACGTGTGCTCTTCCGATC-s-T-3´	AGTTCC
NEBNext Index 15 Primer for Illumina	5´-CAAGCAGAAGACGGCATACGAGATTCTGACATGTGACT GGAGTTCAGACGTGTGCTCTTCCGATC-s-T-3´	ATGTCA
NEBNext Index 16 Primer for Illumina	5´-CAAGCAGAAGACGGCATACGAGATGCGGACGGGTGAC TGGAGTTCAGACGTGTGCTCTTCCGATC-s-T-3´	CCGTCC
NEBNext Index 18 Primer for Illumina	5´-CAAGCAGAAGACGGCATACGAGATGTGCGGACGTGAC TGGAGTTCAGACGTGTGCTCTTCCGATC-s-T-3´	GTCCGC
NEBNext Index 19 Primer for Illumina	5´-CAAGCAGAAGACGGCATACGAGATCGTTTCACGTGACT GGAGTTCAGACGTGTGCTCTTCCGATC-s-T-3´	GTGAAA
NEBNext Index 20 Primer for Illumina	5´-CAAGCAGAAGACGGCATACGAGATAAGGCCACGTGAC TGGAGTTCAGACGTGTGCTCTTCCGATC-s-T-3´	GTGGCC
NEBNext Index 21 Primer for Illumina	5´-CAAGCAGAAGACGGCATACGAGATTCCGAAACGTGAC TGGAGTTCAGACGTGTGCTCTTCCGATC-s-T-3´	GTTTCG
NEBNext Index 22 Primer for Illumina	5´-CAAGCAGAAGACGGCATACGAGATTACGTACGGTGACT GGAGTTCAGACGTGTGCTCTTCCGATC-s-T-3´	CGTACG
NEBNext Index 23 Primer for Illumina	5´-CAAGCAGAAGACGGCATACGAGATATCCACTCGTGACT GGAGTTCAGACGTGTGCTCTTCCGATC-s-T-3´	GAGTGG
NEBNext Index 25 Primer for Illumina	5´-CAAGCAGAAGACGGCATACGAGATATATCAGTGTGACT GGAGTTCAGACGTGTGCTCTTCCGATC-s-T-3´	ACTGAT
NEBNext Index 27 Primer for Illumina	5´-CAAGCAGAAGACGGCATACGAGATAAAGGAATGTGACT GGAGTTCAGACGTGTGCTCTTCCGATC-s-T-3´	ATTCCT
NEBNext Adaptor for Illumina	5´-/5Phos/GAT CGG AAG AGC ACA CGT CTG AAC TCC AGT CUA CAC TCT TTC CCT ACA CGA CGC TCT TCC GAT C-s-T-3´	N/A
NEBNext Universal PCR Primer for Illumina	5´-AAT GAT ACG GCG ACC ACC GAG ATC TAC ACT CTT TCC CTA CAC GAC GCT CTT CCG ATC-s-T-3´	N/A

Appendix 3 – List of Sigma-Aldrich customised primers used for ATACseq

Ad1_universal primer	AATGATACGGCGACCACCGAGATCTACACTCGTCGGCAGCGTCAGATGTG
Ad2.2_CGTACTAG	CAAGCAGAAGACGGCATACGAGATCTAGTACGGTCTCGTGGGCTCGGAGATGT
Ad2.3_AGGCAGAA	CAAGCAGAAGACGGCATACGAGATTTCTGCCTGTCTCGTGGGCTCGGAGATGT
Ad2.4_TCCTGAGC	CAAGCAGAAGACGGCATACGAGATGCTCAGGAGTCTCGTGGGCTCGGAGATGT
Ad2.5_GGACTCCT	CAAGCAGAAGACGGCATACGAGATAGGAGTCCGTCTCGTGGGCTCGGAGATGT
Ad2.6_TAGGCATG	CAAGCAGAAGACGGCATACGAGATCATGCCTAGTCTCGTGGGCTCGGAGATGT
Ad2.7_CTCTCTAC	CAAGCAGAAGACGGCATACGAGATGTAGAGAGGTCTCGTGGGCTCGGAGATGT
Ad2.8_CAGAGAGG	CAAGCAGAAGACGGCATACGAGATCCTCTCTGGTCTCGTGGGCTCGGAGATGT
Ad2.9_GCTACGCT	CAAGCAGAAGACGGCATACGAGATAGCGTAGCGTCTCGTGGGCTCGGAGATGT
Ad2.11_AAGAGGCA	CAAGCAGAAGACGGCATACGAGATTGCCTCTTGTCTCGTGGGCTCGGAGATGT
Ad2.12_GTAGAGGA	CAAGCAGAAGACGGCATACGAGATTCCTCTACGTCTCGTGGGCTCGGAGATGT
Ad2.13_GTCGTGAT	CAAGCAGAAGACGGCATACGAGATATCACGACGTCTCGTGGGCTCGGAGATGT
Ad2.14_ACCACTGT	CAAGCAGAAGACGGCATACGAGATACAGTGGTGTCTCGTGGGCTCGGAGATGT

Appendix 4 – Qiagen 84-chemokine/cytokine array results

		UNC0642		HKMTI-1-005	
Position	Gene Symbol	Fold Change (comparing to IFNγ group)			
		Fold Change	p-value	Fold Change	p-value
B04	Ccl4	11.82	0.060873	17.37	0.128745
C05	Cxcl11	11.56	0.253966	2.05	0.725345
D08	Il12b	9.59	0.041091	0.75	0.973842
D02	Hc	9.27	0.055592	2.36	0.339248
F10	Mstn	8.39	0.374313	0.88	0.910363
A10	Ccl19	5.09	0.170579	44	0.019007
G02	Ppbp	4.51	0.357471	0.76	0.644625
D05	Il10	3.93	0.147522	20.93	0.000607
G08	Tnfsf10	3.43	0.234453	4.09	0.06
A06	Ccl1	3.15	0.171359	4.87	0.121683
B03	Ccl3	2.78	0.371635	4.58	0.246707
F01	Il4	2.42	0.38943	1.52	0.478127
A08	Ccl12	2.31	0.39564	47.81	0.0007
F08	Ltb	2.29	0.998804	0.44	0.466683
A04	Bmp6	2.18	0.08957	3.11	0.192012
D04	Ifng	2.12	0.680755	0.46	0.450364
G05	Thpo	1.95	0.064816	0.47	0.121168
A12	Ccl20	1.83	0.077036	0.5	0.06474
F02	Il5	1.76	0.124181	0.19	0.107899
D07	Il12a	1.7	0.173529	0.18	0.031004
B05	Ccl5	1.6	0.076661	14.45	0.000046
G10	Tnfsf13b	1.59	0.469918	0.4	0.254942
E01	Il17f	1.58	0.225755	3.48	0.005584
H02	B2m	1.56	0.186165	1.6	0.175551
C10	Cxcl5	1.52	0.662993	0.21	0.365159
D10	Il15	1.47	0.060979	1.96	0.010728
F11	Nodal	1.41	0.500656	0.61	0.30745
H03	Gapdh	1.31	0.092891	1.82	0.012692
B02	Ccl24	1.31	0.546409	0.61	0.30745
E10	Il24	1.25	0.267759	58.81	0.32879
E11	Il27	1.24	0.469555	2.78	0.869944
D01	Gpi1	1.15	0.092445	1.24	0.026233
B11	Csf2	1.13	0.531199	4.86	0.003689
C08	Cxcl16	1.04	0.454877	1.23	0.201107
E05	Il1rn	1.04	0.565877	1.13	0.093138
D11	Il16	1.03	0.934816	0.63	0.356392

Appendix 4 – Qiagen 84-chemokine/cytokine array results

		UNC0642		HKMTI-1-005	
Position	Gene Symbol	Fold Change (comparing to IFNγ group)			
		Fold Change	p-value	Fold Change	p-value
G09	Tnfsf11	1	0.79868	0.61	0.305122
B01	Ccl22	0.98	0.882357	0.61	0.30745
B06	Ccl7	0.97	0.762624	3.95	0.013952
H05	Hsp90ab1	0.96	0.559203	0.89	0.16751
C04	Cxcl10	0.95	0.698051	3.15	0.00114
F09	Mif	0.89	0.609265	1.01	0.956383
D12	Il17a	0.85	0.657807	0.61	0.30745
E06	Il2	0.84	0.634834	0.61	0.30745
C01	Ctf1	0.83	0.437999	0.52	0.092732
A02	Bmp2	0.83	0.970775	0.27	0.287127
C02	Cx3cl1	0.81	0.601326	0.66	0.329006
A11	Ccl2	0.74	0.316856	1.13	0.811983
H01	Actb	0.74	0.046139	0.81	0.170382
B09	Cntf	0.71	0.224235	0.65	0.121259
H04	Gusb	0.69	0.046298	0.48	0.009048
B07	Cd40lg	0.67	0.369835	0.61	0.30745
G07	Tnfrsf11b	0.67	0.367623	0.61	0.30745
G03	Spp1	0.66	0.200017	1.02	0.987356
G11	Vegfa	0.66	0.073896	0.82	0.308169
F06	Lif	0.63	0.249797	2.06	0.12864
C12	Fasl	0.62	0.68293	0.55	0.760665
C11	Cxcl9	0.61	0.329345	22.02	0.000674
E04	Il1b	0.61	0.329345	0.61	0.30745
E12	Il3	0.61	0.329345	0.61	0.30745
F12	Osm	0.61	0.329345	0.61	0.30745
C03	Cxcl1	0.57	0.398408	0.03	0.181216
G01	Pf4	0.55	0.96465	0.22	0.189743
G06	Tnf	0.55	0.459996	0.19	0.372076
F04	Il7	0.54	0.339832	1.15	0.749511
A07	Ccl11	0.53	0.569551	0.92	0.958049
A03	Bmp4	0.52	0.061966	0.74	0.19583
A09	Ccl17	0.5	0.084307	0.11	0.014617
C06	Cxcl12	0.49	0.002154	0.15	0.000275
B10	Csf1	0.47	0.030057	0.13	0.002925
D09	Il13	0.44	0.59873	0.18	0.348525
E09	Il23a	0.43	0.166532	0.14	0.067

Appendix 4 – Qiagen 84-chemokine/cytokine array results

		UNC0642		HKMTI-1-005	
Position	Gene Symbol	Fold Change (comparing to IFNγ group)			
		Fold Change	p-value	Fold Change	p-value
F05	Il9	0.4	0.397561	1.44	0.986326
B08	Cd70	0.37	0.031626	0.02	0.007674
G04	Tgfb2	0.34	0.050918	0.13	0.02156
E07	Il21	0.33	0.16531	0.33	0.161159
D06	Il11	0.32	0.002715	0.93	0.448165
D03	Ifna2	0.31	0.448486	0.61	0.426099
B12	Csf3	0.27	0.118574	1.17	0.899362
E08	Il22	0.26	0.369765	0.26	0.369176
C07	Cxcl13	0.26	0.003597	0.02	0.001258
E03	Il1a	0.24	0.487672	0.43	0.344642
E02	Il18	0.22	0.002375	0.02	0.000833
G12	Xcl1	0.14	0.28911	0.18	0.41522
F03	Il6	0.11	0.159282	5.21	0.245897
A01	Adipoq	0.1	0.184982	0.1	0.184629
C09	Cxcl3	0.08	0.003854	0.05	0.002488
F07	Lta	0.05	0.112964	2.02	0.725094
A05	Bmp7	0.03	0.036997	0.06	0.047809

Appendix 5 – In vivo study conducted by CrownBio to define the best tolerated dose of HKMTI-1-005 (named SS-405 below).

Group	Treatment Description	Dose Route	Dose Frequency & Duration	Dose Vol. (ml/kg)
1	Vehicle	*i.p.*	BID x 3 weeks (paused at weekends)	10
2	Compound 1 – SS-405, 20mg/kg	*i.p.*		10
3	Compound 2 – SS-408, 10mg/kg	*i.p.*		10

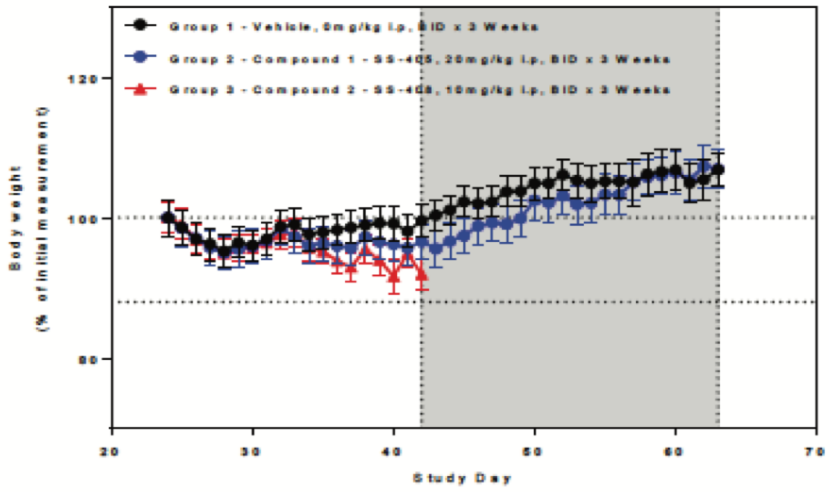

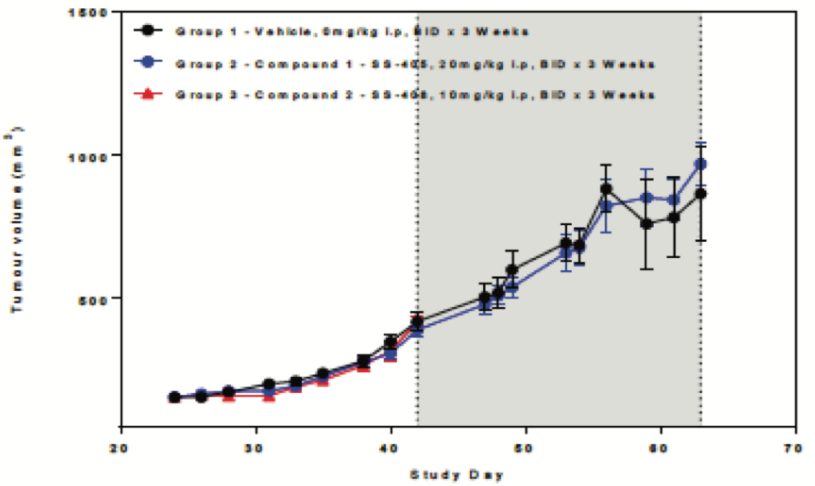

Appendix 6 – Pharmacokinetic studies performed by Institute of Cancer Research (ICR)

Dose (mg/Kg)	Mouse	Route	HL_Lambda_z (hr)	Tmax (hr)	Cmax (nmol/L)	AUCINF_obs (hr*nmol/L)	AUClast (hr*nmol/L)	Cl_obs (L/hr)	Vz_obs (L)	F (AUCinf)	F (AUClast)
5	2	iv	7.47	0.083	36600	72087	65444	0.002	0.024	0.117	0.117
5	3	iv	8.41	0.083	24300	62738	54583	0.003	0.034		
5	4	iv	7.90	0.083	29800	64440	57240	0.003	0.029		
5	6	po	6.86	4	621	7676	6949	0.003	0.026		
5	7	po	7.76	1	709	8047	7070	0.003	0.030		
5	8	po	7.72	4	552	7569	6646	0.003	0.029		
5	10	ip	7.77	0.5	5350	29405	25831	0.006	0.065	0.48	0.46
5	11	ip	7.94	0.5	6400	31207	27096	0.006	0.064		
5	12	ip	9.22	0.5	6350	35470	29062	0.005	0.061		

Appendix 7 – Pharmacokinetic studies performed by Institute of Cancer Research (ICR)

Mouse treatment at 5 mg/kg

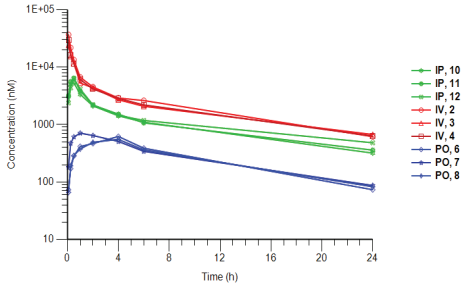

HKMTI-1-005 40 mg/kg IP - simulation

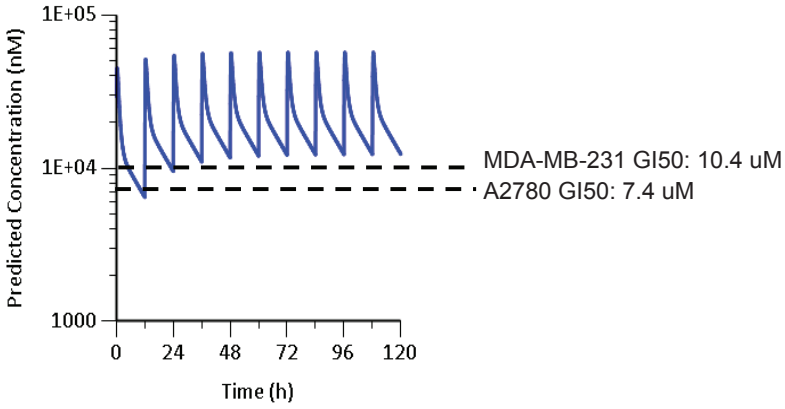

HKMTI-1-005 20 mg/kg IP - simulation

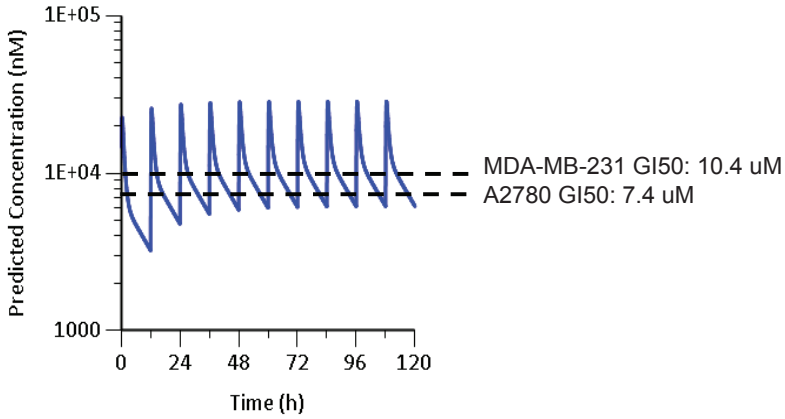

Appendix 8 – Gating strategy for CD44 and CD62L staining

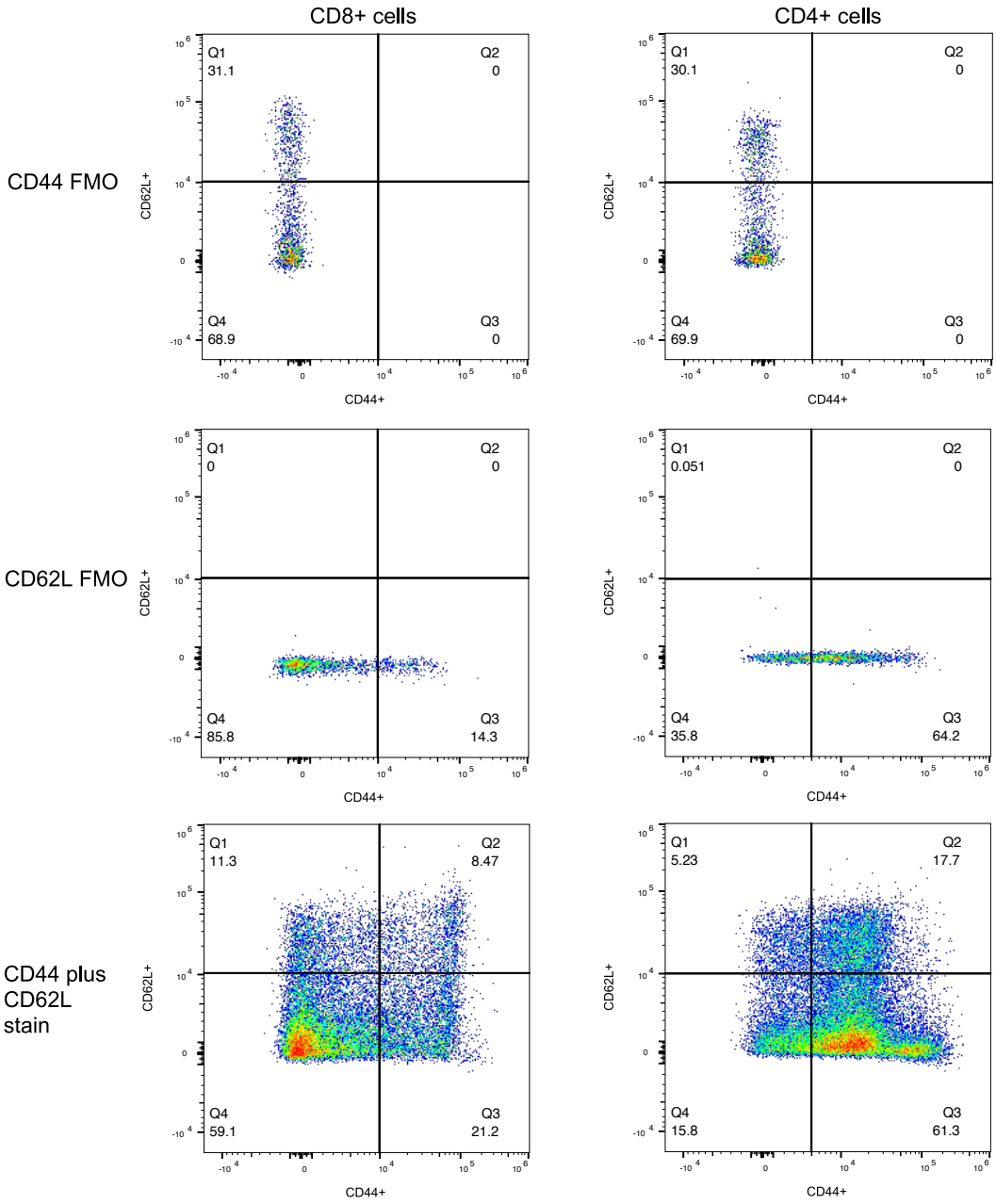

Appendix 9 – Gating strategy for intracellular chemokine staining

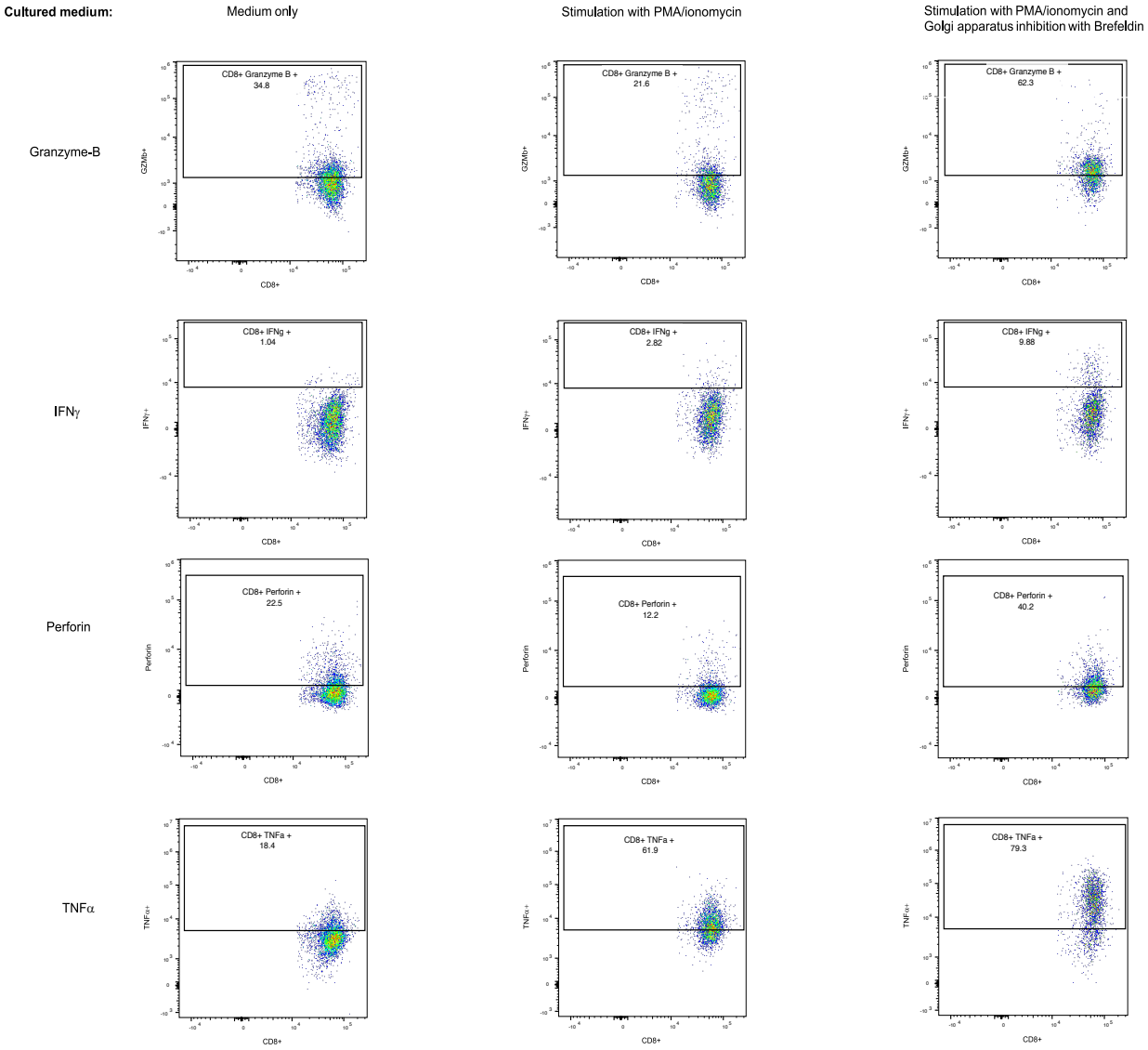

Appendix 10 – Tumour-associated macrophage gating strategy according to the literature

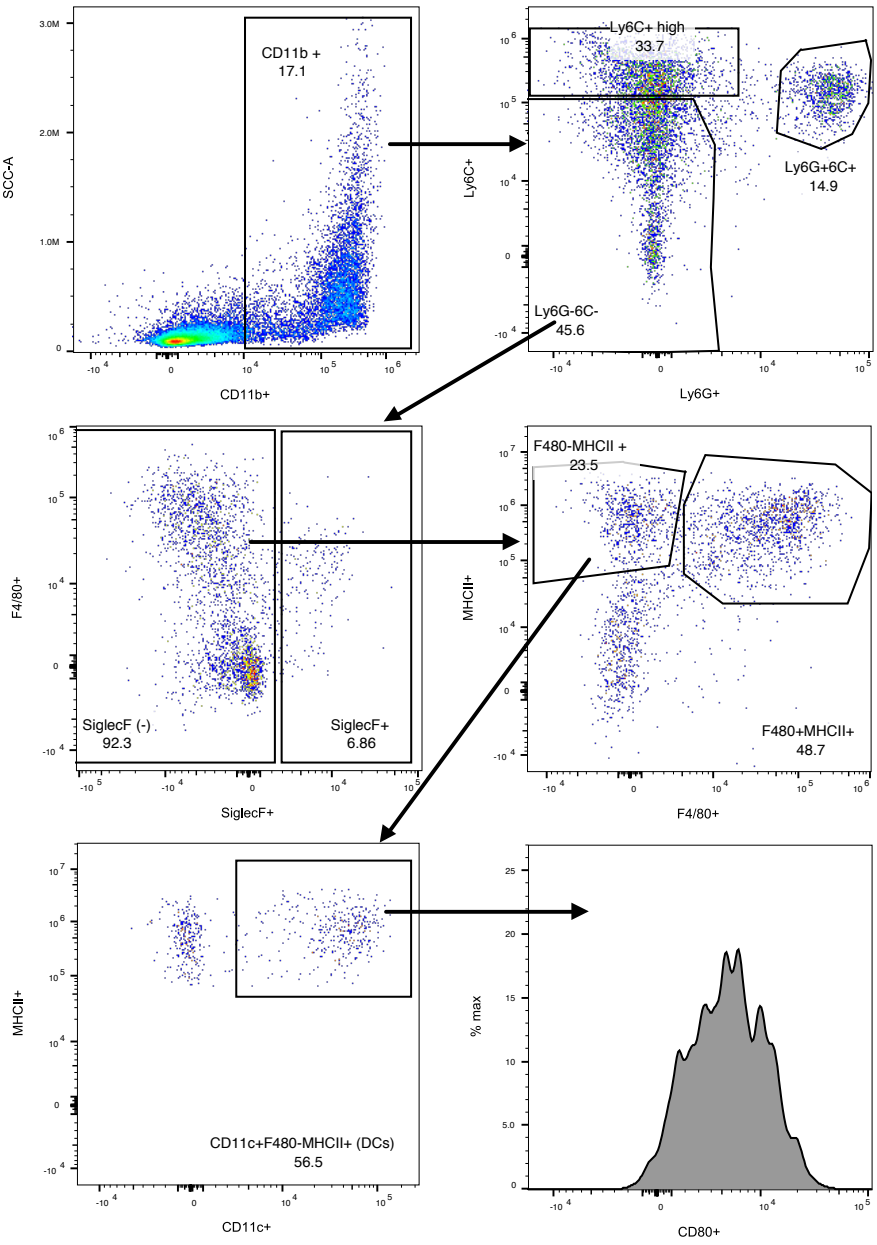

Appendix 11 - Murine blood test results at humane endpoint

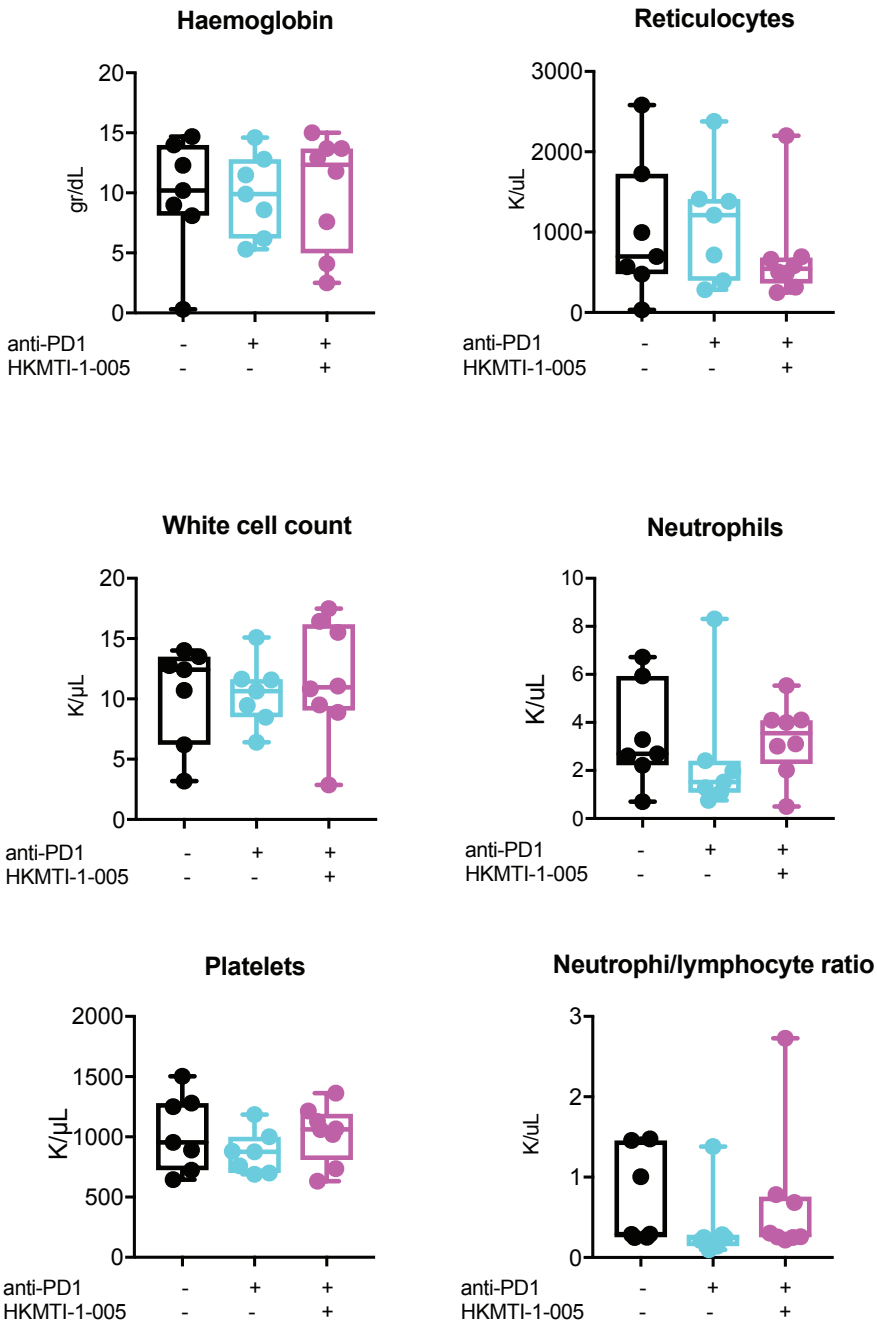

Appendix 12 – Mice weight and tumour weight with 2-week treatment of HKMTI-1-005; four replicate experiments merged

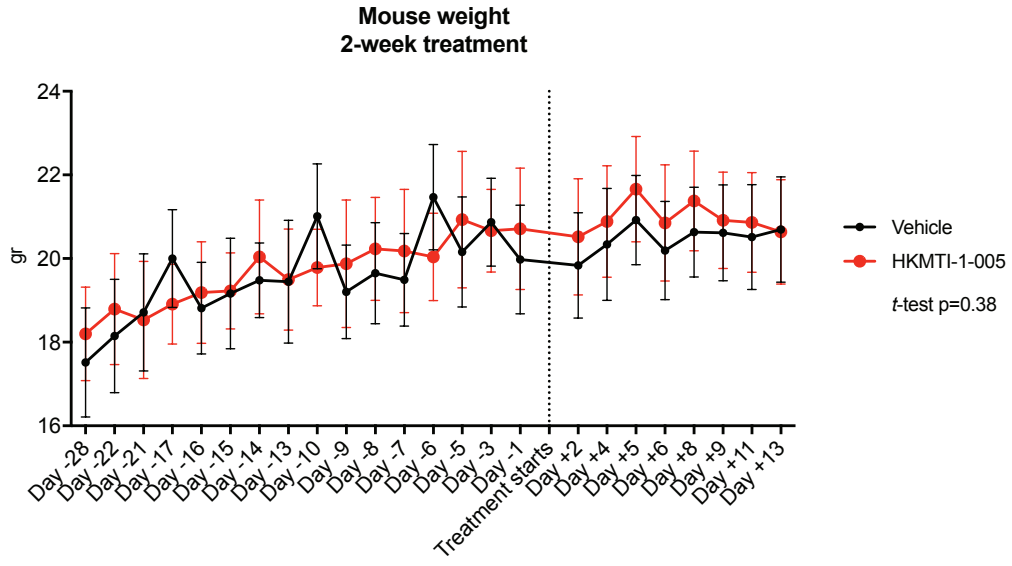

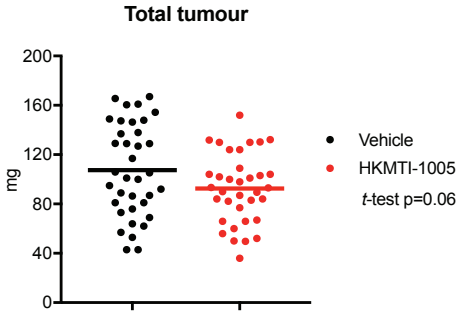

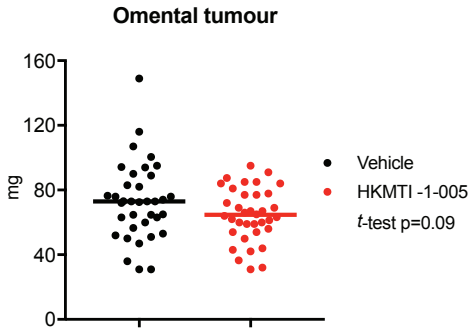

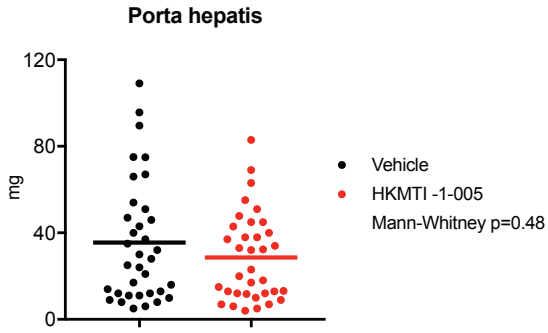

Appendix 13 – RNA electropherograms by Agilent 2200 TapeStation for RIN estimation

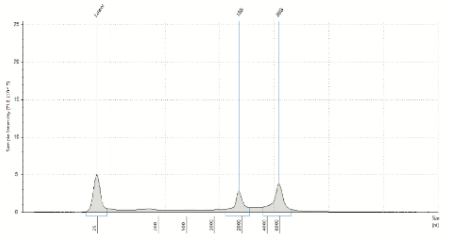

Sample Table

Well	RINe	28S/18S (Area)	Conc. [ng/µl]	Sample Description	Alert	Observations
C1	8.8	1.6	65.5	PS04b		

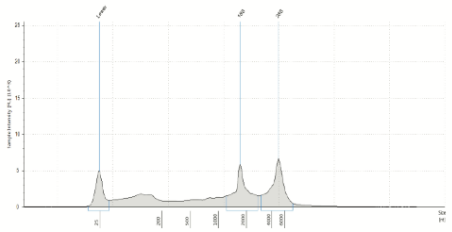

Sample Table

Well	RINe	28S/18S (Area)	Conc. [ng/µl]	Sample Description	Alert	Observations
D1	7.2	1.2	162	PS04c		

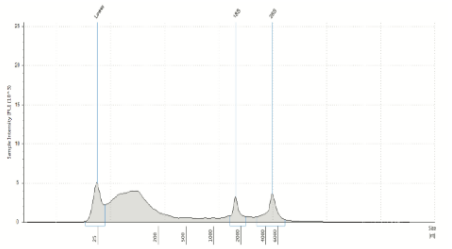

Sample Table

Well	RINe	28S/18S (Area)	Conc. [ng/µl]	Sample Description	Alert	Observations
E1	8.2	1.7	127	PS04d		

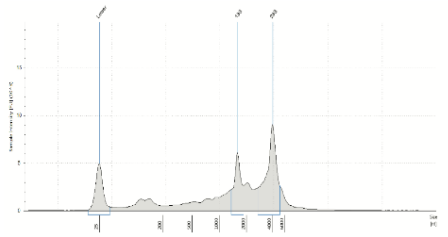

Sample Table

Well	RINe	28S/18S (Area)	Conc. [ng/µl]	Sample Description	Alert	Observations
F1	7.1	2.2	165	e		

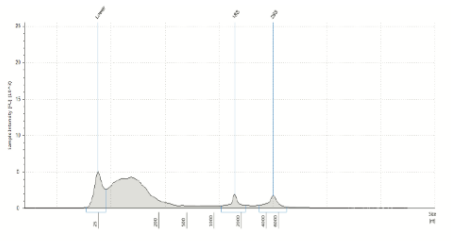

Sample Table

Well	RINe	28S/18S (Area)	Conc. [ng/µl]	Sample Description	Alert	Observations
G1	8.0	1.2	108	PS04f		

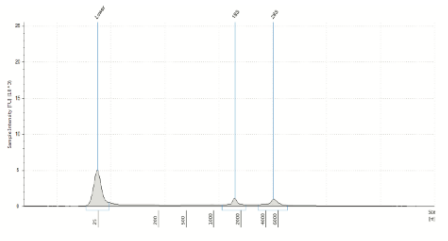

Sample Table

Well	RINe	28S/18S (Area)	Conc. [ng/µl]	Sample Description	Alert	Observations
H1	7.8	1.2	25.3	PS04g		

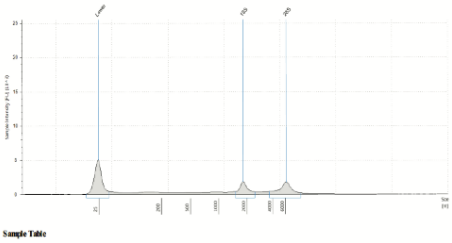

Sample Table

Well	RINe	28S/18S (Area)	Conc. [ng/µl]	Sample Description	Alert	Observations
A2	8.3	1.4	43.6	PS04h		

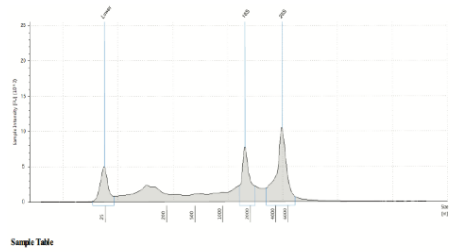

Sample Table

Well	RINe	28S/18S (Area)	Conc. [ng/µl]	Sample Description	Alert	Observations
B2	8.0	1.8	193	PS04i		

Appendix 13 – RNA electropherograms by Agilent 2200 TapeStation for RIN estimation; continued.

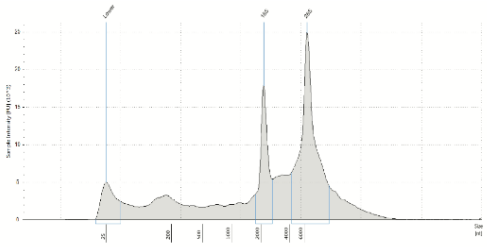

Sample Table

Well	RINe	28S/18S (Area)	Conc. [ng/µl]	Sample Description	Alert	Observations
G1	8.8	2.6	310			

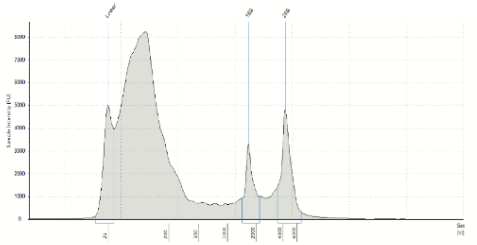

Sample Table

Well	RINe	28S/18S (Area)	Conc. [ng/µl]	Sample Description	Alert	Observations
B1	7.7	1.7	208	PS04k_diluted 1 in 6		

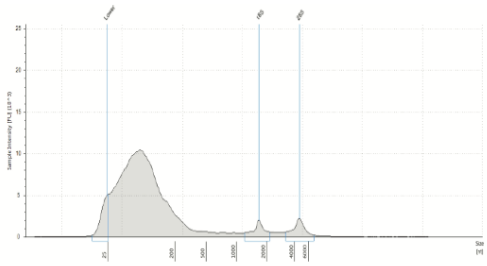

Sample Table

Well	RINe	28S/18S (Area)	Conc. [ng/µl]	Sample Description	Alert	Observations
D2	7.3	1.2	335	PS04m		

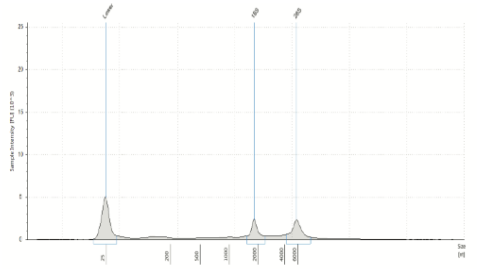

Sample Table

Well	RINe	28S/18S (Area)	Conc. [ng/µl]	Sample Description	Alert	Observations
E2	8.9	1.4	43.6	PS04o		

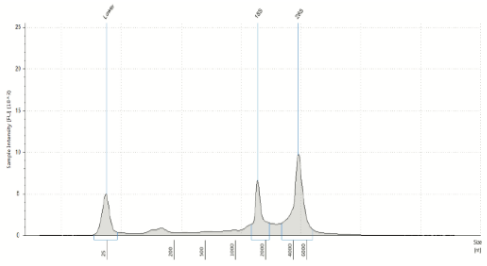

Sample Table

Well	RINe	28S/18S (Area)	Conc. [ng/µl]	Sample Description	Alert	Observations
F2	9.2	2.1	127	PS04o		

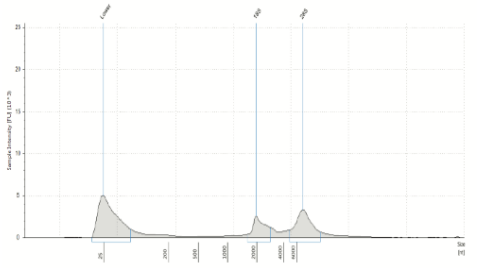

Sample Table

Well	RINe	28S/18S (Area)	Conc. [ng/µl]	Sample Description	Alert	Observations
G2	9.4	1.7	32.4	PS04p		

Appendix 14 – DNA electropherograms by Agilent 2200 TapeStation for samples analysed with downstream RNAseq

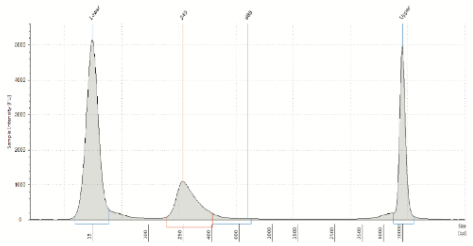

Sample Table

Well	Conc. [ng/µl]	Sample Description	Alert	Observations
B1	2.95	PS04b_repeat		

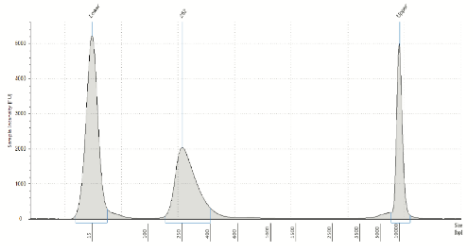

Sample Table

Well	Conc. [ng/µl]	Sample Description	Alert	Observations
C1	5.09	PS04c_repeat		

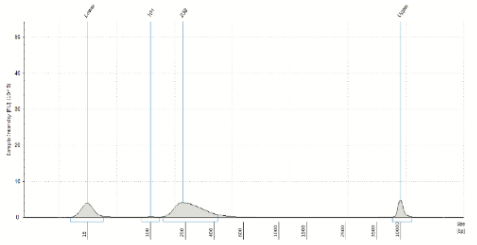

Sample Table

Well	Conc. [ng/µl]	Sample Description	Alert	Observations
D1	15.2	PS04d		

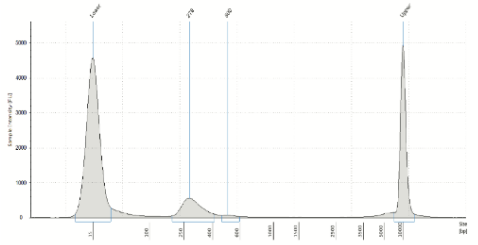

Sample Table

Well	Conc. [ng/µl]	Sample Description	Alert	Observations
D1	1.55	PS03e_dem-up		

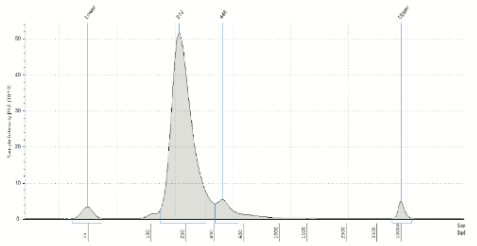

Sample Table

Well	Conc. [ng/µl]	Sample Description	Alert	Observations
F1	127	PS04f		

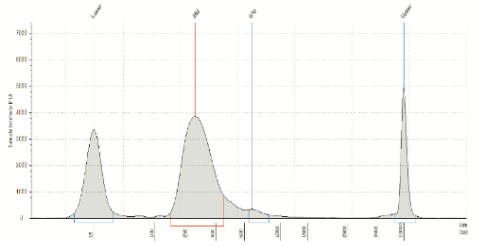

Sample Table

Well	Conc. [ng/µl]	Sample Description	Alert	Observations
B1	13.9	PS04g		

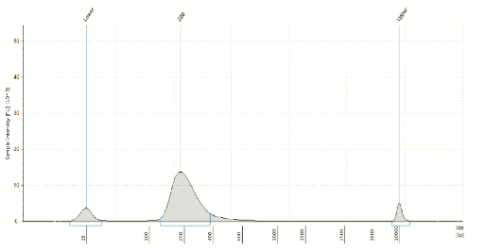

Sample Table

Well	Conc. [ng/µl]	Sample Description	Alert	Observations
H1	42.7	PS04h		

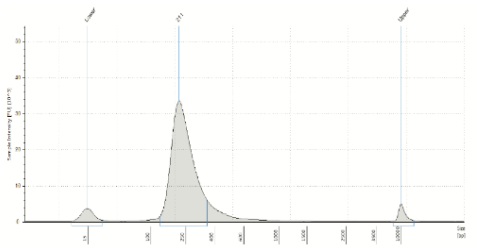

Sample Table

Well	Conc. [ng/µl]	Sample Description	Alert	Observations
A2	81.7	PS04i		

Appendix 14 – DNA electropherograms by Agilent 2200 TapeStation for samples analysed with downstream RNAseq; continued.

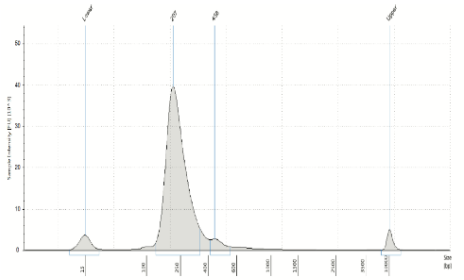

Sample Table

Well	Conc. [ng/µl]	Sample Description	Alert	Observations
B2	95.8	PS04j		

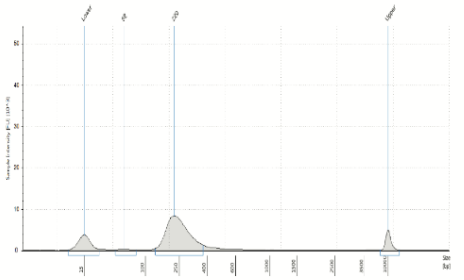

Sample Table

Well	Conc. [ng/µl]	Sample Description	Alert	Observations
C2	25.2	PS04k		

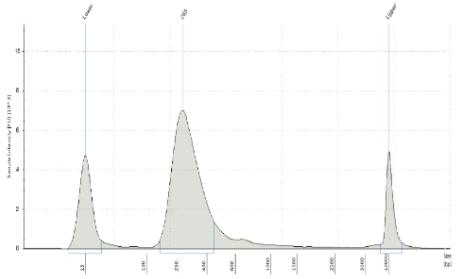

Sample Table

Well	Conc. [ng/µl]	Sample Description	Alert	Observations
B1	20.2	PS04m	⚠	Caution! Expired ScreenTape device (used after two weeks of first use)

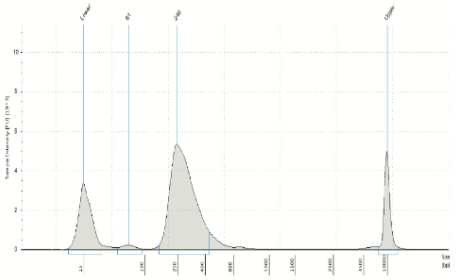

Sample Table

Well	Conc. [ng/µl]	Sample Description	Alert	Observations
C1	16.8	PS04n	⚠	Caution! Expired ScreenTape device (used after two weeks of first use)

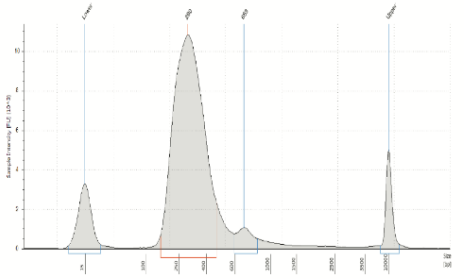

Sample Table

Well	Conc. [ng/µl]	Sample Description	Alert	Observations
D1	41.4	PS04o	⚠	Caution! Expired ScreenTape device (used after two weeks of first use)

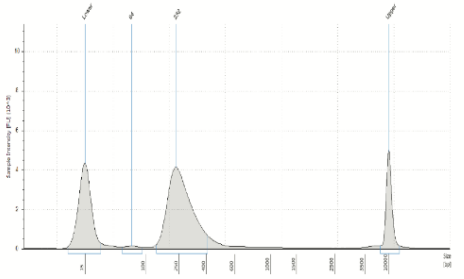

Sample Table

Well	Conc. [ng/µl]	Sample Description	Alert	Observations
E1	12.6	PS04p	⚠	Caution! Expired ScreenTape device (used after two weeks of first use)

Appendix 15 – ssGSEA results for immune pathway signatures

Name	FDR
GSE10239_NAIVE_VS_MEMORY_CD8_TCELL_DN	0.00472785
GSE15767_MED_VS_SCS_MAC_LN_UP	0.00472785
GSE24142_EARLY_THYMIC_PROGENITOR_VS_DN2_THYMOCYTE_ADULT_UP	0.00472785
GSE24142_ADULT_VS_FETAL_DN2_THYMOCYTE_UP	0.00472785
GSE27786_LSK_VS_CD4_TCELL_DN	0.00472785
GSE27786_LSK_VS_NKCELL_DN	0.00472785
GSE27786_LSK_VS_MONO_MAC_DN	0.00472785
GSE27786_LIN_NEG_VS_CD4_TCELL_DN	0.00472785
GSE27786_LIN_NEG_VS_ERYTHROBLAST_UP	0.00472785
GSE27786_LIN_NEG_VS_MONO_MAC_DN	0.00472785
GSE27786_CD8_TCELL_VS_NKCELL_DN	0.00472785
GSE27786_NKCELL_VS_MONO_MAC_UP	0.00472785
GSE27786_NEUTROPHIL_VS_MONO_MAC_UP	0.00472785
GSE339_CD4POS_VS_CD8POS_DC_UP	0.00472785
GSE339_CD4POS_VS_CD4CD8DN_DC_UP	0.00472785
GSE7852_LN_VS_THYMUS_TREG_UP	0.00472785
GSE7852_THYMUS_VS_FAT_TCONV_DN	0.00472785
GSE369_PRE_VS_POST_IL6_INJECTION_IFNG_WT_LIVER_UP	0.00472785
GSE3039_ALPHABETA_CD8_TCELL_VS_B1_BCELL_DN	0.00472785
GSE3039_CD4_TCELL_VS_B1_BCELL_DN	0.00472785
GSE6259_CD4_TCELL_VS_CD8_TCELL_DN	0.00472785
GSE6259_33D1_POS_DC_VS_CD4_TCELL_DN	0.00472785
GSE6259_33D1_POS_DC_VS_CD8_TCELL_DN	0.00472785
GSE6259_FLT3L_INDUCED_DEC205_POS_DC_VS_CD8_TCELL_DN	0.00472785
GSE6259_DEC205_POS_DC_VS_BCELL_DN	0.00472785
GSE7348_UNSTIM_VS_LPS_STIM_MACROPHAGE_DN	0.00472785
GSE14415_ACT_TCONV_VS_ACT_NATURAL_TREG_DN	0.00472785
GSE14415_INDUCED_TREG_VS_FAILED_INDUCED_TREG_DN	0.00472785
GSE15330_HSC_VS_LYMPHOID_PRIMED_MULTIPOTENT_PROGENITOR_DN	0.00472785
GSE15330_HSC_VS_LYMPHOID_PRIMED_MULTIPOTENT_PROGENITOR_UP	0.00472785
GSE18281_SUBCAPSULAR_VS_CENTRAL_CORTICAL_REGION_OF_THYMUS_DN	0.00472785
GSE18281_MEDULLARY_THYMOCYTE_VS_WHOLE_MEDULLA_THYMUS_DN	0.00472785
GSE18281_CORTICAL_VS_MEDULLARY_THYMOCYTE_UP	0.00472785
GSE21360_SECONDARY_VS_QUATERNARY_MEMORY_CD8_TCELL_UP	0.00472785

Appendix 15 – ssGSEA results for immune pathway signatures; continued.

Name	FDR
GSE21360_PRIMARY_VS_QUATERNARY_MEMORY_CD8_TCELL_UP	0.00472785
GSE21360_PRIMARY_VS_TERTIARY_MEMORY_CD8_TCELL_DN	0.00472785
GSE22140_HEALTHY_VS_ARTHRITIC_GERMFREE_MOUSE_CD4_TCELL_DN	0.00472785
GSE22140_HEALTHY_VS_ARTHRITIC_GERMFREE_MOUSE_CD4_TCELL_UP	0.00472785
GSE22196_HEALTHY_VS_OBESE_MOUSE_SKIN_GAMMADELTA_TCELL_UP	0.00472785
GSE19401_UNSTIM_VS_RETINOIC_ACID_AND_PAM2CSK4_STIM_FOLLICULAR_DC_DN	0.00472785
GSE19401_UNSTIM_VS_RETINOIC_ACID_STIM_FOLLICULAR_DC_DN	0.00472785
GSE22432_CONVENTIONAL_CDC_VS_PLASMACYTOID_PDC_DN	0.00472785
GSE22432_MULTIPOTENT_PROGENITOR_VS_CDC_UP	0.00472785
GSE22432_MULTIPOTENT_PROGENITOR_VS_PDC_UP	0.00472785
GSE22432_MULTIPOTENT_VS_COMMON_DC_PROGENITOR_DN	0.00472785
GSE24210_RESTING_TREG_VS_TCONV_UP	0.00472785
GSE25677_MPL_VS_MPL_AND_R848_STIM_BCELL_DN	0.00472785
GSE25677_R848_VS_MPL_AND_R848_STIM_BCELL_DN	0.00472785
GSE32986_CURDLAN_LOWDOSE_VS_CURDLAN_HIGHDOSE_STIM_DC_UP	0.00472785
GSE32986_CURDLAN_LOWDOSE_VS_CURDLAN_HIGHDOSE_STIM_DC_DN	0.00472785
GSE32986_CURDLAN_HIGHDOSE_VS_GMCSF_AND_CURDLAN_HIGHDOSE_STIM_DC_UP	0.00472785
GSE32986_UNSTIM_VS_GMCSF_STIM_DC_DN	0.00472785
GSE35825_IFNA_VS_IFNG_STIM_MACROPHAGE_UP	0.00472785
GSE36009_UNSTIM_VS_LPS_STIM_DC_UP	0.00472785
GSE36891_UNSTIM_VS_POLYIC_TLR3_STIM_PERITONEAL_MACROPHAGE_DN	0.00472785
GSE37605_C57BL6_VS_NOD_FOXP3_IRES_GFP_TREG_UP	0.00472785
GSE37301_MULTIPOTENT_PROGENITOR_VS_COMMON_LYMPHOID_PROGENITOR_DN	0.00472785
GSE37301_MULTIPOTENT_PROGENITOR_VS_GRAN_MONO_PROGENITOR_UP	0.00472785
GSE37301_MULTIPOTENT_PROGENITOR_VS_GRAN_MONO_PROGENITOR_DN	0.00472785
GSE37301_LYMPHOID_PRIMED_MPP_VS_COMMON_LYMPHOID_PROGENITOR_DN	0.00472785
GSE37301_HEMATOPOIETIC_STEM_CELL_VS_CD4_TCELL_UP	0.00472785
GSE37301_MULTIPOTENT_PROGENITOR_VS_COMMON_LYMPHOID_PROGENITOR_UP	0.00472785
GSE37533_PPARG1_FOXP3_VS_FOXP3_TRANSDUCED_CD4_TCELL_DN	0.00472785
GSE37533_PPARG2_FOXP3_VS_FOXP3_TRANSDUCED_CD4_TCELL_DN	0.00472785
GSE36527_CD69_NEG_VS_POS_TREG_CD62L_LOS_KLRG1_NEG_UP	0.00472785
GSE40274_SATB1_VS_FOXP3_AND_SATB1_TRANSDUCED_ACTIVATED_CD4_TCELL_UP	0.00472785
GSE40443_INDUCED_VS_TOTAL_TREG_DN	0.00472785
GSE28737_FOLLICULAR_VS_MARGINAL_ZONE_BCELL_DN	0.00472785

Appendix 15 – ssGSEA results for immune pathway signatures; continued.

Name	FDR
GSE28737_FOLLICULAR_VS_MARGINAL_ZONE_BCELL_BCL6_HET_UP	0.00472785
GSE28737_FOLLICULAR_VS_MARGINAL_ZONE_BCELL_BCL6_HET_DN	0.00472785
GSE28737_WT_VS_BCL6_HET_FOLLICULAR_BCELL_DN	0.00472785
GSE42021_TREG_PLN_VS_TREG_PRECURSORS_THYMUS_DN	0.00472785
GSE42021_TREG_VS_TCONV_PLN_UP	0.00472785
GSE42021_TREG_PLN_VS_CD24INT_TREG_THYMUS_DN	0.00472785
GSE42021_TREG_PLN_VS_CD24LO_TREG_THYMUS_DN	0.00472785
GSE42021_CD24HI_VS_CD24INT_TREG_THYMUS_DN	0.00472785
GSE42021_CD24HI_VS_CD24LOW_TREG_THYMUS_DN	0.00472785
GSE42021_CD24INT_VS_CD24LOW_TREG_THYMUS_DN	0.00472785
GSE42021_CD24HI_VS_CD24LOW_TCONV_THYMUS_DN	0.00472785
GSE42021_CD24INT_VS_CD24LOW_TCONV_THYMUS_DN	0.00472785
GSE42021_TCONV_PLN_VS_CD24HI_TCONV_THYMUS_UP	0.00472785
GSE46242_TH1_VS_ANERGIC_TH1_CD4_TCELL_UP	0.00472785
GSE13229_IMM_VS_INTMATURE_NKCELL_DN	0.00719854
GSE27786_ERYTHROBLAST_VS_NEUTROPHIL_DN	0.00719854
GSE7852_TREG_VS_TCONV_LN_DN	0.00719854
GSE7852_LN_VS_THYMUS_TCONV_UP	0.00719854
GSE3039_NKT_CELL_VS_ALPHAALPHA_CD8_TCELL_DN	0.00719854
GSE6259_FLT3L_INDUCED_33D1_POS_DC_VS_CD4_TCELL_UP	0.00719854
GSE6259_FLT3L_INDUCED_33D1_POS_DC_VS_CD8_TCELL_DN	0.00719854
GSE6259_FLT3L_INDUCED_DEC205_POS_DC_VS_BCELL_UP	0.00719854
GSE6674_UNSTIM_VS_PL2_3_STIM_BCELL_DN	0.00719854
GSE5503_LIVER_DC_VS_PLN_DC_ACTIVATED_ALLOGENIC_TCELL_UP	0.00719854
GSE14415_INDUCED_TREG_VS_TCONV_DN	0.00719854
GSE14415_NATURAL_TREG_VS_TCONV_UP	0.00719854
GSE16266_LPS_VS_HEATSHOCK_AND_LPS_STIM_MEF_DN	0.00719854
GSE21360_PRIMARY_VS_QUATERNARY_MEMORY_CD8_TCELL_DN	0.00719854
GSE19401_UNSTIM_VS_RETINOIC_ACID_AND_PAM2CSK4_STIM_FOLLICULAR_DC_UP	0.00719854
GSE19401_PAM2CSK4_VS_RETINOIC_ACID_AND_PAM2CSK4_STIM_FOLLICULAR_DC_DN	0.00719854
GSE25677_MPL_VS_MPL_AND_R848_STIM_BCELL_UP	0.00719854
GSE25677_MPL_VS_R848_STIM_BCELL_UP	0.00719854
GSE19512_NAUTRAL_VS_INDUCED_TREG_DN	0.00719854
GSE29949_MICROGLIA_BRAIN_VS_MONOCYTE_BONE_MARROW_DN	0.00719854

Appendix 15 – ssGSEA results for immune pathway signatures; continued.

Name	FDR
GSE32533_WT_VS_MIR17_OVEREXPRESS_ACT_CD4_TCELL_DN	0.00719854
GSE27859_MACROPHAGE_VS_DC_UP	0.00719854
GSE32986_GMCSF_VS_GMCSF_AND_CURDLAN_LOWDOSE_STIM_DC_UP	0.00719854
GSE32986_UNSTIM_VS_CURDLAN_HIGHDOSE_STIM_DC_DN	0.00719854
GSE32986_UNSTIM_VS_GMCSF_AND_CURDLAN_LOWDOSE_STIM_DC_DN	0.00719854
GSE32986_CURDLAN_HIGHDOSE_VS_GMCSF_AND_CURDLAN_HIGHDOSE_STIM_DC_DN	0.00719854
GSE37301_HEMATOPOIETIC_STEM_CELL_VS_MULTIPOTENT_PROGENITOR_DN	0.00719854
GSE37301_MULTIPOTENT_PROGENITOR_VS_CD4_TCELL_UP	0.00719854
GSE40274_LEF1_VS_FOXP3_AND_LEF1_TRANSDUCED_ACTIVATED_CD4_TCELL_DN	0.00719854
GSE28737_WT_VS_BCL6_HET_MARGINAL_ZONE_BCELL_DN	0.00719854
GSE42021_CD24HI_VS_CD24INT_TCONV_THYMUS_DN	0.00719854
GSE45365_NK_CELL_VS_CD11B_DC_MCMV_INFECTION_DN	0.00719854
GSE45365_NK_CELL_VS_BCELL_MCMV_INFECTION_DN	0.00719854
GSE45365_HEALTHY_VS_MCMV_INFECTION_CD8A_DC_DN	0.00719854
GSE45365_NK_CELL_VS_CD11B_DC_DN	0.00719854
GSE10239_NAIVE_VS_KLRG1INT_EFF_CD8_TCELL_UP	0.01172441
GSE14308_TH1_VS_NAIVE_CD4_TCELL_DN	0.01172441
GSE14308_TH1_VS_INDUCED_TREG_UP	0.01172441
GSE15324_NAIVE_VS_ACTIVATED_CD8_TCELL_UP	0.01172441
GSE24142_EARLY_THYMIC_PROGENITOR_VS_DN2_THYMOCYTE_FETAL_UP	0.01172441
GSE339_CD8POS_VS_CD4CD8DN_DC_IN_CULTURE_DN	0.01172441
GSE3039_NKT_CELL_VS_ALPHABETA_CD8_TCELL_DN	0.01172441
GSE3039_ALPHAALPHA_VS_ALPHABETA_CD8_TCELL_DN	0.01172441
GSE4535_BM_DERIVED_DC_VS_FOLLICULAR_DC_UP	0.01172441
GSE6259_FLT3L_INDUCED_DEC205_POS_DC_VS_BCELL_DN	0.01172441
GSE21360_SECONDARY_VS_QUATERNARY_MEMORY_CD8_TCELL_DN	0.01172441
GSE21360_TERTIARY_VS_QUATERNARY_MEMORY_CD8_TCELL_UP	0.01172441
GSE21360_TERTIARY_VS_QUATERNARY_MEMORY_CD8_TCELL_DN	0.01172441
GSE22140_HEALTHY_VS_ARTHRITIC_MOUSE_CD4_TCELL_UP	0.01172441
GSE19401_PAM2CSK4_VS_RETINOIC_ACID_STIM_FOLLICULAR_DC_DN	0.01172441
GSE25677_MPL_VS_R848_STIM_BCELL_DN	0.01172441
GSE22313_HEALTHY_VS_SLE_MOUSE_CD4_TCELL_DN	0.01172441
GSE37605_C57BL6_VS_NOD_FOXP3_IRES_GFP_TCONV_DN	0.01172441
GSE37533_PPARG1_FOXP3_VS_PPARG2_FOXP3_TRANSDUCED_CD4_TCELL_DN	0.01172441

Appendix 15 – ssGSEA results for immune pathway signatures; continued.

Name	FDR
GSE40274_FOXP3_VS_FOXP3_AND_GATA1_TRANSDUCED_ACTIVATED_CD4_TCELL_DN	0.01172441
GSE40225_WT_VS_RIP_B7X_DIABETIC_MOUSE_PANCREATIC_CD8_TCELL_UP	0.01172441
GSE42021_TREG_PLN_VS_TREG_PRECURSORS_THYMUS_UP	0.01172441
GSE45365_NK_CELL_VS_CD8_TCELL_MCMV_INFECTION_DN	0.01172441
GSE45365_NK_CELL_VS_CD11B_DC_UP	0.01172441
GSE14308_NAIVE_CD4_TCELL_VS_INDUCED_TREG_UP	0.01769731
GSE20366_TREG_VS_NAIVE_CD4_TCELL_HOMEOSTATIC_CONVERSION_DN	0.01769731
GSE27786_LIN_NEG_VS_CD8_TCELL_DN	0.01769731
GSE27786_CD8_TCELL_VS_NKTCELL_DN	0.01769731
GSE30962_PRIMARY_VS_SECONDARY_CHRONIC_LCMV_INF_CD8_TCELL_DN	0.01769731
GSE7852_TREG_VS_TCONV_THYMUS_UP	0.01769731
GSE9650_NAIVE_VS_EFF_CD8_TCELL_DN	0.01769731
GSE9650_NAIVE_VS_EXHAUSTED_CD8_TCELL_DN	0.01769731
GSE9650_EFFECTOR_VS_MEMORY_CD8_TCELL_UP	0.01769731
GSE1112_HY_CD8AB_VS_HY_CD8AA_THYMOCYTE_RTOC_CULTURE_UP	0.01769731
GSE3039_CD4_TCELL_VS_ALPHAALPHA_CD8_TCELL_DN	0.01769731
GSE3039_CD4_TCELL_VS_ALPHABETA_CD8_TCELL_UP	0.01769731
GSE6259_33D1_POS_DC_VS_BCELL_DN	0.01769731
GSE8621_LPS_PRIMED_UNSTIM_VS_LPS_PRIMED_AND_LPS_STIM_MACROPHAGE_DN	0.01769731
GSE5503_MLN_DC_VS_PLN_DC_ACTIVATED_ALLOGENIC_TCELL_DN	0.01769731
GSE12003_4D_VS_8D_CULTURE_BM_PROGENITOR_UP	0.01769731
GSE14699_DELETIONAL_TOLERANCE_VS_ACTIVATED_CD8_TCELL_UP	0.01769731
GSE27859_CD11C_INT_F480_HI_MACROPHAGE_VS_CD11C_ING_F480_INT_DC_UP	0.01769731
GSE32986_UNSTIM_VS_CURDLAN_LOWDOSE_STIM_DC_DN	0.01769731
GSE37301_MULTIPOTENT_PROGENITOR_VS_LYMPHOID_PRIMED_MPP_DN	0.01769731
GSE37532_VISCERAL_ADIPOSE_TISSUE_VS_LN_DERIVED_TREG_CD4_TCELL_UP	0.01769731
GSE40274_FOXP3_VS_FOXP3_AND_SATB1_TRANSDUCED_ACTIVATED_CD4_TCELL_DN	0.01769731
GSE40274_HELIOS_VS_FOXP3_AND_HELIOS_TRANSDUCED_ACTIVATED_CD4_TCELL_UP	0.01769731
GSE40274_FOXP3_VS_FOXP3_AND_PBX1_TRANSDUCED_ACTIVATED_CD4_TCELL_UP	0.01769731
GSE42021_TCONV_PLN_VS_CD24LO_TCONV_THYMUS_DN	0.01769731
GSE45365_NK_CELL_VS_CD8A_DC_UP	0.01769731
GSE20366_TREG_VS_NAIVE_CD4_TCELL_DEC205_CONVERSION_UP	0.02598178
GSE24142_EARLY_THYMIC_PROGENITOR_VS_DN3_THYMOCYTE_DN	0.02598178
GSE24142_EARLY_THYMIC_PROGENITOR_VS_DN3_THYMOCYTE_ADULT_UP	0.02598178

Appendix 15 – ssGSEA results for immune pathway signatures; continued.

Name	FDR
GSE27786_LIN_NEG_VS_CD4_TCELL_UP	0.02598178
GSE32423_IL7_VS_IL4_MEMORY_CD8_TCELL_DN	0.02598178
GSE7852_TREG_VS_TCONV_LN_UP	0.02598178
GSE7852_TREG_VS_TCONV_FAT_DN	0.02598178
GSE7852_LN_VS_FAT_TREG_DN	0.02598178
GSE9650_NAIVE_VS_MEMORY_CD8_TCELL_UP	0.02598178
GSE9650_EFFECTOR_VS_EXHAUSTED_CD8_TCELL_UP	0.02598178
GSE2585_CTEC_VS_MTEC_THYMUS_UP	0.02598178
GSE2585_CTEC_VS_THYMIC_MACROPHAGE_UP	0.02598178
GSE3039_NKT_CELL_VS_B2_BCELL_DN	0.02598178
GSE3039_CD4_TCELL_VS_B2_BCELL_UP	0.02598178
GSE6259_FLT3L_INDUCED_DEC205_POS_DC_VS_CD4_TCELL_UP	0.02598178
GSE15330_MEGAKARYOCYTE_ERYTHROID_VS_GRANULOCYTE_MONOCYTE_PROGENITOR_UP	0.02598178
GSE15330_LYMPHOID_MULTIPOTENT_VS_PRO_BCELL_DN	0.02598178
GSE16266_LPS_VS_HEATSHOCK_AND_LPS_STIM_MEF_UP	0.02598178
GSE19401_UNSTIM_VS_PAM2CSK4_STIM_FOLLICULAR_DC_DN	0.02598178
GSE24492_LYVE_NEG_VS_POS_MACROPHAGE_DN	0.02598178
GSE23502_BM_VS_COLON_TUMOR_MYELOID_DERIVED_SUPPRESSOR_CELL_UP	0.02598178
GSE23502_BM_VS_COLON_TUMOR_MYELOID_DERIVED_SUPPRESSOR_CELL_DN	0.02598178
GSE24972_MARGINAL_ZONE_BCELL_VS_FOLLICULAR_BCELL_DN	0.02598178
GSE28130_ACTIVATED_VS_INDUCEED_TREG_UP	0.02598178
GSE27859_MACROPHAGE_VS_CD11C_INT_F480_HI_MACROPHAGE_UP	0.02598178
GSE32986_UNSTIM_VS_CURDLAN_LOWDOSE_STIM_DC_UP	0.02598178
GSE37605_NOD_VS_C57BL6_IRES_GFP_TREG_DN	0.02598178
GSE37301_LYMPHOID_PRIMED_MPP_VS_COMMON_LYMPHOID_PROGENITOR_UP	0.02598178
GSE37532_TREG_VS_TCONV_CD4_TCELL_FROM_LN_DN	0.02598178
GSE40274_FOXP3_VS_FOXP3_AND_EOS_TRANSDUCED_ACTIVATED_CD4_TCELL_UP	0.02598178
GSE40274_FOXP3_VS_FOXP3_AND_PBX1_TRANSDUCED_ACTIVATED_CD4_TCELL_DN	0.02598178
GSE42021_CD24INT_VS_CD24LOW_TCONV_THYMUS_UP	0.02598178
GSE42021_CD24HI_TREG_VS_CD24HI_TCONV_THYMUS_UP	0.02598178
GSE14308_NAIVE_CD4_TCELL_VS_NATURAL_TREG_UP	0.0369762
GSE24142_EARLY_THYMIC_PROGENITOR_VS_DN3_THYMOCYTE_FETAL_UP	0.0369762
GSE27786_LSK_VS_NEUTROPHIL_DN	0.0369762
GSE27786_LIN_NEG_VS_BCELL_DN	0.0369762

Appendix 15 – ssGSEA results for immune pathway signatures; continued.

Name	FDR
GSE27786_LIN_NEG_VS_NKTCELL_DN	0.0369762
GSE27786_NKCELL_VS_ERYTHROBLAST_DN	0.0369762
GSE30962_ACUTE_VS_CHRONIC_LCMV_PRIMARY_INF_CD8_TCELL_UP	0.0369762
GSE32423_IL7_VS_IL4_MEMORY_CD8_TCELL_UP	0.0369762
GSE7852_TREG_VS_TCONV_DN	0.0369762
GSE9650_NAIVE_VS_MEMORY_CD8_TCELL_DN	0.0369762
GSE9650_EXHAUSTED_VS_MEMORY_CD8_TCELL_UP	0.0369762
GSE2128_C57BL6_VS_NOD_THYMOCYTE_UP	0.0369762
GSE2128_C57BL6_VS_NOD_THYMOCYTE_DN	0.0369762
GSE2585_CTEC_VS_THYMIC_DC_DN	0.0369762
GSE2585_CTEC_VS_MTEC_THYMUS_DN	0.0369762
GSE2585_THYMIC_MACROPHAGE_VS_MTEC_DN	0.0369762
GSE3039_CD4_TCELL_VS_ALPHAALPHA_CD8_TCELL_UP	0.0369762
GSE6259_FLT3L_INDUCED_33D1_POS_DC_VS_BCELL_DN	0.0369762
GSE6259_FLT3L_INDUCED_33D1_POS_DC_VS_CD4_TCELL_DN	0.0369762
GSE6259_33D1_POS_DC_VS_CD4_TCELL_UP	0.0369762
GSE6259_DEC205_POS_DC_VS_CD8_TCELL_UP	0.0369762
GSE14415_INDUCED_VS_NATURAL_TREG_UP	0.0369762
GSE15330_GRANULOCYTE_MONOCYTE_PROGENITOR_VS_PRO_BCELL_DN	0.0369762
GSE18281_SUBCAPSULAR_VS_CENTRAL_CORTICAL_REGION_OF_THYMUS_UP	0.0369762
GSE19401_UNSTIM_VS_RETINOIC_ACID_STIM_FOLLICULAR_DC_UP	0.0369762
GSE22432_CDC_VS_COMMON_DC_PROGENITOR_UP	0.0369762
GSE26343_UNSTIM_VS_LPS_STIM_MACROPHAGE_DN	0.0369762
GSE37605_FOXP3_FUSION_GFP_VS_IRES_GFP_TREG_NOD_DN	0.0369762
GSE37301_HEMATOPOIETIC_STEM_CELL_VS_MULTIPOTENT_PROGENITOR_UP	0.0369762
GSE37301_CD4_TCELL_VS_GRANULOCYTE_MONOCYTE_PROGENITOR_DN	0.0369762
GSE37301_PRO_BCELL_VS_CD4_TCELL_DN	0.0369762
GSE37532_VISCERAL_ADIPOSE_TISSUE_VS_LN_DERIVED_TCONV_CD4_TCELL_UP	0.0369762
GSE40274_FOXP3_VS_FOXP3_AND_XBP1_TRANSDUCED_ACTIVATED_CD4_TCELL_DN	0.0369762
GSE38304_MYC_NEG_VS_POS_GC_BCELL_DN	0.0369762
GSE45365_NK_CELL_VS_CD8_TCELL_UP	0.0369762

Appendix 16 – ERV analysis with annotation of the exact genomic loci

Repbase	ID	log2FoldChange	p_adjusted
IAPEY3-int|LTR/ERVK	Mmus38.chr1.173575790.173576965.	2.897758355	2.40E-22
ERVB2_1-I_MM|LTR/ERVK	Mmus38.chr1.173571901.173572377.	2.67682232	2.41E-23
ERVB2_1-I_MM|LTR/ERVK	Mmus38.chr1.173568891.173569334.	2.577157137	6.46E-21
ERVB2_1-I_MM|LTR/ERVK	Mmus38.chr1.173571553.173571888.	2.378230738	1.66E-15
IAPEY3-int|LTR/ERVK	Mmus38.chr1.173574889.173575791.	2.346893129	1.10E-17
IAPEY3-int|LTR/ERVK	Mmus38.chr1.173578171.173579793.	2.286622161	1.07E-14
ERVB2_1-I_MM|LTR/ERVK	Mmus38.chr1.173695398.173695781.	2.268340062	2.52E-08
ERVB2_1-I_MM|LTR/ERVK	Mmus38.chr1.173570933.173571475.	2.1862969	1.01E-10
ERVB2_1-I_MM|LTR/ERVK	Mmus38.chr1.173569295.173570173.	2.14685712	5.63E-12
ERVB5_1-I_MM|LTR/ERVK	Mmus38.chr11.83006979.83007707.	2.083804571	1.73E-12
ERVB2_1-I_MM|LTR/ERVK	Mmus38.chr1.173567620.173568006.	1.972468567	2.04E-10
ERVB2_1-I_MM|LTR/ERVK	Mmus38.chr1.173581149.173581397.	1.944731564	5.70E-07
ERVB5_1-I_MM|LTR/ERVK	Mmus38.chr11.83008027.83008317.	1.690926113	2.04E-07
MERVL-int|LTR/ERVL	Mmus38.chr11.83071644.83073467.	1.672614253	3.48E-07
L1_Mm|LINE/L1	Mmus38.chr7.104413779.104415041.	1.645621531	3.68E-07
U6|snRNA L1_Mm|LINE/L1 L1Md_T|LINE/L1	Mmus38.chr7.104423365.104427138.	1.59027723	1.82E-05
RodERV21-int|LTR/ERV1	Mmus38.chr12.99646125.99646460.	1.520709363	0.00208404
ERVB5_1-I_MM|LTR/ERVK	Mmus38.chr11.83006696.83007055.	1.481664912	1.02E-06
MERV1_I-int|LTR/ERV1 RLTR19-int|LTR/ERVK	Mmus38.chr15.74935157.74935435.	1.449133283	8.64E-06
MuRRS4-int|LTR/ERV1	Mmus38.chr10.51528513.51528782.	1.391471517	9.32E-05
RLTR26_Mus|LTR/ERVK MERVK26-int|LTR/ERVK	Mmus38.chr8.70621771.70622610.	1.381838476	0.0047053
ETnERV2-int|LTR/ERVK	Mmus38.chr19.11318063.11318407.	1.352626053	0.00063608
IAPEz-int|LTR/ERVK	Mmus38.chr7.104271650.104273401.	1.278399255	0.01079768
ETnERV2-int|LTR/ERVK	Mmus38.chr19.11318551.11318862.	1.17170315	0.00063608
L1VL2|LINE/L1	Mmus38.chr7.104490208.104491557.	1.113617511	0.00208404
L1Md_A|LINE/L1	Mmus38.chr8.94465654.94466394.	1.070366554	0.01674921
IAPEY4_I-int|LTR/ERVK	Mmus38.chr14.43927534.43928418.	1.055952123	0.04162095
IAPEY4_I-int|LTR/ERVK	Mmus38.chr6.3338265.3338591.	0.975734553	0.00011855
ETnERV-int|LTR/ERVK	Mmus38.chr7.106585437.106586243.	0.935050849	0.02466717

Appendix 16 – ERV analysis with annotation of the exact genomic loci; continued.

Repbase	ID	log2FoldChange	p_adjusted
MERVL_2A-int|LTR/ERVL	Mmus38.chr1.171878140.171878919.	0.93068843	0.04162095
RLTR13D5|LTR/ERVK ERVB2_1A-I_MM|LTR/ERVK ERVB4_1B-I_MM|LTR/ERVK	Mmus38.chr18.60283519.60284016.	0.930444872	0.03003523
L1Md_F2|LINE/L1	Mmus38.chr18.60305643.60305954.	0.884957566	0.0346917
IAPEz-int|LTR/ERVK	Mmus38.chr17.36010204.36012885.	0.881763905	0.00731087
RLTR6-int|LTR/ERV1	Mmus38.chr15.74931985.74932389.	0.861133284	0.0009027
IAPEY4_I-int|LTR/ERVK	Mmus38.chr6.3338919.3339254.	0.851834712	0.00174449
IAPEY4_I-int|LTR/ERVK	Mmus38.chr6.3339424.3339960.	0.761019415	0.00349458
IAPEY4_I-int|LTR/ERVK	Mmus38.chr6.3337831.3338334.	0.682834053	0.01277409
IAPEY4_I-int|LTR/ERVK	Mmus38.chr6.3336678.3337793.	0.632540724	0.03695976
IAPEY4_I-int|LTR/ERVK	Mmus38.chr6.3336125.3336748.	0.620746325	0.02706939
RLTR4_MM-int|LTR/ERV1	Mmus38.chr11.103086489.103089779.	-0.829033672	0.03003523
L1_Mus3|LINE/L1	Mmus38.chr8.73168347.73168919.	-0.914377943	0.04162095
MMERGLN-int|LTR/ERV1	Mmus38.chr17.36101653.36102543.	-1.360865462	0.03952433
MURVY-int|LTR/ERV1	Mmus38.chr2.27500428.27501366.	-1.413627971	0.00839844
MuRRS-int|LTR/ERV1 (AGCGAC)n|Simple_repeat	Mmus38.chr10.11477316.11477744.	-1.434503224	0.04162095
ETnERV3-int|LTR/ERVK	Mmus38.chr19.8277321.8277896.	-1.451917088	0.02209461
MERVL-int|LTR/ERVL	Mmus38.chr3.62357540.62361085.	-1.472871305	0.00328097
MURVY-int|LTR/ERV1	Mmus38.chr2.30233288.30233890.	-1.480371806	0.01730637
MuRRS4-int|LTR/ERV1	Mmus38.chr16.4825970.4826332.	-1.532122922	0.00308297
IAPEz-int|LTR/ERVK	Mmus38.chr9.4494414.4497095.	-1.592932253	0.01371757
MURVY-int|LTR/ERV1	Mmus38.chr12.19713019.19715448.	-1.658798046	0.00026832
MuRRS4-int|LTR/ERV1	Mmus38.chr7.35565655.35566149.	-1.920797378	0.0009027

Appendix 17 – DNA electropherograms by Agilent 2200 TapeStation for samples analysed with downstream ATACseq

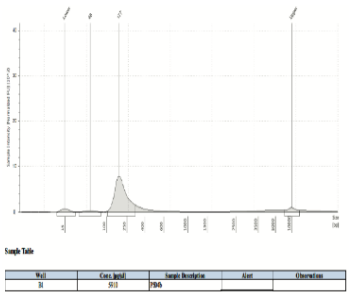
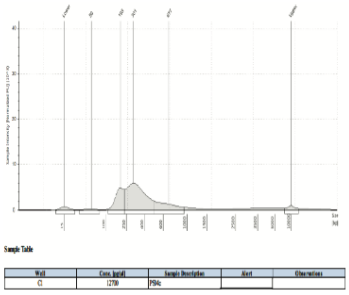
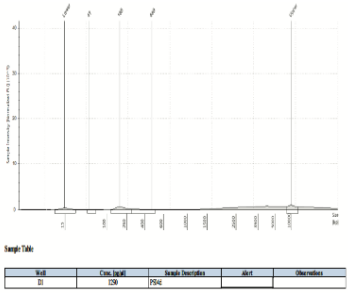
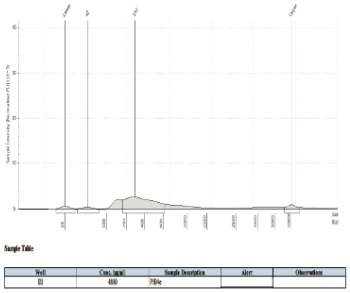
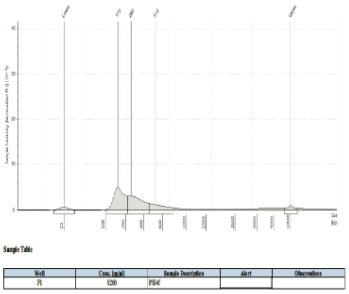
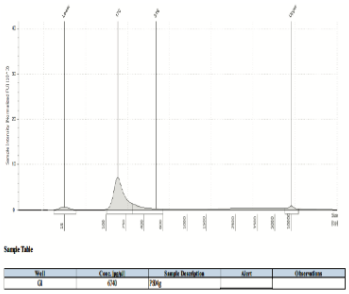
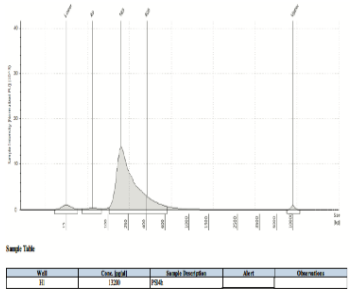
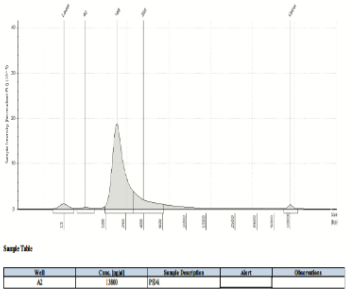
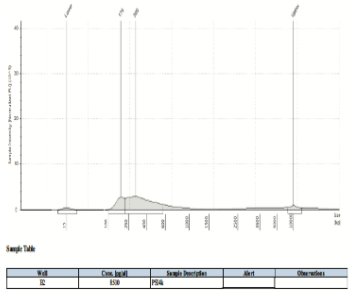
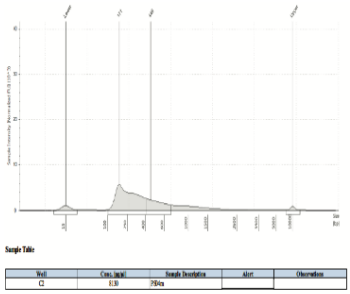
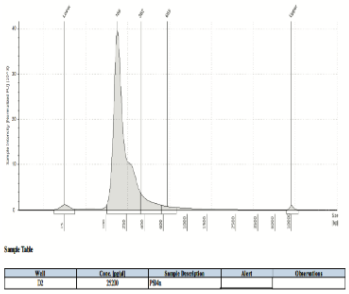
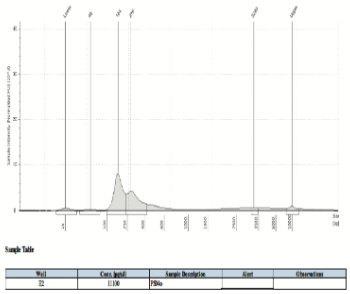

Appendix 18 - Functional annotation of DEGs with present peaks on ATACseq by GO ontology and KEGG pathways

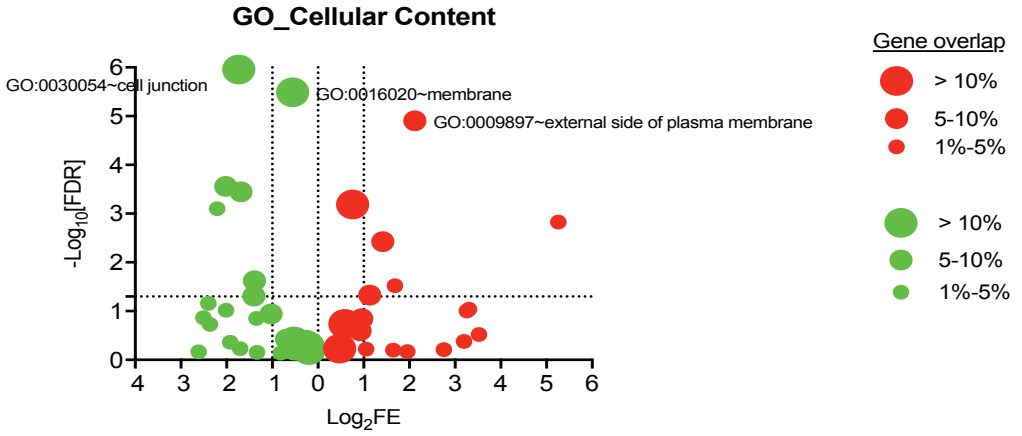

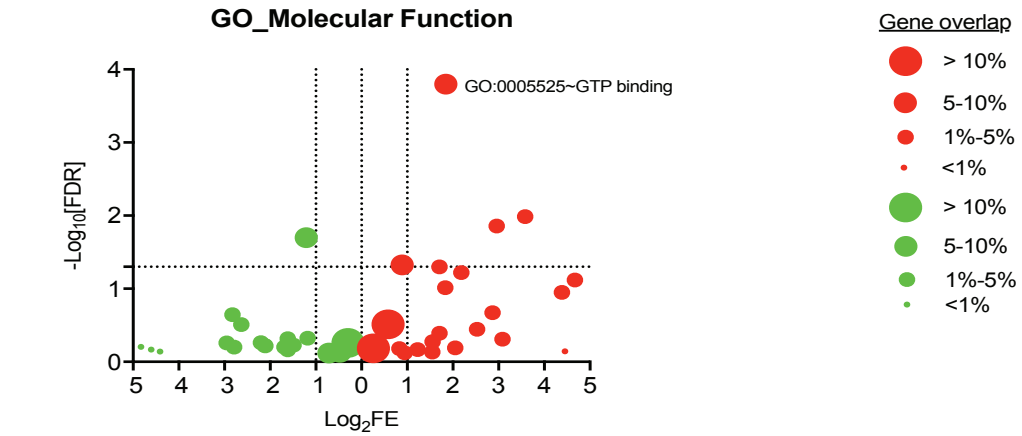

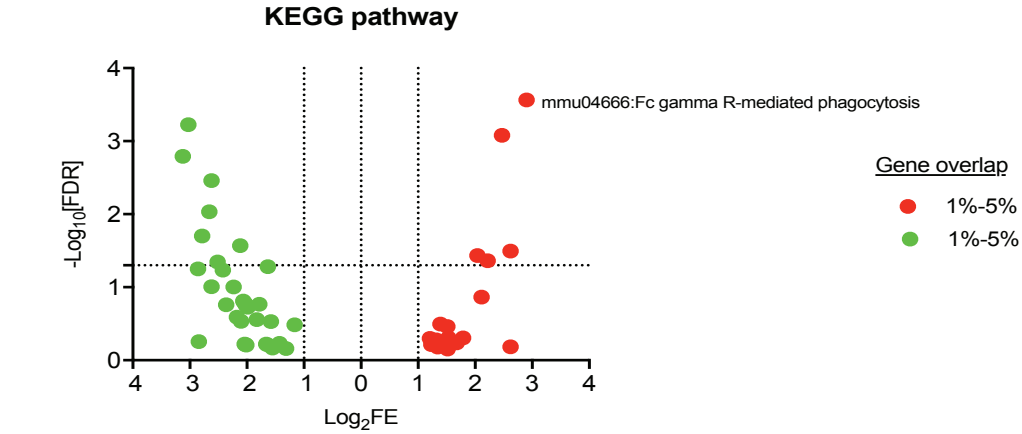

Appendix 19 – Basic clinical characteristics of patients' samples treated with HKMTI-1-005

Randomisation No	Histology	Grade	Stage	BRCA1/2	Disease status
ASC19-026	Serous	High	3B	No BRCA pathogenic mutations found	Relapsed disease
ASC19-029	Serous	High	3C	No BRCA pathogenic mutations found	Primary
ASC19-030	Serous	High	3C	No BRCA pathogenic mutations found	Primary
ASC19-032	Serous	High	3C	No BRCA pathogenic mutations found	Primary
ASC19-033	Serous	High	4B	n/a	Primary
ASC19-038	Endometroid or Serous	High	n/a	No BRCA pathogenic mutations found	Primary
ASC19-040	Serous	High	3C	n/a	Primary

1. Ferlay J, Colombet M, Soerjomataram I, Mathers C, Parkin DM, Pineros M, et al. Estimating the global cancer incidence and mortality in 2018: GLOBOCAN sources and methods. Int J Cancer. 2019;144(8):1941-53.

2. Torre LA, Islami F, Siegel RL, Ward EM, Jemal A. Global Cancer in Women: Burden and Trends. Cancer Epidemiology Biomarkers & Prevention. 2017;26(4):444.

3. Jacobs IJ, Menon U, Ryan A, Gentry-Maharaj A, Burnell M, Kalsi JK, et al. Ovarian cancer screening and mortality in the UK Collaborative Trial of Ovarian Cancer Screening (UKCTOCS): a randomised controlled trial. The Lancet. 2016;387(10022):945-56.

4. Oswald AJ, Gourley C. Low-grade epithelial ovarian cancer: a number of distinct clinical entities? Current Opinion in Oncology. 2015;27(5).

5. Mangili G, Bergamini A, Taccagni G, Gentile C, Panina P, Viganò P, et al. Unraveling the two entities of endometrioid ovarian cancer: A single center clinical experience. Gynecologic Oncology. 2012;126(3):403-7.

6. Callegaro-Filho D, Gershenson DM, Nick AM, Munsell MF, Ramirez PT, Eifel PJ, et al. Small cell carcinoma of the ovary-hypercalcemic type (SCCOHT): A review of 47 cases. Gynecologic Oncology. 2016;140(1):53-7.

7. Witkowski L, Goudie C, Ramos P, Boshari T, Brunet J-S, Karnezis AN, et al. The influence of clinical and genetic factors on patient outcome in small cell carcinoma of the ovary, hypercalcemic type. Gynecologic Oncology. 2016;141(3):454-60.

8. Boussios S, Zarkavelis G, Seraj E, Zerdes I, Tatsi K, Pentheroudakis G. Non-epithelial Ovarian Cancer: Elucidating Uncommon Gynaecological Malignancies. Anticancer Res. 2016;36(10):5031-42.

9. Kindelberger DW, Lee Y, Miron A, Hirsch MS, Feltmate C, Medeiros F, et al. Intraepithelial carcinoma of the fimbria and pelvic serous carcinoma: Evidence for a causal relationship. Am J Surg Pathol. 2007;31(2):161-9.

10. Menon U, Ryan A, Kalsi J, Gentry-Maharaj A, Dawnay A, Habib M, et al. Risk Algorithm Using Serial Biomarker Measurements Doubles the Number of Screen-Detected Cancers Compared With a Single-Threshold Rule in the United Kingdom Collaborative Trial of Ovarian Cancer Screening. Journal of Clinical Oncology. 2015;33(18):2062-71.

11. McGuire WP, Hoskins WJ, Brady MF, Kucera PR, Partridge EE, Look KY, et al. Cyclophosphamide and Cisplatin Compared with Paclitaxel and Cisplatin in Patients with Stage III and Stage IV Ovarian Cancer. New England Journal of Medicine. 1996;334(1):1-6.

12. Bookman MA, Brady MF, McGuire WP, Harper PG, Alberts DS, Friedlander M, et al. Evaluation of new platinum-based treatment regimens in advanced-stage ovarian cancer: a Phase III Trial of the Gynecologic Cancer Intergroup. J Clin Oncol. 2009;27(9):1419-25.

13. du Bois A, Lück H-J, Meier W, Adams H-P, Möbus V, Costa S, et al. A Randomized Clinical Trial of Cisplatin/Paclitaxel Versus Carboplatin/Paclitaxel as First-Line Treatment of Ovarian Cancer. JNCI: Journal of the National Cancer Institute. 2003;95(17):1320-9.

14. Ozols RF, Bundy BN, Greer BE, Fowler JM, Clarke-Pearson D, Burger RA, et al. Phase III Trial of Carboplatin and Paclitaxel Compared With Cisplatin and Paclitaxel in Patients With Optimally Resected Stage III Ovarian Cancer: A Gynecologic Oncology Group Study. Journal of Clinical Oncology. 2003;21(17):3194-200.

15. Vasey PA, Jayson GC, Gordon A, Gabra H, Coleman R, Atkinson R, et al. Phase III Randomized Trial of Docetaxel–Carboplatin Versus Paclitaxel–Carboplatin as First-line Chemotherapy for Ovarian Carcinoma. JNCI: Journal of the National Cancer Institute. 2004;96(22):1682-91.

16. Cannistra SA. Cancer of the ovary. N Engl J Med. 2004;351(24):2519-29.

17. Coleman RL, Monk BJ, Sood AK, Herzog TJ. Latest research and treatment of advanced-stage epithelial ovarian cancer. Nature Reviews Clinical Oncology. 2013;10(4):211-24.

18. George A, Kaye S, Banerjee S. Delivering widespread BRCA testing and PARP inhibition to patients with ovarian cancer. Nature Reviews Clinical Oncology. 2017;14(5):284-96.

19. Ledermann JA. PARP inhibitors in ovarian cancer. Ann Oncol. 2016;27 Suppl 1:i40-i4.

20. Reinthaller A. Antiangiogenic therapies in ovarian cancer. Memo. 2016;9(3):139-43.

21. Mirza MR, Monk BJ, Herrstedt J, Oza AM, Mahner S, Redondo A, et al. Niraparib Maintenance Therapy in Platinum-Sensitive, Recurrent Ovarian Cancer. N Engl J Med. 2016;375(22):2154-64.

22. Matulonis UA, Shapira-Frommer R, Santin AD, Lisyanskaya AS, Pignata S, Vergote I, et al. Antitumor Activity and Safety of Pembrolizumab in Patients with Advanced Recurrent Ovarian Cancer: Results from the Phase 2 KEYNOTE-100 Study. Ann Oncol. 2019.

23. Disis ML, Taylor MH, Kelly K, Beck JT, Gordon M, Moore KM, et al. Efficacy and Safety of Avelumab for Patients With Recurrent or Refractory Ovarian Cancer: Phase 1b Results From the JAVELIN Solid Tumor Trial. JAMA Oncol. 2019.

24. Zhang S, Royer R, Li S, McLaughlin JR, Rosen B, Risch HA, et al. Frequencies of BRCA1 and BRCA2 mutations among 1,342 unselected patients with invasive ovarian cancer. Gynecologic Oncology. 2011;121(2):353-7.

25. Alsop K, Fereday S, Meldrum C, deFazio A, Emmanuel C, George J, et al. BRCA Mutation Frequency and Patterns of Treatment Response in BRCA Mutation–Positive

Women With Ovarian Cancer: A Report From the Australian Ovarian Cancer Study Group. Journal of Clinical Oncology. 2012;30(21):2654-63.

26. Rust K, Spiliopoulou P, Tang CY, Bell C, Stirling D, Phang THF, et al. Routine germline BRCA1 and BRCA2 testing in ovarian carcinoma patients: analysis of the Scottish real life experience. BJOG. 2018.

27. Castilla LH, Couch FJ, Erdos MR, Hoskins KF, Calzone K, Garber JE, et al. Mutations in the BRCA1 gene in families with early-onset breast and ovarian cancer. Nature Genetics. 1994;8(4):387-91.

28. Pennington KP, Swisher EM. Hereditary ovarian cancer: Beyond the usual suspects. Gynecologic Oncology. 2012;124(2):347-53.

29. Bolton KL, Chenevix- Trench G, Goh C, Sadetzki S, Ramus SJ, Karlan BY, et al. Association Between BRCA1 and BRCA2 Mutations and Survival in Women With Invasive Epithelial Ovarian Cancer. JAMA. 2012;307(4):382-9.

30. Liu G, Yang D, Sun Y, Shmulevich I, Xue F, Sood AK, et al. Differing clinical impact of BRCA1 and BRCA2 mutations in serous ovarian cancer. Pharmacogenomics. 2012;13(13):1523-35.

31. Rebbeck TR, Mitra N, Wan F, Sinilnikova OM, Healey S, McGuffog L, et al. Association of Type and Location of BRCA1 and BRCA2 Mutations With Risk of Breast and Ovarian Cancer. JAMA. 2015;313(13):1347-61.

32. D'Andrea AD, Grompe M. The Fanconi anaemia/BRCA pathway. Nature Reviews Cancer. 2003;3(1):23-34.

33. Walsh T, Casadei S, Lee MK, Pennil CC, Nord AS, Thornton AM, et al. Mutations in 12 genes for inherited ovarian, fallopian tube, and peritoneal carcinoma identified by massively parallel sequencing. Proceedings of the National Academy of Sciences. 2011;108(44):18032.

34. Norquist BM, Harrell MI, Brady MF, Walsh T, Lee MK, Gulsuner S, et al. Inherited Mutations in Women With Ovarian Carcinoma. JAMA Oncology. 2016;2(4):482-90.

35. Suwaki N, Klare K, Tarsounas M. RAD51 paralogs: Roles in DNA damage signalling, recombinational repair and tumorigenesis. Seminars in Cell & Developmental Biology. 2011;22(8):898-905.

36. Engel C, Loeffler M, Steinke V, Rahner N, Holinski-Feder E, Dietmaier W, et al. Risks of Less Common Cancers in Proven Mutation Carriers With Lynch Syndrome. Journal of Clinical Oncology. 2012;30(35):4409-15.

37. Ketabi Z, Bartuma K, Bernstein I, Malander S, Grönberg H, Björck E, et al. Ovarian cancer linked to lynch syndrome typically presents as early-onset, non-serous epithelial tumors. Gynecologic Oncology. 2011;121(3):462-5.

38. Crispens MA. Endometrial and ovarian cancer in lynch syndrome. Clin Colon Rectal Surg. 2012;25(2):97-102.

39. Friebel TM, Domchek SM, Rebbeck TR. Modifiers of Cancer Risk in BRCA1 and BRCA2 Mutation Carriers: A Systematic Review and Meta-Analysis. JNCI: Journal of the National Cancer Institute. 2014;106(6).

40. Gaitskell K, Green J, Pirie K, Reeves G, Valerie B, on behalf of the Million Women Study C. Tubal ligation and ovarian cancer risk in a large cohort: Substantial variation by histological type. International Journal of Cancer. 2016;138(5):1076-84.

41. Rice MS, Hankinson SE, Tworoger SS. Tubal ligation, hysterectomy, unilateral oophorectomy, and risk of ovarian cancer in the Nurses' Health Studies. Fertility and Sterility. 2014;102(1):192-8.e3.

42. Domchek SM, Friebel TM, Singer CF, Evans DG, Lynch HT, Isaacs C, et al. Association of Risk-Reducing Surgery in BRCA1 or BRCA2 Mutation Carriers With Cancer Risk and Mortality. JAMA. 2010;304(9):967-75.

43. Wentzensen N, Poole EM, Trabert B, White E, Arslan AA, Patel AV, et al. Ovarian Cancer Risk Factors by Histologic Subtype: An Analysis From the Ovarian Cancer Cohort Consortium. Journal of Clinical Oncology. 2016;34(24):2888-98.

44. Moorman PG, Havrilesky LJ, Gierisch JM, Coeytaux RR, Lowery WJ, Peragallo Urrutia R, et al. Oral Contraceptives and Risk of Ovarian Cancer and Breast Cancer Among High-Risk Women: A Systematic Review and Meta-Analysis. Journal of Clinical Oncology. 2013;31(33):4188-98.

45. Bassuk SS, Manson JE. Oral contraceptives and menopausal hormone therapy: relative and attributable risks of cardiovascular disease, cancer, and other health outcomes. Annals of Epidemiology. 2015;25(3):193-200.

46. Havrilesky LJ, Moorman PG, Lowery WJ, Gierisch JM, Coeytaux RR, Urrutia RP, et al. Oral Contraceptive Pills as Primary Prevention for Ovarian Cancer: A Systematic Review and Meta-analysis. Obstetrics & Gynecology. 2013;122(1).

47. Pearce CL, Chung K, Pike MC, Wu AH. Increased ovarian cancer risk associated with menopausal estrogen therapy is reduced by adding a progestin. Cancer. 2009;115(3):531-9.

48. Mørch LS, Løkkegaard E, Andreasen AH, Krüger-Kjær S, Lidegaard Ø. Hormone Therapy and Ovarian Cancer. JAMA. 2009;302(3):298-305.

49. Hildebrand JS, Gapstur SM, Feigelson HS, Teras LR, Thun MJ, Patel AV. Postmenopausal hormone use and incident ovarian cancer: Associations differ by regimen. International Journal of Cancer. 2010;127(12):2928-35.

50. Collaborative Group on Epidemiological Studies of Ovarian C. Menopausal hormone use and ovarian cancer risk: individual participant meta-analysis of 52 epidemiological studies. The Lancet. 2015;385(9980):1835-42.

51. Eeles RA, Morden JP, Gore M, Mansi J, Glees J, Wenczl M, et al. Adjuvant Hormone Therapy May Improve Survival in Epithelial Ovarian Cancer: Results of the AHT Randomized Trial. Journal of Clinical Oncology. 2015;33(35):4138-44.

52. Keum N, Greenwood DC, Lee DH, Kim R, Aune D, Ju W, et al. Adult Weight Gain and Adiposity-Related Cancers: A Dose-Response Meta-Analysis of Prospective Observational Studies. JNCI: Journal of the National Cancer Institute. 2015;107(2).

53. Olsen CM, Nagle CM, Whiteman DC, Ness R, Pearce CL, Pike MC, et al. Obesity and risk of ovarian cancer subtypes: evidence from the Ovarian Cancer Association Consortium. Endocrine-related cancer. 2013;20(2):251-62.

54. Cannioto RA, Moysich KB. Epithelial ovarian cancer and recreational physical activity: A review of the epidemiological literature and implications for exercise prescription. Gynecologic Oncology. 2015;137(3):559-73.

55. Catherine MO, Christina MN, David CW, Roberta N, Celeste Leigh P, Malcolm CP, et al. Obesity and risk of ovarian cancer subtypes: evidence from the Ovarian Cancer Association Consortium. Endocrine-Related Cancer. 2013;20(2):251-62.

56. Dixon-Suen SC, Nagle CM, Thrift AP, Pharoah PDP, Ewing A, Pearce CL, et al. Adult height is associated with increased risk of ovarian cancer: a Mendelian randomisation study. British Journal of Cancer. 2018;118(8):1123-9.

57. Koushik A, Wang M, Anderson KE, van den Brandt P, Clendenen TV, Eliassen AH, et al. Intake of vitamins A, C, and E and folate and the risk of ovarian cancer in a pooled analysis of 10 cohort studies. Cancer causes & control : CCC. 2015;26(9):1315-27.

58. Xie J, Poole EM, Terry KL, Fung TT, Rosner BA, Willett WC, et al. A prospective cohort study of dietary indices and incidence of epithelial ovarian cancer. Journal of ovarian research. 2014;7:112-.

59. Cassidy A, Huang T, Rice MS, Rimm EB, Tworoger SS. Intake of dietary flavonoids and risk of epithelial ovarian cancer. The American Journal of Clinical Nutrition. 2014;100(5):1344-51.

60. Merritt MA, Poole EM, Hankinson SE, Willett WC, Tworoger SS. Dairy food and nutrient intake in different life periods in relation to risk of ovarian cancer. Cancer Causes & Control. 2014;25(7):795-808.

61. Trabert B, Ness RB, Lo-Ciganic W-H, Murphy MA, Goode EL, Poole EM, et al. Aspirin, Nonaspirin Nonsteroidal Anti-inflammatory Drug, and Acetaminophen Use and Risk of Invasive Epithelial Ovarian Cancer: A Pooled Analysis in the Ovarian Cancer Association Consortium. JNCI: Journal of the National Cancer Institute. 2014;106(2).

62. O'Brien KM, Tworoger SS, Harris HR, Anderson GL, Weinberg CR, Trabert B, et al. Association of Powder Use in the Genital Area With Risk of Ovarian Cancer. JAMA. 2020;323(1):49-59.

63. Terry KL, Karageorgi S, Shvetsov YB, Merritt MA, Lurie G, Thompson PJ, et al. Genital powder use and risk of ovarian cancer: a pooled analysis of 8,525 cases and 9,859 controls. Cancer prevention research (Philadelphia, Pa). 2013;6(8):811-21.

64. Houghton SC, Reeves KW, Hankinson SE, Crawford L, Lane D, Wactawski-Wende J, et al. Perineal Powder Use and Risk of Ovarian Cancer. JNCI: Journal of the National Cancer Institute. 2014;106(9).

65. Narod SA. Talc and ovarian cancer. Gynecologic Oncology. 2016;141(3):410-2.

66. Ahmed AA, Etemadmoghadam D, Temple J, Lynch AG, Riad M, Sharma R, et al. Driver mutations in TP53 are ubiquitous in high grade serous carcinoma of the ovary. J Pathol. 2010;221(1):49-56.

67. Köbel M, Reuss A, Bois Ad, Kommoss S, Kommoss F, Gao D, et al. The biological and clinical value of p53 expression in pelvic high-grade serous carcinomas. The Journal of Pathology. 2010;222(2):191-8.

68. Cancer Genome Atlas Research N. Integrated genomic analyses of ovarian carcinoma. Nature. 2011;474(7353):609-15.

69. Vang R, Shih I-M, Kurman RJ. Fallopian tube precursors of ovarian low- and high-grade serous neoplasms. Histopathology. 2013;62(1):44-58.

70. Carlson JW, Miron A, Jarboe EA, Parast MM, Hirsch MS, Lee Y, et al. Serous Tubal Intraepithelial Carcinoma: Its Potential Role in Primary Peritoneal Serous Carcinoma and Serous Cancer Prevention. Journal of Clinical Oncology. 2008;26(25):4160-5.

71. Medeiros F, Muto MG, Lee Y, Elvin JA, Callahan MJ, Feltmate C, et al. The tubal fimbria is a preferred site for early adenocarcinoma in women with familial ovarian cancer syndrome. Am J Surg Pathol. 2006;30(2):230-6.

72. Macintyre G, Goranova TE, De Silva D, Ennis D, Piskorz AM, Eldridge M, et al. Copy number signatures and mutational processes in ovarian carcinoma. Nature Genetics. 2018.

73. Tothill RW, Tinker AV, George J, Brown R, Fox SB, Lade S, et al. Novel molecular subtypes of serous and endometrioid ovarian cancer linked to clinical outcome. Clin Cancer Res. 2008;14(16):5198-208.

74. Farley J, Brady WE, Vathipadiekal V, Lankes HA, Coleman R, Morgan MA, et al. Selumetinib in women with recurrent low-grade serous carcinoma of the ovary or peritoneum: an open-label, single-arm, phase 2 study. The Lancet Oncology. 2013;14(2):134-40.

75. McLachlan J, Gore M, Banerjee S. Targeting the mitogen-activated protein kinase pathway in low-grade serous carcinoma of the ovary. Pharmacogenomics. 2016;17(12):1353-63.

76. Glasspool RM, McNeish IA. Clear Cell Carcinoma of Ovary and Uterus. Current Oncology Reports. 2013;15(6):566-72.

77. Mabuchi S, Sugiyama T, Kimura T. Clear cell carcinoma of the ovary: molecular insights and future therapeutic perspectives. Journal of gynecologic oncology. 2016;27(3):e31-e.

78. Wiegand KC, Shah SP, Al-Agha OM, Zhao Y, Tse K, Zeng T, et al. ARID1A Mutations in Endometriosis-Associated Ovarian Carcinomas. New England Journal of Medicine. 2010;363(16):1532-43.

79. Jones S, Wang T-L, Shih I-M, Mao T-L, Nakayama K, Roden R, et al. Frequent Mutations of Chromatin Remodeling Gene ARID1A in Ovarian Clear Cell Carcinoma. Science. 2010;330(6001):228.

80. Kuo K-T, Mao T-L, Jones S, Veras E, Ayhan A, Wang T-L, et al. Frequent activating mutations of PIK3CA in ovarian clear cell carcinoma. The American journal of pathology. 2009;174(5):1597-601.

81. Chandler RL, Damrauer JS, Raab JR, Schisler JC, Wilkerson MD, Didion JP, et al. Coexistent ARID1A-PIK3CA mutations promote ovarian clear-cell tumorigenesis through pro-tumorigenic inflammatory cytokine signalling. Nat Commun. 2015;6:6118.

82. Bitler BG, Aird KM, Garipov A, Li H, Amatangelo M, Kossenkov AV, et al. Synthetic lethality by targeting EZH2 methyltransferase activity in ARID1A-mutated cancers. Nat Med. 2015;21(3):231-8.

83. Anglesio MS, George J, Kulbe H, Friedlander M, Rischin D, Lemech C, et al. IL6-STAT3-HIF Signaling and Therapeutic Response to the Angiogenesis Inhibitor Sunitinib in Ovarian Clear Cell Cancer. Clinical Cancer Research. 2011;17(8):2538.

84. Yanaihara N, Anglesio MS, Ochiai K, Hirata Y, Saito M, Nagata C, et al. Cytokine gene expression signature in ovarian clear cell carcinoma. Int J Oncol. 2012;41(3):1094-100.

85. Mabuchi S, Kawase C, Altomare DA, Morishige K, Hayashi M, Sawada K, et al. Vascular Endothelial Growth Factor Is a Promising Therapeutic Target for the Treatment of Clear Cell Carcinoma of the Ovary. Molecular Cancer Therapeutics. 2010;9(8):2411.

86. Xu W, Rush J, Rickett K, Coward JIG. Mucinous ovarian cancer: A therapeutic review. Critical Reviews in Oncology/Hematology. 2016;102:26-36.

87. Babaier A, Ghatage P. Mucinous Cancer of the Ovary: Overview and Current Status. Diagnostics (Basel). 2020;10(1).

88. Cheasley D, Wakefield MJ, Ryland GL, Allan PE, Alsop K, Amarasinghe KC, et al. The molecular origin and taxonomy of mucinous ovarian carcinoma. Nat Commun. 2019;10(1):3935.

89. Anglesio MS, Kommoss S, Tolcher MC, Clarke B, Galletta L, Porter H, et al. Molecular characterization of mucinous ovarian tumours supports a stratified treatment approach with HER2 targeting in 19% of carcinomas. The Journal of Pathology. 2013;229(1):111-20.

90. Chay W-Y, Chew S-H, Ong W-S, Busmanis I, Li X, Thung S, et al. HER2 Amplification and Clinicopathological Characteristics in a Large Asian Cohort of Rare Mucinous Ovarian Cancer. PLOS ONE. 2013;8(4):e61565.

91. Gilks CB, McAlpine J. Human epidermal growth factor receptor 2 overexpression and amplification in mucinous tumours of ovary. Histopathology. 2011;58(7):1173-4.

92. Lin W-L, Kuo W-H, Chen F-L, Lee M-Y, Ruan A, Tyan Y-S, et al. Identification of the Coexisting HER2 Gene Amplification and Novel Mutations in the HER2 Protein-Overexpressed Mucinous Epithelial Ovarian Cancer. Annals of Surgical Oncology. 2011;18(8):2388-94.

93. Yan B, Choo SN, Mulyadi P, Srivastava S, Ong CW, Yong KJ, et al. Dual-colour HER2/chromosome 17 chromogenic in situ hybridisation enables accurate assessment of HER2 genomic status in ovarian tumours. Journal of Clinical Pathology. 2011;64(12):1097.

94. du Bois A, Reuss A, Harter P, Pujade-Lauraine E, Ray-Coquard I, Pfisterer J. Potential Role of Lymphadenectomy in Advanced Ovarian Cancer: A Combined Exploratory Analysis of Three Prospectively Randomized Phase III Multicenter Trials. Journal of Clinical Oncology. 2010;28(10):1733-9.

95. du Bois A, Reuss A, Pujade-Lauraine E, Harter P, Ray-Coquard I, Pfisterer J. Role of surgical outcome as prognostic factor in advanced epithelial ovarian cancer: A combined exploratory analysis of 3 prospectively randomized phase 3 multicenter trials. Cancer. 2009;115(6):1234-44.

96. Bristow RE, Tomacruz RS, Armstrong DK, Trimble EL, Montz FJ. Survival Effect of Maximal Cytoreductive Surgery for Advanced Ovarian Carcinoma During the Platinum Era: A Meta-Analysis. Journal of Clinical Oncology. 2002;20(5):1248-59.

97. Colombo N, Sessa C, du Bois A, Ledermann J, McCluggage WG, McNeish I, et al. ESMO-ESGO consensus conference recommendations on ovarian cancer: pathology and molecular biology, early and advanced stages, borderline tumours and recurrent diseasedagger. Ann Oncol. 2019;30(5):672-705.

98. Piccart MJ, Bertelsen K, James K, Cassidy J, Mangioni C, Simonsen E, et al. Randomized Intergroup Trial of Cisplatin–Paclitaxel Versus Cisplatin–Cyclophosphamide in Women With Advanced Epithelial Ovarian Cancer: Three-Year Results. JNCI: Journal of the National Cancer Institute. 2000;92(9):699-708.

99. Katsumata N, Yasuda M, Isonishi S, Takahashi F, Michimae H, Kimura E, et al. Long-term results of dose-dense paclitaxel and carboplatin versus conventional paclitaxel and carboplatin for treatment of advanced epithelial ovarian, fallopian tube, or primary

peritoneal cancer (JGOG 3016): a randomised, controlled, open-label trial. Lancet Oncol. 2013;14(10):1020-6.

100. Vergote I, Tropé CG, Amant F, Kristensen GB, Ehlen T, Johnson N, et al. Neoadjuvant Chemotherapy or Primary Surgery in Stage IIIC or IV Ovarian Cancer. New England Journal of Medicine. 2010;363(10):943-53.

101. Kehoe S, Hook J, Nankivell M, Jayson GC, Kitchener H, Lopes T, et al. Primary chemotherapy versus primary surgery for newly diagnosed advanced ovarian cancer (CHORUS): an open-label, randomised, controlled, non-inferiority trial. The Lancet. 2015;386(9990):249-57.

102. Burger RA, Brady MF, Bookman MA, Fleming GF, Monk BJ, Huang H, et al. Incorporation of Bevacizumab in the Primary Treatment of Ovarian Cancer. New England Journal of Medicine. 2011;365(26):2473-83.

103. Perren TJ, Swart AM, Pfisterer J, Ledermann JA, Pujade-Lauraine E, Kristensen G, et al. A Phase 3 Trial of Bevacizumab in Ovarian Cancer. New England Journal of Medicine. 2011;365(26):2484-96.

104. Oza AM, Cook AD, Pfisterer J, Embleton A, Ledermann JA, Pujade-Lauraine E, et al. Standard chemotherapy with or without bevacizumab for women with newly diagnosed ovarian cancer (ICON7): overall survival results of a phase 3 randomised trial. The Lancet Oncology. 2015;16(8):928-36.

105. Armstrong DK, Bundy B, Wenzel L, Huang HQ, Baergen R, Lele S, et al. Intraperitoneal Cisplatin and Paclitaxel in Ovarian Cancer. New England Journal of Medicine. 2006;354(1):34-43.

106. Walker JL, Brady MF, Wenzel L, Fleming GF, Huang HQ, DiSilvestro PA, et al. Randomized Trial of Intravenous Versus Intraperitoneal Chemotherapy Plus Bevacizumab in Advanced Ovarian Carcinoma: An NRG Oncology/Gynecologic Oncology Group Study. Journal of Clinical Oncology. 2019;37(16):1380-90.

107. Moore K, Colombo N, Scambia G, Kim BG, Oaknin A, Friedlander M, et al. Maintenance Olaparib in Patients with Newly Diagnosed Advanced Ovarian Cancer. N Engl J Med. 2018;379(26):2495-505.

108. Coleman RL, Fleming GF, Brady MF, Swisher EM, Steffensen KD, Friedlander M, et al. Veliparib with First-Line Chemotherapy and as Maintenance Therapy in Ovarian Cancer. New England Journal of Medicine. 2019;381(25):2403-15.

109. Gonzalez-Martin A, Pothuri B, Vergote I, DePont Christensen R, Graybill W, Mirza MR, et al. Niraparib in Patients with Newly Diagnosed Advanced Ovarian Cancer. N Engl J Med. 2019;381(25):2391-402.

110. Ray-Coquard I, Pautier P, Pignata S, Pérol D, González-Martín A, Berger R, et al. Olaparib plus Bevacizumab as First-Line Maintenance in Ovarian Cancer. New England Journal of Medicine. 2019;381(25):2416-28.

111. Harter P, Bois Ad, Hahmann M, Hasenburg A, Burges A, Loibl S, et al. Surgery in Recurrent Ovarian Cancer: The Arbeitsgemeinschaft Gynaekologische Onkologie (AGO) DESKTOP OVAR Trial. Annals of Surgical Oncology. 2006;13(12):1702-10.

112. Du Bois A, Sehouli J, Vergote I, Ferron G, Reuss A, Meier W, et al. Randomized phase III study to evaluate the impact of secondary cytoreductive surgery in recurrent ovarian cancer: Final analysis of AGO DESKTOP III/ENGOT-ov20. Journal of Clinical Oncology. 2020;38(15_suppl):6000-.

113. Rustin GJS, Marples M, Nelstrop AE, Mahmoudi M, Meyer T. Use of CA-125 to Define Progression of Ovarian Cancer in Patients With Persistently Elevated Levels. Journal of Clinical Oncology. 2001;19(20):4054-7.

114. Salani R, Backes FJ, Fung Kee Fung M, Holschneider CH, Parker LP, Bristow RE, et al. Posttreatment surveillance and diagnosis of recurrence in women with gynecologic malignancies: Society of Gynecologic Oncologists recommendations. American Journal of Obstetrics & Gynecology. 2011;204(6):466-78.

115. Rustin GJS, van der Burg MEL, Griffin CL, Guthrie D, Lamont A, Jayson GC, et al. Early versus delayed treatment of relapsed ovarian cancer (MRC OV05/EORTC 55955): a randomised trial. The Lancet. 2010;376(9747):1155-63.

116. Alvarez RD, Matulonis UA, Herzog TJ, Coleman RL, Monk BJ, Markman M. Moving beyond the platinum sensitive/resistant paradigm for patients with recurrent ovarian cancer. Gynecologic Oncology. 2016;141(3):405-9.

117. Zang R, Zhu J. Which patients benefit from secondary cytoreductive surgery in recurrent ovarian cancer? Journal of gynecologic oncology. 2019;30(6):e116-e.

118. Sehouli J, Grabowski JP. Surgery in recurrent ovarian cancer. Cancer. 2019;125 Suppl 24:4598-601.

119. Ledermann JA, Raja FA, Fotopoulou C, Gonzalez-Martin A, Colombo N, Sessa C, et al. Newly diagnosed and relapsed epithelial ovarian carcinoma: ESMO Clinical Practice Guidelines for diagnosis, treatment and follow-up. Ann Oncol. 2013;24 Suppl 6:vi24-32.

120. Paclitaxel plus platinum-based chemotherapy versus conventional platinum-based chemotherapy in women with relapsed ovarian cancer: the ICON4/AGO-OVAR-2.2 trial. The Lancet. 2003;361(9375):2099-106.

121. Pujade-Lauraine E, Wagner U, Aavall-Lundqvist E, Gebski V, Heywood M, Vasey PA, et al. Pegylated Liposomal Doxorubicin and Carboplatin Compared With Paclitaxel and Carboplatin for Patients With Platinum-Sensitive Ovarian Cancer in Late Relapse. Journal of Clinical Oncology. 2010;28(20):3323-9.

122. Pfisterer J, Plante M, Vergote I, du Bois A, Hirte H, Lacave AJ, et al. Gemcitabine Plus Carboplatin Compared With Carboplatin in Patients With Platinum-Sensitive Recurrent Ovarian Cancer: An Intergroup Trial of the AGO-OVAR, the NCIC CTG, and the EORTC GCG. Journal of Clinical Oncology. 2006;24(29):4699-707.

123. Castells MC, Tennant NM, Sloane DE, Ida Hsu F, Barrett NA, Hong DI, et al. Hypersensitivity reactions to chemotherapy: Outcomes and safety of rapid desensitization in 413 cases. Journal of Allergy and Clinical Immunology. 2008;122(3):574-80.

124. Aghajanian C, Blank SV, Goff BA, Judson PL, Teneriello MG, Husain A, et al. OCEANS: A Randomized, Double-Blind, Placebo-Controlled Phase III Trial of Chemotherapy With or Without Bevacizumab in Patients With Platinum-Sensitive Recurrent Epithelial Ovarian, Primary Peritoneal, or Fallopian Tube Cancer. Journal of Clinical Oncology. 2012;30(17):2039-45.

125. Takebayashi Y, Pourquier P, Zimonjic DB, Nakayama K, Emmert S, Ueda T, et al. Antiproliferative activity of ecteinascidin 743 is dependent upon transcription-coupled nucleotide-excision repair. Nature Medicine. 2001;7(8):961-6.

126. Incalci M, Galmarini CM. A Review of Trabectedin (ET-743): A Unique Mechanism of Action. Molecular Cancer Therapeutics. 2010;9(8):2157.

127. Ventriglia J, Paciolla I, Cecere SC, Pisano C, Di Napoli M, Arenare L, et al. Trabectedin in Ovarian Cancer: is it now a Standard of Care? Clinical Oncology. 2018;30(8):498-503.

128. Poveda A, Vergote I, Tjulandin S, Kong B, Roy M, Chan S, et al. Trabectedin plus pegylated liposomal doxorubicin in relapsed ovarian cancer: outcomes in the partially platinum-sensitive (platinum-free interval 6-12 months) subpopulation of OVA-301 phase III randomized trial. Annals of oncology : official journal of the European Society for Medical Oncology. 2011;22(1):39-48.

129. Pujade-Lauraine E, Ledermann JA, Selle F, Gebski V, Penson RT, Oza AM, et al. Olaparib tablets as maintenance therapy in patients with platinum-sensitive, relapsed ovarian cancer and a BRCA1/2 mutation (SOLO2/ENGOT-Ov21): a double-blind, randomised, placebo-controlled, phase 3 trial. The Lancet Oncology. 2017;18(9):1274-84.

130. Coleman RL, Oza AM, Lorusso D, Aghajanian C, Oaknin A, Dean A, et al. Rucaparib maintenance treatment for recurrent ovarian carcinoma after response to platinum therapy (ARIEL3): a randomised, double-blind, placebo-controlled, phase 3 trial. The Lancet. 2017;390(10106):1949-61.

131. Drew Y, Kaufman B, Banerjee S, Lortholary A, Hong SH, Park YH, et al. Phase II study of olaparib + durvalumab (MEDIOLA): Updated results in germline BRCA-mutated platinum-sensitive relapsed (PSR) ovarian cancer (OC). Annals of Oncology. 2019;30:v485-v6.

132. Pujade-Lauraine E, Hilpert F, Weber B, Reuss A, Poveda A, Kristensen G, et al. Bevacizumab Combined With Chemotherapy for Platinum-Resistant Recurrent Ovarian Cancer: The AURELIA Open-Label Randomized Phase III Trial. Journal of Clinical Oncology. 2014;32(13):1302-8.

133. Poveda AM, Selle F, Hilpert F, Reuss A, Savarese A, Vergote I, et al. Bevacizumab Combined With Weekly Paclitaxel, Pegylated Liposomal Doxorubicin, or Topotecan in Platinum-Resistant Recurrent Ovarian Cancer: Analysis by Chemotherapy Cohort of the

Randomized Phase III AURELIA Trial. Journal of Clinical Oncology. 2015;33(32):3836-8.

134. Huinink WtB, Gore M, Carmichael J, Gordon A, Malfetano J, Hudson I, et al. Topotecan versus paclitaxel for the treatment of recurrent epithelial ovarian cancer. Journal of Clinical Oncology. 1997;15(6):2183-93.

135. Gordon AN, Tonda M, Sun S, Rackoff W, Doxil Study I. Long-term survival advantage for women treated with pegylated liposomal doxorubicin compared with topotecan in a phase 3 randomized study of recurrent and refractory epithelial ovarian cancer. Gynecol Oncol. 2004;95(1):1-8.

136. Colombo N, Gore M. Treatment of recurrent ovarian cancer relapsing 6-12 months post platinum-based chemotherapy. Crit Rev Oncol Hematol. 2007;64(2):129-38.

137. Jackson AL, Eisenhauer EL, Herzog TJ. Emerging therapies: angiogenesis inhibitors for ovarian cancer. Expert Opinion on Emerging Drugs. 2015;20(2):331-46.

138. Gadducci A, Lanfredini N, Sergiampietri C. Antiangiogenic agents in gynecological cancer: State of art and perspectives of clinical research. Critical Reviews in Oncology/Hematology. 2015;96(1):113-28.

139. Matulonis UA, Berlin S, Ivy P, Tyburski K, Krasner C, Zarwan C, et al. Cediranib, an Oral Inhibitor of Vascular Endothelial Growth Factor Receptor Kinases, Is an Active Drug in Recurrent Epithelial Ovarian, Fallopian Tube, and Peritoneal Cancer. Journal of Clinical Oncology. 2009;27(33):5601-6.

140. Zhang B, Chen F, Xu Q, Han L, Xu J, Gao L, et al. Revisiting ovarian cancer microenvironment: a friend or a foe? Protein Cell. 2018;9(8):674-92.

141. Cai DL, Jin LP. Immune Cell Population in Ovarian Tumor Microenvironment. J Cancer. 2017;8(15):2915-23.

142. Meza-Perez S, Randall TD. Immunological Functions of the Omentum. Trends Immunol. 2017;38(7):526-36.

143. Drakes ML, Stiff PJ. Regulation of Ovarian Cancer Prognosis by Immune Cells in the Tumor Microenvironment. Cancers (Basel). 2018;10(9).

144. Fridman WH, Pages F, Sautes-Fridman C, Galon J. The immune contexture in human tumours: impact on clinical outcome. Nat Rev Cancer. 2012;12(4):298-306.

145. Hwang W-T, Adams SF, Tahirovic E, Hagemann IS, Coukos G. Prognostic significance of tumor-infiltrating T cells in ovarian cancer: A meta-analysis. Gynecologic Oncology. 2012;124(2):192-8.

146. Santoiemma PP, Powell DJ. Tumor infiltrating lymphocytes in ovarian cancer. Cancer Biology & Therapy. 2015;16(6):807-20.

147. Hamanishi J, Mandai M, Abiko K, Matsumura N, Baba T, Yoshioka Y, et al. The comprehensive assessment of local immune status of ovarian cancer by the clustering of multiple immune factors. Clinical Immunology. 2011;141(3):338-47.

148. Tomšová M, Melichar B, Sedláková I, Šteiner I. Prognostic significance of CD3+ tumor-infiltrating lymphocytes in ovarian carcinoma. Gynecologic Oncology. 2008;108(2):415-20.

149. Zhang L, Conejo-Garcia JR, Katsaros D, Gimotty PA, Massobrio M, Regnani G, et al. Intratumoral T Cells, Recurrence, and Survival in Epithelial Ovarian Cancer. New England Journal of Medicine. 2003;348(3):203-13.

150. Hwang WT, Adams SF, Tahirovic E, Hagemann IS, Coukos G. Prognostic significance of tumor-infiltrating T cells in ovarian cancer: a meta-analysis. Gynecol Oncol. 2012;124(2):192-8.

151. Sato E, Olson SH, Ahn J, Bundy B, Nishikawa H, Qian F, et al. Intraepithelial CD8+ tumor-infiltrating lymphocytes and a high CD8+/regulatory T cell ratio are associated with favorable prognosis in ovarian cancer. Proc Natl Acad Sci U S A. 2005;102(51):18538-43.

152. Webb JR, Milne K, Watson P, deLeeuw RJ, Nelson BH. Tumor-Infiltrating Lymphocytes Expressing the Tissue Resident Memory Marker CD103 Are Associated with Increased Survival in High-Grade Serous Ovarian Cancer. Clinical Cancer Research. 2014;20(2):434.

153. Komdeur FL, Wouters MCA, Workel HH, Tijans AM, Terwindt ALJ, Brunekreeft KL, et al. CD103+ intraepithelial T cells in high-grade serous ovarian cancer are phenotypically diverse TCRαβ+ CD8αβ+ T cells that can be targeted for cancer immunotherapy. Oncotarget. 2016;7(46):75130-44.

154. Ovarian Tumor Tissue Analysis C, Goode EL, Block MS, Kalli KR, Vierkant RA, Chen W, et al. Dose-Response Association of CD8+ Tumor-Infiltrating Lymphocytes and Survival Time in High-Grade Serous Ovarian Cancer. JAMA Oncol. 2017;3(12):e173290.

155. Hori S, Nomura T, Sakaguchi S. Control of Regulatory T Cell Development by the Transcription Factor Foxp3. Science. 2003;299(5609):1057.

156. Togashi Y, Shitara K, Nishikawa H. Regulatory T cells in cancer immunosuppression - implications for anticancer therapy. Nat Rev Clin Oncol. 2019;16(6):356-71.

157. Landskron J, Helland Ø, Torgersen KM, Aandahl EM, Gjertsen BT, Bjørge L, et al. Activated regulatory and memory T-cells accumulate in malignant ascites from ovarian carcinoma patients. Cancer immunology, immunotherapy : CII. 2015;64(3):337-47.

158. Curiel TJ, Coukos G, Zou L, Alvarez X, Cheng P, Mottram P, et al. Specific recruitment of regulatory T cells in ovarian carcinoma fosters immune privilege and predicts reduced survival. Nature Medicine. 2004;10(9):942-9.

159. Wolf D, Wolf AM, Rumpold H, Fiegl H, Zeimet AG, Muller-Holzner E, et al. The Expression of the Regulatory T Cell–Specific Forkhead Box Transcription Factor FoxP3 Is Associated with Poor Prognosis in Ovarian Cancer. Clinical Cancer Research. 2005;11(23):8326.

160. Shang B, Liu Y, Jiang S-j, Liu Y. Prognostic value of tumor-infiltrating FoxP3+ regulatory T cells in cancers: a systematic review and meta-analysis. Scientific Reports. 2015;5(1):15179.

161. Preston CC, Maurer MJ, Oberg AL, Visscher DW, Kalli KR, Hartmann LC, et al. The ratios of CD8+ T cells to CD4+CD25+ FOXP3+ and FOXP3- T cells correlate with poor clinical outcome in human serous ovarian cancer. PLoS One. 2013;8(11):e80063.

162. Worzfeld T, Pogge von Strandmann E, Huber M, Adhikary T, Wagner U, Reinartz S, et al. The Unique Molecular and Cellular Microenvironment of Ovarian Cancer. Frontiers in oncology. 2017;7:24-.

163. Wong JL, Berk E, Edwards RP, Kalinski P. IL-18–Primed Helper NK Cells Collaborate with Dendritic Cells to Promote Recruitment of Effector CD8+ T Cells to the Tumor Microenvironment. Cancer Research. 2013;73(15):4653.

164. Krockenberger M, Dombrowski Y, Weidler C, Ossadnik M, Hönig A, Häusler S, et al. Macrophage Migration Inhibitory Factor Contributes to the Immune Escape of Ovarian Cancer by Down-Regulating NKG2D. The Journal of Immunology. 2008;180(11):7338.

165. da Silva RF, Yoshida A, Cardozo DM, Jales RM, Paust S, Derchain S, et al. Natural Killer Cells Response to IL-2 Stimulation Is Distinct between Ascites with the Presence or Absence of Malignant Cells in Ovarian Cancer Patients. Int J Mol Sci. 2017;18(5):856.

166. Wennerberg E, Kremer V, Childs R, Lundqvist A. CXCL10-induced migration of adoptively transferred human natural killer cells toward solid tumors causes regression of tumor growth in vivo. Cancer Immunol Immunother. 2015;64(2):225-35.

167. Pollard JW. Tumour-educated macrophages promote tumour progression and metastasis. Nature Reviews Cancer. 2004;4(1):71-8.

168. Elliott LA, Doherty GA, Sheahan K, Ryan EJ. Human Tumor-Infiltrating Myeloid Cells: Phenotypic and Functional Diversity. Frontiers in immunology. 2017;8:86-.

169. Franklin RA, Liao W, Sarkar A, Kim MV, Bivona MR, Liu K, et al. The cellular and molecular origin of tumor-associated macrophages. Science. 2014;344(6186):921.

170. Liu Y, Cao X. The origin and function of tumor-associated macrophages. Cell Mol Immunol. 2015;12(1):1-4.

171. Allavena P, Chieppa M, Bianchi G, Solinas G, Fabbri M, Laskarin G, et al. Engagement of the mannose receptor by tumoral mucins activates an immune suppressive phenotype in human tumor-associated macrophages. Clin Dev Immunol. 2010;2010:547179.

172. Finkernagel F, Reinartz S, Lieber S, Adhikary T, Wortmann A, Hoffmann N, et al. The transcriptional signature of human ovarian carcinoma macrophages is associated with extracellular matrix reorganization. Oncotarget. 2016;7(46).

173. Reinartz S, Schumann T, Finkernagel F, Wortmann A, Jansen JM, Meissner W, et al. Mixed-polarization phenotype of ascites-associated macrophages in human ovarian carcinoma: correlation of CD163 expression, cytokine levels and early relapse. International journal of cancer. 2014;134(1):32-42.

174. Yin M, Li X, Tan S, Zhou HJ, Ji W, Bellone S, et al. Tumor-associated macrophages drive spheroid formation during early transcoelomic metastasis of ovarian cancer. The Journal of clinical investigation. 2016;126(11):4157-73.

175. Zhang Q-w, Liu L, Gong C-y, Shi H-s, Zeng Y-h, Wang X-z, et al. Prognostic Significance of Tumor-Associated Macrophages in Solid Tumor: A Meta-Analysis of the Literature. PLOS ONE. 2012;7(12):e50946.

176. Mempel TR, Henrickson SE, von Andrian UH. T-cell priming by dendritic cells in lymph nodes occurs in three distinct phases. Nature. 2004;427(6970):154-9.

177. Henrickson Sarah E, Perro M, Loughhead Scott M, Senman B, Stutte S, Quigley M, et al. Antigen Availability Determines CD8+ T Cell-Dendritic Cell Interaction Kinetics and Memory Fate Decisions. Immunity. 2013;39(3):496-507.

178. Lutz MB, Schuler G. Immature, semi-mature and fully mature dendritic cells: which signals induce tolerance or immunity? Trends in Immunology. 2002;23(9):445-9.

179. Sabado RL, Balan S, Bhardwaj N. Dendritic cell-based immunotherapy. Cell Research. 2017;27(1):74-95.

180. Garrido F, Perea F, Bernal M, Sánchez-Palencia A, Aptsiauri N, Ruiz-Cabello F. The Escape of Cancer from T Cell-Mediated Immune Surveillance: HLA Class I Loss and Tumor Tissue Architecture. Vaccines (Basel). 2017;5(1):7.

181. Yang D-H, Park J-S, Jin C-J, Kang H-K, Nam J-H, Rhee J-H, et al. The dysfunction and abnormal signaling pathway of dendritic cells loaded by tumor antigen can be overcome by neutralizing VEGF in multiple myeloma. Leukemia Research. 2009;33(5):665-70.

182. Strioga M, Schijns V, Powell DJ, Pasukoniene V, Dobrovolskiene N, Michalek J. Dendritic cells and their role in tumor immunosurveillance. Innate Immunity. 2012;19(1):98-111.

183. Volovitz I, Melzer S, Amar S, Bocsi J, Bloch M, Efroni S, et al. Dendritic Cells in the Context of Human Tumors: Biology and Experimental Tools. International Reviews of Immunology. 2016;35(2):116-35.

184. Lin H, Wei S, Hurt EM, Green MD, Zhao L, Vatan L, et al. Host expression of PD-L1 determines efficacy of PD-L1 pathway blockade-mediated tumor regression. The Journal of clinical investigation. 2018;128(4):1708-.

185. Chen F, Hou M, Ye F, Lv W, Xie X. Ovarian Cancer Cells Induce Peripheral Mature Dendritic Cells to Differentiate Into Macrophagelike Cells In Vitro. International Journal of Gynecologic Cancer. 2009;19(9):1487.

186. Hildner K, Edelson BT, Purtha WE, Diamond M, Matsushita H, Kohyama M, et al. Batf3 Deficiency Reveals a Critical Role for CD8α+ Dendritic Cells in Cytotoxic T Cell Immunity. Science. 2008;322(5904):1097.

187. Spranger S, Dai D, Horton B, Gajewski TF. Tumor-Residing Batf3 Dendritic Cells Are Required for Effector T Cell Trafficking and Adoptive T Cell Therapy. Cancer Cell. 2017;31(5):711-23 e4.

188. Bronger H, Singer J, Windmuller C, Reuning U, Zech D, Delbridge C, et al. CXCL9 and CXCL10 predict survival and are regulated by cyclooxygenase inhibition in advanced serous ovarian cancer. Br J Cancer. 2016;115(5):553-63.

189. Lieber S, Reinartz S, Raifer H, Finkernagel F, Dreyer T, Bronger H, et al. Prognosis of ovarian cancer is associated with effector memory CD8(+) T cell accumulation in ascites, CXCL9 levels and activation-triggered signal transduction in T cells. Oncoimmunology. 2018;7(5):e1424672.

190. Palucka K, Banchereau J. Cancer immunotherapy via dendritic cells. Nature Reviews Cancer. 2012;12(4):265-77.

191. Scarlett UK, Rutkowski MR, Rauwerdink AM, Fields J, Escovar-Fadul X, Baird J, et al. Ovarian cancer progression is controlled by phenotypic changes in dendritic cells. J Exp Med. 2012;209(3):495-506.

192. Leffers N, Fehrmann RS, Gooden MJ, Schulze UR, Ten Hoor KA, Hollema H, et al. Identification of genes and pathways associated with cytotoxic T lymphocyte infiltration of serous ovarian cancer. Br J Cancer. 2010;103(5):685-92.

193. Verhaak RG, Tamayo P, Yang JY, Hubbard D, Zhang H, Creighton CJ, et al. Prognostically relevant gene signatures of high-grade serous ovarian carcinoma. J Clin Invest. 2013;123(1):517-25.

194. Clark-Lewis I, Mattioli I, Gong J-H, Loetscher P. Structure-Function Relationship between the Human Chemokine Receptor CXCR3 and Its Ligands. Journal of Biological Chemistry. 2003;278(1):289-95.

195. Kryczek I, Wei S, Zhu G, Myers L, Mottram P, Cheng P, et al. Relationship between B7-H4, regulatory T cells, and patient outcome in human ovarian carcinoma. Cancer Res. 2007;67(18):8900-5.

196. Dangaj D, Bruand M, Grimm AJ, Ronet C, Barras D, Duttagupta PA, et al. Cooperation between Constitutive and Inducible Chemokines Enables T Cell Engraftment and Immune Attack in Solid Tumors. Cancer Cell. 2019;35(6):885-900 e10.

197. Strieter RM, Burdick MD, Sakkour A, Arnaiz NO, Belperio JA, Keane MP. CXC Chemokines in Cancer. 2005;55:255-88.

198. Au K, Peterson N, Truesdell P, Reid-Schachter G, Khalaj K, Ren R, et al. CXCL10 alters the tumour immune microenvironment and disease progression in a syngeneic murine model of high-grade serous ovarian cancer. Gynecol Oncol. 2017.

199. Cannon MJ, Goyne H, Stone PJB, Chiriva-Internati M. Dendritic cell vaccination against ovarian cancer – tipping the Treg/TH17 balance to therapeutic advantage? Expert Opinion on Biological Therapy. 2011;11(4):441-5.

200. Goyne H, Stone PJB, Cannon MJ. Combinatorial strategies for alleviation of tumor-associated immune suppression and therapeutic vaccination against ovarian cancer. Immunotherapy. 2011;3(7):805-7.

201. Munn DH. Th17 cells in ovarian cancer. Blood. 2009;114(6):1134-5.

202. Middleton GW, Annels NE, Pandha HS. Are we ready to start studies of Th17 cell manipulation as a therapy for cancer? Cancer Immunology, Immunotherapy. 2012;61(1):1-7.

203. Baylin SB, Jones PA. A decade of exploring the cancer epigenome - biological and translational implications. Nat Rev Cancer. 2011;11(10):726-34.

204. Yankulov K. Book review: Epigenetics (second edition, eds. Allis, Caparros, Jenuwein, Reinberg). Front Genet. 2015;6:315.

205. Shen S, Wang G, Zhang R, Zhao Y, Yu H, Wei Y, et al. Development and validation of an immune gene-set based Prognostic signature in ovarian cancer. EBioMedicine. 2019;40:318-26.

206. Allis CJ, T.; Reinberg, D.; Caparros, M. Epigenetics. 2 ed: Cold Spring Harbor Laboratory Press; 2015.

207. Consortium EP. An integrated encyclopedia of DNA elements in the human genome. Nature. 2012;489(7414):57-74.

208. Berger SL, Kouzarides T, Shiekhattar R, Shilatifard A. An operational definition of epigenetics. Genes Dev. 2009;23(7):781-3.

209. Shen H, Laird Peter W. Interplay between the Cancer Genome and Epigenome. Cell. 2013;153(1):38-55.

210. Schneider R, Grosschedl R. Dynamics and interplay of nuclear architecture, genome organization, and gene expression. Genes Dev. 2007;21(23):3027-43.

211. Garraway Levi A, Lander Eric S. Lessons from the Cancer Genome. Cell. 2013;153(1):17-37.

212. You Jueng S, Jones Peter A. Cancer Genetics and Epigenetics: Two Sides of the Same Coin? Cancer Cell. 2012;22(1):9-20.

213. Ahuja N, Sharma AR, Baylin SB. Epigenetic Therapeutics: A New Weapon in the War Against Cancer. Annu Rev Med. 2016;67:73-89.

214. Vavouri T, Lehner B. Human genes with CpG island promoters have a distinct transcription-associated chromatin organization. Genome biology. 2012;13(11):R110-R.

215. Qu G-z, Dubeau L, Narayan A, Yu MC, Ehrlich M. Satellite DNA hypomethylation vs. overall genomic hypomethylation in ovarian epithelial tumors of different malignant potential. Mutation Research/Fundamental and Molecular Mechanisms of Mutagenesis. 1999;423(1):91-101.

216. Widschwendter M, Jiang G, Woods C, Müller HM, Fiegl H, Goebel G, et al. DNA Hypomethylation and Ovarian Cancer Biology. Cancer Research. 2004;64(13):4472.

217. Akers SN, Moysich K, Zhang W, Collamat Lai G, Miller A, Lele S, et al. LINE1 and Alu repetitive element DNA methylation in tumors and white blood cells from epithelial ovarian cancer patients. Gynecologic oncology. 2014;132(2):462-7.

218. Zeimet AG, Fiegl H, Goebel G, Kopp F, Allasia C, Reimer D, et al. DNA ploidy, nuclear size, proliferation index and DNA-hypomethylation in ovarian cancer. Gynecologic oncology. 2011;121(1):24-31.

219. Branch P, Masson M, Aquilina G, Bignami M, Karran P. Spontaneous development of drug resistance: mismatch repair and p53 defects in resistance to cisplatin in human tumor cells. Oncogene. 2000;19(28):3138-45.

220. Plumb JA, Strathdee G, Sludden J, Kaye SB, Brown R. Reversal of Drug Resistance in Human Tumor Xenografts by 2′-Deoxy-5-azacytidine-induced Demethylation of the hMLH1 Gene Promoter. Cancer Research. 2000;60(21):6039.

221. Gifford G, Paul J, Vasey PA, Kaye SB, Brown R. The Acquisition of hMLH1 Methylation in Plasma DNA after Chemotherapy Predicts Poor Survival for Ovarian Cancer Patients. Clinical Cancer Research. 2004;10(13):4420.

222. Brown R, Hirst GL, Gallagher WM, McIlwrath AJ, Margison GP, van der Zee AGJ, et al. hMLH1 expression and cellular responses of ovarian tumour cells to treatment with cytotoxic anticancer agents. Oncogene. 1997;15(1):45-52.

223. Cunningham JM, Cicek MS, Larson NB, Davila J, Wang C, Larson MC, et al. Clinical Characteristics of Ovarian Cancer Classified by BRCA1, BRCA2 and RAD51C Status. Scientific Reports. 2014;4(1):4026.

224. Baldwin RL, Nemeth E, Tran H, Shvartsman H, Cass I, Narod S, et al. BRCA1 Promoter Region Hypermethylation in Ovarian Carcinoma: A Population-based Study. Cancer Research. 2000;60(19):5329.

225. Chaudhry P, Srinivasan R, Patel FD. Utility of Gene Promoter Methylation in Prediction of Response to Platinum-Based Chemotherapy in Epithelial Ovarian Cancer (EOC). Cancer Investigation. 2009;27(8):877-84.

226. Strathdee G, Appleton K, Illand M, Millan DW, Sargent J, Paul J, et al. Primary ovarian carcinomas display multiple methylator phenotypes involving known tumor suppressor genes. The American journal of pathology. 2001;158(3):1121-7.

227. Yang D, Khan S, Sun Y, Hess K, Shmulevich I, Sood AK, et al. Association of BRCA1 and BRCA2 Mutations With Survival, Chemotherapy Sensitivity, and Gene Mutator Phenotype in Patients With Ovarian Cancer. JAMA. 2011;306(14):1557-65.

228. Kaye SB, Lubinski J, Matulonis U, Ang JE, Gourley C, Karlan BY, et al. Phase II, Open-Label, Randomized, Multicenter Study Comparing the Efficacy and Safety of Olaparib, a Poly (ADP-Ribose) Polymerase Inhibitor, and Pegylated Liposomal Doxorubicin in Patients With BRCA1 or BRCA2 Mutations and Recurrent Ovarian Cancer. Journal of Clinical Oncology. 2011;30(4):372-9.

229. Audeh MW, Carmichael J, Penson RT, Friedlander M, Powell B, Bell-McGuinn KM, et al. Oral poly(ADP-ribose) polymerase inhibitor olaparib in patients with BRCA1 or BRCA2 mutations and recurrent ovarian cancer: a proof-of-concept trial. The Lancet. 2010;376(9737):245-51.

230. Ledermann J, Harter P, Gourley C, Friedlander M, Vergote I, Rustin G, et al. Olaparib Maintenance Therapy in Platinum-Sensitive Relapsed Ovarian Cancer. New England Journal of Medicine. 2012;366(15):1382-92.

231. Adeegbe D, Liu Y, Lizotte PH, Kamihara Y, Aref AR, Almonte C, et al. Synergistic Immunostimulatory Effects and Therapeutic Benefit of Combined Histone Deacetylase and Bromodomain Inhibition in Non-small Cell Lung Cancer. Cancer Discov. 2017.

232. Seto E, Yoshida M. Erasers of histone acetylation: the histone deacetylase enzymes. Cold Spring Harbor perspectives in biology. 2014;6(4):a018713-a.

233. Berger SL. The complex language of chromatin regulation during transcription. Nature. 2007;447(7143):407-12.

234. Morey L, Helin K. Polycomb group protein-mediated repression of transcription. Trends in Biochemical Sciences. 2010;35(6):323-32.

235. Schwartz YB, Pirrotta V. A new world of Polycombs: unexpected partnerships and emerging functions. Nature Reviews Genetics. 2013;14(12):853-64.

236. Bracken AP, Helin K. Polycomb group proteins: navigators of lineage pathways led astray in cancer. Nature Reviews Cancer. 2009;9(11):773-84.

237. Hock H. A complex Polycomb issue: the two faces of EZH2 in cancer. Genes Dev. 2012;26(8):751-5.

238. Wagener N, Holland D, Bulkescher J, Crnković-Mertens I, Hoppe-Seyler K, Zentgraf H, et al. The enhancer of zeste homolog 2 gene contributes to cell proliferation and apoptosis resistance in renal cell carcinoma cells. International Journal of Cancer. 2008;123(7):1545-50.

239. Bachmann IM, Halvorsen OJ, Collett K, Stefansson IM, Straume O, Haukaas SA, et al. EZH2 Expression Is Associated With High Proliferation Rate and Aggressive Tumor Subgroups in Cutaneous Melanoma and Cancers of the Endometrium, Prostate, and Breast. Journal of Clinical Oncology. 2006;24(2):268-73.

240. Li H, Zhang R. Role of EZH2 in Epithelial Ovarian Cancer: From Biological Insights to Therapeutic Target. Front Oncol. 2013;3:47.

241. Le DT, Durham JN, Smith KN, Wang H, Bartlett BR, Aulakh LK, et al. Mismatch repair deficiency predicts response of solid tumors to PD-1 blockade. Science. 2017;357(6349):409.

242. Robert C, Schachter J, Long GV, Arance A, Grob JJ, Mortier L, et al. Pembrolizumab versus Ipilimumab in Advanced Melanoma. New England Journal of Medicine. 2015;372(26):2521-32.

243. Motzer RJ, Rini BI, McDermott DF, Redman BG, Kuzel TM, Harrison MR, et al. Nivolumab for Metastatic Renal Cell Carcinoma: Results of a Randomized Phase II Trial. Journal of Clinical Oncology. 2014;33(13):1430-7.

244. Ferris RL, Blumenschein G, Fayette J, Guigay J, Colevas AD, Licitra L, et al. Nivolumab for Recurrent Squamous-Cell Carcinoma of the Head and Neck. New England Journal of Medicine. 2016;375(19):1856-67.

245. Brahmer J, Reckamp KL, Baas P, Crinò L, Eberhardt WEE, Poddubskaya E, et al. Nivolumab versus Docetaxel in Advanced Squamous-Cell Non–Small-Cell Lung Cancer. New England Journal of Medicine. 2015;373(2):123-35.

246. Rizvi NA, Hellmann MD, Snyder A, Kvistborg P, Makarov V, Havel JJ, et al. Cancer immunology. Mutational landscape determines sensitivity to PD-1 blockade in non-small cell lung cancer. Science (New York, NY). 2015;348(6230):124-8.

247. Balachandran VP, Łuksza M, Zhao JN, Makarov V, Moral JA, Remark R, et al. Identification of unique neoantigen qualities in long-term survivors of pancreatic cancer. Nature. 2017;551(7681):512-6.

248. Snyder A, Makarov V, Merghoub T, Yuan J, Zaretsky JM, Desrichard A, et al. Genetic Basis for Clinical Response to CTLA-4 Blockade in Melanoma. New England Journal of Medicine. 2014;371(23):2189-99.

249. Herbst RS, Soria J-C, Kowanetz M, Fine GD, Hamid O, Gordon MS, et al. Predictive correlates of response to the anti-PD-L1 antibody MPDL3280A in cancer patients. Nature. 2014;515(7528):563-7.

250. Patel SJ, Sanjana NE, Kishton RJ, Eidizadeh A, Vodnala SK, Cam M, et al. Identification of essential genes for cancer immunotherapy. Nature. 2017;548(7669):537-42.

251. Topalian SL, Taube JM, Anders RA, Pardoll DM. Mechanism-driven biomarkers to guide immune checkpoint blockade in cancer therapy. Nature Reviews Cancer. 2016;16(5):275-87.

252. Chen P-L, Roh W, Reuben A, Cooper ZA, Spencer CN, Prieto PA, et al. Analysis of Immune Signatures in Longitudinal Tumor Samples Yields Insight into Biomarkers of Response and Mechanisms of Resistance to Immune Checkpoint Blockade. Cancer Discovery. 2016;6(8):827.

253. Joyce JA, Fearon DT. T cell exclusion, immune privilege, and the tumor microenvironment. Science. 2015;348(6230):74-80.

254. Tumeh PC, Harview CL, Yearley JH, Shintaku IP, Taylor EJM, Robert L, et al. PD-1 blockade induces responses by inhibiting adaptive immune resistance. Nature. 2014;515(7528):568-71.

255. Larkin J, Chiarion-Sileni V, Gonzalez R, Grob JJ, Cowey CL, Lao CD, et al. Combined Nivolumab and Ipilimumab or Monotherapy in Untreated Melanoma. New England Journal of Medicine. 2015;373(1):23-34.

256. Sigalotti L, Fratta E, Coral S, Maio M. Epigenetic drugs as immunomodulators for combination therapies in solid tumors. Pharmacol Ther. 2014;142(3):339-50.

257. Chiappinelli KB, Zahnow CA, Ahuja N, Baylin SB. Combining Epigenetic and Immunotherapy to Combat Cancer. Cancer Res. 2016;76(7):1683-9.

258. Gomez S, Tabernacki T, Kobyra J, Roberts P, Chiappinelli KB. Combining epigenetic and immune therapy to overcome cancer resistance. Seminars in Cancer Biology. 2019.

259. James SR, Link PA, Karpf AR. Epigenetic regulation of X-linked cancer/germline antigen genes by DNMT1 and DNMT3b. Oncogene. 2006;25(52):6975-85.

260. Fratta E, Coral S, Covre A, Parisi G, Colizzi F, Danielli R, et al. The biology of cancer testis antigens: Putative function, regulation and therapeutic potential. Molecular Oncology. 2011;5(2):164-82.

261. Weber J, Salgaller M, Samid D, Johnson B, Herlyn M, Lassam N, et al. Expression of the MAGE-1 Tumor Antigen Is Up-Regulated by the Demethylating Agent 5-Aza-2′-Deoxycytidine. Cancer Research. 1994;54(7):1766-71.

262. Fratta E, Coral S, Covre A, Parisi G, Colizzi F, Danielli R, et al. The biology of cancer testis antigens: putative function, regulation and therapeutic potential. Mol Oncol. 2011;5(2):164-82.

263. Coral S, Sigalotti L, Altomonte M, Engelsberg A, Colizzi F, Cattarossi I, et al. 5-aza-2′-deoxycytidine-induced expression of functional cancer testis antigens in human renal cell carcinoma: Immunotherapeutic implications. Clinical Cancer Research. 2002;8(8):2690-5.

264. James SR, Cedeno CD, Sharma A, Zhang W, Mohler JL, Odunsi K, et al. DNA methylation and nucleosome occupancy regulate the cancer germline antigen gene MAGEA11. Epigenetics. 2013;8(8):849-63.

265. Wischnewski F, Pantel K, Schwarzenbach H. Promoter Demethylation and Histone Acetylation Mediate Gene Expression of MAGE-A1, -A2, -A3 and A12 in Human Cancer Cells. Molecular Cancer Research. 2006;4(5):339.

266. Odunsi K, Matsuzaki J, James SR, Mhawech-Fauceglia P, Tsuji T, Miller A, et al. Epigenetic potentiation of NY-ESO-1 vaccine therapy in human ovarian cancer. Cancer Immunol Res. 2014;2(1):37-49.

267. Luo W, Wang X, Kageshita T, Wakasugi S, Karpf AR, Ferrone S. Regulation of high molecular weight-melanoma associated antigen (HMW-MAA) gene expression by promoter DNA methylation in human melanoma cells. Oncogene. 2006;25(20):2873-84.

268. Khan ANH, Gregorie CJ, Tomasi TB. Histone deacetylase inhibitors induce TAP, LMP, Tapasin genes and MHC class I antigen presentation by melanoma cells. Cancer Immunology, Immunotherapy. 2008;57(5):647-54.

269. Setiadi AF, Omilusik K, David MD, Seipp RP, Hartikainen J, Gopaul R, et al. Epigenetic Enhancement of Antigen Processing and Presentation Promotes Immune Recognition of Tumors. Cancer Research. 2008;68(23):9601.

270. Magner WJ, Kazim AL, Stewart C, Romano MA, Catalano G, Grande C, et al. Activation of MHC Class I, II, and CD40 Gene Expression by Histone Deacetylase Inhibitors. The Journal of Immunology. 2000;165(12):7017.

271. Wang L-X, Mei Z-Y, Zhou J-H, Yao Y-S, Li Y-H, Xu Y-H, et al. Low Dose Decitabine Treatment Induces CD80 Expression in Cancer Cells and Stimulates Tumor Specific Cytotoxic T Lymphocyte Responses. PLOS ONE. 2013;8(5):e62924.

272. Maeda T, Towatari M, Kosugi H, Saito H. Up-regulation of costimulatory/adhesion molecules by histone deacetylase inhibitors in acute myeloid leukemia cells. Blood. 2000;96(12):3847-56.

273. Armeanu S, Bitzer M, Lauer UM, Venturelli S, Pathil A, Krusch M, et al. Natural Killer Cell–Mediated Lysis of Hepatoma Cells via Specific Induction of NKG2D Ligands by the Histone Deacetylase Inhibitor Sodium Valproate. Cancer Research. 2005;65(14):6321.

274. López-Soto A, Folgueras AR, Seto E, Gonzalez S. HDAC3 represses the expression of NKG2D ligands ULBPs in epithelial tumour cells: potential implications for the immunosurveillance of cancer. Oncogene. 2009;28(25):2370-82.

275. Gray SM, Amezquita RA, Guan T, Kleinstein SH, Kaech SM. Polycomb Repressive Complex 2-Mediated Chromatin Repression Guides Effector CD8(+) T Cell Terminal Differentiation and Loss of Multipotency. Immunity. 2017;46(4):596-608.

276. Yang X-P, Jiang K, Hirahara K, Vahedi G, Afzali B, Sciume G, et al. EZH2 is crucial for both differentiation of regulatory T cells and T effector cell expansion. Scientific reports. 2015;5:10643-.

277. Pace L, Goudot C, Zueva E, Gueguen P, Burgdorf N, Waterfall JJ, et al. The epigenetic control of stemness in CD8+ T cell fate commitment. Science. 2018;359(6372):177.

278. Abdelsamed HA, Moustaki A, Fan Y, Dogra P, Ghoneim HE, Zebley CC, et al. Human memory CD8 T cell effector potential is epigenetically preserved during in vivo homeostasis. The Journal of experimental medicine. 2017;214(6):1593-606.

279. Pauken KE, Sammons MA, Odorizzi PM, Manne S, Godec J, Khan O, et al. Epigenetic stability of exhausted T cells limits durability of reinvigoration by PD-1 blockade. Science. 2016;354(6316):1160.

280. Ghoneim HE, Fan Y, Moustaki A, Abdelsamed HA, Dash P, Dogra P, et al. De Novo Epigenetic Programs Inhibit PD-1 Blockade-Mediated T Cell Rejuvenation. Cell. 2017;170(1):142-57.e19.

281. Ucar D, Márquez EJ, Chung C-H, Marches R, Rossi RJ, Uyar A, et al. The chromatin accessibility signature of human immune aging stems from CD8+ T cells. Journal of Experimental Medicine. 2017;214(10):3123-44.

282. Peng D, Kryczek I, Nagarsheth N, Zhao L, Wei S, Wang W, et al. Epigenetic silencing of TH1-type chemokines shapes tumour immunity and immunotherapy. Nature. 2015;527(7577):249-53.

283. Zheng H, Zhao W, Yan C, Watson CC, Massengill M, Xie M, et al. HDAC Inhibitors Enhance T-Cell Chemokine Expression and Augment Response to PD-1 Immunotherapy in Lung Adenocarcinoma. Clin Cancer Res. 2016;22(16):4119-32.

284. Wang L, Amoozgar Z, Huang J, Saleh MH, Xing D, Orsulic S, et al. Decitabine Enhances Lymphocyte Migration and Function and Synergizes with CTLA-4 Blockade in a Murine Ovarian Cancer Model. Cancer Immunol Res. 2015;3(9):1030-41.

285. Tumes Damon J, Onodera A, Suzuki A, Shinoda K, Endo Y, Iwamura C, et al. The Polycomb Protein Ezh2 Regulates Differentiation and Plasticity of CD4+ T Helper Type 1 and Type 2 Cells. Immunity. 2013;39(5):819-32.

286. Allan RS, Zueva E, Cammas F, Schreiber HA, Masson V, Belz GT, et al. An epigenetic silencing pathway controlling T helper 2 cell lineage commitment. Nature. 2012;487(7406):249-53.

287. Speiser DE, Ho P-C, Verdeil G. Regulatory circuits of T cell function in cancer. Nature Reviews Immunology. 2016;16(10):599-611.

288. Lu L, Barbi J, Pan F. The regulation of immune tolerance by FOXP3. Nature Reviews Immunology. 2017;17(11):703-17.

289. DuPage M, Chopra G, Quiros J, Rosenthal WL, Morar MM, Holohan D, et al. The Chromatin-Modifying Enzyme Ezh2 Is Critical for the Maintenance of Regulatory T Cell Identity after Activation. Immunity. 2015;42(2):227-38.

290. Delacher M, Imbusch CD, Weichenhan D, Breiling A, Hotz-Wagenblatt A, Träger U, et al. Genome-wide DNA-methylation landscape defines specialization of regulatory T cells in tissues. Nature Immunology. 2017;18(10):1160-72.

291. Zhu H, Bengsch F, Svoronos N, Rutkowski MR, Bitler BG, Allegrezza MJ, et al. BET Bromodomain Inhibition Promotes Anti-tumor Immunity by Suppressing PD-L1 Expression. Cell Rep. 2016;16(11):2829-37.

292. Abel AM, Yang C, Thakar MS, Malarkannan S. Natural Killer Cells: Development, Maturation, and Clinical Utilization. Frontiers in Immunology. 2018;9:1869.

293. Yin J, Leavenworth JW, Li Y, Luo Q, Xie H, Liu X, et al. Ezh2 regulates differentiation and function of natural killer cells through histone methyltransferase activity. Proc Natl Acad Sci U S A. 2015;112(52):15988-93.

294. Bugide S, Green MR, Wajapeyee N. Inhibition of Enhancer of zeste homolog 2 (EZH2) induces natural killer cell-mediated eradication of hepatocellular carcinoma cells. Proc Natl Acad Sci U S A. 2018;115(15):E3509-E18.

295. Cassetta L, Pollard JW. Targeting macrophages: therapeutic approaches in cancer. Nat Rev Drug Discov. 2018.

296. Mantovani A, Marchesi F, Malesci A, Laghi L, Allavena P. Tumour-associated macrophages as treatment targets in oncology. Nat Rev Clin Oncol. 2017;14(7):399-416.

297. Hugo W, Zaretsky JM, Sun L, Song C, Moreno BH, Hu-Lieskovan S, et al. Genomic and Transcriptomic Features of Response to Anti-PD-1 Therapy in Metastatic Melanoma. Cell. 2016;165(1):35-44.

298. Zheng QF, Wang HM, Wang ZF, Liu JY, Zhang Q, Zhang L, et al. Reprogramming of histone methylation controls the differentiation of monocytes into macrophages. FEBS J. 2017;284(9):1309-23.

299. Zhang X, Wang Y, Yuan J, Li N, Pei S, Xu J, et al. Macrophage/microglial Ezh2 facilitates autoimmune inflammation through inhibition of Socs3. Journal of Experimental Medicine. 2018;215(5):1365-82.

300. Neele AE, de Winther MPJ. Repressing the repressor: Ezh2 mediates macrophage activation. J Exp Med. 2018;215(5):1269-71.

301. Phan AT, Goldrath AW, Glass CK. Metabolic and Epigenetic Coordination of T Cell and Macrophage Immunity. Immunity. 2017;46(5):714-29.

302. Park SH, Kang K, Giannopoulou E, Qiao Y, Kang K, Kim G, et al. Type I interferons and the cytokine TNF cooperatively reprogram the macrophage epigenome to promote inflammatory activation. Nature Immunology. 2017;18(10):1104-16.

303. Piccolo V, Curina A, Genua M, Ghisletti S, Simonatto M, Sabò A, et al. Opposing macrophage polarization programs show extensive epigenomic and transcriptional cross-talk. Nature Immunology. 2017;18(5):530-40.

304. Liu P-S, Wang H, Li X, Chao T, Teav T, Christen S, et al. α-ketoglutarate orchestrates macrophage activation through metabolic and epigenetic reprogramming. Nature Immunology. 2017;18(9):985-94.

305. Guerriero JL, Sotayo A, Ponichtera HE, Castrillon JA, Pourzia AL, Schad S, et al. Class IIa HDAC inhibition reduces breast tumours and metastases through anti-tumour macrophages. Nature. 2017;543(7645):428-32.

306. Pan W, Zhu S, Qu K, Meeth K, Cheng J, He K, et al. The DNA Methylcytosine Dioxygenase Tet2 Sustains Immunosuppressive Function of Tumor-Infiltrating Myeloid Cells to Promote Melanoma Progression. Immunity. 2017;47(2):284-97.e5.

307. Tesone AJ, Rutkowski MR, Brencicova E, Svoronos N, Perales-Puchalt A, Stephen TL, et al. Satb1 Overexpression Drives Tumor-Promoting Activities in Cancer-Associated Dendritic Cells. Cell Reports. 2016;14(7):1774-86.

308. Brogdon JL, Xu Y, Szabo SJ, An S, Buxton F, Cohen D, et al. Histone deacetylase activities are required for innate immune cell control of Th1 but not Th2 effector cell function. Blood. 2006;109(3):1123-30.

309. Lander ES, Linton LM, Birren B, Nusbaum C, Zody MC, Baldwin J, et al. Initial sequencing and analysis of the human genome. Nature. 2001;409(6822):860-921.

310. Niwa O, Sugahara T. 5-Azacytidine induction of mouse endogenous type C virus and suppression of DNA methylation. Proceedings of the National Academy of Sciences of the United States of America. 1981;78(10):6290-4.

311. Conklin KF, Coffin JM, Robinson HL, Groudine M, Eisenman R. Role of methylation in the induced and spontaneous expression of the avian endogenous virus ev-1: DNA structure and gene products. Molecular and cellular biology. 1982;2(6):638-52.

312. Roulois D, Loo Yau H, Singhania R, Wang Y, Danesh A, Shen SY, et al. DNA-Demethylating Agents Target Colorectal Cancer Cells by Inducing Viral Mimicry by Endogenous Transcripts. Cell. 2015;162(5):961-73.

313. Chiappinelli KB, Strissel PL, Desrichard A, Li H, Henke C, Akman B, et al. Inhibiting DNA Methylation Causes an Interferon Response in Cancer via dsRNA Including Endogenous Retroviruses. Cell. 2015;162(5):974-86.

314. Yang AS, Gonzalgo ML, Zingg J-M, Millar RP, Buckley JD, Jones PA. The Rate of CpG Mutation inAluRepetitive Elements within the p53 Tumor Suppressor Gene in the Primate Germline. Journal of Molecular Biology. 1996;258(2):240-50.

315. Ohtani H, Liu M, Zhou W, Liang G, Jones PA. Switching roles for DNA and histone methylation depend on evolutionary ages of human endogenous retroviruses. Genome Res. 2018;28(8):1147-57.

316. Ishak CA, Marshall AE, Passos DT, White CR, Kim SJ, Cecchini MJ, et al. An RB-EZH2 Complex Mediates Silencing of Repetitive DNA Sequences. Molecular Cell. 2016;64(6):1074-87.

317. Sheng W, LaFleur MW, Nguyen TH, Chen S, Chakravarthy A, Conway JR, et al. LSD1 Ablation Stimulates Anti-tumor Immunity and Enables Checkpoint Blockade. Cell. 2018;174(3):549-63.e19.

318. Brocks D, Schmidt CR, Daskalakis M, Jang HS, Shah NM, Li D, et al. DNMT and HDAC inhibitors induce cryptic transcription start sites encoded in long terminal repeats. Nature Genetics. 2017;49(7):1052-60.

319. Roby KF, Taylor CC, Sweetwood JP, Cheng Y, Pace JL, Tawfik O, et al. Development of a syngeneic mouse model for events related to ovarian cancer. Carcinogenesis. 2000;21:585–91.

320. Walton J, Blagih J, Ennis D, Leung E, Dowson S, Farquharson M, et al. CRISPR/Cas9-Mediated Trp53 and Brca2 Knockout to Generate Improved Murine Models of Ovarian High-Grade Serous Carcinoma. Cancer Res. 2016;76(20):6118-29.

321. Forshew T, Murtaza M, Parkinson C, Gale D, Tsui DWY, Kaper F, et al. Noninvasive Identification and Monitoring of Cancer Mutations by Targeted Deep Sequencing of Plasma DNA. Science Translational Medicine. 2012;4(136):136ra68.

322. Kok RM, Smith DE, Barto R, Spijkerman AM, Teerlink T, Gellekink HJ, et al. Global DNA methylation measured by liquid chromatography-tandem mass spectrometry: analytical technique, reference values and determinants in healthy subjects. Clin Chem Lab Med. 2007;45(7):903-11.

323. Newman AC, Labuschagne CF, Vousden KH, Maddocks ODK. Use of 13C315N1-Serine or 13C515N1-Methionine for Studying Methylation Dynamics in Cancer Cell Metabolism and Epigenetics. In: Haznadar M, editor. Cancer Metabolism: Methods and Protocols. New York, NY: Springer New York; 2019. p. 55-67.

324. Kirkegaard T, Edwards J, Tovey S, McGlynn LM, Krishna SN, Mukherjee R, et al. Observer variation in immunohistochemical analysis of protein expression, time for a change? Histopathology. 2006;48(7):787-94.

325. Livak KJ, Schmittgen TD. Analysis of Relative Gene Expression Data Using Real-Time Quantitative PCR and the 2−ΔΔCT Method. Methods. 2001;25(4):402-8.

326. GeneGlobe. RT² Profiler PCR Data Analysis: Qiagen; [Available from: https://dataanalysis2.qiagen.com/pcr.

327. Corces MR, Trevino AE, Hamilton EG, Greenside PG, Sinnott-Armstrong NA, Vesuna S, et al. An improved ATAC-seq protocol reduces background and enables interrogation of frozen tissues. Nat Methods. 2017;14(10):959-62.

328. Buenrostro JD, Giresi PG, Zaba LC, Chang HY, Greenleaf WJ. Transposition of native chromatin for fast and sensitive epigenomic profiling of open chromatin, DNA-binding proteins and nucleosome position. Nat Methods. 2013;10(12):1213-8.

329. Buenrostro JD, Wu B, Chang HY, Greenleaf WJ. ATAC-seq: A Method for Assaying Chromatin Accessibility Genome-Wide. Curr Protoc Mol Biol. 2015;109:21 9 1-9.

330. Holmes N. CD45: all is not yet crystal clear. Immunology. 2006;117(2):145-55.

331. Solovjov DA, Pluskota E, Plow EF. Distinct Roles for the α and β Subunits in the Functions of Integrin αMβ2. Journal of Biological Chemistry. 2005;280(2):1336-45.

332. Scheuermann JC, de Ayala Alonso Ag Fau - Oktaba K, Oktaba K Fau - Ly-Hartig N, Ly-Hartig N Fau - McGinty RK, McGinty Rk Fau - Fraterman S, Fraterman S Fau - Wilm M, et al. Histone H2A deubiquitinase activity of the Polycomb repressive complex PR-DUB. (1476-4687 (Electronic)).

333. Dong D, Zheng L, Lin J, Zhang B, Zhu Y, Li N, et al. Structural basis of assembly of the human T cell receptor–CD3 complex. Nature. 2019;573(7775):546-52.

334. Al-Shura AN. 7 - Lymphocytes. In: Al-Shura AN, editor. Advanced Hematology in Integrated Cardiovascular Chinese Medicine: Academic Press; 2020. p. 41-6.

335. Lee PY, Wang J-X, Parisini E, Dascher CC, Nigrovic PA. Ly6 family proteins in neutrophil biology. Journal of Leukocyte Biology. 2013;94(4):585-94.

336. Tateno H, Crocker PR, Paulson JC. Mouse Siglec-F and human Siglec-8 are functionally convergent paralogs that are selectively expressed on eosinophils and recognize 6′-sulfo-sialyl Lewis X as a preferred glycan ligand. Glycobiology. 2005;15(11):1125-35.

337. Merad M, Sathe P, Helft J, Miller J, Mortha A. The dendritic cell lineage: ontogeny and function of dendritic cells and their subsets in the steady state and the inflamed setting. Annual review of immunology. 2013;31:563-604.

338. Schneider CA, Rasband WS, Eliceiri KW. NIH Image to ImageJ: 25 years of image analysis. Nature Methods. 2012;9(7):671-5.

339. Aspeslagh S, Morel D, Soria JC, Postel-Vinay S. Epigenetic modifiers as new immunomodulatory therapies in solid tumours. Ann Oncol. 2018;29(4):812-24.

340. Derissen EJ, Beijnen JH, Schellens JH. Concise drug review: azacitidine and decitabine. Oncologist. 2013;18(5):619-24.

341. Stresemann C, Lyko F. Modes of action of the DNA methyltransferase inhibitors azacytidine and decitabine. Int J Cancer. 2008;123(1):8-13.

342. Mund C, Hackanson B, Stresemann C, Lübbert M, Lyko F. Characterization of DNA Demethylation Effects Induced by 5-Aza-2′-Deoxycytidine in Patients with Myelodysplastic Syndrome. Cancer Research. 2005;65(16):7086.

343. Yang AS, Doshi KD, Choi S-W, Mason JB, Mannari RK, Gharybian V, et al. DNA Methylation Changes after 5-Aza-2′-Deoxycytidine Therapy in Patients with Leukemia. Cancer Research. 2006;66(10):5495.

344. Adair SJ, Hogan KT. Treatment of ovarian cancer cell lines with 5-aza-2′-deoxycytidine upregulates the expression of cancer-testis antigens and class I major histocompatibility complex-encoded molecules. Cancer Immunology, Immunotherapy. 2009;58(4):589-601.

345. Zhang W, Barger CJ, Link PA, Mhawech-Fauceglia P, Miller A, Akers SN, et al. DNA hypomethylation-mediated activation of Cancer/Testis Antigen 45 (CT45) genes is associated with disease progression and reduced survival in epithelial ovarian cancer. Epigenetics. 2015;10(8):736-48.

346. Woloszynska-Read A, Mhawech-Fauceglia P, Yu J, Odunsi K, Karpf AR. Intertumor and intratumor NY-ESO-1 expression heterogeneity is associated with promoter-specific and global DNA methylation status in ovarian cancer. Clin Cancer Res. 2008;14(11):3283-90.

347. Stone ML, Chiappinelli KB, Li H, Murphy LM, Travers ME, Topper MJ, et al. Epigenetic therapy activates type I interferon signaling in murine ovarian cancer to reduce immunosuppression and tumor burden. Proc Natl Acad Sci U S A. 2017;114(51):E10981-E90.

348. Ruijter AJMd, Gennip AHv, Caron HN, Kemp S, Kuilenburg ABPv. Histone deacetylases (HDACs): characterization of the classical HDAC family. Biochemical Journal. 2003;370(3):737-49.

349. Marks PA, Dokmanovic M. Histone deacetylase inhibitors: discovery and development as anticancer agents. Expert Opinion on Investigational Drugs. 2005;14(12):1497-511.

350. Marks PA, Rifkind RA, Richon VM, Breslow R, Miller T, Kelly WK. Histone deacetylases and cancer: causes and therapies. Nature Reviews Cancer. 2001;1:194.

351. Hrabeta J, Stiborova M, Adam V, Kizek R, Eckschlager T. Histone deacetylase inhibitors in cancer therapy. A review. Biomed Pap Med Fac Univ Palacky Olomouc Czech Repub. 2014;158(2):161-9.

352. Cameron EE, Bachman KE, Myöhänen S, Herman JG, Baylin SB. Synergy of demethylation and histone deacetylase inhibition in the re-expression of genes silenced in cancer. Nature Genetics. 1999;21(1):103-7.

353. Murakami T, Sato A, Chun NAL, Hara M, Naito Y, Kobayashi Y, et al. Transcriptional Modulation Using HDACi Depsipeptide Promotes Immune Cell-Mediated

Tumor Destruction of Murine B16 Melanoma. Journal of Investigative Dermatology. 2008;128(6):1506-16.

354. Yang H, Lan P, Hou Z, Guan Y, Zhang J, Xu W, et al. Histone deacetylase inhibitor SAHA epigenetically regulates miR-17-92 cluster and MCM7 to upregulate MICA expression in hepatoma. British Journal Of Cancer. 2014;112:112.

355. Yang D, Torres CM, Bardhan K, Zimmerman M, McGaha TL, Liu K. Decitabine and vorinostat cooperate to sensitize colon carcinoma cells to Fas ligand-induced apoptosis in vitro and tumor suppression in vivo. J Immunol. 2012;188(9):4441-9.

356. Structural Genomic Consortium. Epigenetics probes Collection 2018 [cited 2018 August]. Available from: https://www.thesgc.org/chemical-probes/epigenetics.

357. Schoenborn JR, Wilson CB. Regulation of Interferon-γ During Innate and Adaptive Immune Responses. Advances in Immunology. 96: Academic Press; 2007. p. 41-101.

358. Groom JR, Luster AD. CXCR3 in T cell function. Exp Cell Res. 2011;317(5):620-31.

359. Groom JR, Luster AD. CXCR3 ligands: redundant, collaborative and antagonistic functions. Immunol Cell Biol. 2011;89(2):207-15.

360. Liu M, Guo S, Stiles JK. The emerging role of CXCL10 in cancer (Review). Oncol Lett. 2011;2(4):583-9.

361. Mikucki ME, Fisher DT, Matsuzaki J, Skitzki JJ, Gaulin NB, Muhitch JB, et al. Non-redundant requirement for CXCR3 signalling during tumoricidal T-cell trafficking across tumour vascular checkpoints. Nature Communications. 2015;6(1):7458.

362. Chow MT, Ozga AJ, Servis RL, Frederick DT, Lo JA, Fisher DE, et al. Intratumoral Activity of the CXCR3 Chemokine System Is Required for the Efficacy of Anti-PD-1 Therapy. Immunity. 2019;50(6):1498-512 e5.

363. Khan AN, Tomasi TB. Histone deacetylase regulation of immune gene expression in tumor cells. Immunol Res. 2008;40(2):164-78.

364. Topper MJ, Vaz M, Chiappinelli KB, DeStefano Shields CE, Niknafs N, Yen RC, et al. Epigenetic Therapy Ties MYC Depletion to Reversing Immune Evasion and Treating Lung Cancer. Cell. 2017;171(6):1284-300 e21.

365. Sun W, Lv S, Li H, Cui W, Wang L. Enhancing the Anticancer Efficacy of Immunotherapy through Combination with Histone Modification Inhibitors. Genes (Basel). 2018;9(12).

366. Luster AD, Ravetch JV. Biochemical characterization of a gamma interferon-inducible cytokine (IP-10). The Journal of Experimental Medicine. 1987;166(4):1084.

367. Liu F, Barsyte-Lovejoy D, Li F, Xiong Y, Korboukh V, Huang XP, et al. Discovery of an in vivo chemical probe of the lysine methyltransferases G9a and GLP. J Med Chem. 2013;56(21):8931-42.

368. Tachibana M, Sugimoto K, Fukushima T, Shinkai Y. Set domain-containing protein, G9a, is a novel lysine-preferring mammalian histone methyltransferase with hyperactivity and specific selectivity to lysines 9 and 27 of histone H3. J Biol Chem. 2001;276(27):25309-17.

369. Tachibana M, Sugimoto K, Nozaki M, Ueda J, Ohta T, Ohki M, et al. G9a histone methyltransferase plays a dominant role in euchromatic histone H3 lysine 9 methylation and is essential for early embryogenesis. Genes Dev. 2002;16(14):1779-91.

370. Tachibana M, Ueda J, Fukuda M, Takeda N, Ohta T, Iwanari H, et al. Histone methyltransferases G9a and GLP form heteromeric complexes and are both crucial for methylation of euchromatin at H3-K9. Genes Dev. 2005;19(7):815-26.

371. Moore Kaitlyn E, Carlson Scott M, Camp Nathan D, Cheung P, James Richard G, Chua Katrin F, et al. A General Molecular Affinity Strategy for Global Detection and Proteomic Analysis of Lysine Methylation. Molecular Cell. 2013;50(3):444-56.

372. Greer EL, Shi Y. Histone methylation: a dynamic mark in health, disease and inheritance. Nat Rev Genet. 2012;13(5):343-57.

373. Patnaik D, Chin HG, Esteve PO, Benner J, Jacobsen SE, Pradhan S. Substrate specificity and kinetic mechanism of mammalian G9a histone H3 methyltransferase. J Biol Chem. 2004;279(51):53248-58.

374. Wu H, Chen X, Xiong J, Li Y, Li H, Ding X, et al. Histone methyltransferase G9a contributes to H3K27 methylation in vivo. Cell Res. 2011;21(2):365-7.

375. Kubicek S, O'Sullivan RJ, August EM, Hickey ER, Zhang Q, Teodoro ML, et al. Reversal of H3K9me2 by a small-molecule inhibitor for the G9a histone methyltransferase. Mol Cell. 2007;25(3):473-81.

376. Sweis RF, Pliushchev M, Brown PJ, Guo J, Li F, Maag D, et al. Discovery and development of potent and selective inhibitors of histone methyltransferase g9a. ACS Med Chem Lett. 2014;5(2):205-9.

377. Pappano WN, Guo J, He Y, Ferguson D, Jagadeeswaran S, Osterling DJ, et al. The Histone Methyltransferase Inhibitor A-366 Uncovers a Role for G9a/GLP in the Epigenetics of Leukemia. PLoS One. 2015;10(7):e0131716.

378. Vedadi M, Barsyte-Lovejoy D, Liu F, Rival-Gervier S, Allali-Hassani A, Labrie V, et al. A chemical probe selectively inhibits G9a and GLP methyltransferase activity in cells. Nature Chemical Biology. 2011;7(8):566-74.

379. Cao H, Li L, Yang D, Zeng L, Yewei X, Yu B, et al. Recent progress in histone methyltransferase (G9a) inhibitors as anticancer agents. European Journal of Medicinal Chemistry. 2019;179:537-46.

380. Kim Y, Lee HM, Xiong Y, Sciaky N, Hulbert SW, Cao X, et al. Targeting the histone methyltransferase G9a activates imprinted genes and improves survival of a mouse model of Prader-Willi syndrome. Nat Med. 2017;23(2):213-22.

381. Curry E, Green I, Chapman-Rothe N, Shamsaei E, Kandil S, Cherblanc FL, et al. Dual EZH2 and EHMT2 histone methyltransferase inhibition increases biological efficacy in breast cancer cells. Clin Epigenetics. 2015;7:84.

382. Mozzetta C, Pontis J, Fritsch L, Robin P, Portoso M, Proux C, et al. The histone H3 lysine 9 methyltransferases G9a and GLP regulate polycomb repressive complex 2-mediated gene silencing. Mol Cell. 2014;53(2):277-89.

383. Cao R, Wang L, Wang H, Xia L, Erdjument-Bromage H, Tempst P, et al. Role of Histone H3 Lysine 27 Methylation in Polycomb-Group Silencing. Science. 2002;298(5595):1039.

384. Margueron R, Reinberg D. The Polycomb complex PRC2 and its mark in life. Nature. 2011;469(7330):343-9.

385. Kuzmichev A, Nishioka K, Erdjument-Bromage H, Tempst P, Reinberg D. Histone methyltransferase activity associated with a human multiprotein complex containing the Enhancer of Zeste protein. Genes Dev. 2002;16(22):2893-905.

386. Wang Z, Zang C, Rosenfeld JA, Schones DE, Barski A, Cuddapah S, et al. Combinatorial patterns of histone acetylations and methylations in the human genome. Nature Genetics. 2008;40(7):897-903.

387. Yuan P, Han J, Guo G, Orlov YL, Huss M, Loh Y-H, et al. Eset partners with Oct4 to restrict extraembryonic trophoblast lineage potential in embryonic stem cells. Genes Dev. 2009;23(21):2507-20.

388. Bilodeau S, Kagey MH, Frampton GM, Rahl PB, Young RA. SetDB1 contributes to repression of genes encoding developmental regulators and maintenance of ES cell state. Genes Dev. 2009;23(21):2484-9.

389. Simon Jeffrey A, Kingston Robert E. Occupying Chromatin: Polycomb Mechanisms for Getting to Genomic Targets, Stopping Transcriptional Traffic, and Staying Put. Molecular Cell. 2013;49(5):808-24.

390. Coward WR, Brand OJ, Pasini A, Jenkins G, Knox AJ, Pang L. Interplay between EZH2 and G9a Regulates CXCL10 Gene Repression in Idiopathic Pulmonary Fibrosis. American journal of respiratory cell and molecular biology. 2018;58(4):449-60.

391. Srimongkolpithak N, Sundriyal S, Li F, Vedadi M, Fuchter MJ. Identification of 2,4-diamino-6,7-dimethoxyquinoline derivatives as G9a inhibitors. MedChemComm. 2014;5(12):1821-8.

392. Green IL. The biological impact of noverl dual methyltransferase inhibitors 2015.

393. Brown R, Fuchter MJ, Chapman-Rothe N, Srimongkolpithak N, Caron J, Synder J, et al. Quinazoline compounds and their use in therapy 2013 [Available from: https://patentscope.wipo.int/search/en/detail.jsf?docId=WO2013140148&recNum=4&docAn=GB2013050689&queryString=EN_ALL:nmr%20AND%20PA:%22EMORY%20UNIVERSITY%22&maxRec=364.

394. Moser B, Wolf M, Walz A, Loetscher P. Chemokines: multiple levels of leukocyte migration control. Trends Immunol. 2004;25(2):75-84.

395. Griffith JW, Sokol CL, Luster AD. Chemokines and chemokine receptors: positioning cells for host defense and immunity. Annu Rev Immunol. 2014;32:659-702.

396. Proudfoot AEI. Chemokine receptors: multifaceted therapeutic targets. Nature Reviews Immunology. 2002;2(2):106-15.

397. Ji R-R, Chasalow SD, Wang L, Hamid O, Schmidt H, Cogswell J, et al. An immune-active tumor microenvironment favors clinical response to ipilimumab. Cancer Immunology, Immunotherapy. 2012;61(7):1019-31.

398. Bedognetti D, Spivey TL, Zhao Y, Uccellini L, Tomei S, Dudley ME, et al. CXCR3/CCR5 pathways in metastatic melanoma patients treated with adoptive therapy and interleukin-2. British Journal of Cancer. 2013;109(9):2412-23.

399. Moran CJ, Arenberg DA, Huang C-C, Giordano TJ, Thomas DG, Misek DE, et al. RANTES Expression Is a Predictor of Survival in Stage I Lung Adenocarcinoma. Clinical Cancer Research. 2002;8(12):3803.

400. Humblin E, Kamphorst AO. CXCR3-CXCL9: It's All in the Tumor. Immunity. 2019;50(6):1347-9.

401. Borthwick LA. The IL-1 cytokine family and its role in inflammation and fibrosis in the lung. Semin Immunopathol. 2016;38(4):517-34.

402. Land WG. The Role of Damage-Associated Molecular Patterns in Human Diseases: Part I - Promoting inflammation and immunity. Sultan Qaboos Univ Med J. 2015;15(1):e9-e21.

403. Dinarello CA. Immunological and Inflammatory Functions of the Interleukin-1 Family. Annual Review of Immunology. 2009;27(1):519-50.

404. Dinarello CA. Interleukin-1 in the pathogenesis and treatment of inflammatory diseases. Blood. 2011;117(14):3720-32.

405. Karantanos T, Chistofides A, Barhdan K, Li L, Boussiotis VA. Regulation of T Cell Differentiation and Function by EZH2. Front Immunol. 2016;7:172.

406. Tan J, Yang X, Zhuang L, Jiang X, Chen W, Lee PL, et al. Pharmacologic disruption of Polycomb-repressive complex 2-mediated gene repression selectively induces apoptosis in cancer cells. Genes Dev. 2007;21(9):1050-63.

407. Lukens JR, Kanneganti T-D. Beyond canonical inflammasomes: emerging pathways in IL-1-mediated autoinflammatory disease. Semin Immunopathol. 2014;36(5):595-609.

408. Vince JE, Silke J. The intersection of cell death and inflammasome activation. Cell Mol Life Sci. 2016;73(11-12):2349-67.

409. Beaufort CM, Helmijr JC, Piskorz AM, Hoogstraat M, Ruigrok-Ritstier K, Besselink N, et al. Ovarian cancer cell line panel (OCCP): clinical importance of in vitro morphological subtypes. PLoS One. 2014;9(9):e103988.

410. Domcke S, Sinha R, Levine DA, Sander C, Schultz N. Evaluating cell lines as tumour models by comparison of genomic profiles. Nat Commun. 2013;4:2126.

411. Hua K-T, Wang M-Y, Chen M-W, Wei L-H, Chen C-K, Ko C-H, et al. The H3K9 methyltransferase G9a is a marker of aggressive ovarian cancer that promotes peritoneal metastasis. Molecular Cancer. 2014;13(1):189.

412. Watson ZL, Yamamoto TM, McMellen A, Kim H, Hughes CJ, Wheeler LJ, et al. Histone methyltransferases EHMT1 and EHMT2 (GLP/G9A) maintain PARP inhibitor resistance in high-grade serous ovarian carcinoma. Clinical Epigenetics. 2019;11(1):165.

413. Pan M-R, Hsu M-C, Luo C-W, Chen L-T, Shan Y-S, Hung W-C. The histone methyltransferase G9a as a therapeutic target to override gemcitabine resistance in pancreatic cancer. Oncotarget. 2016;7(38).

414. Wei L, Chiu DK-C, Tsang FH-C, Law C-T, Cheng CL-H, Au SL-K, et al. Histone methyltransferase G9a promotes liver cancer development by epigenetic silencing of tumor suppressor gene RARRES3. Journal of Hepatology. 2017;67(4):758-69.

415. Hu Y, Zheng Y, Dai M, Wang X, Wu J, Yu B, et al. G9a and histone deacetylases are crucial for Snail2-mediated E-cadherin repression and metastasis in hepatocellular carcinoma. Cancer Science. 2019;110(11):3442-52.

416. Qin J, Li Q, Zeng Z, Wu P, Jiang Y, Luo T, et al. Increased expression of G9A contributes to carcinogenesis and indicates poor prognosis in hepatocellular carcinoma. Oncology letters. 2018;15(6):9757-65.

417. Qin J, Zeng Z, Luo T, Li Q, Hao Y, Chen L. Clinicopathological significance of G9A expression in colorectal carcinoma. Oncology letters. 2018;15(6):8611-9.

418. Zhang C, Wei S, Hu J, Xiong Z. Upregulated expression of G9a is correlated with poor prognosis of gastric cancer patients. Medicine. 2019;98(48):e18212.

419. Mayr C, Helm K, Jakab M, Ritter M, Shrestha R, Makaju R, et al. The histone methyltransferase G9a: a new therapeutic target in biliary tract cancer. Human Pathology. 2018;72:117-26.

420. Cao Y-p, Sun J-y, Li M-q, Dong Y, Zhang Y-h, Yan J, et al. Inhibition of G9a by a small molecule inhibitor, UNC0642, induces apoptosis of human bladder cancer cells. Acta Pharmacologica Sinica. 2019;40(8):1076-84.

421. Tu WB, Shiah YJ, Lourenco C, Mullen PJ, Dingar D, Redel C, et al. MYC Interacts with the G9a Histone Methyltransferase to Drive Transcriptional Repression and Tumorigenesis. Cancer Cell. 2018;34(4):579-95 e8.

422. Casciello F, Al-Ejeh F, Kelly G, Brennan DJ, Ngiow SF, Young A, et al. G9a drives hypoxia-mediated gene repression for breast cancer cell survival and tumorigenesis. Proceedings of the National Academy of Sciences. 2017;114(27):7077.

423. Li H, Cai Q, Wu H, Vathipadiekal V, Dobbin ZC, Li T, et al. SUZ12 Promotes Human Epithelial Ovarian Cancer by Suppressing Apoptosis via Silencing HRK. Molecular Cancer Research. 2012;10(11):1462.

424. Rao Z-Y, Cai M-Y, Yang G-F, He L-R, Mai S-J, Hua W-F, et al. EZH2 supports ovarian carcinoma cell invasion and/or metastasis via regulation of TGF-β1 and is a predictor of outcome in ovarian carcinoma patients. Carcinogenesis. 2010;31(9):1576-83.

425. Rizzo S, Hersey JM, Mellor P, Dai W, Santos-Silva A, Liber D, et al. Ovarian cancer stem cell-like side populations are enriched following chemotherapy and overexpress EZH2. Mol Cancer Ther. 2011;10(2):325-35.

426. Lu C, Han HD, Mangala LS, Ali-Fehmi R, Newton CS, Ozbun L, et al. Regulation of Tumor Angiogenesis by EZH2. Cancer Cell. 2010;18(2):185-97.

427. Kleer CG, Cao Q, Varambally S, Shen R, Ota I, Tomlins SA, et al. EZH2 is a marker of aggressive breast cancer and promotes neoplastic transformation of breast epithelial cells. Proceedings of the National Academy of Sciences. 2003;100(20):11606.

428. Bachmann IM, Halvorsen OJ, Collett K, Stefansson IM, Straume O, Haukaas SA, et al. EZH2 expression is associated with high proliferation rate and aggressive tumor subgroups in cutaneous melanoma and cancers of the endometrium, prostate, and breast. J Clin Oncol. 2006;24(2):268-73.

429. Varambally S, Dhanasekaran SM, Zhou M, Barrette TR, Kumar-Sinha C, Sanda MG, et al. The polycomb group protein EZH2 is involved in progression of prostate cancer. Nature. 2002;419(6907):624-9.

430. Puppe J, Opdam M, Schouten PC, Jozwiak K, Lips E, Severson T, et al. EZH2 Is Overexpressed in BRCA1-like Breast Tumors and Predictive for Sensitivity to High-Dose Platinum-Based Chemotherapy. Clin Cancer Res. 2019;25(14):4351-62.

431. Zingg D, Debbache J, Schaefer SM, Tuncer E, Frommel SC, Cheng P, et al. The epigenetic modifier EZH2 controls melanoma growth and metastasis through silencing of distinct tumour suppressors. Nat Commun. 2015;6:6051.

432. Zingg D, Arenas-Ramirez N, Sahin D, Rosalia RA, Antunes AT, Haeusel J, et al. The Histone Methyltransferase Ezh2 Controls Mechanisms of Adaptive Resistance to Tumor Immunotherapy. Cell Rep. 2017;20(4):854-67.

433. Chen G, Zhu L, Yang Y, Long Y, Li X, Wang Y. Prognostic Role of Neutrophil to Lymphocyte Ratio in Ovarian Cancer: A Meta-Analysis. Technol Cancer Res Treat. 2018;17:1533033818791500-.

434. Chen F, Yin S, Niu L, Luo J, Wang B, Xu Z, et al. Expression of the Chemokine Receptor CXCR3 Correlates with Dendritic Cell Recruitment and Prognosis in Gastric Cancer. Genet Test Mol Biomarkers. 2018;22(1):35-42.

435. Kim CH, Rott L, Kunkel EJ, Genovese MC, Andrew DP, Wu L, et al. Rules of chemokine receptor association with T cell polarization in vivo. The Journal of clinical investigation. 2001;108(9):1331-9.

436. Yoneyama H, Narumi S, Zhang Y, Murai M, Baggiolini M, Lanzavecchia A, et al. Pivotal role of dendritic cell-derived CXCL10 in the retention of T helper cell 1 lymphocytes in secondary lymph nodes. The Journal of experimental medicine. 2002;195(10):1257-66.

437. Tokunaga R, Zhang W, Naseem M, Puccini A, Berger MD, Soni S, et al. CXCL9, CXCL10, CXCL11/CXCR3 axis for immune activation - A target for novel cancer therapy. Cancer Treat Rev. 2018;63:40-7.

438. Lim TS, Goh JK, Mortellaro A, Lim CT, Hammerling GJ, Ricciardi-Castagnoli P. CD80 and CD86 differentially regulate mechanical interactions of T-cells with antigen-presenting dendritic cells and B-cells. PLoS One. 2012;7(9):e45185.

439. Bronte V, Brandau S, Chen SH, Colombo MP, Frey AB, Greten TF, et al. Recommendations for myeloid-derived suppressor cell nomenclature and characterization standards. Nat Commun. 2016;7:12150.

440. Movahedi K, Laoui D, Gysemans C, Baeten M, Stange G, Van den Bossche J, et al. Different tumor microenvironments contain functionally distinct subsets of macrophages derived from Ly6C(high) monocytes. Cancer Res. 2010;70(14):5728-39.

441. Bohm S, Montfort A, Pearce OM, Topping J, Chakravarty P, Everitt GL, et al. Neoadjuvant Chemotherapy Modulates the Immune Microenvironment in Metastases of Tubo-Ovarian High-Grade Serous Carcinoma. Clin Cancer Res. 2016;22(12):3025-36.

442. Walton JB, Farquharson M, Mason S, Port J, Kruspig B, Dowson S, et al. CRISPR/Cas9-derived models of ovarian high grade serous carcinoma targeting Brca1, Pten and Nf1, and correlation with platinum sensitivity. Sci Rep. 2017;7(1):16827.

443. Loetscher M, Gerber B, Loetscher P, Jones SA, Piali L, Clark-Lewis I, et al. Chemokine receptor specific for IP10 and mig: structure, function, and expression in activated T-lymphocytes. The Journal of experimental medicine. 1996;184(3):963-9.

444. Loetscher M, Loetscher P, Brass N, Meese E, Moser B. Lymphocyte-specific chemokine receptor CXCR3: regulation, chemokine binding and gene localization. European Journal of Immunology. 1998;28(11):3696-705.

445. Yamamoto J, Adachi Y, Onoue Y, Adachi YS, Okabe Y, Itazawa T, et al. Differential expression of the chemokine receptors by the Th1- and Th2-type effect or populations within circulating CD4+ T cells. Journal of Leukocyte Biology. 2000;68(4):568-74.

446. Kuo PT, Zeng Z, Salim N, Mattarollo S, Wells JW, Leggatt GR. The Role of CXCR3 and Its Chemokine Ligands in Skin Disease and Cancer. Frontiers in Medicine. 2018;5:271.

447. Metzemaekers M, Vanheule V, Janssens R, Struyf S, Proost P. Overview of the Mechanisms that May Contribute to the Non-Redundant Activities of Interferon-Inducible CXC Chemokine Receptor 3 Ligands. Frontiers in Immunology. 2018;8:1970.

448. Kim CH, Nagata K, Butcher EC. Dendritic cells support sequential reprogramming of chemoattractant receptor profiles during naive to effector T cell differentiation. J Immunol. 2003;171(1):152-8.

449. Cella M, Jarrossay D, Facchetti F, Alebardi O, Nakajima H, Lanzavecchia A, et al. Plasmacytoid monocytes migrate to inflamed lymph nodes and produce large amounts of type I interferon. Nature Medicine. 1999;5(8):919-23.

450. Franciszkiewicz K, Boissonnas A, Boutet M, Combadiere C, Mami-Chouaib F. Role of chemokines and chemokine receptors in shaping the effector phase of the antitumor immune response. Cancer Res. 2012;72(24):6325-32.

451. Peng W, Liu C, Xu C, Lou Y, Chen J, Yang Y, et al. PD-1 Blockade Enhances T-cell Migration to Tumors by Elevating IFN-γ Inducible Chemokines. Cancer Research. 2012;72(20):5209.

452. Vivier E, Raulet DH, Moretta A, Caligiuri MA, Zitvogel L, Lanier LL, et al. Innate or adaptive immunity? The example of natural killer cells. Science. 2011;331(6013):44-9.

453. Mulé JJ, Custer M, Averbook B, Yang JC, Weber JS, Goeddel DV, et al. RANTES Secretion by Gene-Modified Tumor Cells Results in Loss of Tumorigenicity In Vivo: Role of Immune Cell Subpopulations. Human Gene Therapy. 1996;7(13):1545-53.

454. Angell H, Galon J. From the immune contexture to the Immunoscore: the role of prognostic and predictive immune markers in cancer. Curr Opin Immunol. 2013;25(2):261-7.

455. Galon J, Angell HK, Bedognetti D, Marincola FM. The continuum of cancer immunosurveillance: prognostic, predictive, and mechanistic signatures. Immunity. 2013;39(1):11-26.

456. Chen DS, Mellman I. Oncology meets immunology: the cancer-immunity cycle. Immunity. 2013;39(1):1-10.

457. Liu J, Li F, Ping Y, Wang L, Chen X, Wang D, et al. Local production of the chemokines CCL5 and CXCL10 attracts CD8(+) T lymphocytes into esophageal squamous cell carcinoma. Oncotarget. 2015;6(28):24978-89.

458. Sckisel GD, Mirsoian A, Minnar CM, Crittenden M, Curti B, Chen JQ, et al. Differential phenotypes of memory CD4 and CD8 T cells in the spleen and peripheral tissues following immunostimulatory therapy. J Immunother Cancer. 2017;5:33.

459. Qian B-Z, Li J, Zhang H, Kitamura T, Zhang J, Campion LR, et al. CCL2 recruits inflammatory monocytes to facilitate breast-tumour metastasis. Nature. 2011;475(7355):222-5.

460. Stromnes IM, Burrack AL, Hulbert A, Bonson P, Black C, Brockenbrough JS, et al. Differential Effects of Depleting versus Programming Tumor-Associated Macrophages on Engineered T Cells in Pancreatic Ductal Adenocarcinoma. Cancer Immunol Res. 2019;7(6):977-89.

461. Hathcock KS, Laszlo G, Pucillo C, Linsley P, Hodes RJ. Comparative analysis of B7-1 and B7-2 costimulatory ligands: expression and function. The Journal of experimental medicine. 1994;180(2):631-40.

462. Miller JC, Brown BD, Shay T, Gautier EL, Jojic V, Cohain A, et al. Deciphering the transcriptional network of the dendritic cell lineage. Nature Immunology. 2012;13(9):888-99.

463. Broz Miranda L, Binnewies M, Boldajipour B, Nelson Amanda E, Pollack Joshua L, Erle David J, et al. Dissecting the Tumor Myeloid Compartment Reveals Rare Activating Antigen-Presenting Cells Critical for T Cell Immunity. Cancer Cell. 2014;26(5):638-52.

464. Sánchez-Paulete AR, Cueto FJ, Martínez-López M, Labiano S, Morales-Kastresana A, Rodríguez-Ruiz ME, et al. Cancer Immunotherapy with Immunomodulatory Anti-CD137 and Anti–PD-1 Monoclonal Antibodies Requires BATF3-Dependent Dendritic Cells. Cancer Discovery. 2016;6(1):71.

465. Roberts EW, Broz ML, Binnewies M, Headley MB, Nelson AE, Wolf DM, et al. Critical Role for $CD103^{+}/CD141^{+}$ Dendritic Cells Bearing CCR7 for Tumor Antigen Trafficking and Priming of T Cell Immunity in Melanoma. Cancer Cell. 2016;30(2):324-36.

466. Salmon H, Idoyaga J, Rahman A, Leboeuf M, Remark R, Jordan S, et al. Expansion and Activation of CD103⁺ Dendritic Cell Progenitors at the Tumor Site Enhances Tumor Responses to Therapeutic PD-L1 and BRAF Inhibition. Immunity. 2016;44(4):924-38.

467. Segovia C, San Jose-Eneriz E, Munera-Maravilla E, Martinez-Fernandez M, Garate L, Miranda E, et al. Inhibition of a G9a/DNMT network triggers immune-mediated bladder cancer regression. Nat Med. 2019;25(7):1073-81.

468. Mager DL, Stoye JP. Mammalian Endogenous Retroviruses. Microbiology Spectrum. 2015;3(1).

469. Stengel S, Fiebig U, Kurth R, Denner J. Regulation of human endogenous retrovirus-K expression in melanomas by CpG methylation. Genes, Chromosomes and Cancer. 2010;49(5):401-11.

470. Gimenez J, Montgiraud C, Pichon J-P, Bonnaud B, Arsac M, Ruel K, et al. Custom human endogenous retroviruses dedicated microarray identifies self-induced HERV-W family elements reactivated in testicular cancer upon methylation control. Nucleic Acids Research. 2010;38(7):2229-46.

471. Romanish MT, Cohen CJ, Mager DL. Potential mechanisms of endogenous retroviral-mediated genomic instability in human cancer. Seminars in Cancer Biology. 2010;20(4):246-53.

472. Groh S, Schotta G. Silencing of endogenous retroviruses by heterochromatin. Cellular and Molecular Life Sciences. 2017;74(11):2055-65.

473. Kassiotis G, Stoye JP. Immune responses to endogenous retroelements: taking the bad with the good. Nat Rev Immunol. 2016;16(4):207-19.

474. Liu M, Thomas SL, DeWitt AK, Zhou W, Madaj ZB, Ohtani H, et al. Dual Inhibition of DNA and Histone Methyltransferases Increases Viral Mimicry in Ovarian Cancer Cells. Cancer Res. 2018;78(20):5754-66.

475. Zeng M, Hu Z, Shi X, Li X, Zhan X, Li X-D, et al. MAVS, cGAS, and endogenous retroviruses in T-independent B cell responses. Science. 2014;346(6216):1486.

476. Smith CC, Beckermann KE, Bortone DS, De Cubas AA, Bixby LM, Lee SJ, et al. Endogenous retroviral signatures predict immunotherapy response in clear cell renal cell carcinoma. J Clin Invest. 2018;128(11):4804-20.

477. Badal B, Solovyov A, Di Cecilia S, Chan JM, Chang L-W, Iqbal R, et al. Transcriptional dissection of melanoma identifies a high-risk subtype underlying TP53 family genes and epigenome deregulation. JCI Insight. 2017;2(9).

478. Solovyov A, Vabret N, Arora KS, Snyder A, Funt SA, Bajorin DF, et al. Global Cancer Transcriptome Quantifies Repeat Element Polarization Between Immunotherapy Responsive and T cell Suppressive Classes. bioRxiv. 2017:145946.

479. Andrews S. FastQC: a quality control tool for high throughput sequence data. 2019 [Available from: http://www.bioinformatics.babraham.ac.uk/projects/fastqc/.

480. BBMap: Joint Genome Institute; 2019 [Available from: https://sourceforge.net/projects/bbmap/.

481. Dobin A, Davis CA, Schlesinger F, Drenkow J, Zaleski C, Jha S, et al. STAR: ultrafast universal RNA-seq aligner. Bioinformatics. 2012;29(1):15-21.

482. Liao Y, Smyth GK, Shi W. The R package Rsubread is easier, faster, cheaper and better for alignment and quantification of RNA sequencing reads. Nucleic Acids Research. 2019;47(8):e47-e.

483. Love MI, Huber W, Anders S. Moderated estimation of fold change and dispersion for RNA-seq data with DESeq2. Genome Biology. 2014;15(12):550.

484. Anders S, Huber W. Differential expression analysis for sequence count data. Genome Biology. 2010;11(10):R106.

485. Ewels P, Magnusson M, Lundin S, Käller M. MultiQC: summarize analysis results for multiple tools and samples in a single report. Bioinformatics (Oxford, England). 2016;32(19):3047-8.

486. Mota A, Triviño JC, Rojo-Sebastian A, Martínez-Ramírez Á, Chiva L, González-Martín A, et al. Intra-tumor heterogeneity in TP53 null High Grade Serous Ovarian Carcinoma progression. BMC Cancer. 2015;15(1):940.

487. Yanai H, Negishi H, Taniguchi T. The IRF family of transcription factors: Inception, impact and implications in oncogenesis. Oncoimmunology. 2012;1(8):1376-86.

488. Justesen J, Hartmann R, Kjeldgaard NO. Gene structure and function of the 2′-5′-oligoadenylate synthetase family. Cellular and Molecular Life Sciences CMLS. 2000;57(11):1593-612.

489. Bergamaschi A, Tagliabue E, Sørlie T, Naume B, Triulzi T, Orlandi R, et al. Extracellular matrix signature identifies breast cancer subgroups with different clinical outcome. The Journal of Pathology. 2008;214(3):357-67.

490. Georgoudaki A-M, Prokopec Kajsa E, Boura Vanessa F, Hellqvist E, Sohn S, Östling J, et al. Reprogramming Tumor-Associated Macrophages by Antibody Targeting Inhibits Cancer Progression and Metastasis. Cell Reports. 2016;15(9):2000-11.

491. La Fleur L, Boura VF, Alexeyenko A, Berglund A, Pontén V, Mattsson JSM, et al. Expression of scavenger receptor MARCO defines a targetable tumor-associated macrophage subset in non-small cell lung cancer. International Journal of Cancer. 2018;143(7):1741-52.

492. Huang DW, Sherman BT, Lempicki RA. Systematic and integrative analysis of large gene lists using DAVID bioinformatics resources. Nature Protocols. 2009;4(1):44-57.

493. Ashburner M, Ball CA, Blake JA, Botstein D, Butler H, Cherry JM, et al. Gene Ontology: tool for the unification of biology. Nature Genetics. 2000;25(1):25-9.

494. The Gene Ontology Consortium. The Gene Ontology Resource: 20 years and still GOing strong. Nucleic Acids Research. 2018;47(D1):D330-D8.

495. Fabregat A, Jupe S, Matthews L, Sidiropoulos K, Gillespie M, Garapati P, et al. The Reactome Pathway Knowledgebase. Nucleic Acids Research. 2017;46(D1):D649-D55.

496. Kanehisa M, Goto S. KEGG: Kyoto Encyclopedia of Genes and Genomes. Nucleic Acids Research. 2000;28(1):27-30.

497. Newman AM, Liu CL, Green MR, Gentles AJ, Feng W, Xu Y, et al. Robust enumeration of cell subsets from tissue expression profiles. Nature Methods. 2015;12(5):453-7.

498. Racle J, de Jonge K, Baumgaertner P, Speiser DE, Gfeller D. Simultaneous enumeration of cancer and immune cell types from bulk tumor gene expression data. Elife. 2017;6.

499. Chen Z, Quan L, Huang A, Zhao Q, Yuan Y, Yuan X, et al. seq-ImmuCC: Cell-Centric View of Tissue Transcriptome Measuring Cellular Compositions of Immune Microenvironment From Mouse RNA-Seq Data. Frontiers in Immunology. 2018;9:1286.

500. Barbie DA, Tamayo P, Boehm JS, Kim SY, Moody SE, Dunn IF, et al. Systematic RNA interference reveals that oncogenic KRAS-driven cancers require TBK1. Nature. 2009;462(7269):108-12.

501. Subramanian A, Tamayo P, Mootha VK, Mukherjee S, Ebert BL, Gillette MA, et al. Gene set enrichment analysis: A knowledge-based approach for interpreting genome-wide expression profiles. Proceedings of the National Academy of Sciences. 2005;102(43):15545.

502. Mootha VK, Lindgren CM, Eriksson K-F, Subramanian A, Sihag S, Lehar J, et al. PGC-1α-responsive genes involved in oxidative phosphorylation are coordinately downregulated in human diabetes. Nature Genetics. 2003;34(3):267-73.

503. ssGSEA2.0: Broad Institute; 2019 [Available from: https://github.com/broadinstitute/ssGSEA2.0.

504. Godec J, Tan Y, Liberzon A, Tamayo P, Bhattacharya S, Butte AJ, et al. Compendium of Immune Signatures Identifies Conserved and Species-Specific Biology in Response to Inflammation. Immunity. 2016;44(1):194-206.

505. Wherry EJ, Ha S-J, Kaech SM, Haining WN, Sarkar S, Kalia V, et al. Molecular Signature of CD8+ T Cell Exhaustion during Chronic Viral Infection. Immunity. 2007;27(4):670-84.

506. Sarkar S, Kalia V, Haining WN, Konieczny BT, Subramaniam S, Ahmed R. Functional and genomic profiling of effector CD8 T cell subsets with distinct memory fates. The Journal of Experimental Medicine. 2008;205(3):625-40.

507. Baranek T, Vu Manh T-P, Alexandre Y, Maqbool Muhammad A, Cabeza Joaquin Z, Tomasello E, et al. Differential Responses of Immune Cells to Type I Interferon Contribute to Host Resistance to Viral Infection. Cell Host & Microbe. 2012;12(4):571-84.

508. Konuma T, Nakamura S, Miyagi S, Negishi M, Chiba T, Oguro H, et al. Forced expression of the histone demethylase Fbxl10 maintains self-renewing hematopoietic stem cells. Experimental Hematology. 2011;39(6):697-709.e5.

509. Chiossone L, Chaix J, Fuseri N, Roth C, Vivier E, Walzer T. Maturation of mouse NK cells is a 4-stage developmental program. Blood. 2009;113(22):5488-96.

510. Weiss JM, Bilate AM, Gobert M, Ding Y, Curotto de Lafaille MA, Parkhurst CN, et al. Neuropilin 1 is expressed on thymus-derived natural regulatory T cells, but not mucosa-generated induced Foxp3+ T reg cells. The Journal of Experimental Medicine. 2012;209(10):1723-42.

511. Haribhai D, Lin W, Edwards B, Ziegelbauer J, Salzman NH, Carlson MR, et al. A Central Role for Induced Regulatory T Cells in Tolerance Induction in Experimental Colitis. The Journal of Immunology. 2009;182(6):3461.

512. Wei G, Wei L, Zhu J, Zang C, Hu-Li J, Yao Z, et al. Global Mapping of H3K4me3 and H3K27me3 Reveals Specificity and Plasticity in Lineage Fate Determination of Differentiating CD4+ T Cells. Immunity. 2009;30(1):155-67.

513. Zheng Y, Zha Y, Spaapen RM, Mathew R, Barr K, Bendelac A, et al. Egr2-dependent gene expression profiling and ChIP-Seq reveal novel biologic targets in T cell anergy. Molecular Immunology. 2013;55(3):283-91.

514. Foster SL, Hargreaves DC, Medzhitov R. Gene-specific control of inflammation by TLR-induced chromatin modifications. Nature. 2007;447(7147):972-8.

515. Min L, Mohammad Isa SAB, Fam WN, Sze SK, Beretta O, Mortellaro A, et al. Synergism between Curdlan and GM-CSF Confers a Strong Inflammatory Signature to Dendritic Cells. The Journal of Immunology. 2012;188(4):1789.

516. Nakagawa S, Takahashi MU. gEVE: a genome-based endogenous viral element database provides comprehensive viral protein-coding sequences in mammalian genomes. Database (Oxford). 2016;2016.

517. gEVE version 1.1: Biomedical Informatics Laboratory, Tokai University School of Medicine; 2016 [Available from: http://geve.med.u-tokai.ac.jp.

518. Haase K, Mösch A, Frishman D. Differential expression analysis of human endogenous retroviruses based on ENCODE RNA-seq data. BMC Med Genomics. 2015;8:71-.

519. Bolger AM, Lohse M, Usadel B. Trimmomatic: a flexible trimmer for Illumina sequence data. Bioinformatics. 2014;30(15):2114-20.

520. Li H. Aligning sequence reads, clone sequences and assembly contigs with BWA-MEM. arXiv:13033997 [q-bioGN]. 2013.

521. Okonechnikov K, Conesa A, García-Alcalde F. Qualimap 2: advanced multi-sample quality control for high-throughput sequencing data. Bioinformatics (Oxford, England). 2016;32(2):292-4.

522. Picard Toolkit: Broad Institute; 2019 [Available from: http://broadinstitute.github.io/picard/.

523. Li H, Handsaker B, Wysoker A, Fennell T, Ruan J, Homer N, et al. The Sequence Alignment/Map format and SAMtools. Bioinformatics (Oxford, England). 2009;25(16):2078-9.

524. Zhang Y, Liu T, Meyer CA, Eeckhoute J, Johnson DS, Bernstein BE, et al. Model-based Analysis of ChIP-Seq (MACS). Genome Biology. 2008;9(9):R137.

525. Quinlan AR, Hall IM. BEDTools: a flexible suite of utilities for comparing genomic features. Bioinformatics. 2010;26(6):841-2.

526. Dewannieux M, Heidmann T. Endogenous retroviruses: acquisition, amplification and taming of genome invaders. Current Opinion in Virology. 2013;3(6):646-56.

527. Maksakova IA, Mager DL, Reiss D. Endogenous retroviruses. Cellular and Molecular Life Sciences. 2008;65(21):3329-47.

528. Crichton JH, Dunican DS, Maclennan M, Meehan RR, Adams IR. Defending the genome from the enemy within: mechanisms of retrotransposon suppression in the mouse germline. Cell Mol Life Sci. 2014;71(9):1581-605.

529. Hayward A, Katzourakis A. Endogenous retroviruses. Curr Biol. 2015;25(15):R644-6.

530. Rowe HM, Trono D. Dynamic control of endogenous retroviruses during development. Virology. 2011;411(2):273-87.

531. Lau CM, Broughton C, Tabor AS, Akira S, Flavell RA, Mamula MJ, et al. RNA-associated autoantigens activate B cells by combined B cell antigen receptor/Toll-like receptor 7 engagement. The Journal of Experimental Medicine. 2005;202(9):1171-7.

532. Ebert PJR, Jiang S, Xie J, Li Q-J, Davis MM. An endogenous positively selecting peptide enhances mature T cell responses and becomes an autoantigen in the absence of microRNA miR-181a. Nature Immunology. 2009;10(11):1162-9.

533. Young GR, Ploquin MJY, Eksmond U, Wadwa M, Stoye JP, Kassiotis G. Negative Selection by an Endogenous Retrovirus Promotes a Higher-Avidity CD4+ T Cell Response to Retroviral Infection. PLOS Pathogens. 2012;8(5):e1002709.

534. Mullins CS, Linnebacher M. Endogenous retrovirus sequences as a novel class of tumor-specific antigens: an example of HERV-H env encoding strong CTL epitopes. Cancer Immunology, Immunotherapy. 2012;61(7):1093-100.

535. Rakoff-Nahoum S, Kuebler PJ, Heymann JJ, E Sheehy M, Ortiz GM, S Ogg G, et al. Detection of T lymphocytes specific for human endogenous retrovirus K (HERV-K) in patients with seminoma. AIDS Res Hum Retroviruses. 2006;22(1):52-6.

536. Schiavetti F, Thonnard J, Colau D, Boon T, Coulie PG. A Human Endogenous Retroviral Sequence Encoding an Antigen Recognized on Melanoma by Cytolytic T Lymphocytes. Cancer Research. 2002;62(19):5510.

537. Wang-Johanning F, Radvanyi L, Rycaj K, Plummer JB, Yan P, Sastry KJ, et al. Human Endogenous Retrovirus K Triggers an Antigen-Specific Immune Response in Breast Cancer Patients. Cancer Research. 2008;68(14):5869.

538. Wentzensen N, Coy JF, Knaebel H-P, Linnebacher M, Wilz B, Gebert J, et al. Expression of an endogenous retroviral sequence from the HERV-H group in gastrointestinal cancers. International Journal of Cancer. 2007;121(7):1417-23.

539. Takahashi Y, Harashima N, Kajigaya S, Yokoyama H, Cherkasova E, McCoy JP, et al. Regression of human kidney cancer following allogeneic stem cell transplantation is associated with recognition of an HERV-E antigen by T cells. The Journal of Clinical Investigation. 2008;118(3):1099-109.

540. Kassiotis G, Stoye JP. Making a virtue of necessity: the pleiotropic role of human endogenous retroviruses in cancer. Philosophical Transactions of the Royal Society B: Biological Sciences. 2017;372(1732):20160277.

541. Nakamura M, Bax HJ, Scotto D, Souri EA, Sollie S, Harris RJ, et al. Immune mediator expression signatures are associated with improved outcome in ovarian carcinoma. Oncoimmunology. 2019;8(6):e1593811.

542. Maniati E, Berlato C, Gopinathan G, Heath O, Kotantaki P, Lakhani A, et al. Mouse Ovarian Cancer Models Recapitulate the Human Tumor Microenvironment and Patient Response to Treatment. Cell Rep. 2020;30(2):525-40 e7.

543. Perets R, Wyant GA, Muto KW, Bijron JG, Poole BB, Chin KT, et al. Transformation of the fallopian tube secretory epithelium leads to high-grade serous ovarian cancer in Brca;Tp53;Pten models. Cancer Cell. 2013;24(6):751-65.

544. Wang-Johanning F, Liu J, Rycaj K, Huang M, Tsai K, Rosen DG, et al. Expression of multiple human endogenous retrovirus surface envelope proteins in ovarian cancer. International Journal of Cancer. 2007;120(1):81-90.

545. Perry AK, Chen G, Zheng D, Tang H, Cheng G. The host type I interferon response to viral and bacterial infections. Cell Research. 2005;15(6):407-22.

546. Sharma S, tenOever BR, Grandvaux N, Zhou G-P, Lin R, Hiscott J. Triggering the Interferon Antiviral Response Through an IKK-Related Pathway. Science. 2003;300(5622):1148.

547. Kim KH, Roberts CW. Targeting EZH2 in cancer. Nat Med. 2016;22(2):128-34.

548. Gulati N, Béguelin W, Giulino-Roth L. Enhancer of zeste homolog 2 (EZH2) inhibitors. Leuk Lymphoma. 2018;59(7):1574-85.

549. Ramakrishnan S, Granger V, Rak M, Hu Q, Attwood K, Aquila L, et al. Inhibition of EZH2 induces NK cell-mediated differentiation and death in muscle-invasive bladder cancer. Cell Death Differ. 2019.

550. Cardenas H, Zhao J, Vieth E, Nephew KP, Matei D. EZH2 inhibition promotes epithelial-to-mesenchymal transition in ovarian cancer cells. Oncotarget. 2016;7(51).

551. Hu S, Yu L, Li Z, Shen Y, Wang J, Cai J, et al. Overexpression of EZH2 contributes to acquired cisplatin resistance in ovarian cancer cells in vitro and in vivo. Cancer Biology & Therapy. 2010;10(8):788-95.

552. Yi X, Guo J, Guo J, Sun S, Yang P, Wang J, et al. EZH2-mediated epigenetic silencing of TIMP2 promotes ovarian cancer migration and invasion. Scientific Reports. 2017;7(1):3568.

553. Italiano A, Soria J-C, Toulmonde M, Michot J-M, Lucchesi C, Varga A, et al. Tazemetostat, an EZH2 inhibitor, in relapsed or refractory B-cell non-Hodgkin lymphoma and advanced solid tumours: a first-in-human, open-label, phase 1 study. The Lancet Oncology. 2018;19(5):649-59.

554. Morschhauser F, Tilly H, Chaidos A, McKay P, Phillips T, Assouline S, et al. Tazemetostat for patients with relapsed or refractory follicular lymphoma: an open-label, single-arm, multicentre, phase 2 trial. The Lancet Oncology.

555. Truax AD, Thakkar M, Greer SF. Dysregulated Recruitment of the Histone Methyltransferase EZH2 to the Class II Transactivator (CIITA) Promoter IV in Breast Cancer Cells. PLOS ONE. 2012;7(4):e36013.

556. Cao Q, Yu J, Dhanasekaran SM, Kim JH, Mani RS, Tomlins SA, et al. Repression of E-cadherin by the polycomb group protein EZH2 in cancer. Oncogene. 2008;27(58):7274-84.

557. Bracken AP, Pasini D, Capra M, Prosperini E, Colli E, Helin K. EZH2 is downstream of the pRB-E2F pathway, essential for proliferation and amplified in cancer. EMBO J. 2003;22(20):5323-35.

558. Chang C-J, Yang J-Y, Xia W, Chen C-T, Xie X, Chao C-H, et al. EZH2 Promotes Expansion of Breast Tumor Initiating Cells through Activation of RAF1-b-Catenin Signaling. Cancer Cell. 2011;19(1):86-100.

559. Du J, Li L, Ou Z, Kong C, Zhang Y, Dong Z, et al. FOXC1, a target of polycomb, inhibits metastasis of breast cancer cells. Breast Cancer Research and Treatment. 2012;131(1):65-73.

560. Xu K, Wu ZJ, Groner AC, He HH, Cai C, Lis RT, et al. EZH2 oncogenic activity in castration-resistant prostate cancer cells is Polycomb-independent. Science (New York, NY). 2012;338(6113):1465-9.

561. Chen H, Tu S-w, Hsieh J-T. Down-regulation of Human DAB2IP Gene Expression Mediated by Polycomb Ezh2 Complex and Histone Deacetylase in Prostate Cancer. Journal of Biological Chemistry. 2005;280(23):22437-44.

562. Beke L, Nuytten M, Van Eynde A, Beullens M, Bollen M. The gene encoding the prostatic tumor suppressor PSP94 is a target for repression by the Polycomb group protein EZH2. Oncogene. 2007;26(31):4590-5.

563. Yu J, Cao Q, Yu J, Wu L, Dallol A, Li J, et al. The neuronal repellent SLIT2 is a target for repression by EZH2 in prostate cancer. Oncogene. 2010;29(39):5370-80.

564. Min J, Zaslavsky A, Fedele G, McLaughlin SK, Reczek EE, De Raedt T, et al. An oncogene-tumor suppressor cascade drives metastatic prostate cancer by coordinately activating Ras and nuclear factor-kappaB. Nature medicine. 2010;16(3):286-94.

565. Shin YJ, Kim J-H. The Role of EZH2 in the Regulation of the Activity of Matrix Metalloproteinases in Prostate Cancer Cells. PLOS ONE. 2012;7(1):e30393.

566. Jia N, Li Q, Tao X, Wang J, Hua K, Feng W. Enhancer of zeste homolog 2 is involved in the proliferation of endometrial carcinoma. Oncol Lett. 2014;8(5):2049-54.

567. Eskander RN, Ji T, Huynh B, Wardeh R, Randall LM, Hoang B. Inhibition of enhancer of zeste homolog 2 (EZH2) expression is associated with decreased tumor cell proliferation, migration, and invasion in endometrial cancer cell lines. International journal of gynecological cancer : official journal of the International Gynecological Cancer Society. 2013;23(6):997-1005.

568. Fan T, Jiang S, Chung N, Alikhan A, Ni C, Lee C-CR, et al. EZH2-Dependent Suppression of a Cellular Senescence Phenotype in Melanoma Cells by Inhibition of p21/CDKN1A Expression. Molecular Cancer Research. 2011;9(4):418.

569. Lee J, Son MJ, Woolard K, Donin NM, Li A, Cheng CH, et al. Epigenetic-Mediated Dysfunction of the Bone Morphogenetic Protein Pathway Inhibits Differentiation of Glioblastoma-Initiating Cells. Cancer Cell. 2008;13(1):69-80.

570. Hussain M, Rao M, Humphries AE, Hong JA, Liu F, Yang M, et al. Tobacco Smoke Induces Polycomb-Mediated Repression of Dickkopf-1 in Lung Cancer Cells. Cancer Research. 2009;69(8):3570.

571. Yan J, Ng S-B, Tay JL-S, Lin B, Koh TL, Tan J, et al. EZH2 overexpression in natural killer/T-cell lymphoma confers growth advantage independently of histone methyltransferase activity. Blood. 2013;121(22):4512-20.

572. Sudo T, Utsunomiya T, Mimori K, Nagahara H, Ogawa K, Inoue H, et al. Clinicopathological significance of EZH2 mRNA expression in patients with hepatocellular carcinoma. British journal of cancer. 2005;92(9):1754-8.

573. Weikert S, Christoph F, Köllermann J, Müller M, Schrader M, Miller K, et al. Expression levels of the EZH2 polycomb transcriptional repressor correlate with aggressiveness and invasive potential of bladder carcinomas. Int J Mol Med. 2005;16(2):349-53.

574. Raman JD, Mongan NP, Tickoo SK, Boorjian SA, Scherr DS, Gudas LJ. Increased Expression of the Polycomb Group Gene, *EZH2,* in Transitional Cell Carcinoma of the Bladder. Clinical Cancer Research. 2005;11(24):8570.

575. Morin RD, Johnson NA, Severson TM, Mungall AJ, An J, Goya R, et al. Somatic mutations altering EZH2 (Tyr641) in follicular and diffuse large B-cell lymphomas of germinal-center origin. Nature Genetics. 2010;42(2):181-5.

576. Yap DB, Chu J, Berg T, Schapira M, Cheng SWG, Moradian A, et al. Somatic mutations at EZH2 Y641 act dominantly through a mechanism of selectively altered PRC2 catalytic activity, to increase H3K27 trimethylation. Blood. 2011;117(8):2451-9.

577. Caganova M, Carrisi C, Varano G, Mainoldi F, Zanardi F, Germain P-L, et al. Germinal center dysregulation by histone methyltransferase EZH2 promotes lymphomagenesis. The Journal of clinical investigation. 2013;123(12):5009-22.

578. Sneeringer CJ, Scott MP, Kuntz KW, Knutson SK, Pollock RM, Richon VM, et al. Coordinated activities of wild-type plus mutant EZH2 drive tumor-associated hypertrimethylation of lysine 27 on histone H3 (H3K27) in human B-cell lymphomas. Proceedings of the National Academy of Sciences. 2010;107(49):20980.

579. McCabe MT, Graves AP, Ganji G, Diaz E, Halsey WS, Jiang Y, et al. Mutation of A677 in histone methyltransferase EZH2 in human B-cell lymphoma promotes hypertrimethylation of histone H3 on lysine 27 (H3K27). Proceedings of the National Academy of Sciences of the United States of America. 2012;109(8):2989-94.

580. Liu XR, Zhou LH, Hu JX, Liu LM, Wan HP, Zhang XQ. UNC0638, a G9a inhibitor, suppresses epithelialmesenchymal transitionmediated cellular migration and invasion in triple negative breast cancer. Mol Med Rep. 2018;17(2):2239-44.

581. Larkin J, Chiarion-Sileni V, Gonzalez R, Grob JJ, Cowey CL, Lao CD, et al. Combined Nivolumab and Ipilimumab or Monotherapy in Untreated Melanoma. N Engl J Med. 2015;373(1):23-34.